Horizontal Well and Near-Well Region Simulation Using Coupled Axial-Radial Productivity Models

by

©Jie Cao

A thesis submitted to the
School of Graduate Studies
in partial fulfillment of
the requirements for the degree of

Doctor of Philosophy

Faculty of Engineering and Applied Science

Memorial University of Newfoundland

November 2016

St. John's Newfoundland and Labrador

Letter of Transmittal

Abstract

Directional drilling technologies have dramatically increased the application of advanced wells in reservoir development since the 1990s, including horizontal, deviated, multilateral and smart wells. The great demand for highly accurate and efficient well models arrives from the fact that drilling technology has outpaced simulation techniques. The well model, usually coupled with the reservoir model, is crucial for productivity estimation and prediction. The main objectives of this research are to develop a well/near-well model and associated simulation techniques using coupled axial-radial productivity models for advanced wells.

The analytical coupled axial-radial flow models were recently developed and described in research notes. These ideas originate from the observation that the axial reservoir pressure gradient cannot be ignored since pressure gradients exist in horizontal wellbores. The analytical models consider both axial reservoir flow and radial well inflow in the near-well reservoir, physically representing a two dimensional problem. These models were solved under both steady state and semi-steady state conditions, using external boundary pressure and average reservoir/grid block pressure, thereby generating the coupled axial-radial productivity (CARP) models.

The main focus in this work is to apply the CARP models in the construction of a numerical scheme for horizontal well and near-well region simulation (i.e. the well/near-well model), in which wellbore hydraulics are included. In steady state and semi steady state flow, the pressure solutions are analytical in each grid block and result in curved surfaces of near-well

reservoir pressure, contrary to the constant pressure distribution used in the finite difference method. Hence, the new numerical scheme is demonstrated, and proved in the steady state case, to be a higher order method than the standard finite difference method. The simulation results show that the new method requires less grid block refinement to achieve the same accuracy compared to the finite difference method. The CPU time needed for the same grid blocks to achieve the same accuracy is greatly reduced using the new method compared to the finite difference method. This reduces the need for grid block refinement in the near-well region.

Furthermore, the numerical well/near-well models are applied in heterogeneous reservoirs and special cases where cross flow occurs. Wide permeability ranges can be dealt with in these models in a stable manner without special treatment. Both the axial and radial flow directions are solved as unknowns in these models; hence the cross flow between the well and the near-well reservoir can be represented. Besides, the new well/near-well model can be coupled with standard finite difference reservoir simulators such that both the well completion effects and remote reservoir effects are taken into consideration. An iterative coupling scheme is used in this research, and calculated examples considering unevenly distributed skin factors also demonstrate the application of the new well/near-well model and the stability of the coupling scheme.

The well/near-well model is also developed for anisotropic reservoirs using average reservoir pressure. Based on previous research notes, this is achieved through a permeability tensor used for axial reservoir flow and well inflow equations. This permeability tensor is generated using a unique transformation that converts the anisotropic media into a virtually equivalent isotropic media in the axial and radial directions. This transformation is only applied in the near-well region without changing boundary conditions, and it preserves volume, flow rates and pressure. The cylindrical near-well region is transformed into elliptical cylinders; consequently, Dietz shape factors for ellipses are used in productivity models.

Acknowledgements

I feel that it is a great privilege to have pursued a Ph.D degree at Memorial University, as well as having been involved in a very interesting research topic. It is also a great city of St. John's that I enjoyed living in just like in my hometown.

I sincerely thank my research co-supervisors, Dr. Thormod Johansen and Dr. Lesley James for their elaborate guidance, thoughtful help and financial support. You are my source of knowledge and power, without which I cannot make the progress enjoyable. I would also like to express my appreciation to my colleges in the Hibernia EOR group, whom I feel inspiring to work with. Thanks to Norah for helping me to revise all kinds of materials I wrote. Thanks also goes to the EOR lab engineers and researchers, and graduate office of Faculty of Engineering and Applied Science for the help of all kinds.

I would also like to express my most appreciation to my wife Nan Zhang, for being on the roller coaster of my life no matter up or down. Thanks to my parents and older sister for their consistent love and support, which is beyond my word to express.

Table of Contents

List of Tables

List of Figures

List of Nomenclature

Symbols

a, b, c, d, e, f	Coefficients in pressure solutions to SS and SSS flow
B	Formation volume factor
C_0	Coefficient; constant in semi-steady state flow, $[Pa/s]$
C_A	Dietz shape factor
C_t	Total compressibility , $[bar^{-1}]$
D	Diameter, $[m]$
d_c	Choke diameter, $[m]$
d_p	Pipe diameter, $[m]$
dx	Grid block length in $x-$ direction, $[m]$
dy	Grid block length in $y-$ direction, $[m]$
dz	Grid block length in $z-$ direction, $[m]$
f	Darcy friction factor
f_{tp}	Fanning friction factor
g	Gravity acceleration, $[m/s^{-2}]$
h	Depth, $[m]$
I_{ani}	Anisotropy ratio
J	Jacobian matrix
K	Formation/rock absolute permeability, $[D]$

k	Effective permeability, $[D]$
k_d	Damaged zone permeability, $[D]$
k_r	Relative permeability
$\underline{K}$	Permeability tensor, $[D]$
L	Length, $[m]$
L_w	Total well length, $[m]$
N	Number of grid blocks/segments
P, p	Pressure, $[Pa]$
Q, q	Flow rate, $[m^3/s]$
Q_{net}	Net inflow rate in semi-steady state flow, $[m^3/s]$
R, r	Radius, $[m]$
R_e	Reynolds number
R_v	Axial to radial flow velocity ratio
r_w	Wellbore radius, $[m]$
$\tilde{r_w}$	Effective wellbore radius, $[m]$
r_e	External radius, $[m]$
S	Skin
T	Transmissibility, , $[m^3/(s \cdot Pa)]$
V	Volume, $[m^3]$
v	Velocity, $[m/s]$
x	Distance in $x-$ or axial direction, $[m]$
y	Distance in $y-$ direction, $[m]$

Greek Symbols

α_1,α_2,α_3	Coefficients in axial flow for semi-steady state flow, $[m^3/(Pa \cdot s)]$
γ	Constant, equals to 1.781
μ	Viscosity, $[Pa \cdot s]$
ϕ	Porosity
ρ	Density, $[kg/m^3]$
τ	Ratio of wellbore pressure loss to reservoir drawdown
τ_{res}	Ratio of axial pressure difference to total pressure drop
τ_{well}	Ratio of wellbore pressure drop to total pressure drop
σ	Radius ratio, R/r_e
σ_0	Radius ratio, r_w/r_e
ε	Relative error terms in numerical method
ϵ	Relative error terms in numerical method
ϵ	Absolute pipe roughness, $[m]$
Γ	Space transformation
ξ	Constant, $\sqrt[4]{\frac{K_x}{K_z}}$

Subscripts

BH	Bottom hole
e	External
H	Horizontal direction
V	Vertical direction
x	Axial
r	Radial
w	Well

Unit Conversion

Parameter	SI Unit	Field Unit	Conversion factor from SI to Field (multiply)
Length	$[m]$	$[ft]$	3.281
Mass	$[kg]$	$[pound]$	2.205
Pressure	$[Pa]$	$[psi]$	$1.45 \cdot 10^{-4}$
Permeability	$[m^2]$	$[mD]$	$1.1013 \cdot 10^{15}$
Rate	$[m^3/s]$	$[stb/d]$	$5.434 \cdot 10^{5}$
Viscosity	$[Pa \cdot s]$	$[cP]$	10^{-3}

Chapter 1

Introduction and Overview

1.1 Background

The ability to accurately predict reservoir behavior and well performance is integral to petroleum engineering. Numerical reservoir simulators are powerful tools used to meet that demand. Numerical simulation techniques have been used since the 1960s and are now routine practice for most reservoir engineers. Modern reservoir simulators contain complicated packages for different types of reservoirs and recovery mechanisms. They solve the mass and momentum balance equations for multiple components in three phases (oil, gas and water) in heterogeneous and anisotropic permeable media under various boundary conditions.

An integrated oil field model represents the fluid flow from the reservoir to the wellbore and from the wellbore to the surface. The oil field model can then be divided into three parts, the reservoir model, the well model and the surface facility model. In this research, the focus is to model horizontal/directional wells, and simulate the well and near-well reservoir flow performance.

Horizontal well technologies have been widely used in the oil and gas industry since the

1990s due to improvements in drilling and completions technology. Horizontal wells (mainly defined as directionally drilled wells with long wellbores) can dramatically increase productivity by enhancing the contact area with the reservoir. They are especially suitable for thin pay zone reservoirs, naturally fractured reservoirs and reservoirs with gas/water coning.

However, simulation tools for predicting horizontal well performance have not been concurrently developed. The representation of a horizontal wellbore is more complicated than that for a vertical wellbore. Besides, as the cost of a horizontal well is much higher than that of a vertical well, the need for accurate productivity and economic evaluation of horizontal wells is significant. The cost of a new horizontal well from the surface was around 1.5 to 2.5 times (is much larger now) more than that of a vertical well in US (Joshi, 2003). It is recently reported that the average cost of horizontal well drilling ranges from \$1.8 MM to \$2.6 MM (U.S. EIA, 2016) and account for 27% to 38% of a well's total cost. As a consequence, accurate horizontal well modeling and efficient simulation techniques are in great demand.

The simulation of a horizontal well usually focuses on the flow performance in the near-well region and the wellbore hydraulics. Hence, a horizontal well simulation method should be able to calculate the pressure gradient inside the well, and to determine the flow performance into the well and in the near-well reservoir accurately. In general, the pressure and flow rates in the horizontal well and near-well reservoir are solved simultaneously or iteratively with those of the reservoir, which means that the well model is usually coupled with the reservoir model. Therefore, the complexity of the well model significantly affects the computational efficiency and convergence of the whole simulation process. A well model that is simple in form and efficient in numerical methods is required.

For advanced wells completed with downhole equipment such as valves, chokes and inflow control devices, extra features are required for the well model and simulation method. The pressure gradients and flow rate variation through these downhole devices and in the annulus need to be accurately represented. In the case of multiphase flow, slippage effects need to be considered and local fluid properties, instead of overall averages, need to be calculated.

If cross flow occurs (Holmes, 2001), for example in cases with completion across poorly communicating reservoir compartments or with an annulus packer, the well model should provide capabilities to determine the cross flow.

The simulation model should also be capable of incorporating the effects of permeability anisotropy and permeability heterogeneity (hereafter termed anisotropy and heterogeneity). In general, a reservoir formation has different horizontal and vertical permeabilities, and the vertical permeability (K_V) is usually smaller than the horizontal permeability (K_H) (Lake, 1988). The reservoir is considered severely anisotropic if the vertical to lateral permeability ratio (K_V/K_H) is smaller than 0.1. The horizontal well productivity may be dramatically reduced in a severely anisotropic formation since the vertical flow is restricted. Hence, ignoring anisotropy could result in large overestimation of well productivity in an anisotropic reservoir. The optimization of the well trajectory is important in this case. The effect of well deviation in anisotropic media can be treated using the deviation skin factor (Cinco-Lay et al., 1975), which can be added to the well inflow equations directly.

Reservoir heterogeneity is another significant factor in simulating the flow performance and pressure in the near-well region. Many reservoir properties (for example permeability, porosity and net-to-gross ratio) are often heterogeneous. In addition to formation heterogeneity, formation damage caused during drilling, completion and formation stimulation through acidizing and fracturing contribute to heterogeneity in the near-well region. In this region, the pressure and flow rates change sharply and are therefore sensitive to heterogeneity.

Another challenge in near-well region simulation is choosing appropriate simulation grids. This problem stems from the difference in flow patterns and scales between the reservoir and the wellbore. It is not sufficiently accurate to use coarse grid blocks only and not efficient to use all fine grid blocks. A better choice is a combination of coarse grids for the reservoir and fine grids for the wellbore and near-well region. Local grid refinements (LGR) serve this purpose in the near-well region, where pressure and saturation change sharply. LGR, using Cartesian, hybrid grids or unstructured grids, improve the prediction of fluid saturation

and pressure distribution (Pedrosa and Aziz, 1986; Palagi and Aziz, 1994; Karimi-Fard and Durlofsky, 2012). The increase in the number of grid blocks in LGR results in increased calculation time, however, is not guaranteed to improve accuracy (Aziz, 1993).

Multiscale methods are also an available option in choosing appropriate and efficient grid systems. The major advantage of this approach is that various degrees of grid resolution and flexible grids are allowed. Multiscale methods were developed in the context of finite element methods (Chen and Hou, 2003), finite volume methods (Jenny et al., 2003 and Wolfsteiner et al., 2006) and mixed finite element mehtods (Krogstad and Durlofsky, 2007). It is challenging to choose a grid system and a numerical method since the performance of each method varies from case to case. The finite difference method is a major numerical method that is widely used in commercial simulation software. Further research is needed into other possible numerical methods and flexible grids (like locally orthogonal grids and unstructured grids) before they become widely used.

All the aforementioned requirements and challenges provide strong motivation to develop a highly efficient and accurate simulation technique for horizontal wells and the near-well region. This research generally aims at developing modeling and simulation techniques (finite difference method) that can be used to improve simulation of the flow performance. These objectives are achieved through the application of Coupled Axial-Radial Productivity (CARP) models and associate higher order numerical techniques in the new near-well/well model.

1.2 Objectives and methodology outline

The main objective of this research is to develop an accurate well/near-well model for horizontal wells superior to existing models. This numerical model strives to i) incorporate the pressure gradient in the wellbore, ii) model the complicated flow performance in the near-well region, iii) consider the anisotropy and heterogeneity in the near-well region and iv)

achieve higher order numerical efficiency. These four capabilities are significant in practice and are crucial in predicting the well productivity efficiently.

It is usually assumed that the well inflow is radial and normal to the wellbore trajectory, as shown in Figure 1.1 (a). This is based on the assumption that the wellbore is a line source with infinite conductivity. In this case, the pressure inside the wellbore is uniform, which ignores pressure losses. However, the frictional pressure loss cannot be ignored for long horizontal and advanced wells. This implies that the pressure losses in the near-well reservoir along the well trajectory cannot be ignored either. As a result, both inflow into the well (radial component of the flux) and the axial flow along the well trajectory (axial component of the flux) exist, as is shown in Figure 1.1 (b). This physical analysis motivates the development of the coupled axial and radial flow model as an accurate representation of the flow performance in the near-well region.

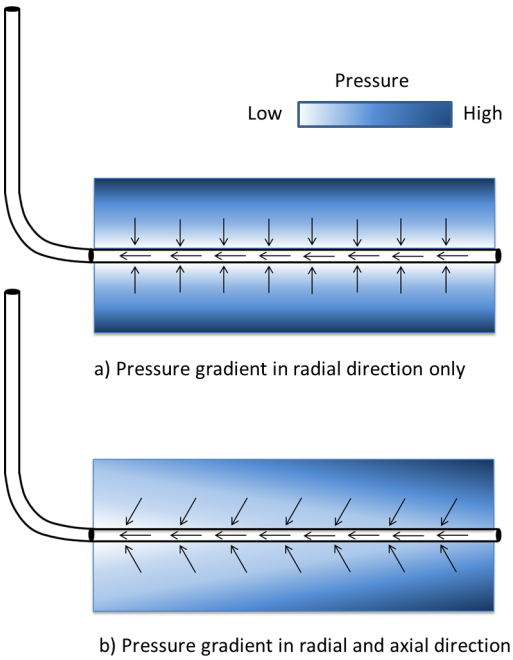

Figure 1.1: Pressure distribution in the near-well region

Most current simulators, for example Eclipse^{TM} and NETool^{TM}, represent well inflow using simple radial productivity models and solve the axial flow numerically. The coupled axial-

radial flow model, the fundamental mathematical model studied in this research, represents axial reservoir flow along the wellbore and radial inflow into the well simultaneously. It represents a two-dimensional physical problem while the classical model (radial flow model) represents an one-dimensional problem. It is solved analytically under different flow conditions. The analytical solutions provide coupled axial-radial productivity equations and are implemented in each well and near-well reservoir segment. The use of the new productivity model to simulate flow in the horizontal well and near-well region, together with the numerical performance compared to standard finite difference methods, will be investigated.

The first objective in this research was to present a comprehensive description of the CARP model by solving the coupled axial-radial flow model under different boundary conditions. The analytical solutions to the coupled axial-radial flow are generated for two different types of flow conditions, steady state flow (Johansen, 2012a) and semi-steady state flow (Johansen, 2012b). The solutions are developed using external boundary pressure and average reservoir (the near-well reservoir) pressure. This guarantees the flexibility of using the new productivity model in numerical simulations.

The second objective is to implement the coupled axial-radial productivity model in the numerical simulation to determine the flow performance in the wellbore and near-well region. This numerical algorithm is proved to be a high-order method. It is also applicable to heterogeneous reservoirs and special cases with cross flow. The results indicate that it achieves the same accuracy with fewer grid blocks as the standard finite difference method. Accuracy and efficiency are discussed based on several comparisons with standard finite difference methods subject to grid refinements.

The third objective is to develop integrated simulation techniques to incorporate the anisotropy effects on the near-well reservoir. A widely used mathematical transformation, described by Muskat (1937), is applied in the near-well region to convert the anisotropic media into a virtual isotropic media by stretching the dimensions. The objective here is to determine the new permeabilities in the near-well region.

The structure of the research methodology development is shown in Figure 1.2. The research notes referenced above first solved the coupled axial-radial flow model and presented the methodology of anisotropy treatment. The major challenges in this research thesis were to apply the new productivity models (CARP) in numerical simulation of well and near-well flow performance. This well/near-well model is capable of incorporating pressure losses in the wellbore, dealing with heterogeneous and anisotropic media, representing cross flow in near-well reservoir, predicting well inflow and axial reservoir flow rates accurately and coupling with the reservoir model in a stable manner.

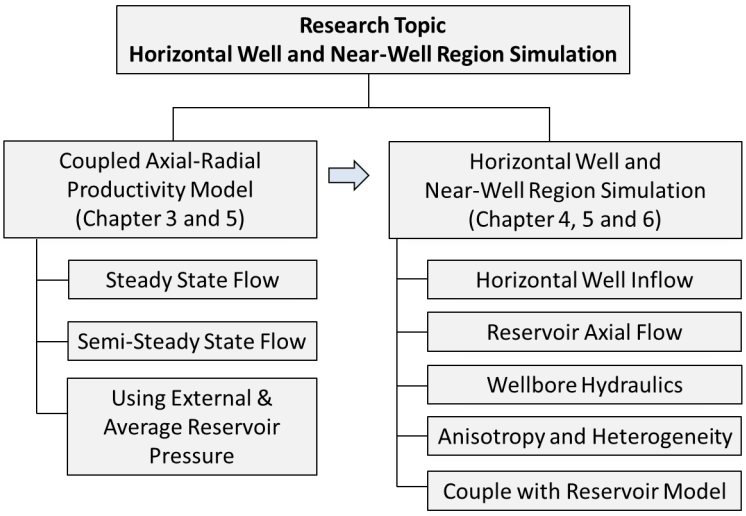

Figure 1.2: The structure of this research development

A literature review of related topics is given in Chapter 2. The body of the research is presented in four manuscripts. The first manuscript in Chapter 3 (Johansen et al., 2015) focuses on the new analytical model for coupled axial-radial flow. The coupled axial-radial model solution for steady state flow is developed and applied to the horizontal well productivity calculation. The analytical solution results in a linear pressure distribution in the axial direction and a logarithmic pressure distribution in the radial direction. The analytical solution is investigated for two special cases: it reduces to the classical radial inflow model when the axial pressure gradient is zero and reduces to the linear Darcy equation when radial inflow is zero. The new productivity model is also used to evaluate the well

flow rates when the skin effect is included. Using the new model, the axial to radial flow ratio is calculated to quantify the importance of including axial flow in calculations of well performance and axial flow distribution.

The second manuscript is presented in Chapter 4 (Cao et al., 2015). In this manuscript, the new productivity model is implemented in the formulation of numerical schemes for horizontal well and near-well region simulation (well/near-well model). The analytical solution is applied in each segment of wellbore and near-well region, in which the reservoir pressure is linear and logarithmic in the axial and radial directions, respectively. The mass and momentum balance equations, together with the nonlinear hydraulic equations, are solved numerically using Newton-Raphson iterative methods. It is proved that this numerical scheme is a high-order method compared to the standard finite difference method. The numerical results from the new method and a standard finite difference method are compared. The results show that this high order method is a substantial improvement of the standard method demanding fewer grid blocks to achieve the same accuracy. The numerical solution also verifies that the axial flow in the reservoir in general cannot be ignored. Furthermore, the application of the new well/near-well model to heterogeneous reservoirs, cross flow cases, formation damaged reservoirs, and coupling with standard finite difference reservoir simulators are presented. These applications will be considered as additional publications.

In Chapter 5, the analytical model for coupled axial-radial flow together with its numerical application in near-well region modeling are presented. It includes the third manuscript focusing on analytical solution using CARP for semi-steady state flow, which has been accepted by the International Journal of Petroleum Engineering (Johansen et al., 2016a). This model results in a quadratic pressure profile in the axial direction and a quadratic-logarithmic pressure profiles in the radial direction. The analytical solution reduces to the classical inflow equation for semi-steady state flow when the axial flow is ignored. The new productivity equations are formulated by using both external pressure and average

reservoir pressure in addition to flowing wellbore pressure. Under certain simplifications, they are proven to be identical with classical well inflow equations in terms of both external and average reservoir pressure. Furthermore, the analytical solution is implemented in a numerical simulation of a horizontal well and near-well reservoir. The simulation result is presented and compared with that from using standard finite difference methods, in which the axial flow is determined numerically based on linear Darcy flow. It is also shown that the new method is a substantial improvement over standard finite difference methods in that it requires one to two orders of magnitudes of grid blocks less to achieve the same accuracy. The numerical applications for semi-steady state flow will be considered as an additional publication.

In the forth manuscript (Cao et al., 2016) in Chapter 6, methodology to apply the coupled axial and radial productivity model in an anisotropic reservoir is presented. The analytical solution to coupled axial and radial flow in semi-steady state flow is generated using average reservoir pressure. This solution brings flexibility in choosing the configuration of reservoir grids and only requires the Dietz shape factor of the grid configuration. It also keeps consistency with the classical semi-steady state well inflow equations using average reservoir pressure. A transformation method (Johansen et al., 2016b) is applied to convert the anisotropic reservoir to an equal virtual isotropic media in the cross sectional plane. This transformation preserves the volume and pressure, however transforms the circular near-well cylinder into an elliptical cylinder. This requires the Dietz shape factor of the ellipse, which is determined numerically in this paper. The coupled axial and radial productivity model is implemented in the numerical model taking into consideration the anisotropy and wellbore hydraulics.

In Chapter 7, the main conclusions from the research are summarized and potential further research is discussed.

In general, the newly developed well/near-well model incorporates coupled axial-radial flow analytically, and also incorporates wellbore hydraulics, anisotropy and heterogeneity in the

near-well reservoir. The high efficiency and accuracy of the methods reduce the need for local grid refinement in reservoir simulation. This will be revealed and proved step-by-step through the research work in this thesis.

1.3 Co-authorship Statement

The thesis is presented in the manuscript format, consisting of four manuscripts in Chapters 3 to 6. All four papers are co-authored with Dr. Johansen and Dr. James and the research work is under the supervision of both. They are in agreement with my thesis format using these four manuscripts.

The four papers are developed step-by-step in the logic of methodology development to simulate horizontal well and near-well reservoir flow performance. The first one presented the CARP model in steady state flow, followed by numerical methods of using the new model in the second paper. The analytical model is extended to semi-steady state flow condition and numerical application in the third paper. The fourth paper considers reservoir anisotropy and presents applications of new simulation methods in anisotropic reservoirs.

Focusing on the horizontal well and near-well reservoir, the research comprises both analytical model and numerical simulation techniques. The initial derivation of the coupled axial-radial flow model was presented in (Johansen, 2012a) for steady state flow and (Johansen, 2012b) for semi-steady state flow. The thesis author contribute to the further developments of these models. The development of numerical well/near-well model and associated simulation techniques together with systematic case studies are attributable to the thesis author.

Chapter 2

Literature Review

The literature reviewed is divided into two major sections. The first section focuses on well productivity modeling, including analytical and numerical approaches. It summarizes important and useful productivity models and associated boundary conditions and limitations. The second section presents the results of previous research on simulation techniques for the near-well region, including choosing appropriate and efficient grid systems, and flow performance modeling in the near-well region.

2.1 Horizontal/Advanced well modeling

2.1.1 Horizontal well productivity models

The classical productivity models are solutions to one-dimensional radial flow for vertical wells at different flow conditions (steady state, transient and semi-steady state flow). In reservoir simulation, well grid block representation methods have been developed and used for vertical wells (Peaceman, 1983). The simple equivalent wellbore radius is used in the inflow equation, which makes the model popular for vertical wells. This approach, however,

cannot be directly used for horizontal wells because of reservoir anisotropy. Various other approaches, including analytical and numerical models, have been developed to estimate horizontal well productivity.

Most of the analytical horizontal well models assume steady state (Joshi, 1988) and semi-steady state flow conditions (Babu and Odeh, 1989), which apply to certain shapes of reservoirs, such as a cuboid, elliptical cylinder or ellipsoid. As an example, a horizontal well draining from an elliptical cylinder geometry (shown in Figure 2.1) has the steady-state inflow equation given by Joshi (1988) as

$$q = \frac{2\pi k_H h \Delta p}{\mu B_o \left\{ ln\left[\frac{a+\sqrt{a^2-(L/2)^2}}{L/2}\right] + \frac{\beta h}{L}\left[ln\left(\frac{\beta h}{2r_w}\right) + S\right]\right\}}. \tag{2.1}$$

Here, q is the flow rate, k_H is the horizontal permeability, h is the thickness of the reservoir, Δp is the difference between external pressure (p_e) and bottom hole pressures (p_{BH}), μ is the fluid viscosity, B_o is the oil formation volume factor, L is the length of the well, a is the ellipse major half axis and β is the anisotropy ratio ($\sqrt{k_H/k_V}$). In the above equation, Joshi (1988) assumes that the lateral drainage area is an ellipse and the outer boundary pressure and bottom hole pressure are constant.

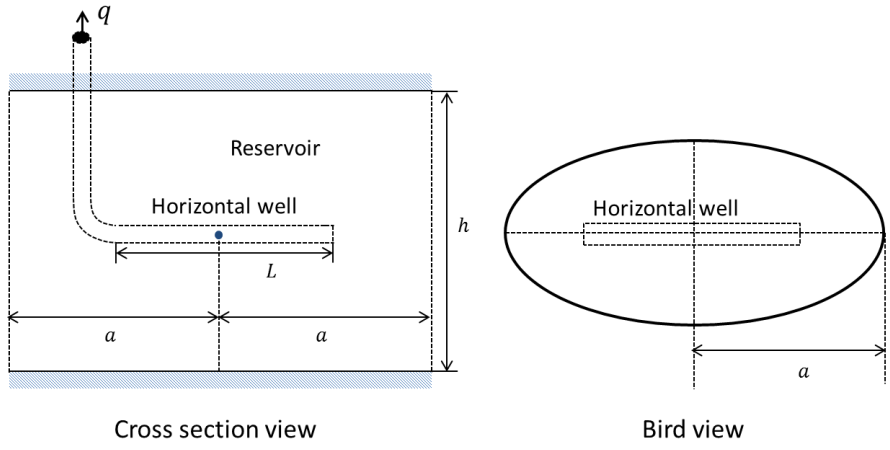

Figure 2.1: Horizontal well model in elliptical geometry (after Joshi, 1988)

Another simplified productivity equation based on the analytical solution of the governing

three-dimensional partial differential flow equation was presented by Babu and Odeh (1989). The inflow equation in semi-steady state flow is given in field units as

$$q = \frac{7.08 \times 10^{-3} b \sqrt{k_x k_z}\,(\overline{p_R} - p_{wf})}{\mu B_o \left[ln\left(\frac{\sqrt{A}}{r_w}\right) + lnC_H - 0.75 + S_R \right]}. \tag{2.2}$$

Here, k_x and k_z are the principal permeabilities, p_R is the average reservoir pressure, p_{wf} is the wellbore pressure, A is the reservoir area, r_w is the wellbore radius, C_H is the geometry factor, which is approximated by :

$$ln(C_H) = 6.28\frac{a}{h}\sqrt{k_z/k_x}\left[\frac{1}{3} - \frac{x_0}{a} + \left(\frac{x_0}{a}\right)^2\right] - ln\left(sin\frac{180 z_0}{h}\right) - 0.5 ln\left[(a/h)\sqrt{k_z/k_x}\right] - 1.088, \tag{2.3}$$

where x_0 and z_0 are coordinates of the well center. Furthermore, S_R is the skin factor resulting from partial penetration and given by Babu and Odeh (1989) for various cases. This productivity equation assumes a box reservoir as shown in Figure 2.2.

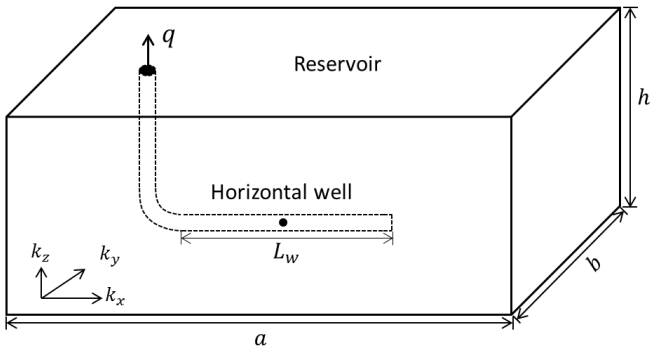

Figure 2.2: Horizontal well model in rectangular geometry (after Babu and Odeh, 1990)

Both productivity equations (Eq. (2.1) and (2.2)) have the same form as the classical inflow equations, incorporating other effects in the skin term. These equations assume 1) the influx for the horizontal well is uniform, and 2) the well is treated as the line source/sink. Under these assumptions, the total flow rate is the summation of the inflow along the length of the wellbore, while the axial reservoir flow and well inflow are symmetric about the center plane along the well and perpendicular to the well .

Most analytical models are easy to use and it is straightforward to calculate a productivity

index ($PI = q/\Delta p$). However, they are restricted by certain outer and inner boundary conditions. The outer boundary conditions include no flow boundaries with certain shaped reservoirs such as an elliptic reservoir (Giger et al., 1984), laterally infinite slab reservoir (Cinco-Lay et al., 1975) and a box reservoir (Joshi, 1988; Babu and Odeh, 1989). The inner boundary conditions are either uniform flux or uniform pressure in the wellbore. The uniform flux condition assumes that the inflow along the well trajectory is constant, which results in a symmetrical pressure distribution decreasing from both ends of the wellbore to the middle. The bottom hole pressure can be determined by taking the average pressure along the well trajectory (Kuchuk et al., 1990) or taking the midpoint pressure (Babu and Odeh, 1989). The uniform pressure condition assumes the pressure is constant inside the wellbore and the well has an infinite conductivity. The uniform pressure condition is more realistic considering that the flow rates increase from the toe to the heel in real cases.

These simple equations are of great importance for the initial estimation of well productivity and developing the productivity index. However, because the pressure losses due to friction and acceleration are ignored in these analytical models, Dikken (1990) presented an analytical method coupling single-phase turbulent well flow with stabilized reservoir flow. Pressure losses, especially those caused by friction in turbulent flow, along the horizontal well is considered as a significant factor in productivity calculations. This work was the first to consider more sophisticated and realistic conditions for predicting horizontal well productivity.

In practice, it is observed that the pressure decreases from the toe to the heel, primarily due to friction in the well, and the inflow into the well varies accordingly. A realistic wellbore pressure profile and flow rate distribution for an open-hole horizontal well and the near-well region is shown in Figure 2.3. These results can be achieved by numerical simulation methods, which is also one of the objectives of this research thesis.

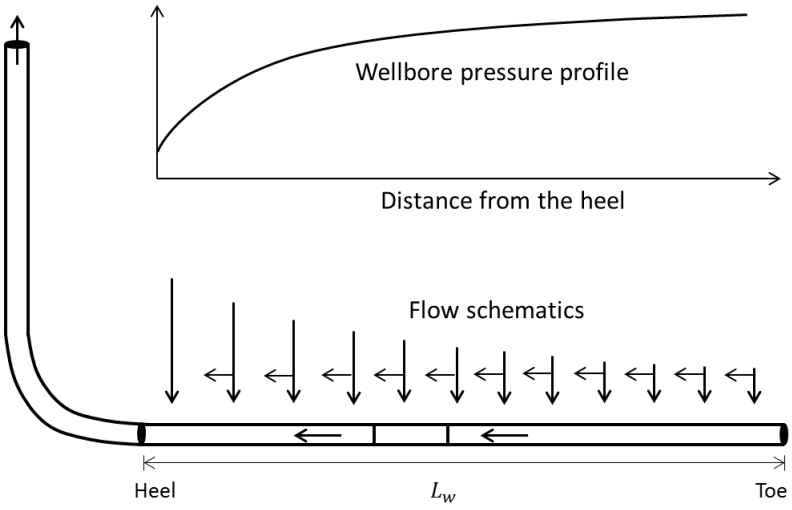

Figure 2.3: Schematics of flow rate distribution and wellbore pressure profiles

2.1.2 Pressure losses within the well

The pressure gradient within a pipe consists of three components–the friction gradient, the hydrostatic gradient and the acceleration gradient– expressed in steady state flow as

$$\frac{\partial p}{\partial x} = \tau \frac{\pi D}{A} + \rho g sin\left(\theta\right) + \rho v \frac{dv}{dx}, \tag{2.4}$$

where θ is the angle between the pipe and horizontal plane, τ is the wall shear stress; D is the well cross section diameter; A is the cross section area, v is the flow velocity, and ρ is the density of the fluid mixture for homogenized flow. In addition, the general pressure gradient due to acceleration caused by radial inflow (Schulkes et al., 1999) is

$$\left.\frac{\partial p}{\partial x}\right|_{acc}^{inflow} = \Delta\left(\rho v^2\right). \tag{2.5}$$

This is different from the pressure gradient due to acceleration caused by varying wellbore diameter, which is

$$\left.\frac{\partial p}{\partial x}\right|_{acc} = \frac{1}{2}\Delta\left(\rho v^2\right). \tag{2.6}$$

The friction factor is the ratio between wall shear stress and kinetic energy density and can be used to evaluate frictional pressure loss. For example, the Darcy friction factor results in

$$\tau = f\frac{\rho v^2}{2}. \tag{2.7}$$

The Fanning friction factor (f_{tp}) is also often used, which is $\frac{1}{4}$ of the Darcy friction factor. For a smooth pipe, the Darcy friction factor can be used to account for the pressure drop due to friction using the Blasius formula

$$f = \frac{0.3164}{Re^{1/4}}. \tag{2.8}$$

Here, Re is the Reynolds number, defined by

$$Re = \frac{\rho v D}{\mu}. \tag{2.9}$$

The flow is laminar when Reynolds number is less than 2000, turbulent when Reynolds number is larger than 4000 and transitional when Reynolds number in intermediate. The friction factor for a rough pipe is given, for example, by Haaland (1983) as

$$f = \frac{1}{[1.8\log(\frac{6.9}{Re} + (\frac{\epsilon}{3.7D})^{\frac{10}{9}})]^2}, \tag{2.10}$$

where ϵ is the absolute pipe roughness. Usually, the acceleration pressure loss can be ignored in the pressure gradient, since it is small compared to the friction pressure loss (Novy, 1996). However, the pressure loss due to the downhole gauges and valves should be accounted for in certain cases. Models for pressure loss are usually provided by the gauge manufacturer. For example, the relationship between flow rate and pressure drop across a valve, as shown in Figure 2.4, is written as

$$q = CA\sqrt{\frac{2g_c\Delta p}{\rho}}, \tag{2.11}$$

where C is the discharge coefficient of the valve and A is the cross sectional area. The flow coefficient for nozzles can be found in Crane (1957) in a chart format, given the Reynolds number in the nozzle and the ratio of the nozzle diameter to the pipe diameter (d_c/d_p).

Su and Gudmundsson (1994) conducted single phase flow experiment in perforated pipes to account the pressure loss due to well inflow, and found that four individual pressure drops, due to friction, acceleration, perforation and mixing effects, contribute to the total pressure

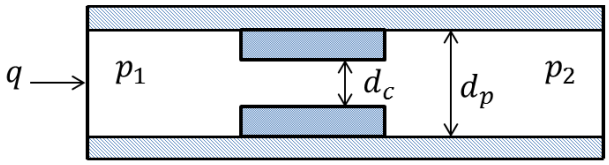

Figure 2.4: Schematic of the choke

drops. The friction pressure loss is dominant and accounts for 80% in high rate wells.

Ouyang et al. (1998) formulated the extra pressure drop that occurs when there is inflow into the wellbore. The effects of inflow into the wellbore were determined based on experiments, which can be expressed as

$$\frac{\partial p}{\partial x} = \rho_m g sin(\theta) + \frac{2 f_{tp} \rho_m V_m^2}{D} + \frac{2 q_m \rho_m V_m}{A}, \tag{2.12}$$

where ρ_m is the mixture density; V_m is the mixture volume; q_m is the mixture reservoir inflow and f_{tp} is the Fanning friction factor (Ouyang et al., 1998).

Meanwhile, Schulkes and Utvik (1998) demonstrated through experiments that the radial inflow lubricates the axial flow in the pipe if the ratio of the radial to axial flow velocity (R_v) is small. In contrast, it disturbs the axial pipe flow and causes pressure drop increase if the velocity ratio is large. The correlation of pressure loss for $R_v << 1$ was given while more experiments are required to formulate quantitative description of pressure loss for $R_v > 1$.

In cases where the well is completed with for example a liner, the fluids flow first from the reservoir to the annulus and then from the annulus to the liner/pipe. Annulus flow in these cases needs to be incorporated in the well model. The friction flow in the annulus is usually treated in the same manner as flow in a pipe, except the hydraulic diameter $D_a - D_r$ being used, where D_a and D_p is the inner annulus diameter and outer liner diameter. This can be derived easily by considering only friction term in a pipe, i.e.

$$\left.\frac{\partial p}{\partial x}\right|_{fric} = \tau \frac{\pi D}{A} = \frac{4\tau}{D}; \tag{2.13}$$

and in the annulus

$$\left.\frac{\partial p}{\partial x}\right|_{fric} = \tau\frac{\pi D_a}{A_a - A_p} + \tau\frac{\pi D_p}{A_a - A_p} = \frac{4\tau}{D_a - D_p}. \tag{2.14}$$

Schulkes and King (2002) presented the coupled hydraulic model for flow in the wellbore with an annulus and a liner (or the "base pipe" in the reference paper). The governing equations were derived by applying momentum balance equation and mass balance for single phase flow in both the annulus and the liner. The pressure gradients included three terms accounting for acceleration, friction and inflow through the pipe wall. The inflow from annulus to the liner is assumed to be similar to the flow from the reservoir to the annulus; both have linear relationship with the pressure gradient. The model was solved analytically and numerically to investigate the simultaneous effects of the reservoir boundary layer and the annulus boundary layer.

For multi-phase flow, the vertical pressure loss can be calculated by the Hagedorn-Brown correlation (1965); and the horizontal/deviated sections can be determined by the Beggs and Brill correlation (1973). Although, more advanced and accurate correlations can be found in the literature, correlations for pressure gradients in pipes are not essential to this research since only homogenized flow is considered. Fundamental equations and methods can be found in the monograph by Brill and Mukherjee (1999).

2.1.3 Methods to couple the well model to the reservoir model

The existing methods of coupling the horizontal well model and the reservoir model are reviewed in this subsection. A modular approach was initially presented for wellbore and reservoir simulation by Brekke et al. (1993). This iterative modular approach, coupling a horizontal well simulator (HOSIM) with a reservoir simulator (FRONTSIM), was used to evaluate complex completion configurations, potential cross flow and performance optimization of production or injection. This was found to be feasible and efficient in completion design optimization since fully coupled and implicit simulation was not available at that

time (1993). Simulating production for a high permeability reservoir after free gas breakthrough was achieved with satisfactory results. Several methods to speed up convergence, for example productivity index adjustment, was also discussed in this research (Brekke et al., 1993).

The "network solver", or network model, was developed for predicting long wellbore horizontal well performance (Brekke and Thompson, 1996). The network model contains three flow regions: flow in the outer reservoir, flow through the near-wellbore reservoir and flow through the well completion. An iterative coupling scheme was used in the numerical reservoir simulation for the well and near-well reservoir, and the nonlinear equations describing the relationship between pressure loss and flow rate were solved by iterative methods.

A “multisegment well model” was proposed for advanced horizontal wells by Holmes et al. (1998). In this model, the horizontal wellbore was represented by a number of segments and flow control devices were considered. The flow rate and pressure equations were fully coupled and solved implicitly. Two case studies investigated the adjusted inflow into a wellbore and compared the results with the "Well Friction Model". The results showed that the model predicts the flow path and pressure distribution accurately. The axial reservoir flow and well inflow are calculated separately based on Darcy’s law and productivity models in the multisegment well model.

Besides numerical models, a semi-analytical model for transient reservoir/wellbore coupled models for infinite and finite conductivity wellbores were developed by Penmatcha and Aziz (1999). This method applied the uniform flux model in every well segment and included friction and acceleration pressure loss between well segments. Superposition in space and time were used for each well segment under different conditions. The total flow rate was treated as the accumulation of each segment of the well, instead of the observed result that it is continuously increasing from the toe to the heel. The effect of fluid inflow was taken into consideration, while flow in the reservoir parallel to the well trajectory was ignored. The model could be used as a first estimation of horizontal well production and to compare with

other numerical simulation results. Also, the reservoir has to be homogeneous to use analytical solutions (based on the line source assumption). Heterogeneity was accounted for by a pseudo-skin factor in each segment using an overall homogeneous background permeability.

A coupled reservoir and horizontal well flow model was implemented in a three dimensional simulator by Vicente et al. (2002). It was developed for both single phase and two-phase flow and applied Local Grid Refinement (LGR) technology around the horizontal well based on Pedrosa and Aziz (1986). The horizontal well blocks were represented by linear equations of pressure difference, given by Peaceman (1978). The resulting momentum and material balances are linear equations and are solved implicitly. Based on this simulator, a number of transient case studies were used to simulate the pressure and flow rate distribution. The results were in good agreement with the well testing results and commercial simulation results using Eclipse E100 (Schlumberger, 2010).

Johansen and Khoriakov (2007) presented an iterative methodology combining the pressure gradient in the well, in the near-well reservoir and through well completions. The iterative methods for transient and steady state multiphase flow were used. In this research, such complex issues as three phase flow, general boundary conditions, phase slippage, flow regimes, multi-lateral wells, and coupled well flow and reservoir flow were considered. The reliability and accuracy of the solver were demonstrated and the complexity of advanced completions and flow regimes were included.

Khoriakov et al. (2012) proposed a transient well flow model for advanced well completions by extending the original model by Johansen and Khoriakov (2007). The procedure used to couple well flow with reservoir flow was examined, where the transient flow equation was derived and a transient tank model was used for the remote reservoir. Case studies proved the flexibility of the model and the results demonstrated the accuracy of this method.

Kabir and Sanchez (2009) presented a method to couple a commercial reservoir simulator and a commercial wellbore simulator to determine the inflow profile for horizontal wells.

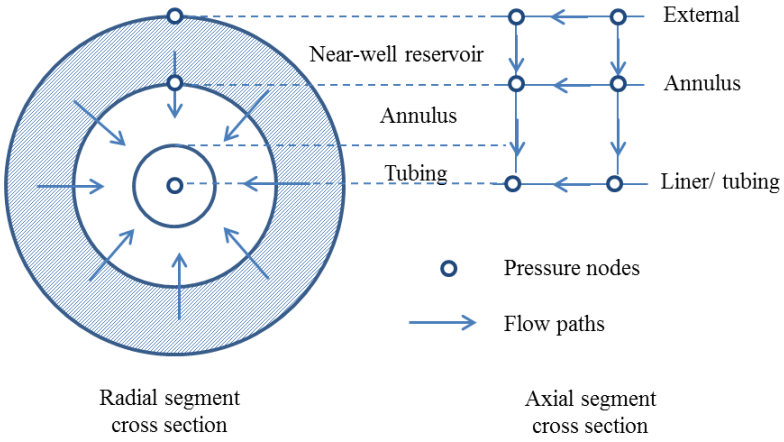

Figure 2.5: Well Model cross section view

The methodology runs the simulators separately and couples the results by sharing the boundary conditions at the interface of the reservoir and the well.

In this research thesis, the focus is on well and near-well flow modeling and simulation. The well can consist of any number of concentric (circular) cylinders representing the near-well reservoir and well completion details with possible multiple annuli, as shown in Figure 2.5. This has been coupled with a reservoir model, like Eclipse, iteratively. The coupling scheme, shown in Figure 2.6, is similar to the coupling scheme by Brekke et al. (1993), in which the inflow performance relationship was built to relate the pressure and flow rate at the sand face. The coupling used in this research will be presented in details in Section 4.5.1. It can directly deliver the pressure and flow rate from the Reservoir model to the Well model since the the Well model contains the near-well reservoir region. Details and examples of the coupling will be presented in Chapter 4. In this way, the coupled model is forced to incorporate detailed information which would not be possible if the two models were used as stand-alone models; for example the grid block pressure as influenced by large scale (remote) reservoir effects (faults, other wells ect.) and the well annulus pressures as influenced by completion details (inflow devices, perforations, any well flow restriction).

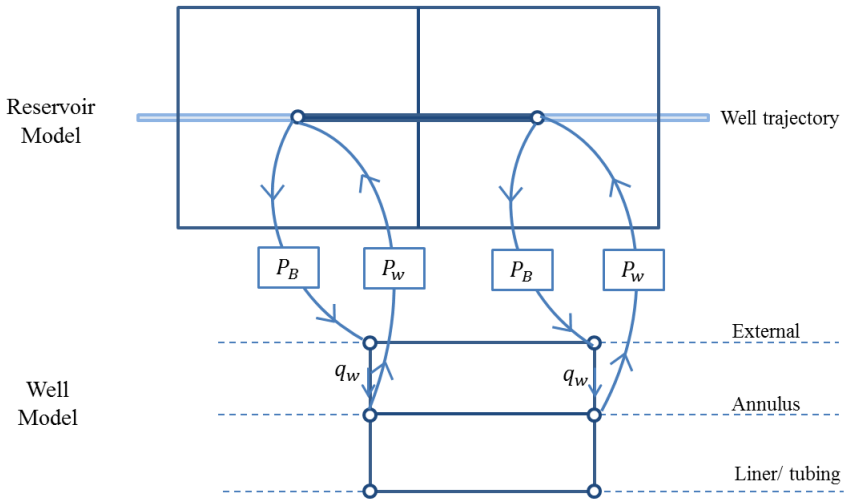

Figure 2.6: Coupling scheme with Reservoir Model and Well Model

2.2 Near-well region modeling

2.2.1 Grid system for the near-well region

Since the requirement for accuracy in simulation is increasing, much research has focused on the near-well region, where pressure and flow rates change sharply. Consider the reservoir simulation grid system with a horizontal well, as is shown in Figure 2.7. Since the reservoir grid blocks (coarse grid blocks) are larger than the wellbore grid blocks (fine grid blocks), the coarse grid system is not able to yield accurate results of wellbore pressure and flow performance in the near-well region. Also, it is not practical to use fine grids for both the near-well region and the entire reservoir. Hence, multi-scale or mixed scale simulation techniques are necessary for accuracy in the near-well region and efficiency on the reservoir scale. Local grid refinement (LGR) in the near-well region is one of the most widely used finite-difference simulation techniques.

The hybrid grid method was proposed by Pedrosa and Aziz (1986) as a better way to represent well in reservoir simulation. A hybrid grid uses a curvilinear grid (cylindrical or

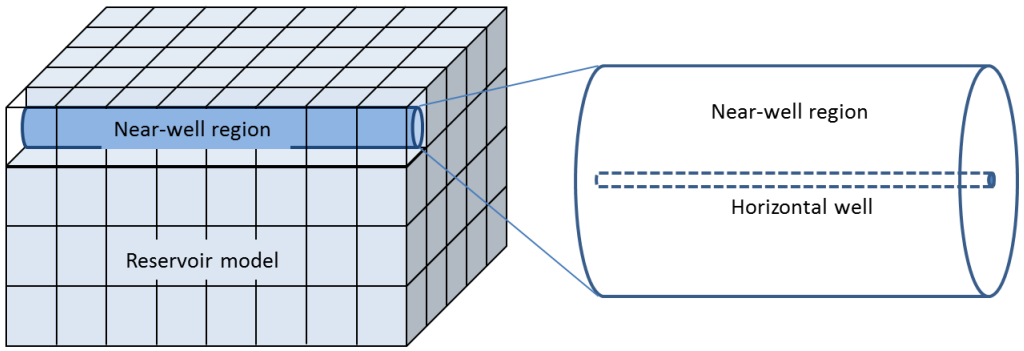

Figure 2.7: Schematic of simulation grid scale for the reservoir and near-well region

elliptical) in the near-well region and a rectangular grid elsewhere in the reservoir. A method to deal with irregular blocks in between the two types of grids was also developed. This hybrid grid technique respected the radial flow nature in the near-well region and improved the calculation of water cut and gas oil ratio. Cases were presented to demonstrate the accuracy of using hybrid grids.

The use of Voronoi grids, first introduced by Voronoi (1908), in reservoir simulation was investigated by Palagi and Aziz (1994). The Voronoi grid is a flexible gridding technique, also know as perpendicular bisection grid (PEBI). It is advantageous in cases with complicated boundary conditions since its flexibility generates arbitrary grid allocation. Examples of Voronoi grid systems are shown in Figure 2.8. These grid systems easily implement fine grids in the near-well region. The well model using a Voronoi grid was a Peaceman type (using effective wellbore radius), however, not developed specifically for horizontal well simulation.

In addition to finite difference appraoch like Pedrosa and Aziz (1986), a multiscale mixed finite element method to couple the wellbore and near-well flow was presented by Krogstad and Durlofsky (2007). This multiscale method included fine grid blocks resolving the well trajectory and coarse grid blocks representing the reservoir. Heterogeneity was considered

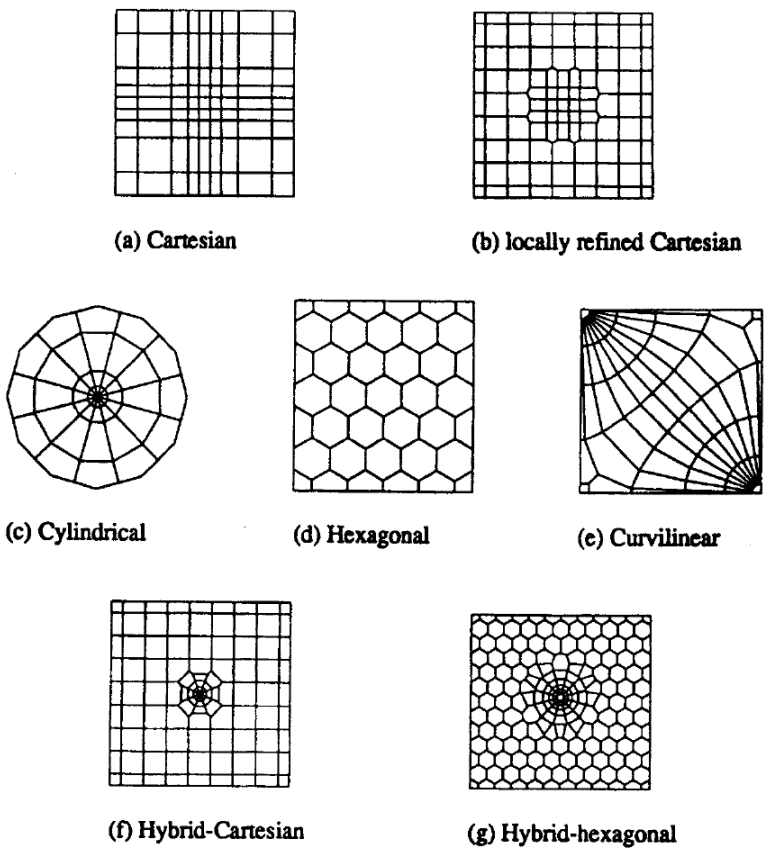

Figure 2.8: Examples of Voronoi grid systems (Palagi and Aziz, 1994)

down to the well scale based on geological interpretation. The wellbore and reservoir two-phase flow models were coupled within a multiscale finite element context. The results were compared with numerical simulations in cases of vertical and deviated wells in a heterogeneous reservoir and demonstrated the accuracy of the multiscale mixed finite element method.

Besides numerical approaches, a semi-analytical representation method was proposed to determine the well and near-well flow convergence problems in reservoir simulation (Kurtoglu et al., 2008). As opposed to the finite difference and finite element methods, this method used the analytical solution to potential problems (Green's third identity) to determine the pressure at any point in the well and near-well subdomain. The boundary values of the sub-

domain are required and can be generated from standard simulation for the reservoir taking the well as a source term. The solution domain can be divided into finite blocks, which have unique homogeneous properties, so that the method is capable of solving heterogeneous problems.

In order to account for anisotropy and heterogeneity accurately in the near-well region, fine grids of all kinds are preferable. Another approach is to use the radial upscaling method in the near-well region (Wolfsteiner and Durlofsky, 2002). The multiblock grid (globally unstructured and locally structured) approach was implemented in order to achieve a flexible grid scale. Fine grids are used along the well trajectory and well productivity is upscaled from the near-well region.

In this research thesis, cylindrical grid systems are used since the major domain of interest is the near-well region. The higher order method presented in this work can potentially decrease the need for local grid refinement.

2.2.2 Flow performance in the near-well region

The flow performance in the near-well region is greatly influenced by well completion details. Horizontal wells are usually completed using open hole, slotted liner, wire-wrapped screen, perforations or gravel-pack completion methods. The completion method can be represented by a skin factor and incorporated in the productivity index. Several models for horizontal well completion methods are presented below.

Pucknell and Clifford (1991) extended the former researches on types of well skin factors for particular cases and provided an approximation of total skin factors. They emphasized that the partial completion and deviation skin cannot be calculated separately but must be determined together. The deviation skin in their research was derived from the steady state flow equation in a Cartesian coordinate system.

Furui et al. (2002a) developed the skin factor for perforated horizontal wells analogous to the way Karakas and Tariq (1991) developed the skin factor for vertical wells. The deviation skin was divided into three parts: two-dimensional plane flow skin accounting for the existence of the wellbore in the radial flow plane, wellbore blockage skin due to the un-perforated wellbore and three-dimensional flow convergence skin.

Moreover, Furui et al. (2004a) developed a theoretical turbulence skin factor for gravel-packed completions. Three parts of pressure drops are considered for gravel pack completions: the pressure drop through the gravel between the casing and the screen (usually small and can be ignored); the pressure drop through perforation tunnels between the casing/cement and the formation; the pressure drop due to flow convergence to the perforations. Simple skin expressions for various perforation and gravel pack conditions are determined based on finite element simulation studies.

Furthermore, a comprehensive skin factor model for horizontal well completion methods was presented by Furui et al. (2004b). The model includes slotted liner, perforated liners and cased and perforated completion methods, accounting for inflow convergence, formation and perforation damage, slot plugging, turbulent flow and the interaction between these effects. It was highlighted through calculation examples that turbulence effects are significant if slots are plugged and that perforation can alleviate formation damage effects.

Besides completion skin models, a formation damage skin model was developed by Furui et al. (2002b) based on Peaceman's solution (1983) to wellbore pressure. Anisotropy and skin heterogeneity were taken into consideration, resulting in a solution analogous to Hawkin's skin equation for damaged wells (Hawkin, 1956). In the calculation example, the model presents a higher value for skin effects than a similar model proposed in Frick and Economides (1993). It also stated that the formation damage skin is relatively small in a thin reservoir in which linear flow dominates while significant in a thick reservoir in which radial flow dominates.

Hwang (2000) investigated the nonlinear interactions between near-well flow restrictions (skin factors) and presented the total skin as a nonlinear combination of individual skin factors. This research extended the investigation on the condensate dropout skin effects (non-linear) related to other skin components by Hwang and Odeh (1995). Instead of assuming that the total skin is the summation of each skin effect, it was stated that there is a strong nonlinear interaction between each skin factor (mainly four types: mechanical skin S_m, altered formation skin S_a, partial completion skin S_p and non-Darcy skin S_d). The total effective skin factor equation for a single layer reservoir was proposed as

$$S_T = S_p + \frac{1}{\gamma}\left(\frac{h}{h_p}\right) S_a + \frac{S_m}{k_{rg}(1)} + \left\{1 + \sum D_r(i)\right\} \frac{h}{h_p}^2 S_d, \tag{2.15}$$

where γ relates to the anisotropy ratio (k_V/k_H) and $\gamma = 1$ when anisotropy is ignored; $k_{rg}(1)$ is the $r-$directional gas permeability in cell 1; h is the reservoir thickness; h_p is the thickness of partially completed section; $D_r(i)$ is defined and determined in the paper. The model for a multi-layer reservoir was also given, although not presented here because of its complexity. The results were verified with simulation results using a fine grid in the near-well region.

The near-well region flow performance is also affected by the anisotropy and heterogeneity. For an anisotropic medium, the permeability is a second order tensor;

$$\underline{K} = \begin{bmatrix} K_{xx} & K_{xy} & K_{xz} \\ K_{yx} & K_{yy} & K_{yz} \\ K_{zx} & K_{zy} & K_{zz} \end{bmatrix}. \tag{2.16}$$

This means that the representation of the permeability tensor varies using different coordinate systems. When the coordinate axes are parallel to the principal permeability directions, the permeability tensor in Cartesian coordinates becomes diagonal:

$$\underline{K} = \begin{bmatrix} K_x & 0 & 0 \\ 0 & K_y & 0 \\ 0 & 0 & K_z \end{bmatrix}. \tag{2.17}$$

It is often observed, in a sandstone reservoir, that the permeabilities in the horizontal plane

(parallel to bedding) are equal (i.e. $K_x = K_y = K_H$) and are generally greater than the permeability ($K_z = K_V$) in the vertical direction (normal to bedding). A common expression of anisotropy is the vertical to horizontal anisotropy ratio, given by $I_{ani} = \sqrt{(K_V/K_H)}$. The literature reviewed below mainly implements spatial transformations to convert the real anisotropic medium into a virtual isotropic medium.

To specify the effects of anisotropy on horizontal wells, Cinco-Lay et al. (1975) first introduced the pseudo skin factor for slanted wells (including a horizontal well which has a deviation of $\pi/2$). The wells are assumed to have infinite conductivity, i.e. zero pressure gradients in the wellbore. The deviated well is treated as a line source and the line source is divided into many segments. The dimensionless wellbore pressure is found from the solution of the dimensionless diffusivity equation. The pseudo skin is the difference between dimensionless wellbore pressures for a vertical well (p_D) and a deviated well (p_{wD});

$$S_{\theta+p} = \lim_{t_D \to \infty} (p_{wD} - p_D)\,, \tag{2.18}$$

where $S_{\theta+p}$ is the pseudo skin (caused by slant and partial penetration); t_D is dimensionless time. Several cases with different combinations of reservoir/well position and well deviation were calculated and showed that the deviation skin is negative, which means the productivity is increased if the well is deviated.

In fact, the deviation of the well affects other near-well skin factors like mechanical skin (formation damage due to drilling and completion), partial completion etc. Skin effects are used to represent all the factors in the near-well region that result in a reduction or sometimes increment in productivity. When discussing skin effects, the external boundary conditions are inconsequential. The deviation of the well actually affects the radial inflow nature in the near-well region and this effect can also be measured by a skin factor.

The research of Cinco-Lay et al. (1975) was based on the assumption that the formation is homogeneous and isotropic. Besson and Aquitaine (1990) developed a semi-analytical simulator to determine the deviation skin for anisotropic media and compared the results

with several other methods. They also presented a transformation method to determine the deviation skin factor for anisotropic media based on the reservoir and well size using the anisotropy ratio.

Economides et al. (1996) generalized the productivity index for different well configurations in anisotropic media. This was accomplished by combining the skin effects to the general well productivity index,

$$J = \frac{q}{\overline{p} - p_{wf}} = \frac{\overline{k} x_e}{887.22 B \mu \left(p_D + \frac{x_e}{2\pi L}\right) \sum S}, \tag{2.19}$$

where $\overline{k}$ is the average permeability; x_e is the reservoir length along well trajectory direction; p_D is dimensionless pressure and accounts for early-time transients and all geometric and permeability interactions and $\sum S$ refers to total skins including damage skin, turbulence and/or other pseudoskin factors. The transient pressure response was identified for different flow regimes. Effects of horizontal well orientation on the productivity index in anisotropic media were investigated by several calculation cases.

In the near well region, heterogeneity is usually caused by formation damage. Formation damage in horizontal wells has brought continuous interest because of its significant influence on the productivity of horizontal wells. Unlike vertical wells, the formation damage to a horizontal well can be more severe due to a longer exposure of muds to the formation during the drilling process. In the overbalanced drilling process, the drilling muds invade the formation and particles and polymers in the mud will impair the permeability generally by blocking the pore space. This results in a reduction of permeability in the near-well region. Since the exposed time of muds varies along the horizontal wellbore, the formation damage is usually unevenly distributed.

The mechanisms of formation damage, both mechanical and chemical, are comprehensively presented in Civan (2011); specific investigation to the horizontal wells have been well discussed through laboratory experiments (Zain et al., 2000, Francis, 1997, Longeron et al., 2000) and modeling methods (Semmelbeck et al., 1995, Ding et al., 2004 and Lohne et al.,

2010). For open hole completed horizontal wells, the formation damage happens during the invasion and back flow processes. The mud cake (or filter cake) is formed on the sand surface mainly in the initial spurt loss period. It changes dynamically in the filtration period and blocks the invasion of the mud particles. The thickness of the mud cake is changing with time until it eventually achieves a dynamic balance: deposition rate of mud particle due to filtration equals the erosion rate of particles. When the production starts after drilling, the oil back flows through the mud cake and naturally cleans up most of the mud cake.

The reduction in the permeability is caused by different phase trapping mechanisms for oil-based muds and water-based muds. The water-based muds filtrate is an imbibition process, resulting in higher water saturation in the near-well region and therefore reduces the relative permeability of oil production. In this case, the effective permeability (k_e) of oil is reduced by damaged absolute formation permeability (K) and results in a lower oil relative permeability ($k_{ro} = k_e/K$). For oil-based muds, this does not happen since the transport in the formation is miscible. In order to eliminate or minimize the effects of formation damage on horizontal well productivity, drilling mud screening and cleanup processes are usually necessary.

The permeability alteration in the near-well region is usually represented by a non-uniform skin distribution and then the skin can be applied in productivity models. In the skin models by Frick and Economides (1993) and Furui et al. (2003) for example, the formation damage was treated as an extra pressure drop and represented by the skin factor, assuming an infinite conductivity of the wellbore. Ozkan and Raghavan (1997) investigated the effects of combined wellbore friction and wellbore damage using a flux dependent skin and permeability alternation skin. Although the concept of total skin is simple in application, the flow performance is more accurate using heterogeneous permeability distribution and uniform pressure gradient along the wellbore.

In practice, a total skin term is usually interpreted through well testing. This skin accounts for the total mechanical skin effects. Well completion skin terms, for example the perforation skin, are added to the total skin term.

Permeability heterogeneity can also be represented by assigning different permeabilities to each grid block in numerical methods, which is also used in this research thesis. Upscaling techniques can be used for the reservoir grids and sometimes in the near-well region. Formation damage modeling, a dynamic process of fluid transport in the near-well region, can be found in open literature but is beyond the scope of this research. The objective of this research is to estimate the horizontal well productivity and flow performance in the near-well region given nonuniform formation damage, determined from a formation damage model. It is generally found that most of the invaded water is produced in the first few days (Suryanarayana et al., 2007). The formation damage effects considered here are long term damage effects after natural cleanup.

The near-well effects on the flow performance are usually determined as skin factors, like completion skin factors. The skin factors are practical in using productivity models and can also be easily implemented in the CARP model for each well segment. The anisotropy and heterogeneity effects of the near-well reservoir are also incorporated in the numerical modeling of near-well flow performance in this research.

Chapter 3

Coupled Axial-Radial Productivity Model for Horizontal Wells in Steady State Flow

3.1 Overview

This Chapter is mostly a reprint of the paper "Analytical Coupled Axial and Radial Productivity Model for Steady-State Flow in Horizontal Wells" (Johansen et al., 2015). With some further developments and case studies, it was published in International Journal of Petroleum Engineering.[1] This paper is fundamental to the whole thesis topic. It will be applied in numerical modeling in later Chapters.

Coupled axial-radial flow model was presented and first solved by Johansen (2012a) for steady state flow and verified to coincide with current productivity equations when conditions are simplified. The author of this thesis developed calculation examples to verify

[1] Johansen, T.E., James, L.A., and **Cao, J.**. Analytical Coupled Axial and Radial Productivity Model for Steady-State Flow in Horizontal Wells, *International Journal of Petroleum Engineering*, Vol.1, No.4, pp.290 - 307, 2015.

the solutions and to explain how this analytical solution could be used in determining productivity and frictional pressure loss by using the analytical model in design of numerical methods. Furthermore, the author of this thesis extended the numerical model to quantify the skin effects on the flow performance in the near-well region.

3.2 Introduction

Horizontal wells have been widely used in the oil and gas industry since the nineties, due to improvements in drilling and completions technology. Horizontal well technology can dramatically increase productivity by increasing the contact area with the reservoir, and is especially suitable for thin pay zone reservoirs and reservoirs with a modest anisotropy. However, simulation tools for predicting advanced well performance have not been developed concurrently with completion and drilling technologies.

The horizontal well deliverability for multi-phase flow is summarized in details by Economides et al. (1994). Most of the analytical models, such as Joshi (1988) and Babu and Odeh (1989) are for steady state or semi-steady state flow and for certain reservoir geometry. Joshi (1988) presented an inflow equation in steady state flow of a horizontal well draining from an elliptical cylinder reservoir. Babu and Odeh (1989) presented the analytical solution to the well productivity in a box shaped reservoir. An analytical approach incorporating well and reservoir flow was introduced by Penmatcha and Aziz (1999), with the well itself being treated as a line source. This research incorporates the pressure loss in the wellbore in a semi-analytical fashion. In the wellbore, pressure gradients due to friction cannot in general be ignored, which was first demonstrated by Dikken (1990). Therefore, numerical schemes are needed to include the pressure loss inside the well bore.

In reservoir simulation, a well model needs to be coupled with the reservoir model such that e.g. pressures and flow rates can be solved simultaneously and implicitly. A comprehensive approach incorporating a full field scale reservoir with multiple advanced wells was presented

by Holmes et al. (1998). If a comparison is made between a full field reservoir model using this approach with an advanced well completion and the same reservoir model with a simple completion, the computational time is considerably higher with the advanced completion. Coupled wellbore and reservoir models have also been developed for advanced completions in Aziz (2001), Johansen and Khoriakov (2007) and Khoriakov et al. (2012).

Previously, axial reservoir flow in modeling of advanced well completions has been mostly ignored in analytical approaches. However, the frictional pressure loss for advanced wells cannot in general be ignored and the axial flow along the well trajectory must be considered. In this research, a two-dimensional analytical solution for the simultaneous axial and radial flow in a homogeneous and isotropic reservoir well segment is developed. The axial flow in the near-well reservoir is incorporated in the analytical model for the first time. This analytical pressure distribution is linear in the axial direction and logarithmic in the radial direction (Section 3.2.1). Under simplifying assumptions, the coupled axial and radial model reduces to the classical radial flow equation and linear flow equation given by Darcy's Law (Section 3.2.2). As an example on the use of the new model, the deviation from pure radial and axial flow is calculated as a function of radial pressure variance over a segment (Section 3.3.1). As a second example, it is demonstrated how flow rates and frictional pressure losses can be easily calculated by the new model using a multi-segment approach (Section 3.3.2). Using the new model, the axial to radial flow ratio is calculated to quantify the importance of including axial flow in calculations of well performance and axial flow distribution as functions of reservoir parameters (Section 3.2.3).

3.3 Methodology

3.3.1 Coupled axial-radial flow model

We approximate a given well trajectory by a series of linear segments and then focus on the detailed flow analysis associated with one such segment, shown in Figure 3.1. This

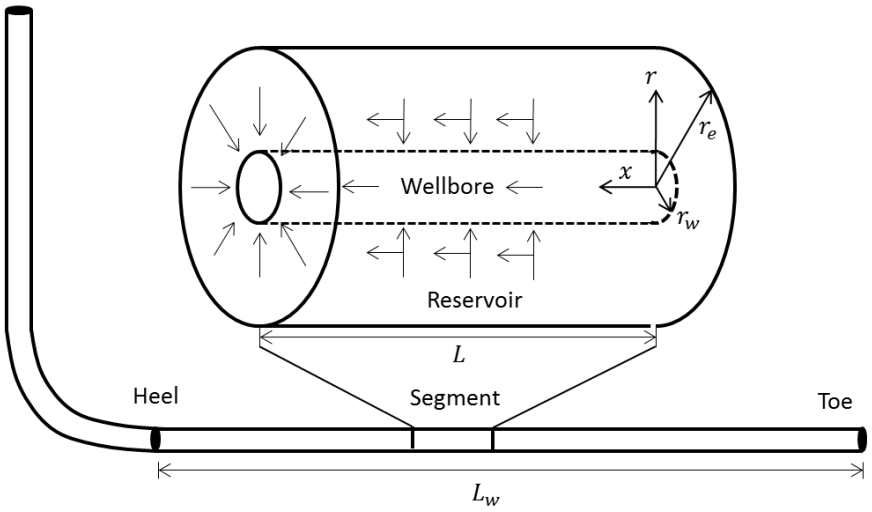

Figure 3.1: Well segment model

is achieved through the derivation of an analytical solution for axial and radial flow rates for such a segment. The segment consists of a well segment surrounded by a cylindrical homogeneous and isotropic reservoir domain with permeability K. We assume the model is two-dimensional with no flow in the angular direction, only in the $x-$ and $r-$ directions. The steady state flow of a single incompressible fluid at an arbitrary point (x, r) in the reservoir is given by

$$\frac{1}{r}\frac{\partial}{\partial r}\left(Kr\frac{\partial p}{\partial r}\right)+\frac{\partial}{\partial x}\left(K\frac{\partial p}{\partial x}\right)=0 \tag{3.1}$$

where $p(x, r)$ is the pressure at any location in the segment. We assume the boundary conditions for the segment in Figure 3.1 are given by

$$p\left(r_e, 0\right)=p_e^0; \quad p\left(r_e, L\right)=p_e^L; \quad p\left(r_w, 0\right)=p_w^o; \quad p\left(r_w, L\right)=p_w^L, \tag{3.2}$$

i.e. the pressures are given (and fixed) at the upstream and downstream boundaries at the external radius and at the internal radii. It is then convenient to introduce the pressure

differences (see Figure 3.2):

$$\begin{aligned} \Delta_x p_w &= p\,(r_w, 0) - p\,(r_w, L)\,; \\ \Delta_x p_e &= p\,(r_e, 0) - p\,(r_e, L)\,; \\ \Delta_r p_0 &= p\,(r_e, 0) - p\,(r_w, 0)\,; \\ \Delta_r p_L &= p\,(r_e, L) - p\,(r_w, L)\,. \end{aligned} \tag{3.3}$$

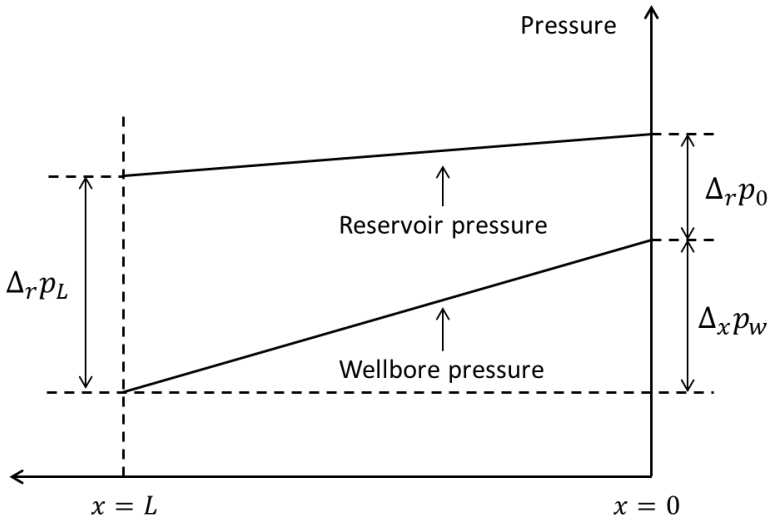

Figure 3.2: Pressure differences in a near-well segment

For boundary conditions as described above, there will be both axial (along-well) and radial flow (well inflow). The analytical determination of the associated flow rates is the main result of this paper:

1) *The total steady state radial flow rate for the segment in Figure 3.1 is given by*

$$Q_r = \frac{2\pi K L \overline{\Delta_r p}}{\mu ln(r_e/r_w)} \tag{3.4}$$

where $\overline{\Delta_r p}$ *is the average draw down over the segment, i.e.* $\overline{\Delta_r p} = [\Delta_r p_L + \Delta_r p_0]/2$ *and the pressure differences are given by Eq.(3.3).*

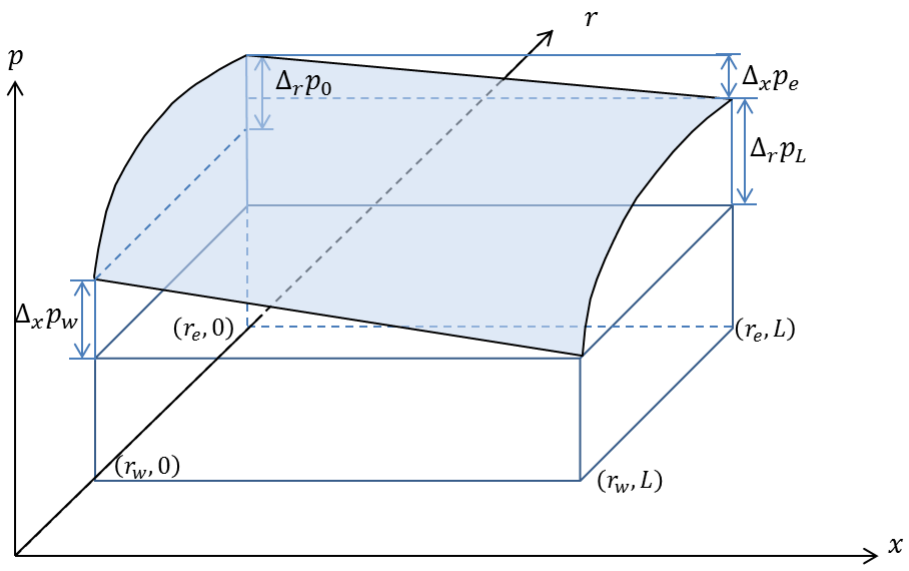

Figure 3.3: Pressure surface for a near-well segment

2) *The total steady state axial flow rate for the segment is given by*

$$Q_x = \frac{\pi K}{\mu L ln(r_e/r_w)} \left[r_e^2 ln\left(\frac{r_e}{r_w}\right) + \frac{1}{2} r_w^2 - \frac{1}{2} r_e^2 \right] (\Delta_r p_0 - \Delta_r p_L) + \frac{\pi K \left(r_e^2 - r_w^2\right)}{\mu L} \Delta_x p_w. \quad (3.5)$$

To see this, we first make the observation that the pressure given by

$$p(x, r) = ax' ln(r') + bx' + cln(r') + d \quad (3.6)$$

satisfies Eq. (3.1) where $x' = x/L; r' = r/r_w$ and a, b, c, d are constants. Figure 3.3 shows the pressure surface in one segment, as well as the pressure differences defined in Eq. (3.3). It is then straight forward to show that $p(r, x)$ given by (3.6) also satisfies the boundary conditions (3.2) when the coefficients are given by

$$a = \frac{\Delta_r p_L - \Delta_r p_0}{ln(r_e/r_w)}; b = -\Delta_x p_w; c = \frac{\Delta_r p_0}{ln(r_e/r_w)}; d = p(r_w, 0). \quad (3.7)$$

Let dq_r be the radial flow rate over an infinitesimal sub-segment with length dx. Using Darcy's Law in the radial direction and Eq.(3.6), the flow rate dq_r in the infinitesimal slice

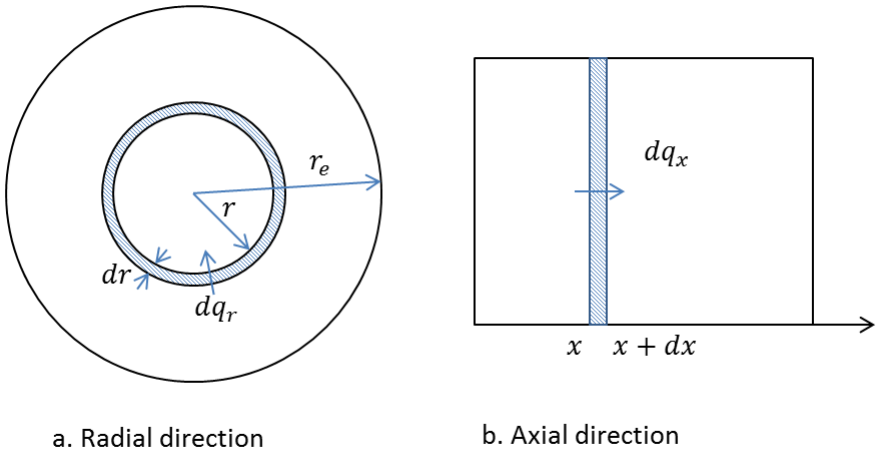

Figure 3.4: Integration of flow rates in radial and axial direction

dx (Figure 3.4a) is

$$dq_r = \frac{2\pi K r}{\mu}\frac{\partial p}{\partial r}dx = \frac{2\pi K}{\mu}\left[\frac{a}{L}x + c\right]dx. \tag{3.8}$$

The radial flow rate over the whole segment is then obtained by integration

$$Q_r = \int_0^L dq_x = \frac{2\pi K}{\mu}\int_0^L \left[\frac{a}{L}x + c\right]dx, \tag{3.9}$$

which becomes

$$Q_r = \frac{2\pi KL}{\mu \ln(r_e/r_w)}\frac{\Delta_r p_L + \Delta_r p_0}{2}, \tag{3.10}$$

i.e. the total radial flow rate is proportional to the average radial pressure difference over the segment. This proves Eq. (3.4).

Consider next an infinitesimal ring of radius r and thickness dr in a cross section of the segment, shown in Figure 3.4 b. Let the axial flow rate in the ring be dq_x. From Darcy's Law and Eq. (3.6),

$$dq_x = \frac{2\pi K r}{\mu}\frac{\partial p}{\partial x}dr = \frac{2\pi K r}{\mu}\left[\frac{a}{L}\ln\left(\frac{r}{r_w}\right) + \frac{b}{L}\right]dr. \tag{3.11}$$

The total axial flow rate is determined by integration of Eq. (3.11);

$$Q_x = \int_{r_w}^{r_e} dq_x = \frac{2\pi K}{\mu L}\int_{r_w}^{r_e}\left[ar\ln\left(\frac{r}{r_w}\right)\right]dr, \tag{3.12}$$

which becomes

$$Q_x = \frac{\pi K}{\mu L ln(r_e/r_w)} \left[r_e^2 ln\left(\frac{r_e}{r_w}\right) + \frac{1}{2} r_w^2 - \frac{1}{2} r_e^2 \right] (\Delta_r p_0 - \Delta_r p_L) + \frac{\pi K \left(r_e^2 - r_w^2\right)}{\mu L} \Delta_x p_w. \quad (3.13)$$

This proves Eq. (3.5), and thereby the main result of this chapter.

3.3.2 Classical radial and axial flow models

We next consider two special cases of boundary conditions, for which analytical solutions already exist (i.e. the classical solutions for radial and linear flow).

We demonstrate below that the solution (3.4), (3.5) will reduce to these known classical solutions in these special cases. We also answer the question: If flow occurs simultaneously in both the radial and axial direction, exactly when (if at all) are the classical formulas for flow in any one direction valid independently of the flow in the other direction?

Consider first the special case when there is no pressure gradient in the axial direction, i.e. the flow is purely radial. Eq. (3.10) should then reduce to the steady-state formula for radial flow, i.e.

$$Q_r = \frac{2\pi K L \Delta_r p}{\mu ln(r_e/r_w)}. \quad (3.14)$$

This is indeed true since in this case $\Delta_r p_L = \Delta_r p_0 = \Delta_r p$ and (3.4) reduces to (3.14). Furthermore, Eq. (3.13) should reduce to zero, which is true since $\Delta_r p_L = \Delta_r p_0$ and $\Delta_x p_w = 0$ in Eq. (3.13).

Consider next the special case when reservoir pressure and wellbore pressure are equal. In this case, the equation for axial flow should reduce to the linear Darcy's Law and the equation for radial flow should vanish. The assumption made in this special case translates to $\Delta_r p_L = \Delta_r p_0$. Therefore, the radial flow Eq. (3.10) indeed vanishes, and the first term in the axial equation (13) also vanishes, leaving only the second term non-zero. Since in

this case $p_w = p_r$ for all values of x , the second term in Eq. (3.13) is Darcy's Law for axial flow in a cross sectional torus of area $\pi(r_e^2 - r_w^2)$.

We finally in this section make the observation that when pressure gradients satisfy $\Delta_x p_e = \Delta_x p_w = \Delta_x p$ and $\Delta_r p_L = \Delta_r p_0 = \Delta_r p$, the radial equation (3.4) and the axial equation (3.5) reduce to

$$Q_r = \frac{2\pi K L \Delta_r p}{\mu ln(r_e/r_w)}; \quad Q_x = \frac{\pi K \left(r_e^2 - r_w^2\right)}{\mu L} \Delta_x p. \tag{3.15}$$

This shows that the standard equation (3.15) for radial and axial flow are valid even if flow occurs simultaneously in both directions, if and only if the pressure draw down along the segment is constant. This never holds true when frictional pressure loss is significant.

3.4 Results and analysis

3.4.1 Calculated examples on axial and radial flow

Following the results of Section 3.2, in this Section we demonstrate through two calculated examples how the coupled axial and radial flow model approach the classical formulas as the boundary conditions approach those for the classical cases. The basic parameters used are shown in Table 3.1.

In the first example, the well bore pressures are fixed at both $x = 0$ and $x = L$, resulting in no pressure gradient in axial direction, i.e. $\Delta_x p_w = 0$. The reservoir pressure $p(r_e, L)$ is

Table 3.1: Parameters for calculation examples

Parameter	Unit	Case 1	Case 2
K	$[D]$	1	1
μ	$[cP]$	1	1
L	$[m]$	20	20
r_w	$[m]$	0.1	0.1
r_e	$[m]$	10	10
$\Delta_r p_L$	$[kPa]$	2	2
$\Delta_r p_0$	$[kPa]$	[2,4]	[1,2]
$\Delta_x p_w$	$[kPa]$	0	2

kept constant while $p(r_e, 0)$ varies to approach $\Delta_r p_L = \Delta_r p_0$. The pressure difference in a macroscopic segment is shown in Figure 3.5. In this case, the radial flow rate approaches the pure radial flow rate given by the steady state radial flow equation as $\Delta_r p_0$ approaches $\Delta_r p_L$. In Figure 3.6, the axial and radial flow rates are plotted as a function of the axial pressure gradient. As the radial pressure gradient at $x = L$ approaches the radial pressure gradient at $x = 0$, i.e. $\Delta_r p_L \to \Delta_r p_0$, the radial flow rate approaches the classical flow rate (4.7 m^3/day) given by Eq. (3.14) and the axial flow rate approaches 0 m^3/day when axial pressure gradient approaches zero.

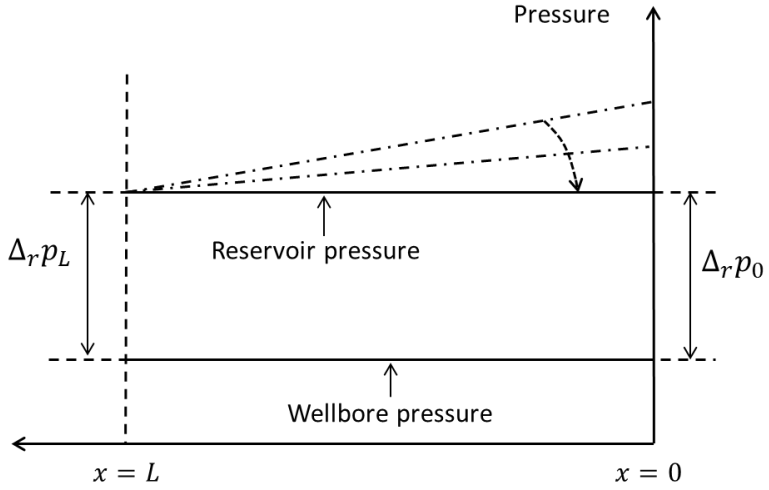

Figure 3.5: Pressure difference in a macroscopic segment, example 1

In example 2, the pressure difference $\Delta_r p_0$ increases from 1 kPa to 2 kPa. The pressure difference in the segment is shown in Figure 3.7. In this example, both axial and radial pressure gradients exist and the reservoir pressure and the wellbore pressures are approaching parallel, i.e. $\Delta_x p_e \to \Delta_x p_w$ and $\Delta_r p_0 \to \Delta_r p_L$. Therefore, the radial and axial flow rates approach the pure radial and pure axial flow rates calculated by Eq. (3.15) of 4.7 m^3/day and 2.7 m^3/day, respectively. This is shown in Figure 3.8.

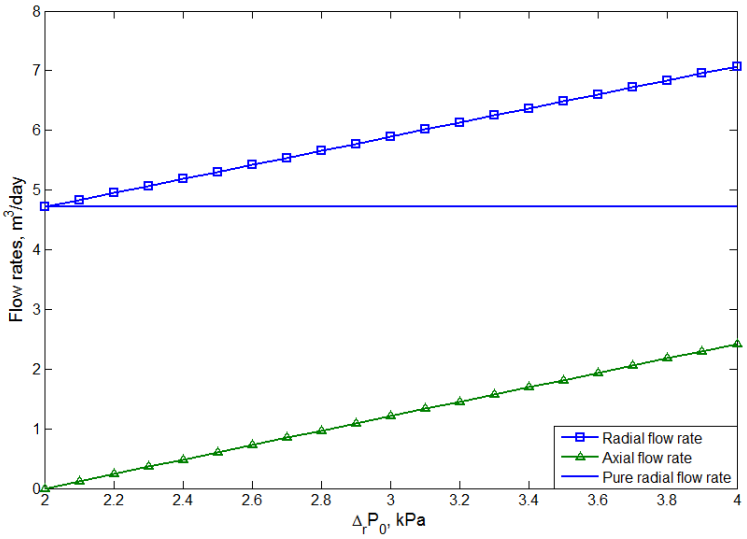

Figure 3.6: Radial and axial flow rates vs pressure gradient, example 1

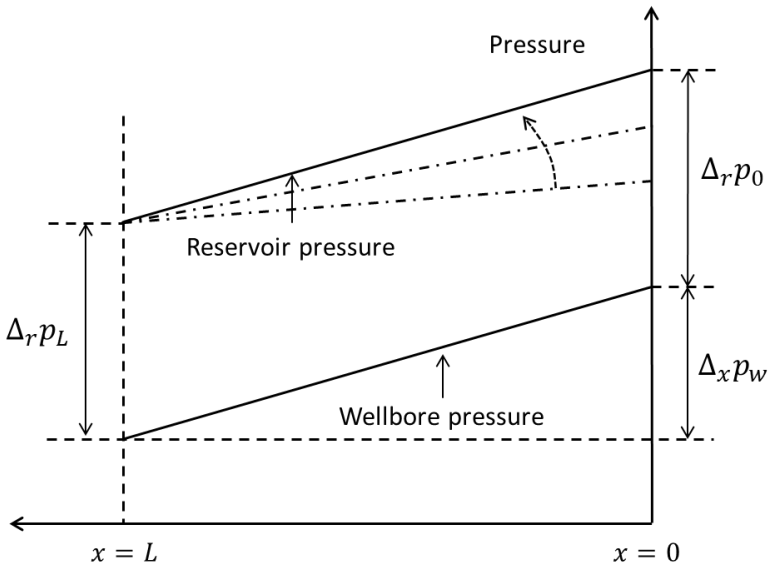

Figure 3.7: Pressure difference in a macroscopic segment, example 2

3.4.2 Pressure distribution in multi-segment wells

Pressure distribution and flow rates are calculated in Section 3.3.1 for one well segment. For real cases, the well will be divided into multiple segments and a simple calculation example of a multi-segment well is presented in this section. Consider a multi-segment model with five segments and each of them is the same as that shown in Figure 3.1 except for pressures

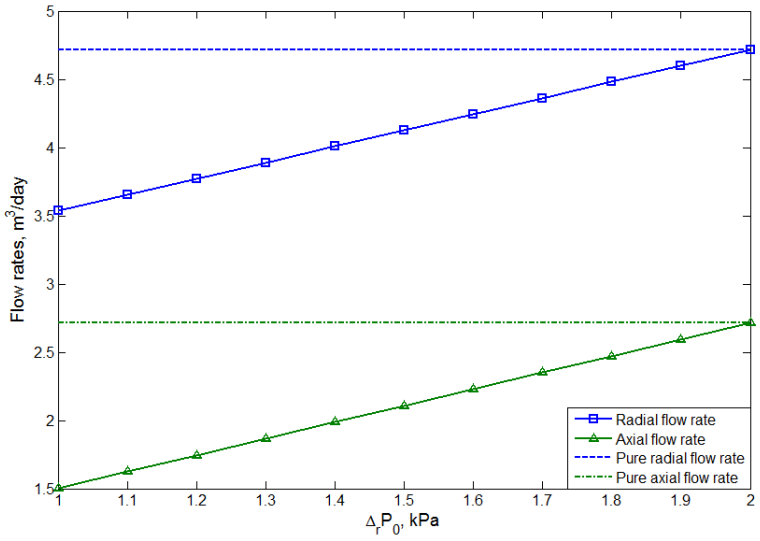

Figure 3.8: Radial and axial flow rates vs pressure gradient, example 2

and flow rates. The external reservoir pressure is assumed to be constant and the pressure distribution is determined iteratively:

1) Assume the wellbore pressure for each segment is the same, $p_i = p_{heel}$.

2) Calculate the well inflow $q_r(i)$, axial flow rate $q_x(i)$ according to Eq. (3.4) and (3.5).

3) Determine the pressure gradient along the wellbore caused by friction,

$$\frac{\Delta p}{L} = \frac{f\rho v^2}{2D}, \tag{3.16}$$

where f is the Darcy friction factor; ρ is the fluid density; v is the velocity and D is the diameter of the wellbore. The flow rate inside the wellbore is determined by mass balance, i.e. net fluid accumulation in a segment equals to zero.

4) Determine the wellbore pressure using the frictional pressure loss from step 3).

5) Repeat steps 2) to 4) with wellbore pressure from 4) until the pressure is converged, which means the flow is steady state.

Following the calculation algorithm given above, a simple calculation is performed with data from Table 3.2. The convergence criteria used in this example is that the total relative error

Table 3.2: Basic parameters for multi-segment case

Parameter	Unit	Value
K	$[D]$	1
μ	$[cP]$	1
L	$[m]$	1000
r_w	$[m]$	0.1
r_e	$[m]$	10
ρ	kg/m^3	800
p_{res}	kPa	2
p_{heel}	kPa	0.1

is less than 10^{-4}, i.e.

$$\sum_{i}^{N_x+1} |\frac{p_i^{n+1} - p_i^n}{p_i^n}| < 10^{-4}, \tag{3.17}$$

where $N_x = 5$ is the number of segments; n is the iteration step; i is the segment number with $i = 1$ at the heel. The result after each iteration step is shown in Table 3.3. The pressure profile is shown in Figure 3.9. The pressure distribution for multi-segments is piecewise linear in each segment, different from the piecewise constant obtained by finite difference methods.

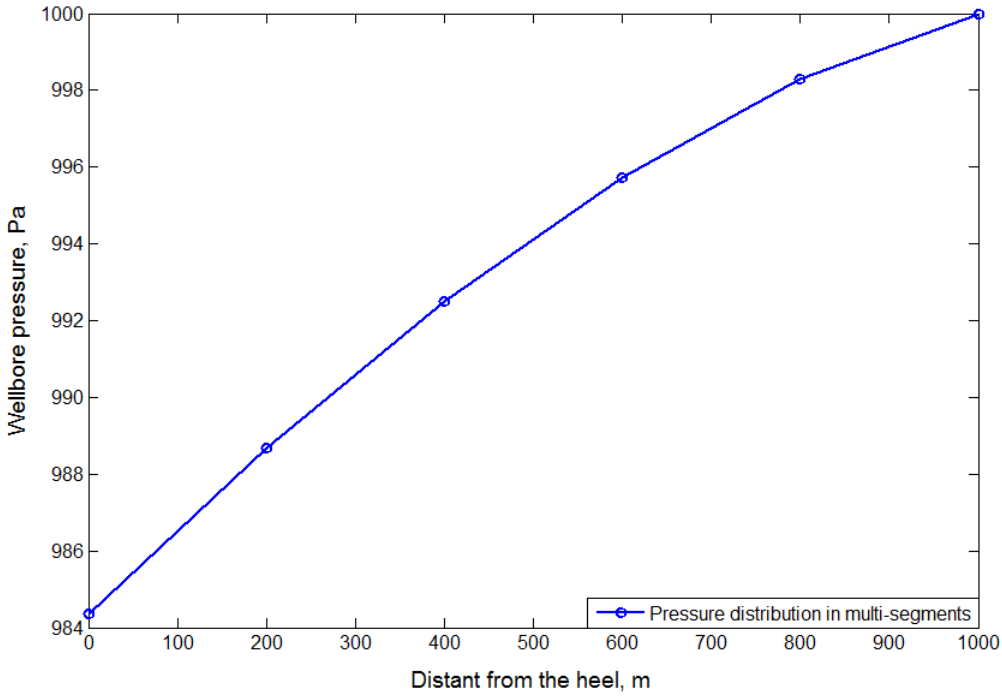

Figure 3.9: Pressure distribution in the wellbore with multiple segments

Table 3.3: Results from each iteration step

n Step	p_1 Pa	p_2 p_3 Pa	p_4 Pa	p_5 Pa	p_6 Pa	η Pa	%
0	1000	1000	1000	1000	1000	1000	N/A
1	1000	998.2804	995.7251	992.5035	988.7063	984.3927	4.04
2	1000	998.2795	995.7214	992.4939	988.6863	984.3567	0.007
3	1000	998.2795	995.7214	992.4939	988.3686	984.3566	$7.87 \times 10^{-}5$

3.4.3 Axial and radial flow ratio

In this Section we first investigate the flow rate ratios Q_r/Q_x , to arrive at a precise method for evaluating when it is adequate to ignore axial flow rate in well inflow calculations. Thereafter, we investigate the ratio of the axial flow rate close to the well and the total axial flow rate in the entire cylindrical reservoir region in Figure 3.1.

In order to investigate the behavior of the ratio Q_r/Q_x we make the simplifying assumption that the reservoir pressure is constant. First, note that by considering the equations (3.4), (3.5), this ratio does not depend explicitly on permeability. We define directional transmissibilities according to these formulas as

$$\begin{aligned} T_r &= \tfrac{\pi LK}{\mu \ln(r_e/r_w)}, \\ T_{x1} &= \tfrac{\pi K}{\mu L \ln(r_e/r_w)}[r_e^2 \ln\left(\tfrac{r_e}{r_w}\right) + \tfrac{1}{2}r_w^2 - \tfrac{1}{2}r_e^2], \\ T_{x2} &= \tfrac{\pi K(r_e^2 - r_w^2)}{\mu L}, \end{aligned} \tag{3.18}$$

where subscripts r and x are for radial and axial flow, respectively. Then, Eq. (3.4) and Eq. (3.5) read

$$\begin{aligned} Q_x &= T_{x1}[\Delta_r p_0 - \Delta_r p_L] + T_{x2}\Delta_x p_w, \\ Q_r &= T_r(\Delta_r p_L + \Delta_r p_0). \end{aligned} \tag{3.19}$$

Using the assumption of constant reservoir pressure, we find

$$Q_x = (T_{x2} - T_{x1})\Delta_x p_w \tag{3.20}$$

and

$$Q_r = T_r(2\Delta_r p_0 + \Delta_x p_w). \tag{3.21}$$

Therefore,

$$\frac{Q_r}{Q_x} = \frac{T_r(2+\tau)}{(T_{x2} - T_{x1})\tau}, \tag{3.22}$$

where

$$\tau = \frac{\Delta_x p_w}{\Delta_r p_0}. \tag{3.23}$$

This is the ratio of wellbore pressure loss to reservoir drawdown, which is the same quantity introduced in Penmatcha and Aziz (1999) to quantify the importance of including frictional pressure drop in well hydraulics calculations. Interestingly, the above shows that it is the same ratio that determines when it is adequate to ignore axial flow in well inflow calculations.

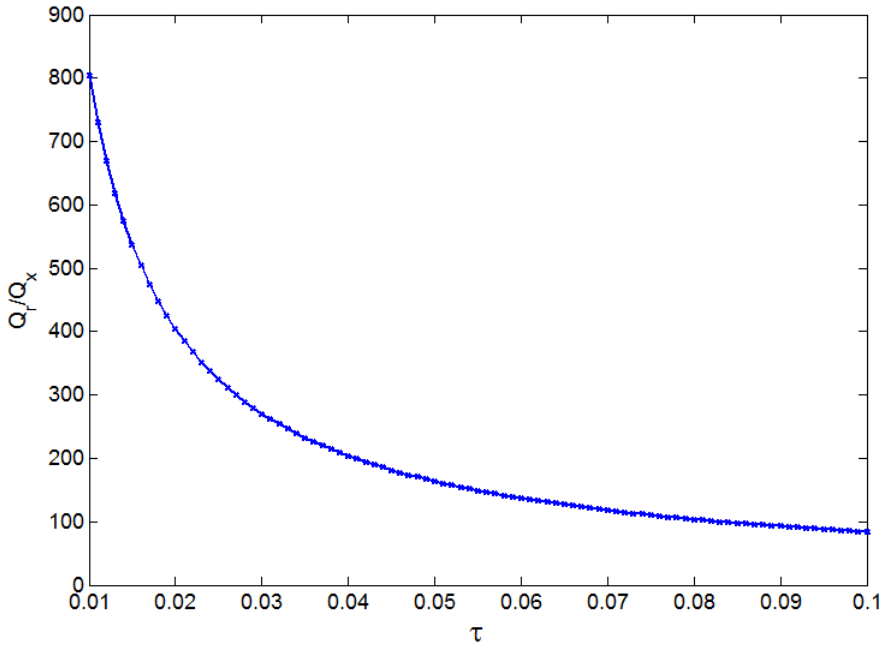

Figure 3.10: Radial to axial flow ratio, small τ value

In Figure 3.10 and Figure 3.11, we have plotted the ratio Q_r/Q_x as a function of the quantity τ in Eq. (3.23). Here, L and r_e were chosen 100 m and $r_w = 0.1$ m; other parameters used are from Table 3.1. Figure 3.10 and Figure 3.11 show the ratio Q_r/Q_x as a function of τ in the range [0.01, 1.0], and in the range [0.1, 5.0], respectively. Clearly, for small values of τ corresponding to low frictional loss/high drawdown, it is adequate to ignore axial flow effects. This is typical for low permeability/low productivity wells. As τ increases, Q_r/Q_x

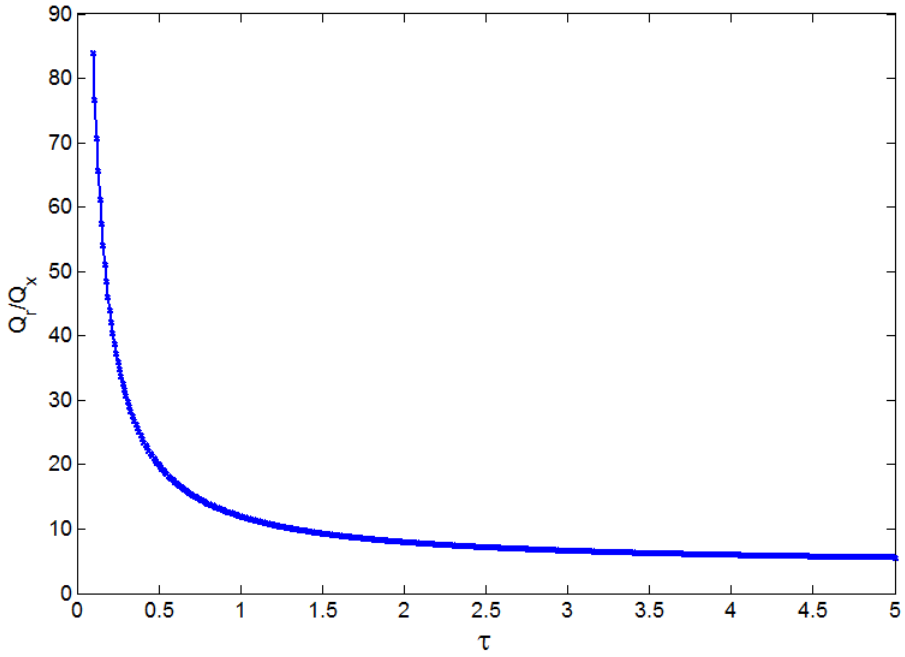

Figure 3.11: Radial to axial flow ratio, large τ value

decreases asymptotically to $T_r/\left[T_{x2}-T_{x1}\right]$. For large values of τ corresponding to high frictional loss/low drawdown, the axial flow cannot be ignored.

We observe that although the flow ratio Q_r/Q_x is independent of permeability and viscosity, it does depend on the length (L), the outer radius (r_e) and wellbore radius (r_w).

Finally, in this section we investigate the ratio Q_x^t/Q_x and Q_x^n/Q_x where Q_x^t is the axial flow rate in the torus between radii R and r_e; Q_x^n is the axial flow rate in the torus between R and r_w and Q_x is the total axial flow rate given by Eq.(3.19), as seen in Figure 3.12. To find Q_x^t and Q_x^n we use the concept from Eq.(3.12):

$$Q_x^t = -\frac{2\pi K}{\mu L}\int_R^{r_e}\left[ar\ln\left(\frac{r}{r_w}\right)+br\right]dr, \tag{3.24}$$

$$Q_x^n = -\frac{2\pi K}{\mu L}\int_{r_w}^{R}\left[ar\ln\left(\frac{r}{r_w}\right)+br\right]dr, \tag{3.25}$$

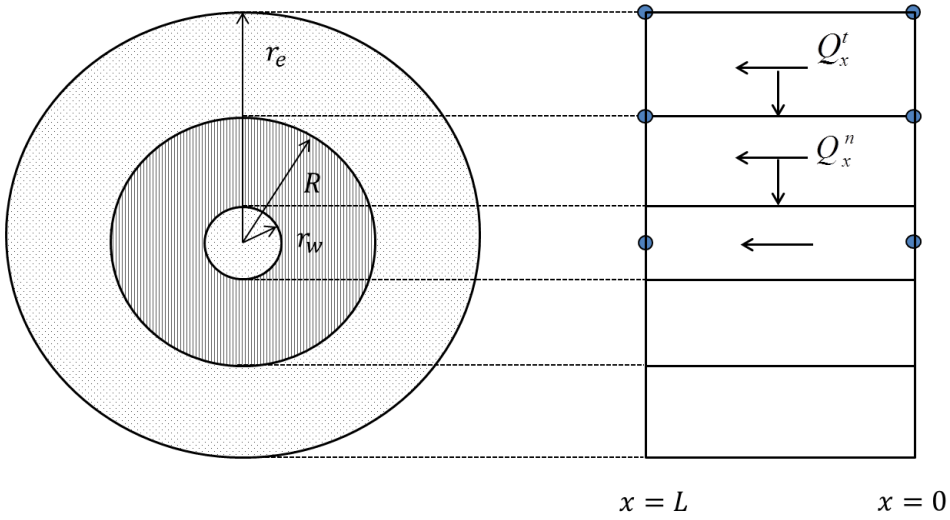

Figure 3.12: Fraction of total axial flow rate in the ring of radius R

where a and b are given by Eq.(3.7). We then have

$$Q_x^t = \frac{\pi K}{\mu L \ln\left(\frac{r_e}{r_w}\right)}\left[r_e^2\ln(r_e/r_w) - R^2 ln(R/r_w) + \frac{1}{2}R^2 - \frac{1}{2}r_e^2\right](\Delta_r p_0 - \Delta_r p_L) + \frac{\pi K(r_e^2 - R^2)}{\mu L}\Delta_x p_w. \quad (3.26)$$

and

$$Q_x^n = \frac{\pi K}{\mu L \ln\left(\frac{r_e}{r_w}\right)}\left[R^2\ln(R/r_w) - \frac{1}{2}R^2 + \frac{1}{2}r_w^2\right](\Delta_r p_0 - \Delta_r p_L) + \frac{\pi K(R^2 - r_w^2)}{\mu L}\Delta_x p_w. \quad (3.27)$$

Using the assumption that the outer reservoir pressure is constant, we find

$$\frac{Q_x^t}{Q_x} = \frac{2(1-\sigma^2)ln\sigma_0 + 2ln\sigma_0 + 2\sigma^2 ln(\sigma/\sigma_0) + 1 - \sigma^2}{2(1-\sigma_0^2)ln\sigma_0 + 2ln\sigma_0 + 1 - \sigma_0^2}, \quad (3.28)$$

where $\sigma = R/r_e$; $\sigma_0 = r_w/r_e$. Obviously, the ratio is 0 for $R = r_e$ and 1 for $R = r_w$. Similarly,

$$\frac{Q_x^n}{Q_x} = \frac{2(\sigma^2 - \sigma_0^2)ln\sigma_0 - 2\sigma^2 ln(\sigma/\sigma_0) + \sigma^2 - \sigma_0^2}{2(1-\sigma_0^2)ln\sigma_0 + 2ln\sigma_0 + 1 - \sigma_0^2}. \quad (3.29)$$

The ratio in Eq. (3.29) is actually the axial flow rate ratio of the "near well region" applied to the whole reservoir cylinder. The ratio equals 0 when $R = r_w$ and 1 when $R = r_e$. Clearly, $Q_x = Q_x^t + Q_x^n$. Note that the above ratios both only depend weakly on the dimensions

through $ln(\sigma_0)$ since L is absent in these formulas. This is illustrated in Figure 3.13 and Figure 3.14, where the ratios in Eqs. (3.28), (3.29) are plotted as a function of σ on the same scale.

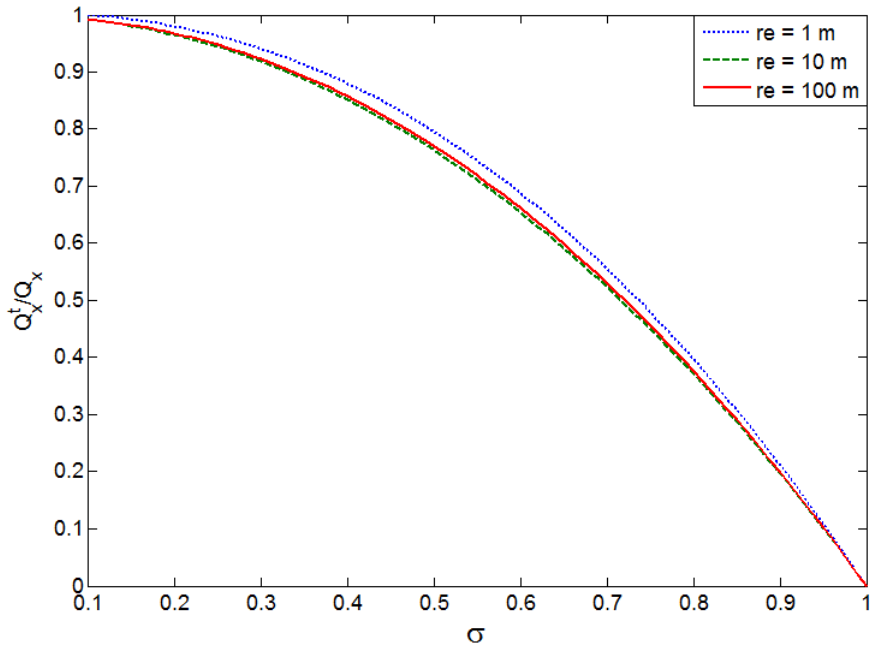

Figure 3.13: Flow rates ratio Q_x^t/Q_x vs. radii ratio σ

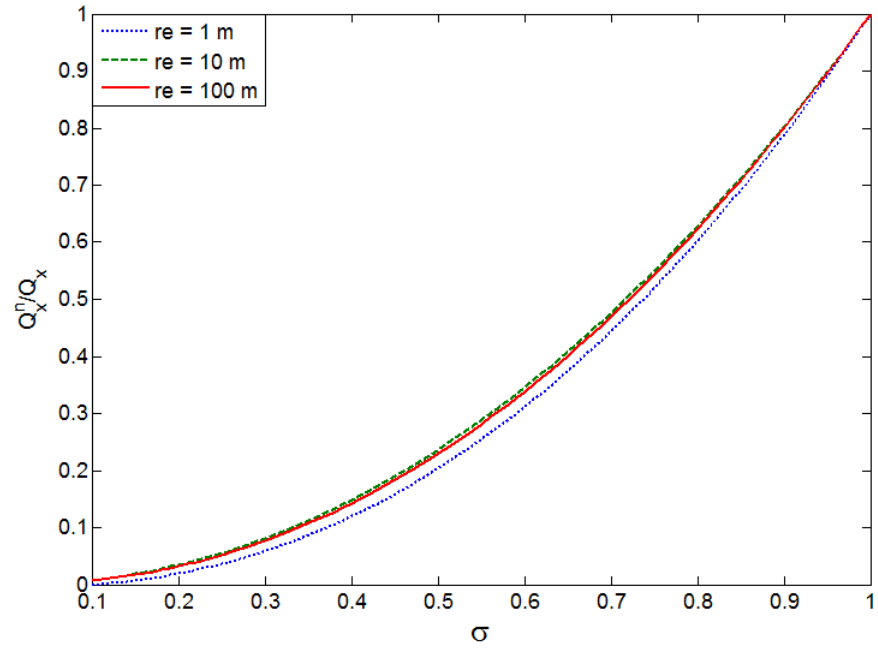

Figure 3.14: Flow rates ratio Q_x^n/Q_x vs. radii ratio σ

If the near-well region has a different permeability from the reservoir permeability, increased permeability caused by stimulation or decreased permeability due to formation damage, the axial and radial flow in the near-well region will be affected. It is easy to derive the flow equations if the skin factor is considered. The radial inflow equation (Eq. 3.4) then becomes

$$Q_r = \frac{2\pi K L \overline{\Delta_r p}}{\mu \left[ln(r_e/r_w) + S\right]}, \tag{3.30}$$

where $S = \left(\frac{K}{K_d} - 1\right) ln\left(r_d/r_w\right)$. It is straightforward but cumbersome for the axial flow equations since it combines Eq. (3.26) and (3.27) evaluated in two regions, similar to flow rates from multi-layers. The calculation example uses the permeability of $K_d = 0.1K$, $K_d = K$ and $K_d = 5K$ in the near-well region; $r_e = 1\ m$ and other parameters are from Table 1. The fraction of axial flow in near-well region is expressed by $Q_x^n/[Q_x^t + Q_x^n]$ where Q_x^t is evaluated with reservoir permeability while Q_x^n is evaluated with the permeability in the near-well region, according to equations (3.24) and (3.25), respectively. The flow rate ratio with different permeability in the near-well region is plotted in Figure 15. It is demonstrated that the axial flow is more important when the well is stimulated (for after acidizing) and less important when the near-well region has damages.

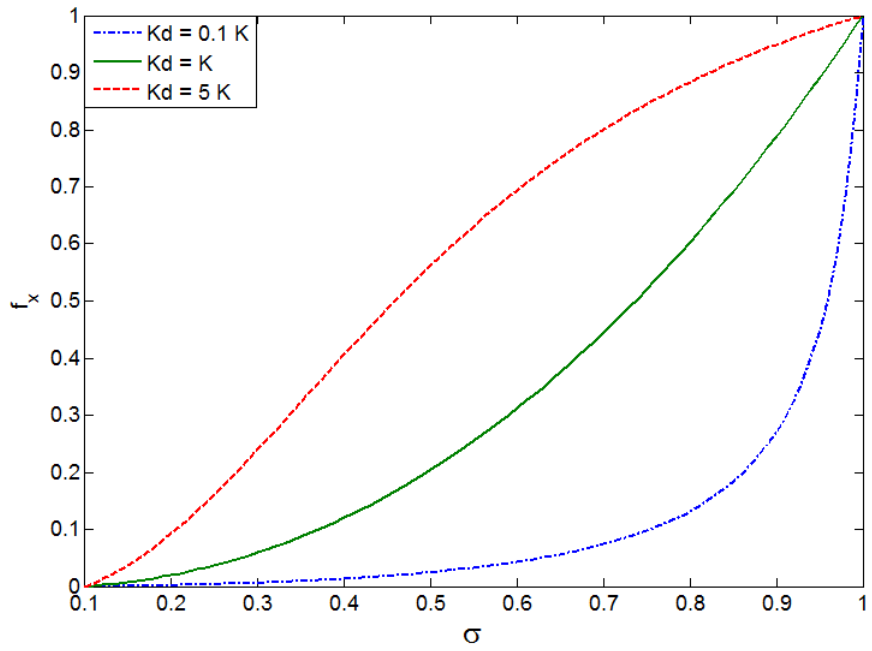

Figure 3.15: Flow rates ratio Q_x^t/Q_x vs. radii ratio in different near-well region permeabilities

3.5 Conclusions

A new two-dimensional analytical solution for coupled axial and radial flow in a homogeneous well segment is derived. In this model, axial flow along a well trajectory is coupled with radial flow for the first time. It results in a linear pressure distribution in the axial direction and a logarithmic distribution in the radial direction. The analytical solution is investigated for two special cases where one-dimension analytical solution already exists and they are found to coincide. The analytical results also verify that the axial flow along the well trajectory cannot be ignored, especially for reservoirs with high permeability and high productivity wells. The analytical model includes the axial flow in the near well region. It provides a simple well inflow equation and an axial near-well reservoir flow equation. It is also demonstrated how the analytical solution can be used in numerical method for the entire well trajectory and near-well region.

References

- Aziz, K., 2001. A general single-phase wellbore/reservoir coupling model for multilateral wells, *SPE Reservoir Evaluation & Engineering*, 4(4): 327-335.

- Babu, D. K. and Odeh, A., 1989. Productivity of a Horizontal Well', *SPE Reservoir Engineering*, 4(4), 417-421.

- Dikken, B., 1990. Pressure drop in horizontal wells and its effect on production performance, *Journal of Petroleum Technology*, 42(11): 1426-1433.

- Economides, M. J., Hill, A. D. and Ehlig-Economides, C., 1994. Petroleum production systems', New Jersey: Prentice Hall.

- Holmes, J. A., Barkve, T., and Lund, O. 1988, Application of a multisegment well model to simulate flow in advanced wells, Paper SPE 50646 presented at the European Petroleum Conference, 20-22 October, The Hague, Netherlands

- Joshi, S. D., 1988. Augmentation of well productivity with slant and horizontal wells (includes associated papers 24547 and 25308), *Journal of Petroleum Technology*, 40.06: 729-739.

- Johansen, T. E. and Khoriakov, V., 2007. Iterative techniques in modeling of multi-phase flow in advanced wells and the near well region, *Journal of Petroleum Science and Engineering*, 58(1): 49-67.

- Johansen, T.E., 2012a, A Generalization of the Steady State Inflow Model Incorporating Axial Flow, `www.petreng-thormod.ca` .

- Johansen, T.E., James, L.A., and Cao, J.. Analytical Coupled Axial and Radial Productivity Model for Steady-State Flow in Horizontal Wells, *Internation Journal of Petroleum Engineering*, Vol.1, No.4, pp.290 - 307, 2015.

- Khoriakov, V., Johansen, A. C. and Johansen, T. E., 2012. Transient flow modeling of advanced wells, *Journal of Petroleum Science and Engineering*, 86, 99-110.

- Penmatcha, V. and Aziz, K., 1999. Comprehensive reservoir/wellbore model for horizontal wells, *SPE Journal*, 4(3): 224-234.

Chapter 4

High-Order Numerical Simulation Methods for Well/Near-Well Modeling using Coupled Axial-Radial Productivity Model

4.1 Overview

This Chapter is based on the paper "A New Coupled Axial-Radial Productivity Model for Horizontal Wells with Application to High Order Numerical Modeling", presented at SPE Reservoir Characterization and Simulation Conference and Exhibition.[1] It is reprinted in Section 4.2, 4.3, 4.4 and Appendix 4-A. This is an application of the coupled axail-radail productivity model in Chapter 3 for steady state flow in horizontal well and near-well region simulation, i.e. the numerical well/near-well model.

[1] **Cao, J.**, James, L.A., and Johansen, T.E., 2015. A New Coupled Axial-Radial Productivity Model with Application to High Order Numerical Well Modeling. Presented at SPE Reservoir Characterisation and Simulation Conference and Exhibition, Abu Dhabi, UAE, September.

Furthermore, this chapter presents applications of the model in heterogeneous reservoirs and cases when cross flow occurs in Section 4.5. The methodology of coupling the well/near-well model with current numerical reservoir simulators is also developed. The application of the new model is also demonstrated through an example of horizontal wells with unevenly distributed skin factors in Section 4.5.

The thesis author contributed to this Chapter mainly on the aspects of developing the numerical model using coupled axial-radail productivity model, analyzing the numerical error and verifying the order of accuracy, programming the horizontal well and near-well simulator (in MATLAB^{TM}), presenting calculation examples, and preparing the manuscripts.

4.2 Introduction

Horizontal well simulation methods are in great demand as drilling technology has outpaced simulation techniques used to predict inflow performance. The horizontal well model should be able to not only determine the pressure loss inside the well but also calculate the flow performance into the well and in the near-well reservoir. In general, pressure and flow rates in the horizontal well and near-well reservoir are coupled with the reservoir and solved simultaneously.

The wellbore length and direction are the major differences between horizontal and vertical wells. The representation of well segments for a horizontal well is usually far more complicated than for a vertical well. The horizontal well model needs to account for pressure loss due to acceleration and friction, demonstrated by Dikken (1990). The frictional pressure drop was formulated in a correlation form by Archer and Agbongiator (2005) to easily evaluate horizontal well productivity. Also, the horizontal well model should couple easily with the reservoir model, like the mostly used representation by Peaceman (1983). A modular modeling method coupling the reservoir and the well was proposed by Brekke et al. (1993). The application of a multisegment well model was described by Holmes et al. (1998) where

they divided the wellbore into segments and considered well flow performance and pressure loss in advanced completions in a fully integrated and implicit manner. The reservoir inflow to the wellbore and the flow within the wellbore are coupled in a semi-analytical model by Tabatabaei and Ghalambor (2011) to predict performance of horizontal and multilateral wells. Johansen and Khoriakov (2007) presented a comprehensive network model for multi phase flow in advanced wells. These models are used in industry software as they are highly efficienct and accurate.

The analytical solutions to horizontal well flow have been given by Babu and Odeh (1989), Economides et al. (1996) and Joshi (1988) for simplified geometries using a line source assumption for the well trajectory. As such, they are genuinely analytical solutions, and therefore represent all details of the reservoir flow rigorously subject to the assumptions for which they were derived. However, they do not incorporate such effects as frictional losses analytically and are also based on no-flow or constant pressure boundaries and are therefore difficult to use in local well inflow calculations. In Ouyang et al. (1998), the line source assumption was also used to represent well segments, which also incorporates frictional losses semi-analytically. However, they do not consider detailed reservoir descriptions and well completions. The recently developed coupled axial-radial flow model for horizontal wells (Johansen et al., 2015) provides the analytical solution to the coupled flow situation as shown in Fig 4.1. Our work applies this coupled axial-radial productivity model in a coupling between the well/near-well model and a reservoir simulation model.

In this Chapter, the two dimensional analytical solution for coupled axial-radial flow in a homogeneous and isotropic reservoir well segment is briefly reviewed and applied in numerical model of the near-well region and the horizontal well (Section 4.3). This analytical pressure distribution is linear in the axial direction and logarithmic in the radial direction. The analytical solution is implemented in a numerical scheme for the entire well trajectory and the near-well region, where the trajectory is broken up into finite segments with homogeneous reservoir properties. Therefore, the pressure distribution is piecewise linear/logarithmic

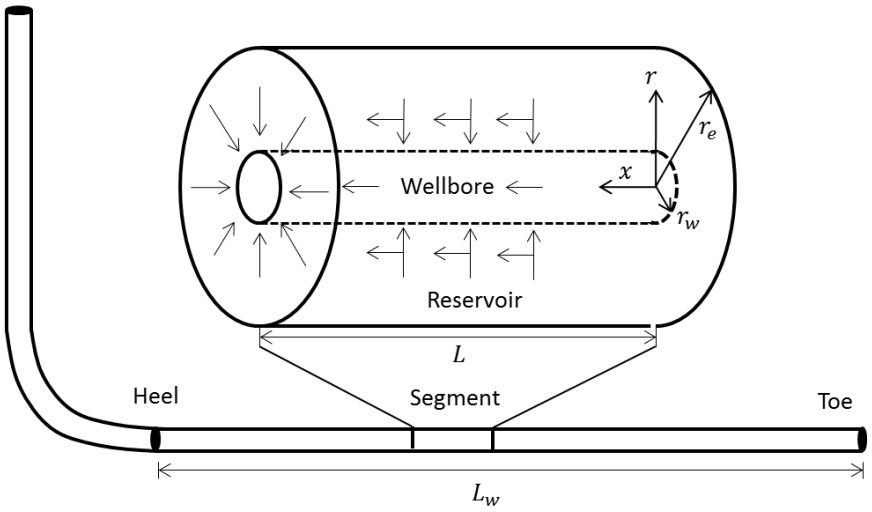

Figure 4.1: Segment model with coupled axial-radial flow (Johansen et al., 2015)

as opposed to piecewise constant distribution in a standard finite difference method. The numerical performance of the well/near-well model is analyzed in Section 4.4. The finite difference approach is implemented for comparison. It is proved in the paper (see Appendix 4-A) that the new approach is superior to the standard approach in the sense that the new method achieves higher order accuracy than the standard finite difference method. In Section 4.5.1, a coupling scheme between the new well/near-well model and a standard finite difference simulator is described. It uses a Cartesian grid in the reservoir simulator and a cylindrical grid in the analytically based well/near-well method. This coupling therefore can represent both remote reservoir characteristics and detailed well/near-well flow accurately without the use of very fine grids.The well/near-well model is applied in heterogeneous cases in Section 4.5.2 and in various external pressure cases where cross flow may happen in Section 4.5.3. In Section 4.5.4, the coupling between the well model and the reservoir model are demonstrated and applied in studying the formation damage for horizontal wells.

4.3 Methodology of the well/near-well numerical model

The numerical approach in this research focuses on near-well and well flow performances, considering coupled axial-radial flow in the near-well region and frictional flow in the well pipe. The near-well region is divided into multi segment units as shown in Figure 4.2, consisting the wellbore and reservoir segments. Each segment in the reservoir is assumed to be homogeneous and isotropic, consisting of four pressure nodes located at the segment corners. This is in contrast to a standard finite difference grid where pressure nodes are located in the center of homogeneous grid blocks. Based on the solution of the analytical model, the pressure distribution is then piecewise linear and logarithmic in the axial and radial directions, respectively. This is contrary to the piecewise constant case for a standard finite difference method. The results from both the new method and the standard finite difference method will be compared in the next section.

The horizontal well is assumed to be fully penetrated from toe to heel with a cylindrical reservoir around it. Both ends of the reservoir segment are treated as no flow boundaries. The pressure in the leftmost bottom hole segment and the external reservoir pressures are imposed as boundary conditions. For each well segment, two of the pressure nodes in the radial direction are equal since wellbore pressures are distributed only along the well trajectory direction.

Consider a grids segment, consisting of a well segment i and a reservoir segment $i + N_x$, as shown in Figure 4.2. The material balance for single phase flow can be expressed as:

$$\sum_j (q_{i,j}) = 0; \tag{4.1}$$

where j represents all the flow connected to segment i, including axial inflow $Q_{x,i-1}$ and outflow $Q_{x,i}$ as well as radial inflow $Q_{r,i+N_x}$ and outflow $Q_{r,i}$; N_x is the total segment number in each row. For reservoir segment $i + N_x$, axial outflow is determined by the four corner pressures of this segment while axial inflow is determined by the four corner pressures of the upstream segment. For well segment i, the flow including friction in this segment is treated

as constant, noted by $Q_{f,i}$.

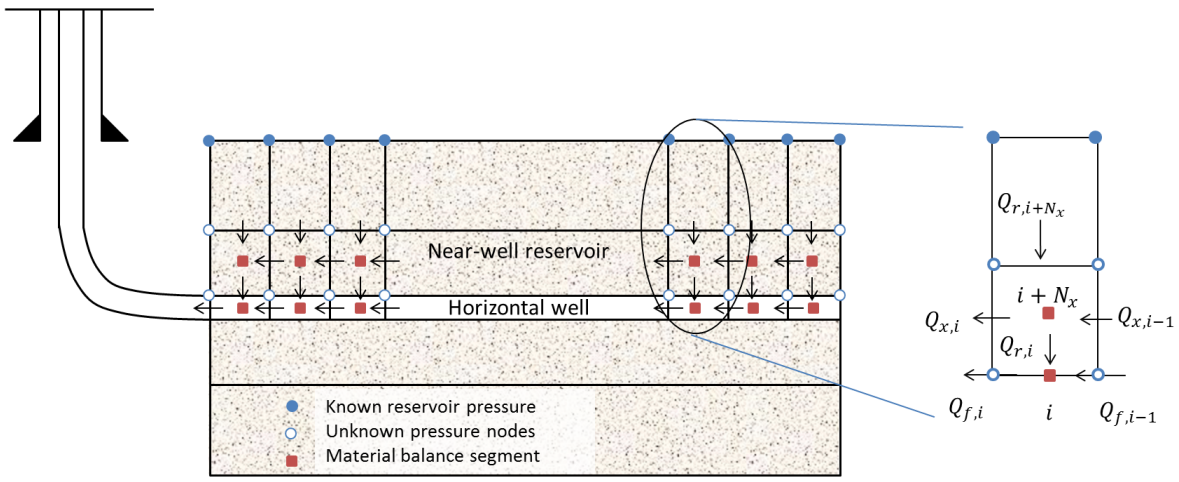

Figure 4.2: Numerical schematic of the segment model and segment unit

For each segment in the near-well region and in the well, conservation equations for momentum and mass are used. The numerical model in this paper is built on the discritization shown in Figure 4.2, which depicts the cross section of a cylindrical reservoir with two reservoir tori; and only one reservoir torus and one well annulus.

The reservoir part of each segment is assumed to be homogeneous and isotropic, consisting of four pressure nodes located at the segment "corners". Two of them are at the outer torus surface and two on the inner surface. In a finite difference simulator, these two outermost nodes correspond to the pressure nodes of adjacent grid blocks along the well trajectory. Based on the solution of the analytical model, the pressure distribution is then piecewise linear and logarithmic in the axial and radial directions, respectively. This is contrary to the piecewise constant distribution for a standard finite difference method.

The coupled axial-radial flow model for a horizontal well and the near-well reservoir is presented in previous Chapter (Johansen et al., 2015) and summarized briefly below. A given well trajectory is approximated by a curve composed of piecewise linear segments. Consider one such segment as shown in Figure 4.1; the well is surrounded by a cylindrical

reservoir domain, which for a given segment is assumed to be homogeneous and isotropic with permeability k. We assume the model is two dimensional with flow in the $x-$ and $r-$ directions but not in the angular direction. The steady state flow of a single incompressible fluid is solved in previous Chapter.

The results of axial and radial flow rates are

$$q_r = T_r \left(\Delta_r p_L + \Delta_r p_0\right), \tag{4.2}$$

$$q_x = T_{x1} \left(\Delta_r p_0 - \Delta_r p_L\right) + T_{x2} \Delta_x p_w, \tag{4.3}$$

where

$$T_r = \frac{\pi k L}{\mu \ln\left(r_e/r_w\right)}; T_{x1} = \frac{\pi k}{\mu \mathrm{L} \ln\left(r_e/r_w\right)} \left[r_e^2 \ln\left(\frac{r_e}{r_w}\right) + \frac{1}{2} r_w^2 - \frac{1}{2} r_e^2\right]; T_{x2} = \frac{\pi k \left(r_e^2 - r_w^2\right)}{\mu L}. \tag{4.4}$$

Hence, the analytical solution to the coupled flow model determines both the radial inflow and the axial reservoir flow along the well trajectory.

The horizontal well completion is along the axis of a cylindrical reservoir. The heel and the toe ends of the near-well reservoir are treated as no flow boundaries. The volumetric flow rate or wellbore pressure at the heel segment together with the external reservoir pressures are imposed as boundary conditions. Alternatively, the total volumetric flow rate can be used as boundary condition. Therefore, any combination thereoff such as target rate with limiting bottom hole pressure can also easily be implemented.

The momentum balance equation for flow between adjacent reservoir segments is described by Eq. (4.12) and (4.13). For the frictional flow between adjacent well segments in tubing, the momentum balance equation is expressed as:

$$\frac{\partial p_f}{\partial x} = -\frac{f \rho v^2}{2D}. \tag{4.5}$$

where, f is the Darcy friction factor. For turbulent flow in smooth pipes, $f = \frac{0.3164}{\sqrt[4]{Re}}$ and for laminar pipe flow $f = \frac{64}{Re}$, where Re is the Reynolds number. For a rough pipe, friction

factor is given explicitly by Haaland (1983) as:

$$f = \frac{1}{[1.8\log(\frac{6.9}{Re} + (\frac{e}{3.7D})^{\frac{10}{9}})]^2}, \tag{4.6}$$

where e is the absolute roughness of the pipe wall. In the case of considering friction pressure loss only in the pipe,

$$Q_f = T_f \Delta P^{(\frac{4}{7})}. \tag{4.7}$$

Note that T_f is the frictional flow transmissibility;

$$T_f = \frac{2^{(\frac{9}{7})}\pi r_w^{(\frac{19}{7})}}{(0.3164)^{\frac{4}{7}}\rho^{(\frac{3}{7})}\mu^{(\frac{1}{7})}\Delta x^{(\frac{4}{7})}}. \tag{4.8}$$

Then the complete numerical model is given by Eq. (4.13) and (4.24) and the associated parameters described above. The unknowns consist of $4N$ flow rates and $2N+2$ pressures. The equations we have are $4N$ momentum balances, $2N$ material balances and 2 boundary conditions. Therefore, the problem is closed by an equal number of equations and number of unknowns. Since most of the equations are non-linear, an iterative method must be used. The Newton-Raphson method was chosen for this.

4.4 Cases study and analysis

In this section, several cases of calculated examples are described to illustrate the numerical performance of the well/near-well model as stand alone simulation. A standard finite difference method is also used to compare the results with the new method introduced in this paper. First, refinement of grid blocks is used to approximate the true solution. Then pressure profiles calculated using both methods are compared. Next, the accuracy and efficiency of the new method is analyzed. Finally, the axial to radial flow ratio $\frac{Q_x}{Q_r}$ is determined based on the numerical results and whether the axial reservoir flow can be ignored is discussed.

Table 4.1: Parameters for calculation examples

Parameter	Unit	Value
K	$[D]$	1
ρ	$[kg/m^3]$	800
μ	$[cP]$	1
L_w	$[m]$	1000
r_w	$[m]$	0.1
r_e	$[m]$	40
p_{res}	$[bar]$	300.3
p_{BH}	$[bar]$	300

4.4.1 Real solution approximation

We first try to approximate the true solution using numerical methods. Basic parameters used are shown in Table 4.1. Generally, for a given numerical method, the higher number of segments used, the more accurate numerical results will be. Therefore, a process of refinement, in both the axial and radial directions, was used to approach the true solution. The standard finite difference method includes the axial flow in reservoir numerically using Darcy's Law, flow in the well with friction and radial flow given by steady state inflow equation. Under a constant bottom-hole pressure condition, the toe pressure and the total flow rate at the heel, are chosen for measurements of accuracy. First, the number of segments in the axial direction was increased from 20 to 5000 while using two rings (wellbore and near-well reservoir rings) in the radial direction. In this process, the total well length is constant and

$$L_w = \Delta_x N_x. \tag{4.9}$$

In the second refinement process, the number of well and near-well reservoir rings (N_r) increases from 20 to 200, fixing $N_x = 100$. The wellbore radius and reservoir external radius are constant while the number of the rings used satisfies

$$r_j = r_w \left(r_e/r_w\right)^{\frac{j-1}{N_y-1}}, \tag{4.10}$$

where $j = 1, 2, \cdots, N_y$.

Figure 4.3 shows that as the N_x increases, the total flow rate at the heel is increasing, while the toe pressure is decreasing. However, both parameters are almost invariant when

$N_x > 3000$, i.e. both curves become essentially flat. Therefore, we assume that the result with $N_x = 5000$ is the real solution for the case with only one near-well reservoir row. The same response is observed in Figure 4.4 when $N_y > 150$, hence the results using $N_y = 200$ are assumed as the real solution with fixed axial grid block number. Note that P_{sln} is the solution pressure. The two refinement processes will be used in different scenario of calculations.

4.4.2 Pressure and flow rates profiles

The pressure distributions were calculated by the new method and compared with the result from the standard finite difference method, as shown in Figure 4.5 and Figure 4.6. The pressure profiles from both methods are consistent. However, the pressure resulting from the new method consists of a continuous series of linear pieces while that from the standard method is a series of constant points. The linear pressure distribution in each segment shows a superiority in approaching the solution pressure compared with the piecewise constant steps from the standard method. Furthermore, the method is more accurate in the region near the heel (specifically within 200 meters from the heel in Figure 4.5 and 4.6 than the standard method. It is significant to have a higher accuracy in the vicinity of the heel because it is where a major pressure drop occurs. The deviation of pressure determined by standard method near the heel means significant inaccuracy in high permeability reservoirs.

The radial wellbore inflow and axial reservoir flow rates determined from the standard finite difference and the new method are plotted and compared with the true solution. The radial inflow rates in Figure 4.7 show a similar trend with pressure plots that the new method is closer to the solution than the standard finite difference method near the heel and are almost overlapped with the standard method around the toe. This indicates that the new method in general is more accurate using same number of segments, especially in the vicinity of the heel. The axial flow rates, shown in Figure 4.8, first start from zero at the toe due to the no flow boundary and increases and then drop to zero at the heel because of another

no flow boundary. It demonstrates that the new method achieves higher accuracy than the standard method in axial flow rate calculation.

In most analytical productivity models, the axial flow rate is ignored in the near-well reservoir. In order to examine whether the axial flow can be ignored, we use standard methods to solve the pressure for two cases, including axial flow (case A) and excluding axial flow (case B) in the near-well region. Note that the refinement of grid bocks in radial direction will improve the result of case A but has no effects on case B since flow rates and pressures in case B are linear superposition in the radial direction. This can be explained by

$$q_i = \sum_{j=1}^{N_y} T_r \left(p_{i,j+1} - p_{i,j}\right) = T_r \left(p_{i,j+1} - p_{i,j}\right), \tag{4.11}$$

where P_{i,N_y} and $P_{i,1}$ are the external pressure and the well bore pressure at column i, respectively. Then, we calculated the pressure and flow rates in the wellbore for both case A and case B, where case A applies refined segments in radial direction ($N_r = 50$) and case B does not. The results are given in Figure 4.9 and Figure 4.10. They show a significant overestimatation, more than 30%, in both well bore pressure and well productivity, if axial flow is ignored in the near-region. When axial flow is ignored, the pressure gradient supporting axial flow is ignored, which results in a larger radial pressure drop. Hence, the radial wellbore inflow is larger, so is the well productivity; and the frictional pressure loss in the wellbore is also larger due to higher flow rates in the wellbore. The results indicate that axial flow cannot be ignored in general.

4.4.3 Accuracy and efficiency

To study accuracy of both methods, the relative errors are calculated and plotted in Figure 4.11 and Figure 4.12. Here, we define the relative error γ as

$$\gamma = \frac{\Delta p}{\Delta p_{DD}}, \tag{4.12}$$

where $\Delta p = p_{N_x} - p_{sln}$; p_{sln} is the true solution of pressure and $\Delta p_{DD} = p_{res} - p_{heel}$.

The results verify the higher accuracy of the new method when compared to the standard method for pressure near the heel. The accuracy for pressure increases from the toe to the heel for the new method while the standard method decreases. Though higher accuracy could be achieved by refining the number of segments for the standard method, it is obvious that the new method needs less number of segments than the standard method to achieve the same accuracy. The efficiency of the new method is guaranteed given the proof that the new method is a higher order method than the standard finite difference method.

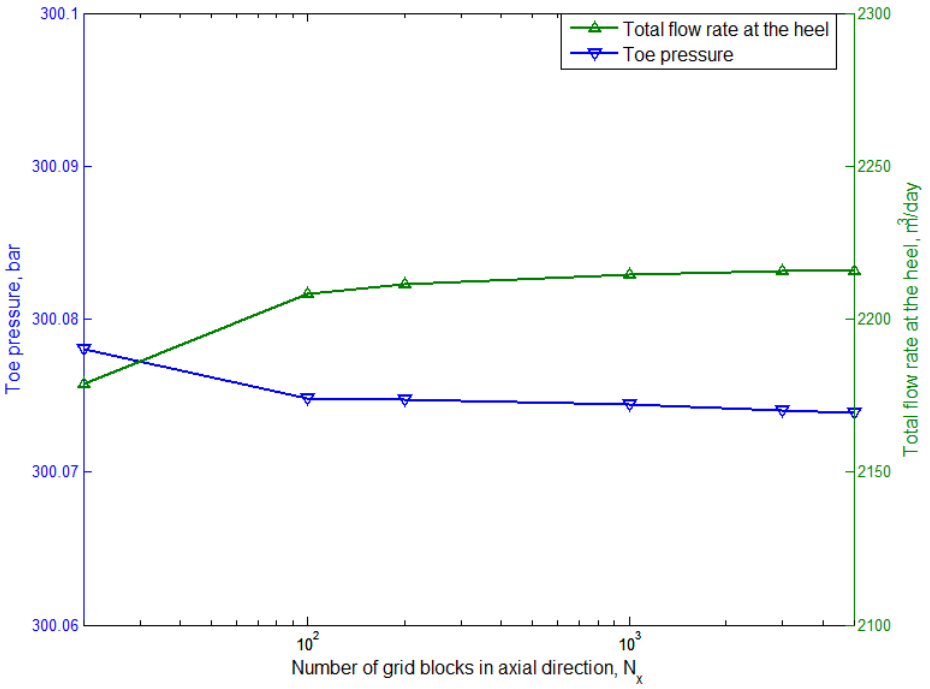

Figure 4.3: Segment refinement in axial direction

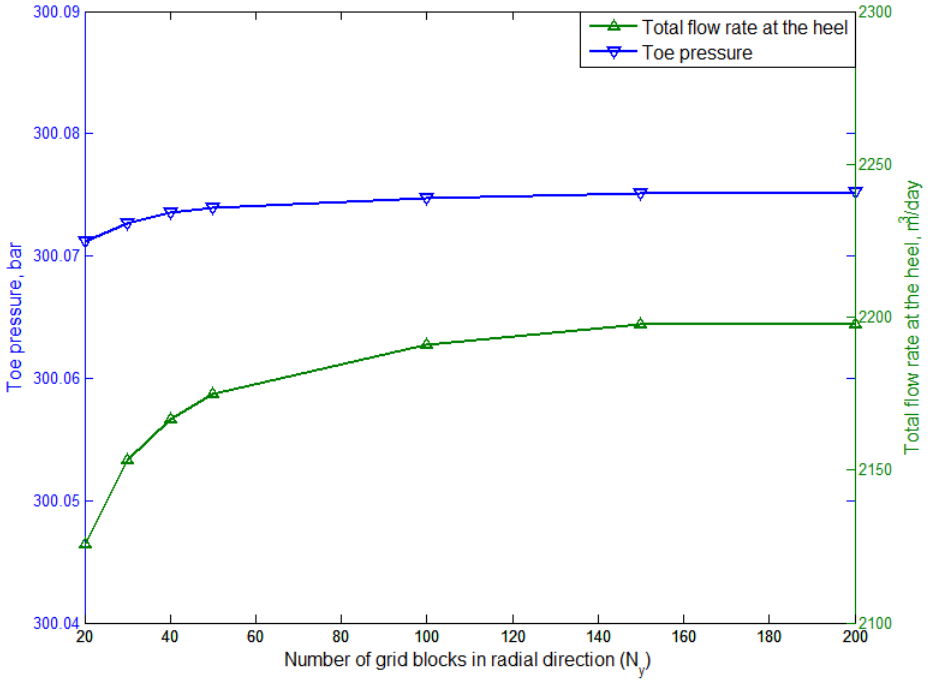

Figure 4.4: Segment refinement in radial direction

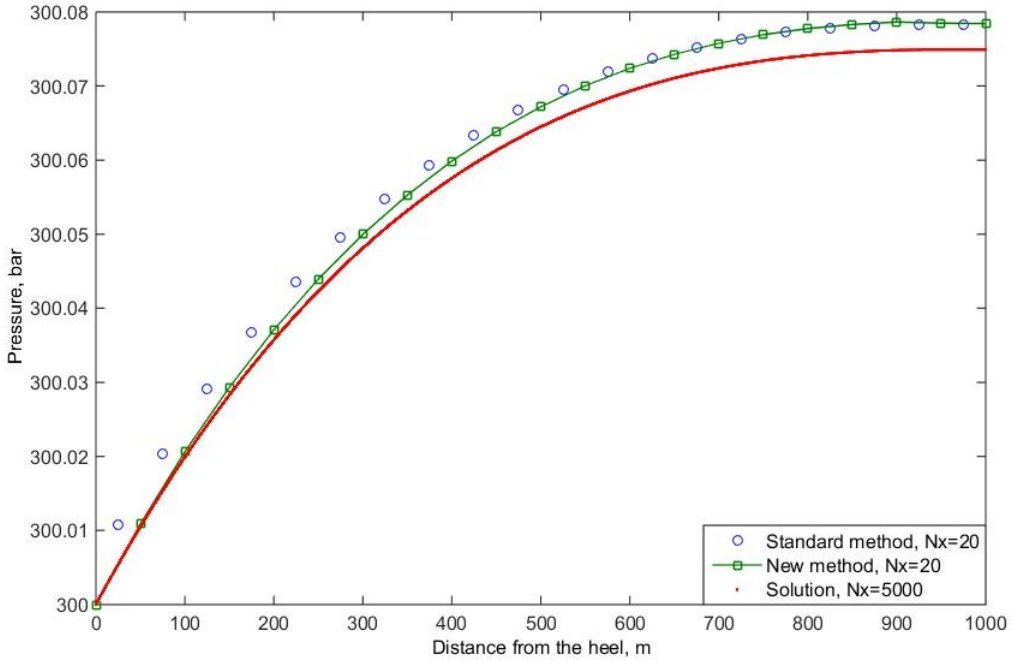

Figure 4.5: Pressure profile of the wellbore

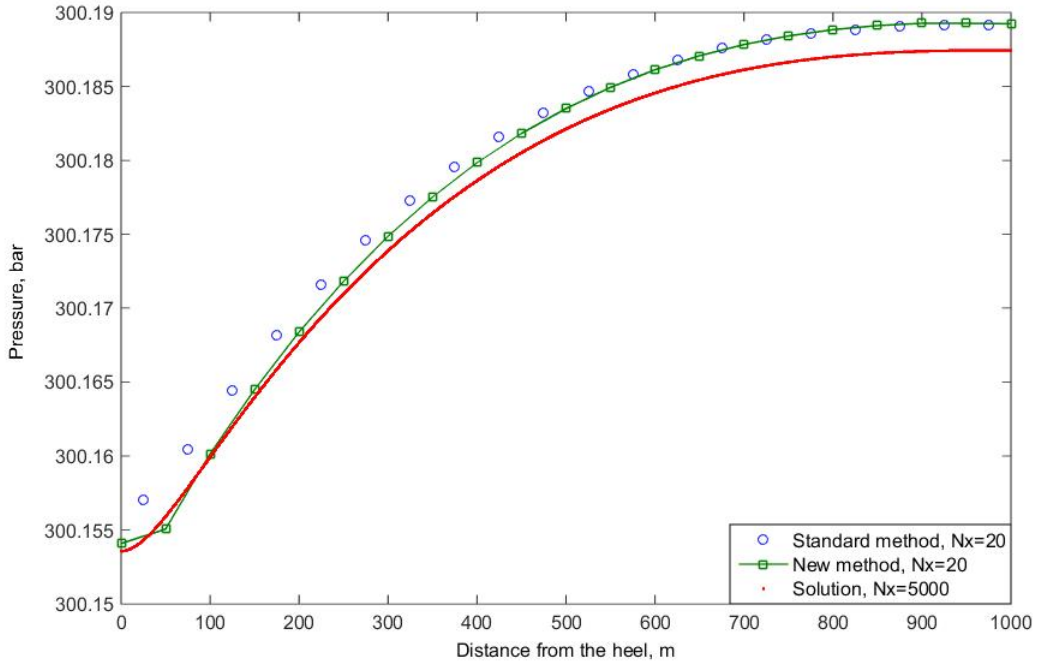

Figure 4.6: Wellbore inflow rate

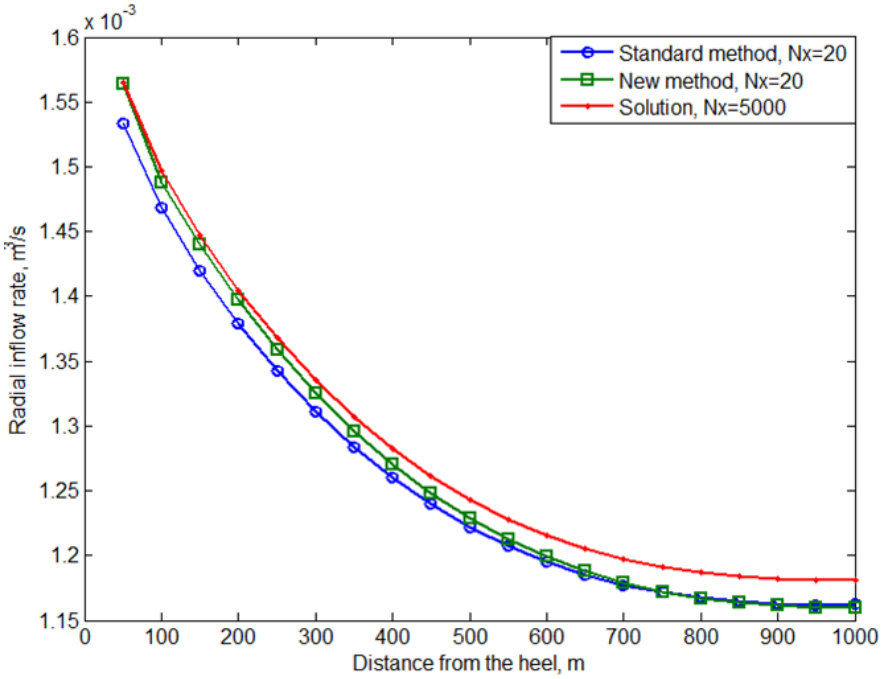

Figure 4.7: Wellbore inflow rate

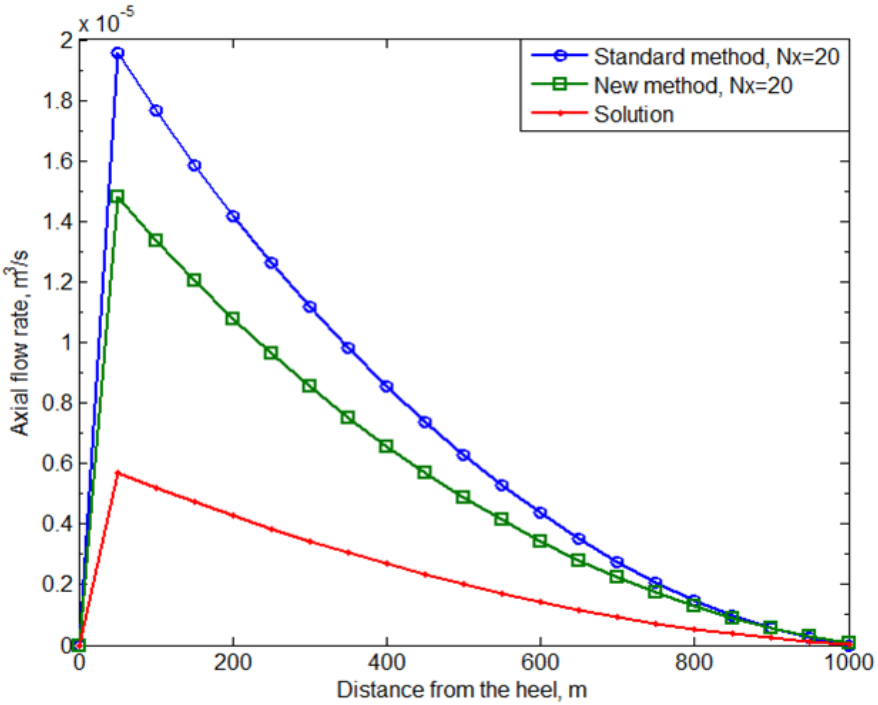

Figure 4.8: Axial reservoir flow rate

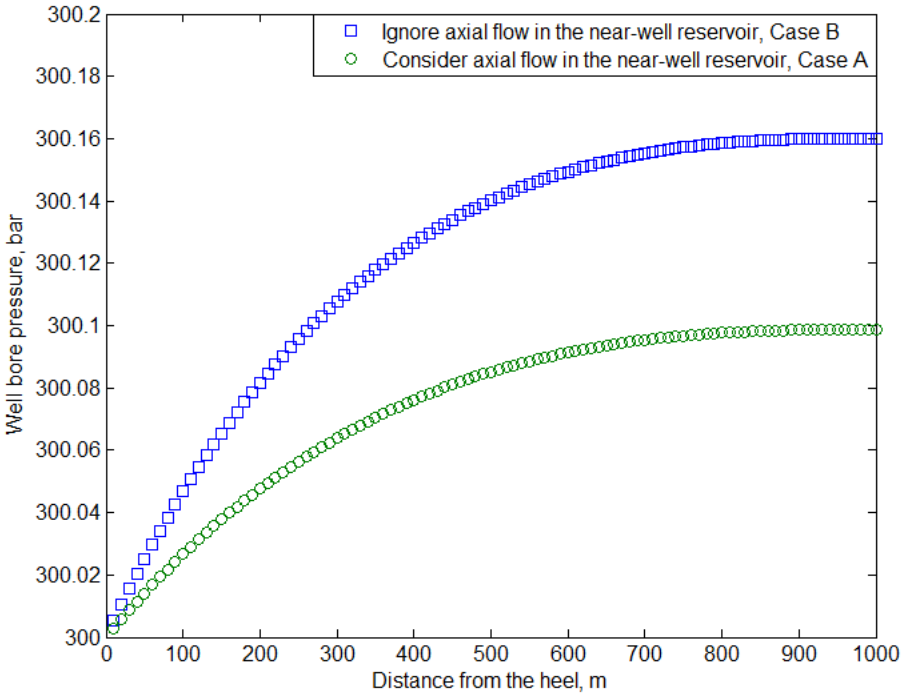

Figure 4.9: Wellbore pressure distribution

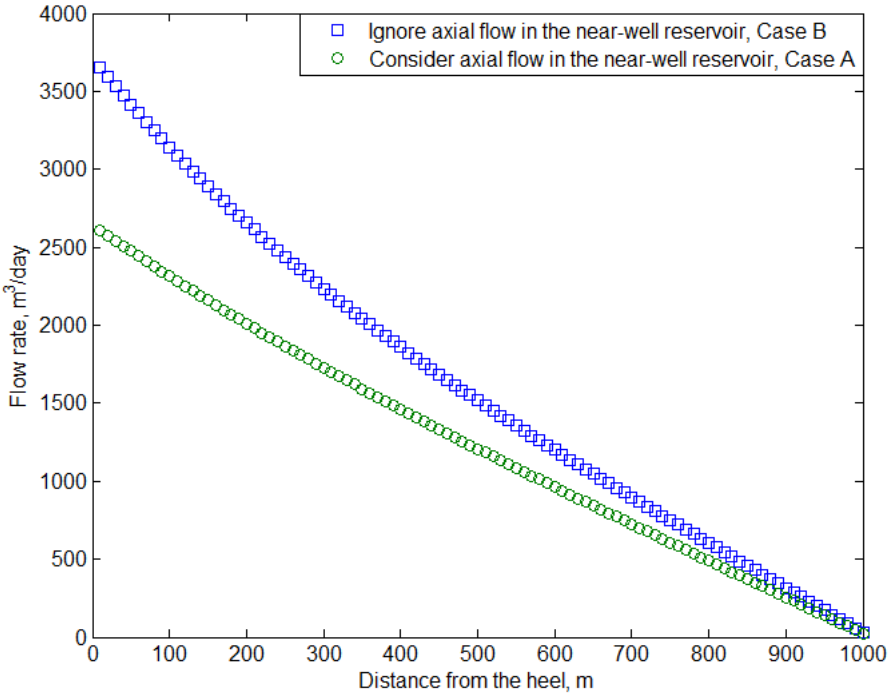

Figure 4.10: Flow rates in the wellbore

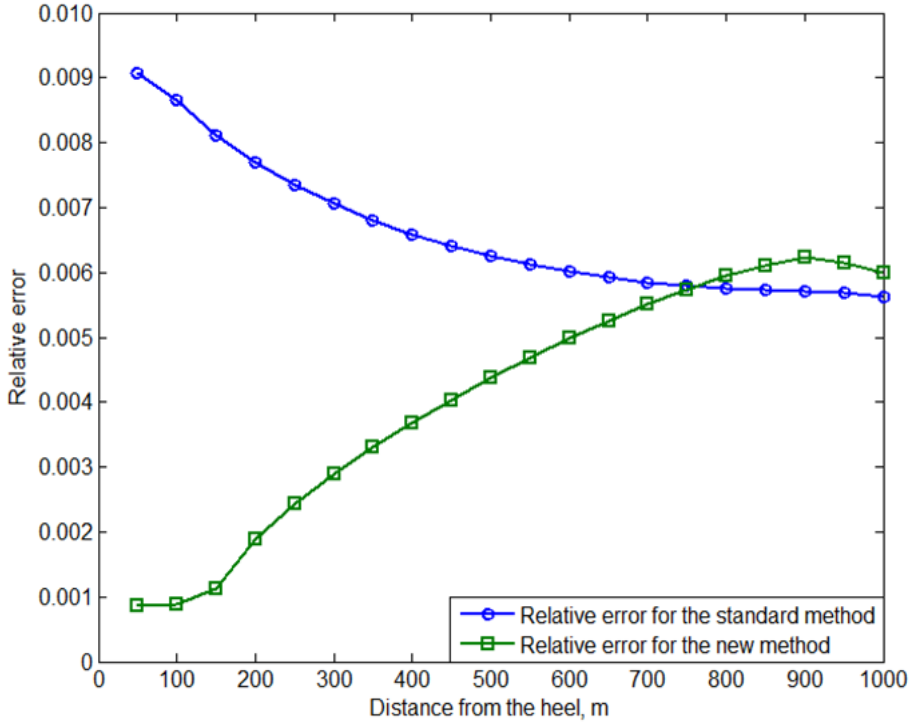

Figure 4.11: Relative error of the wellbore pressure

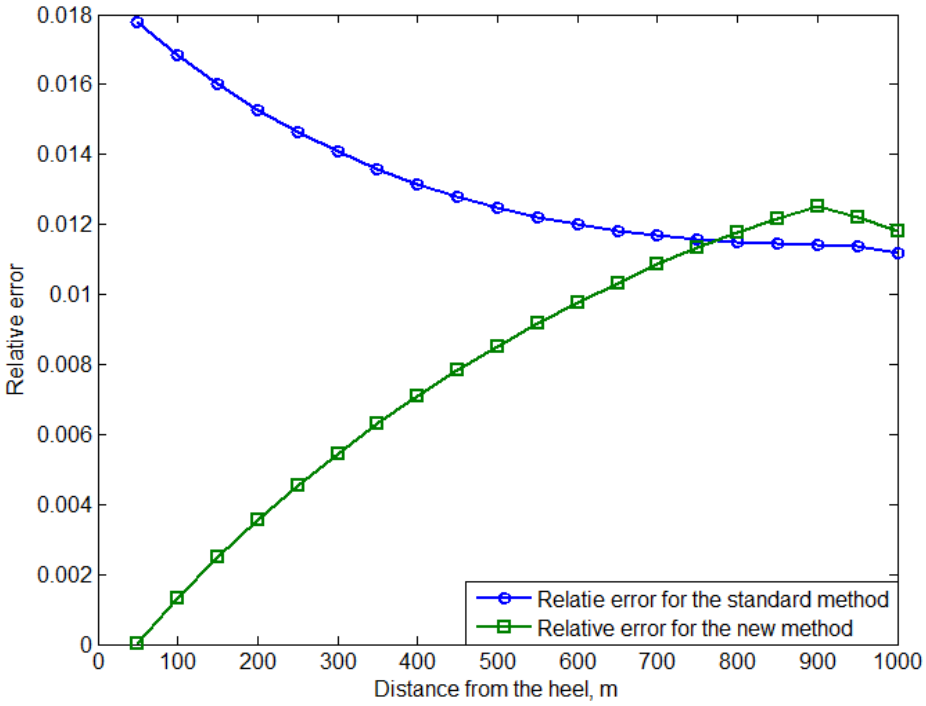

Figure 4.12: Relative error of the near-well reservoir pressure

4.5 Further applications

In this Section, further developments and applications of the well/near-well model are presented. Section 4.5.1 describes the coupling scheme with the well/near-well model and the reservoir model. Subsection 4.5.2 presents the application of the model in heterogeneous reservoirs. Various heterogeneity distributions in the near-well region are used in the model and results show that the model can accurately represent large permeability ranges in a stable manner without special treatment. In Subsection 4.5.3, various external reservoir pressure profiles are imposed using the model. In a the poorly communicating reservoir, the well inflow rates are negative in some parts of the reservoir, which means the flow direction is from the well to the reservoir, i.e. cross flow occurs. In this case, the cross flow is captured by the new model. In the last Subsection 4.5.4, the coupling of a reservoir model with the well/near-well model is demonstrated and compared with coupling a reservoir model with a simple well model with friction. An application is also presented for a horizontal well with unevenly distribution skin factors.

4.5.1 Coupling Well/Near-Well Model and Reservoir Model

The well/near-well model (below denoted Well Model) can consist of any number of concentric (circular) cylinders representing the near well reservoir and well completion details with possibly multiple annuli. Here, we assume only one annulus such as for a liner in an open hole completion where the annulus is a damaged reservoir, as shown in Figure 4.13. Hence, the flow rates from the reservoir to the annulus and from the annulus to the liner are both linearly proportional to the pressure differences.

In the Well Model, a segment has the same length as the distance between two adjacent grid block pressure nodes in the direction of the well trajectory. Also in Figure 4.14., we notice that the reservoir simulation model (briefly denoted Reservoir Model) pressure nodes are the same as the well segment external pressure nodes. The two simulation grids

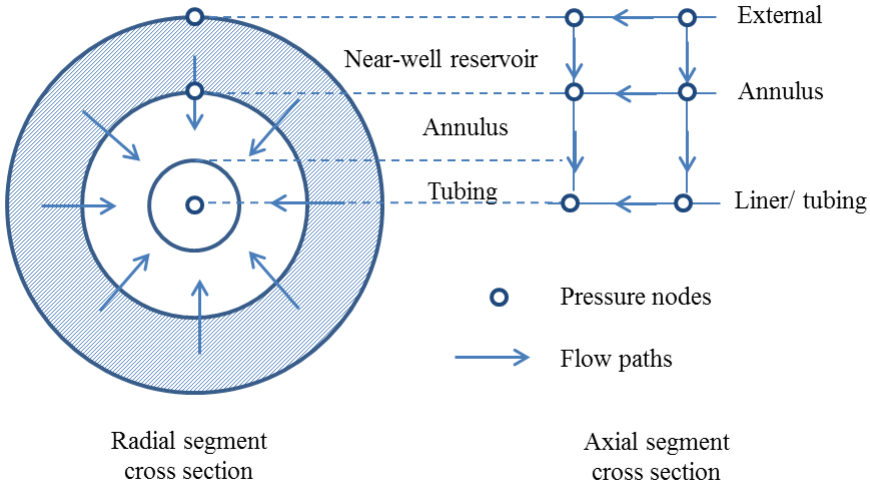

Figure 4.13: Well Model cross section view

are staggered; the external Well Model pressures are taken from the simulation grid block pressures. In cases where there are different permeabilities in adjacent Reservoir Model grid blocks, upscaled permeability in the axial direction is used in the Well Model with harmonic average of the two permeabilities. Therefore, if the permeability contrast is large, a finer grid may be necessary near such a contrast.

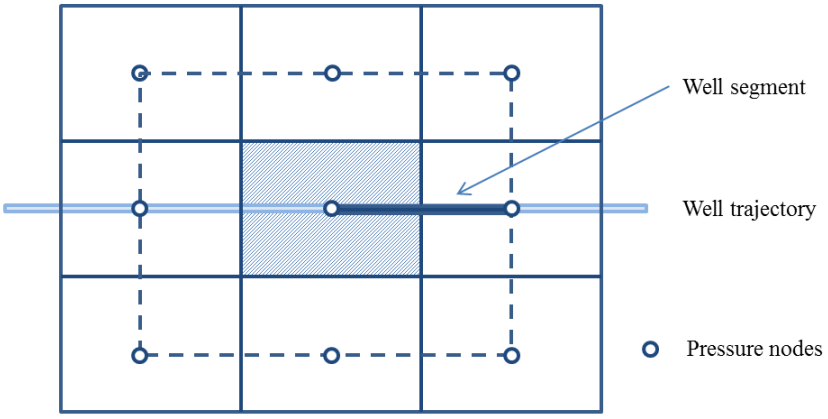

Figure 4.14: Grid blocks/ well segment

In coupled simulations, the communication between the two models takes place at two

levels. The grid block pressures are used in the Well Model as the external pressures. In addition, the annulus pressures from the Well Model are used as flowing wellbore (connection) pressures in the Reservoir Model. When running the reservoir simulator as stand-alone, a connection factor for each well grid block is used to calculate the well inflow, such as the Peaceman model (1983). As we shall see, this is needed only on the first time step in the coupled model. In this way, the coupled model is forced to incorporate detailed information which would not be possible if the two models were used as stand-alone models; for example the grid block pressure is influenced by large scale (remote) reservoir effects (faults, other wells ect.) and the well annulus pressures is influenced by completion details (inflow devices, perforations, any well flow restriction).

The coupling between the Well Model and the Reservoir Model is iterative on each reservoir simulation time step and has been described in previous publications like Breleke et al. (1993) and Johansen and Khoriakov (2007). Different from previous research, this well/near-well model, the Well Model used in this research, accounts for near-well reservoir flow performance. The near-well reservoir region solved by the Well Model and the Reservoir Model in an iterative fashion, instead of being solved once in the Reservoir Model in previous coupling schemes. This feature of the well/near-well model enables the coupling scheme to better capture the cross flow, represent the near-well heterogeneity, evaluate formation damage effects and converge in a more stable manner.

It is assumed that only slow transients are important; in and near the well the transients are is fast and a steady state well model is therefore used. In Figure 4.15, the iterative coupling is illustrated for one well segment. This iteration is performed on all segments simultaneously, and on each time step. The grid block pressures P_B from the Reservoir Model are used as external pressures in the Well Model, and the annulus pressures P_w from the Well Model are used as flowing wellbore pressure in the Reservoir Model. We describe an iteration cycle $k \rightarrow k+1$ which starts ($k = 1$) at the end of a reservoir simulation time step $n\Delta t$, where Δt is the time step and n is the number of time steps.

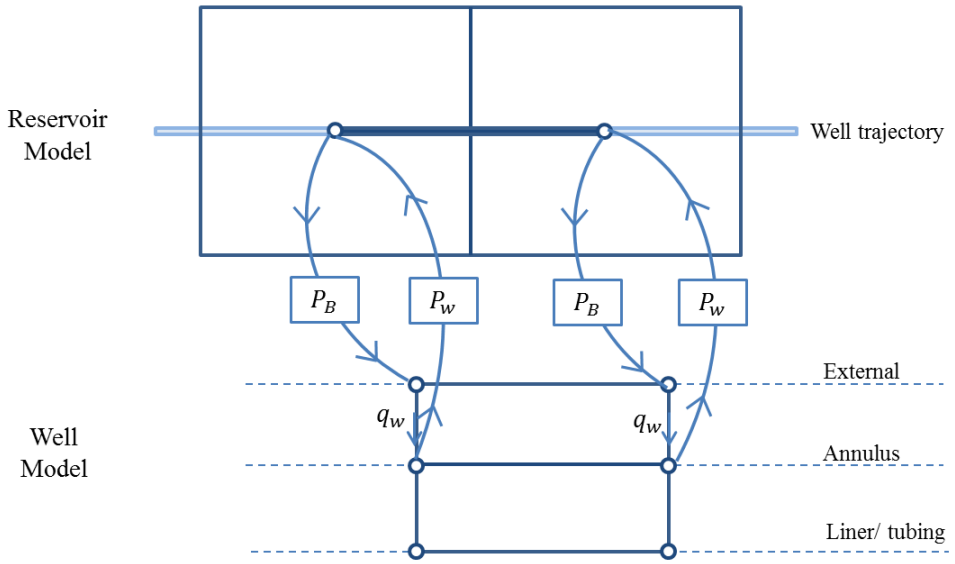

Figure 4.15: Coupling scheme with Reservoir Model and Well Model

First, the Reservoir Model is started at $n\Delta t$ using a constant flowing wellbore pressure (P_{BH}) over the time step. This produces estimates of reservoir grid block pressure $P_B^{(k)}$ and well connection inflow rate $q_B^{(k)}$ at time $(n+1)\Delta t$. Second, the Well Model is using $P_B^{(k)}$ as external node pressures and is run to produce annulus pressure $P_w^{(k)}$ and flow rates $q_w^{(k)}$ from external nodes to adjacent annulus nodes. Therefore, the connection factor $\omega^{(k)}$ for grid blocks are then calculated using

$$\omega^{(k)} = \frac{q_w^{(k)}}{P_B^{(k)} - P_w^{(k)}}. \tag{4.13}$$

Foror a given tolerance ϵ and reference flow rate q_o, if

$$\left[\sum_{i=1}^{N}\left(q_{B,i}^{(k)} - q_{w,i}^{(k)}\right)^2\right]^{(1/2)} < \epsilon q_o, \tag{4.14}$$

the iterations are stopped and values at time $(n+1)\Delta t$ are: $P_w^{(k)}$ is flowing well connection bottom hole pressure, $P_B^{(k)}$ is grid block pressure and $\omega^{(k)}$ is well connection factor; k here being the last iteration count. In Eq. (4.14) the sum is over all the segments. If Eq. (4.14) is not satisfied, $k := k+1$; and the procedure is repeated using values from the previous iteration. The flow chart in Figure 4.16 shows the procedures of the coupling

scheme described above from time $n\Delta t$ to time $(n+1)\Delta t$.

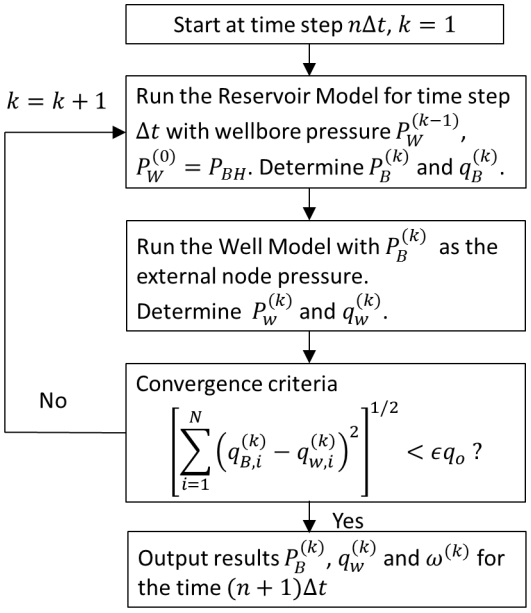

Figure 4.16: Flow chart of the coupling scheme with Reservoir Model and Well Model

In the above iteration process, both the Reservoir Model and the Well Model are run with the same overall well operating conditions, such as heel bottom hole pressure or total flow rate. It is also worthwhile to note that in the coupled simulation, the only time when conventional connection factors are used is for $n = 1$, i.e. the very first time step. In this time step, the Reservoir Model is using the heel bottom hole pressure as flowing well connection pressure in all connection, i.e. the detailed completion data resulting from local pressure losses (for example friction) in the well and near-well region are ignored. However, through the iterations these details are represented by updated connection factors ω (Eq. (4.14)) and well connection pressures.

In the coupling process, transients are present through the time stepping of the Reservoir Model. To allow interpretation of transient well tests in long, horizontal well completions, it requires wellbore transients for wellbore storage calculations as well as reservoir transients. Hence, the well model of this paper must be extended to transient flow of compressible fluids in wells, as presented by Khoriakov et al. (2012). This consistutes as further development

of this model.

The above coupling was described for single phase flow. For multi-phase flow, the saturations at well completion grid blocks are calculated by the Reservoir Model and can therefore be included in the iterations by using reservoir flow rates for each phase as $k_r(S) * q_B$, where k_r is relative permeability, and well flow rates as $\alpha * q$ where α is phase hold up. This was described in detail in Johansen and Khoriakov (2007).

4.5.2 Application to heterogeneous reservoirs

Reservoir permeability is usually heterogeneous. In numerical models, such heterogeneity results in changes of transmissibility between adjacent reservoir grid blocks, and between well blocks and wellbores. In the new well/near well model, calculation of flow rates and pressures are segment-based, which means that each segment of well and near-well reservoir is given unique properties including permeability. In this subsection, various distributions of permeability are used in the model to verify the convergence of the simulation. Basic parameters used here are given in Table 4.2.

Table 4.2: Parameters used in the heterogeneous examples Ex. K-1, K-2 and K-3

Parameter	Unit	Value
L_w	$[m]$	1000
r_w	$[m]$	0.1
r_e	$[m]$	20
μ_o	$[cP]$	1.18
B_o		1.3
ρ_o	$[kg/m^3]$	800
P_e	$[bar]$	320
P_w	$[bar]$	300

Ex. K-1: Homogeneous reservoir permeability distribution

We start with a homogeneous case, where the constant permeability is 50 mD. The permeability distribution and the pressure distribution solutions are shown in Figure 4.17 and 4.18. This example is mainly used for the comparison reason as a base case.

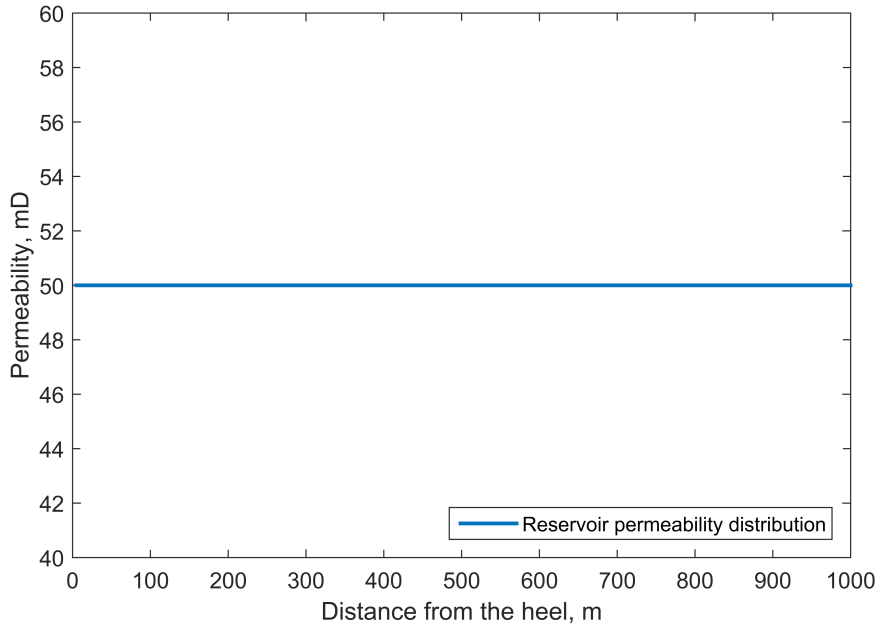

Figure 4.17: Permeability distribution in homogeneous case

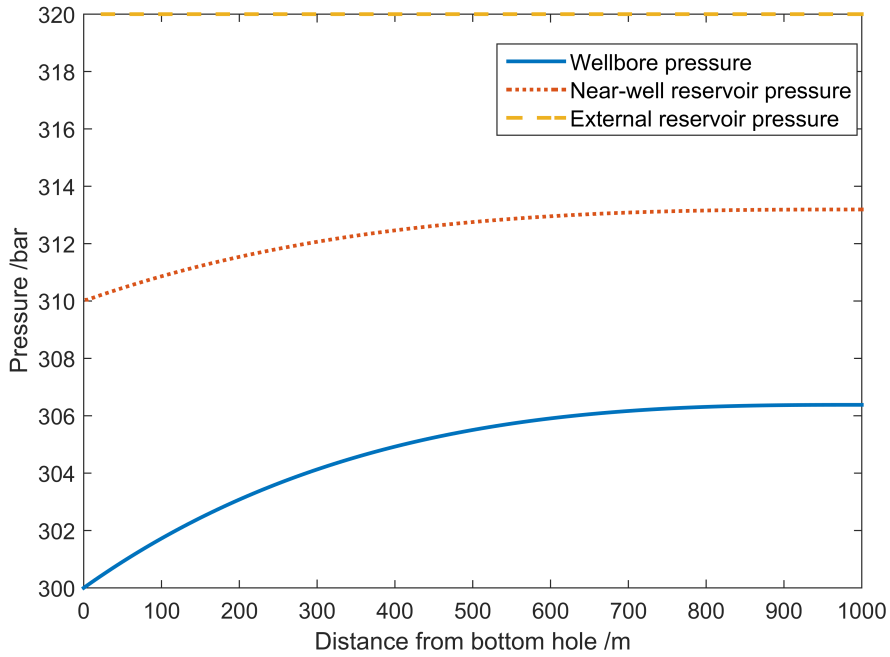

Figure 4.18: Pressure distribution with homogeneous permeability

Ex. K-2: Step wise reservoir permeability distribution

Next, a step wise permeability distribution is given with left half reservoir having $k = 5\ mD$ while the right half reservoir having $k = 1000\ mD$, as shown in Figure 4.19. The calculated pressure profiles (Figure 4.20), the well inflow rate (accumulative inflow rate per segment) and the well flow rate are shown in Figure 4.21 and Figure 4.22, respectively. The well inflow per segment, where the segments have equal length, first increases from toe to the middle due to increasing pressure difference between the wellbore and near-well reservoir. The well inflow still increases from the middle to the heel although are much smaller values since permeability is much lower. Hence, the pipe flow inside the wellbore, accumulation of well inflow from the heel to the toe, first increases sharply from heel to the middle and then increases flatly from the middle to the heel, which corresponds to the well inflow rate in Figure 4.21.

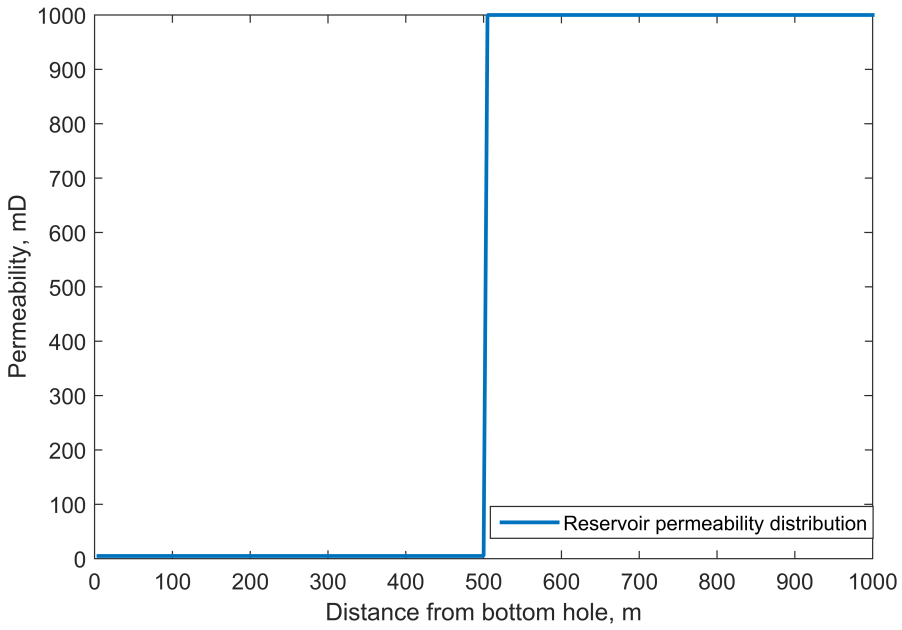

Figure 4.19: Step wise permeability distribution

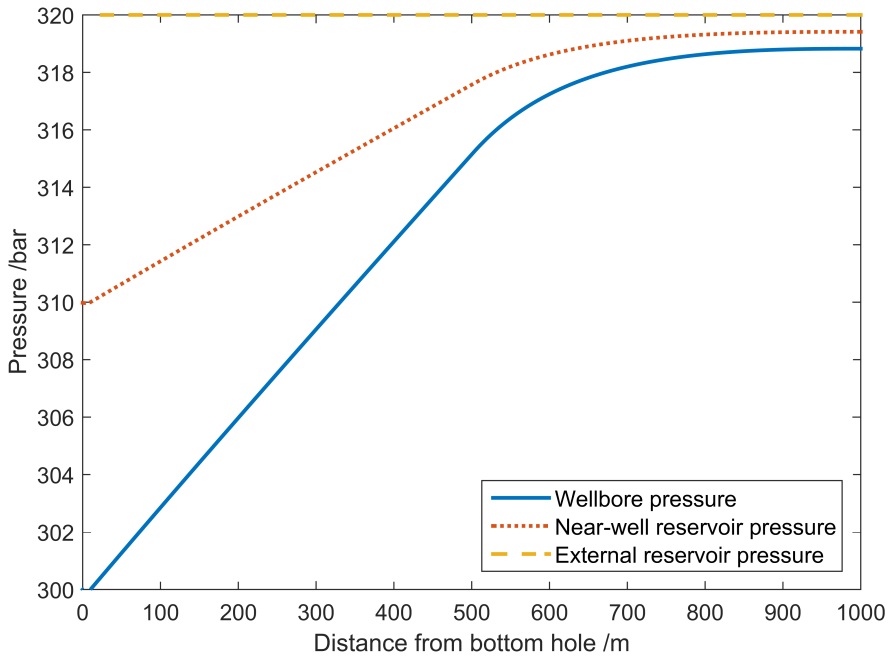

Figure 4.20: Pressure distribution with step wise permeability

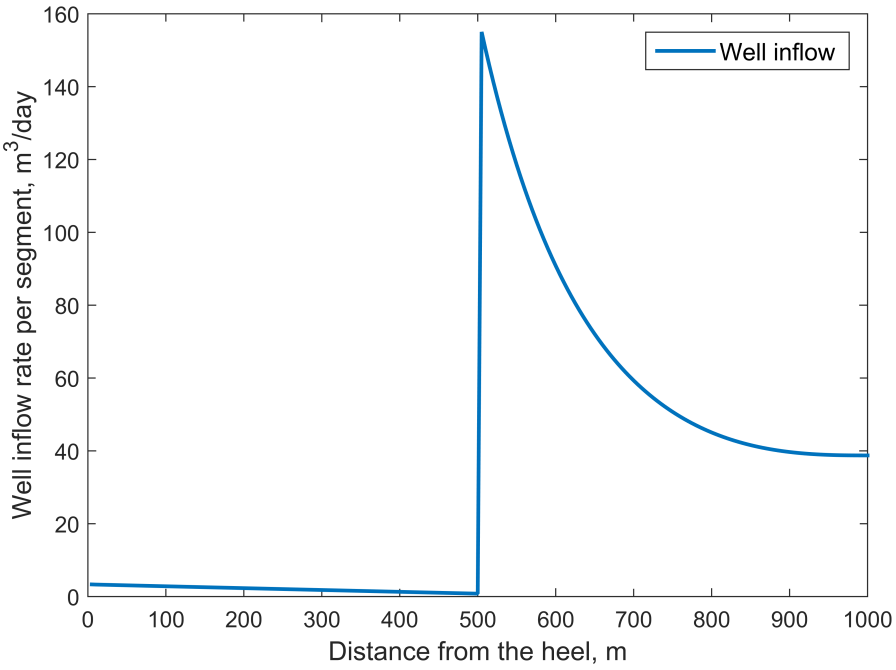

Figure 4.21: Well inflow rate with step wise permeability

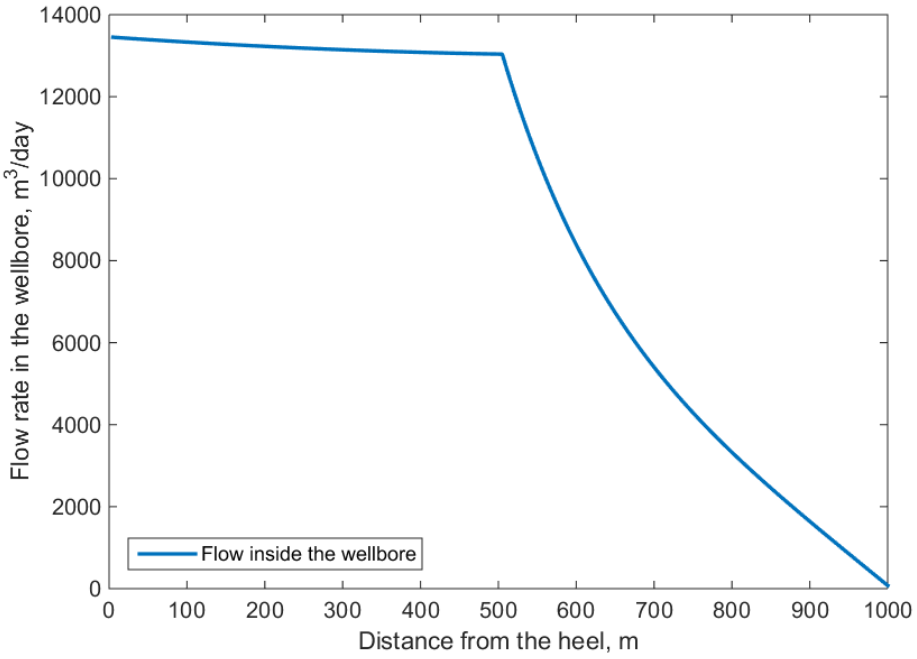

Figure 4.22: Wellbore pipe flow rate with step wise permeability

Ex. K-3: Randomized reservoir permeability distribution

Then, a randomized permeability distribution within the range from 20 to 200 mD is given to the near-well model. In real reservoirs, the permeability often varies in a more smooth way with certain continuity, which is computationally much easier than the permeability shown in Figure 4.23. In this case, the pressure is solved without additional numerical treatment and shows smooth behavior in the wellbore and the near-well reservoir pressures (Figure 4.24). The well inflow per segment in Figure 4.25 oscillates from the toe to the heel due to permeability heterogeneity but generally reflects an increasing trend. The pipe flow inside the wellbore generally increases from toe to heel as shown in Figure 4.26, also reflecting strongly varying inflow rates.

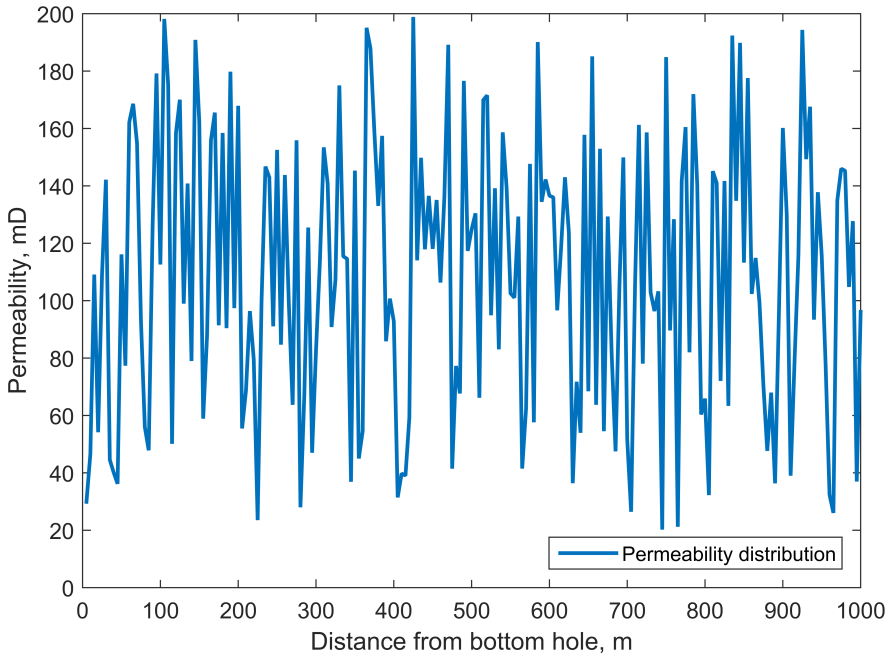

Figure 4.23: Randomized permeability distribution

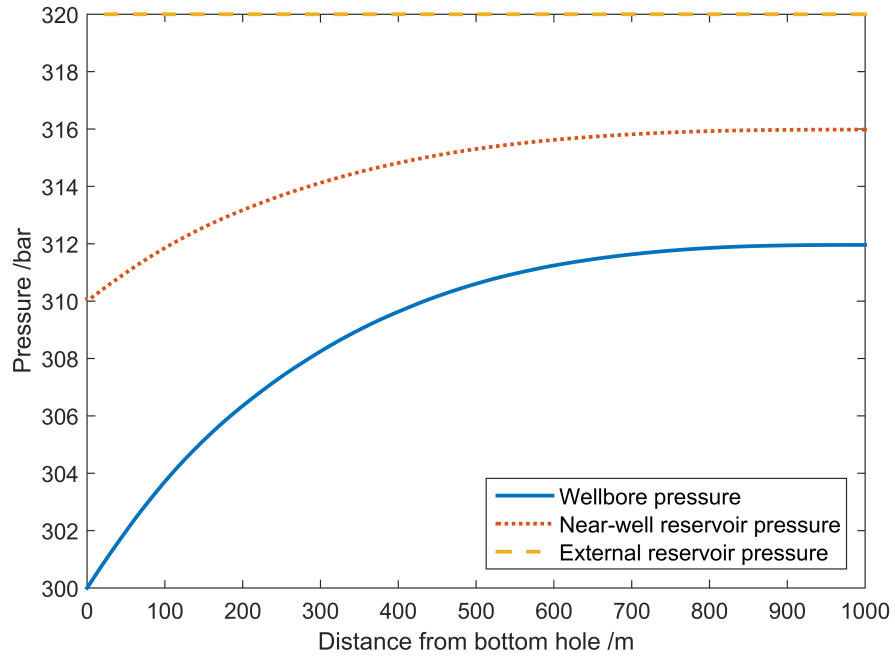

Figure 4.24: Pressure distribution with randomized permeability

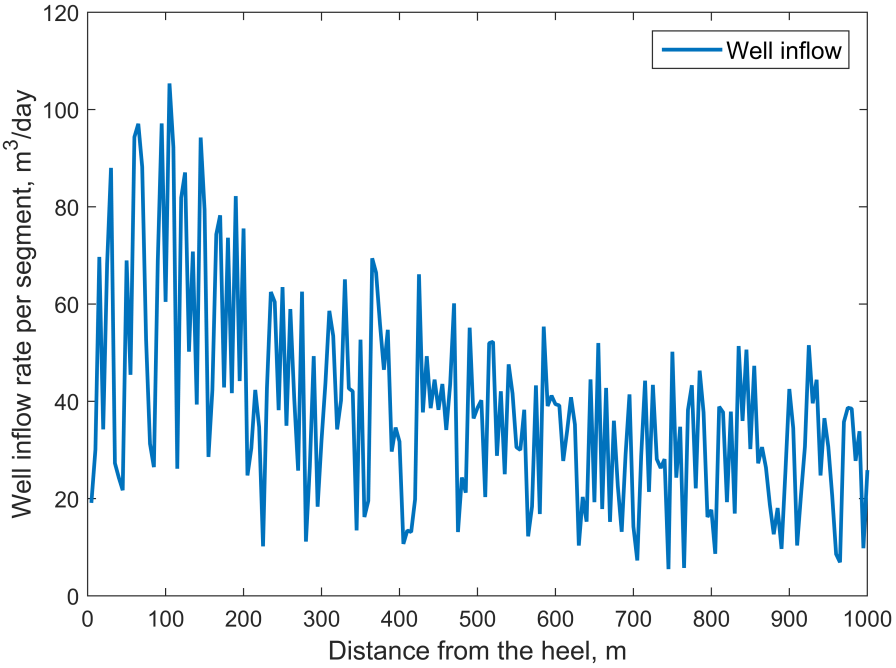

Figure 4.25: Well inflow rate with randomized permeability

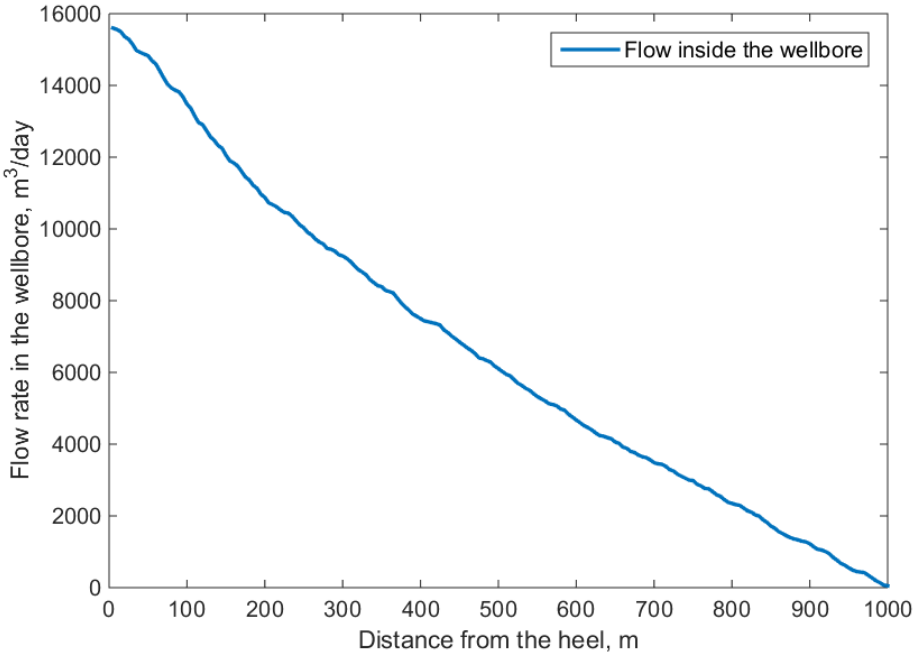

Figure 4.26: Wellbore pipe flow rate with randomized permeability

4.5.3 Application to various external reservoir pressure distributions

In the well/near-well model, the flow rate is determined automatically with flow directions. The positive direction in well inflow means from near-well reservoir to the well and in axial near-well reservoir flow means from toe to heel. Given various external reservoir pressures, the flow may become negative. Two representative types of special external reservoir distributions are used in this Subsection. Basic parameters used are the same as in previous Subsection except that the permeability is 100 mD and the external reservoir pressure is not constant in this Subsection.

Ex. P-1: Linearly decreasing external reservoir pressure

In the first example, the external reservoir pressure is decreasing linearly from the heel to the toe. The solution of the wellbore pressure and near-well reservoir pressure in this case is plotted in Figure 4.27. The well inflow in Figure 4.28 is generally increasing from toe to the heel while the axial reservoir flow in Figure 4.29 is partly negative. This means that in the section from around 300 m to the toe, the axial reservoir flow is toward the toe side, as shown in Figure 4.30.

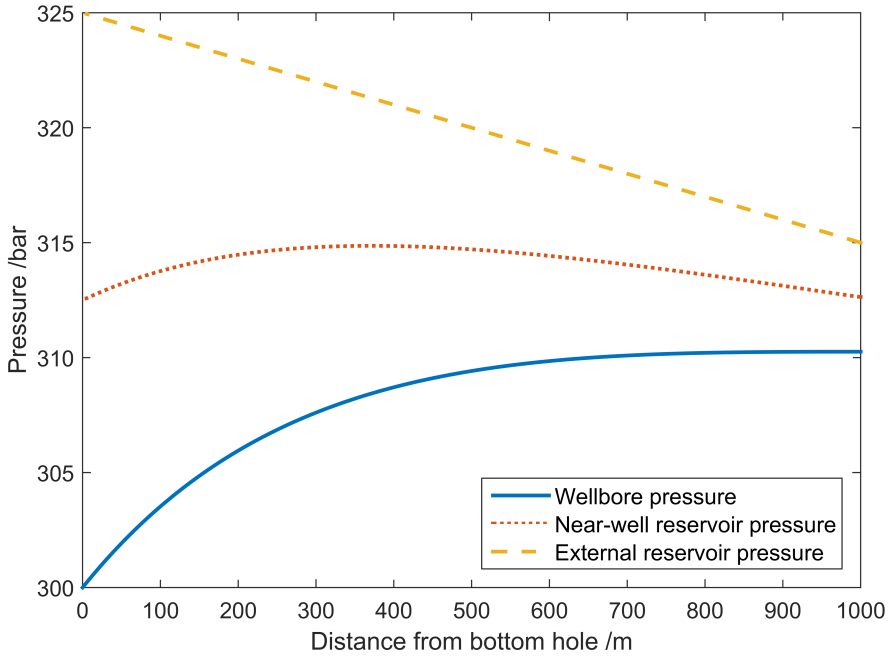

Figure 4.27: Pressure profiles with linear external reservoir pressure

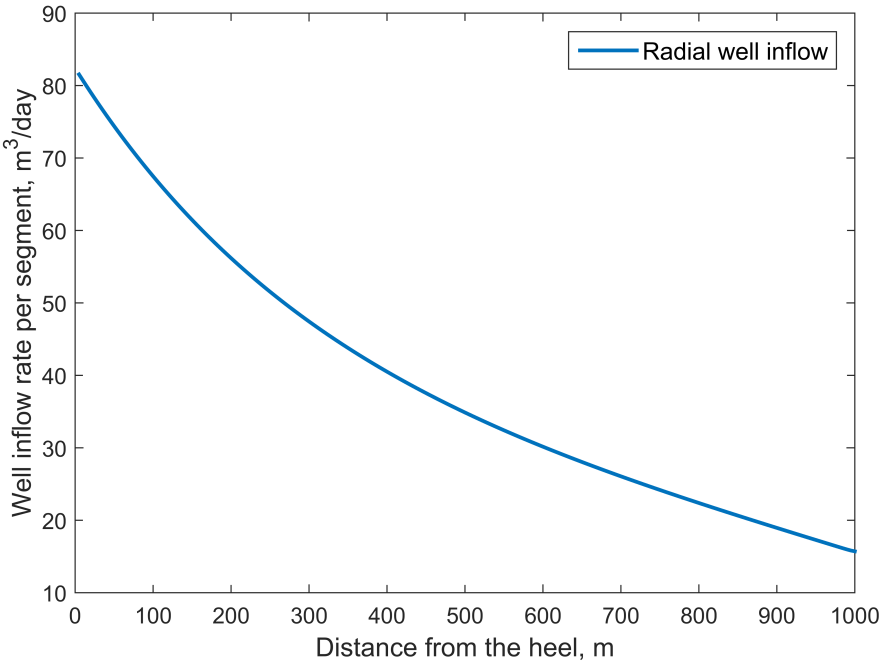

Figure 4.28: Well inflow rate with linear external reservoir pressure

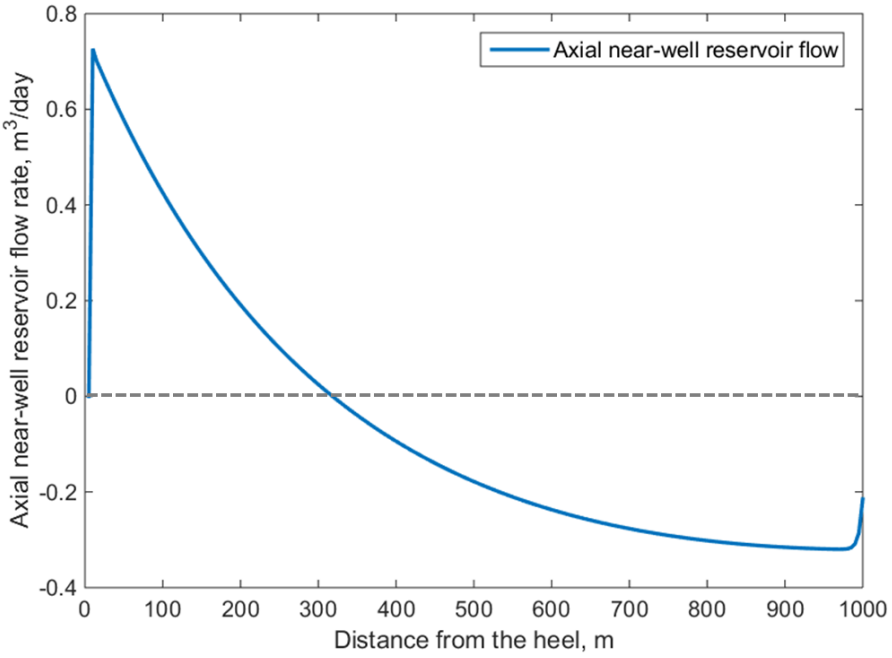

Figure 4.29: Axial near-well reservoir rate with linear external reservoir pressure

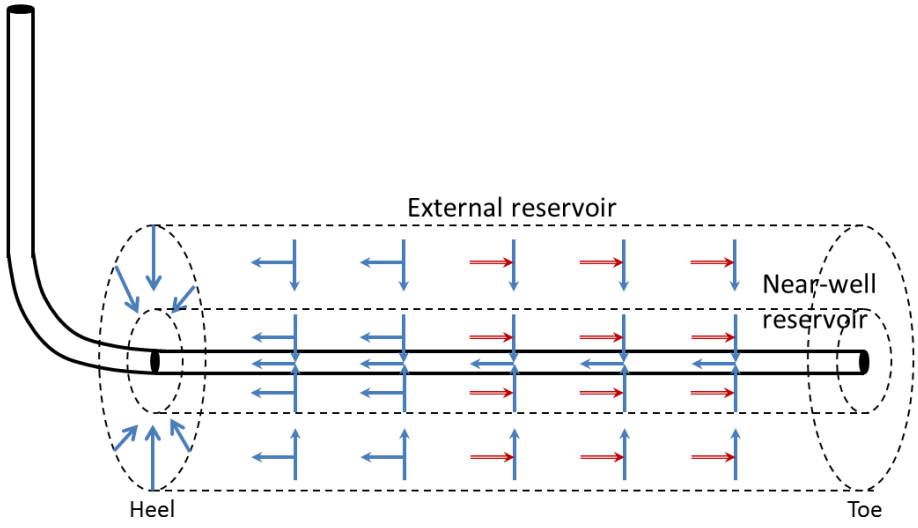

Figure 4.30: The flow direction in the well/near-well model given linear external reservoir pressure

Ex. P-2: Low pressure region in the external reservoir pressure

In the second example, the external reservoir has a low pressure region due to lack of communication because of reservoir compartments. The external reservoir pressure are 330 *bar* and 315 *bar*. The bottom hole pressure used is 310 *bar*. The solution of the pressure distribution is shown in Figure 4.31, where in the low pressure region, the wellbore pressure is actually larger than near-well reservoir pressure, which is larger than external reservoir pressure. In this special case, cross flow from the wellbore to the near-well reservoir occurs, which is unwanted in real production. As shown in Figure 4.32, the well inflow is negative in the low pressure region, represented by the well/near-well model. In the axial near-well reservoir flow in Figure 4.33 , there are two jumps in flow rates due to the sharp change of pressure. The flow directions are shown in Figure 4.34 to represent the cross flow.

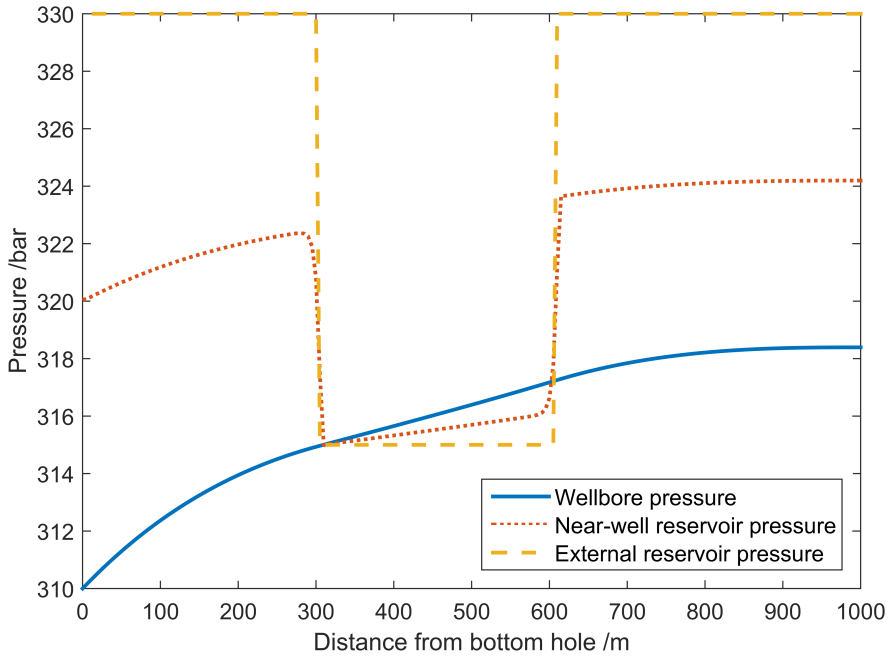

Figure 4.31: Pressure profiles with a low external reservoir region

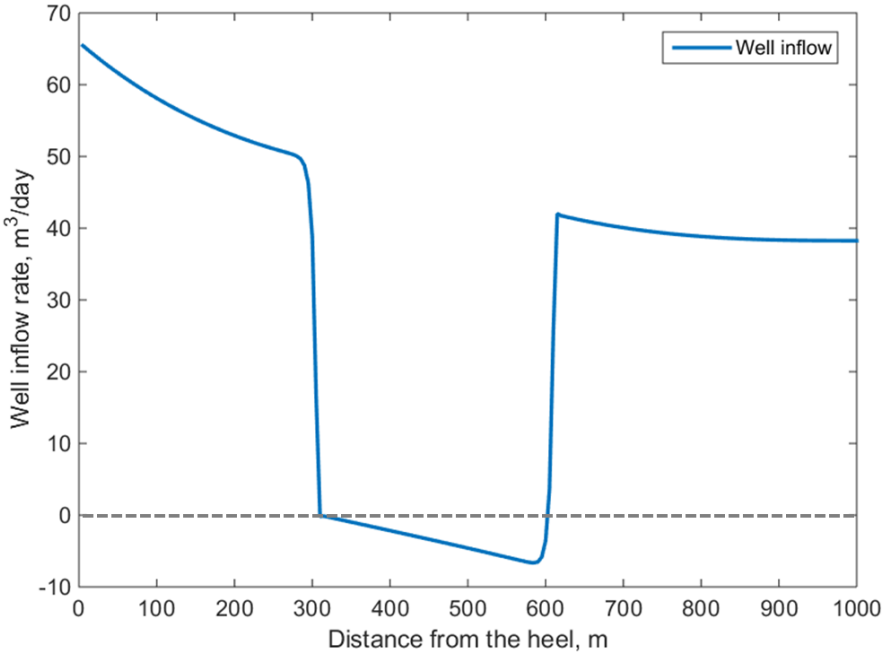

Figure 4.32: Well inflow rate with a low external reservoir region

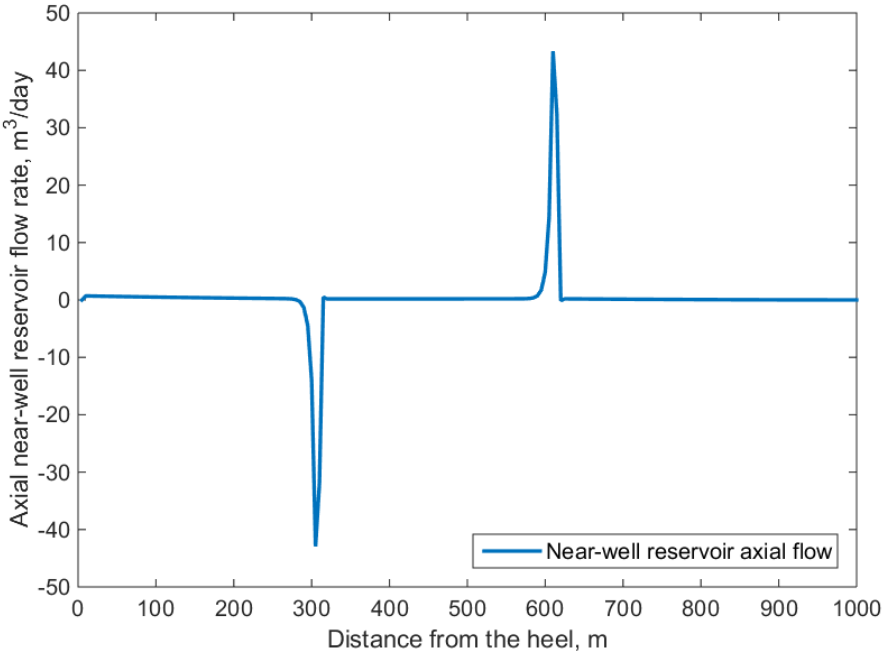

Figure 4.33: Axial near-well reservoir rate with a low external reservoir region

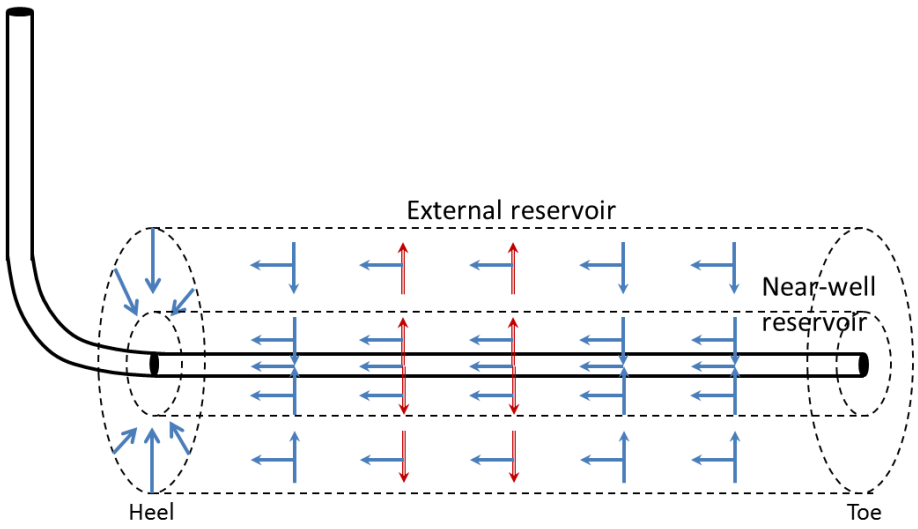

Figure 4.34: The flow direction in the well/near-well model given a low external reservoir region

4.5.4 Application to coupling with reservoir simulation

The coupling scheme described in Section 4.5.1 is demonstrated through two examples. The first example (Ex. S-1) follows the coupling scheme with a reservoir model (an available finite difference simulator) and a well model considering a constant skin factor. For convenience of comparison, two well models are used; one is the new well/near-well model of this thesis and one is a simple Friction model. Friction model is a simple well model that only considers frictional pressure loss inside the wellbore. The second calculation example (Ex S-2) demonstrates the applicability of the coupling with the new well/near-well model by modeling a horizontal well with unevenly distributed skin factors. The basic information used in both the Reservoir Model and the Well Mode are shown in Table 4.3.

The reservoir model has $20 \times 10 \times 5$ grid blocks and the horizontal well is located in the middle layer of the reservoir with all 20 well blocks completed open hole. Since the Cartisan and Cylindrical grids are used in the Reservoir Model and the Well Model, respectively, the volume of the well block is made the same as the volume of the near-well segment. Therefore, we have $\pi r_e^2 = dx \cdot dy$ for the cross section area using the same length. This

Table 4.3: Parameters used in the coupling examples, Ex. S-1 and S-2

Parameter	Unit	Value
K	$[mD]$	200
$k_{ro}(S_{wc})$		0.7
S_{wc}		0.1
dx	m	50
dy	m	50
dz	m	50
dt	Day	0.5
ϕ		0.2
P_{init}	$[bar]$	300
P_{heel}	$[bar]$	250
ϵ		1%

determines the external reservoir radius used in the well model. Initial reservoir pressures are all given as $p_{init} = 300$ bar and wellbore pressure is 250 bar throughout. Following the coupling scheme, the reservoir model is coupled with the well models (both Friction Model and the new model noted as CARP model) in each time step until convergence tolerance, $\epsilon < 1\%$, is satisfied. Then the results of pressure and saturation are recorded and used as the starting point for the next time step.

Ex. S-1: Constant skin factor

In the first example, the iteration process for the first time step are shown in Figure 4.35 and 4.36 for wellbore pressure and well inflow, respectively. The results of the first time step from both the CARP model and the Friction model are compared in terms of wellbore pressure (Figure 4.37), well inflow rate (Figure 4.38) and well block pressure (Figure 4.39). The difference between the two well models are indistinguishable, and with largest relative error less than 1%. Continuing the coupling for 5 time steps, the total well productivity from both models are compared in Figure 4.40. The two well models show a good agreement. The main reason is that in low permeability reservoirs, the axial flow rate is small and can possibly be ignored; which means well inflow is the dominant flow in the near-well region.

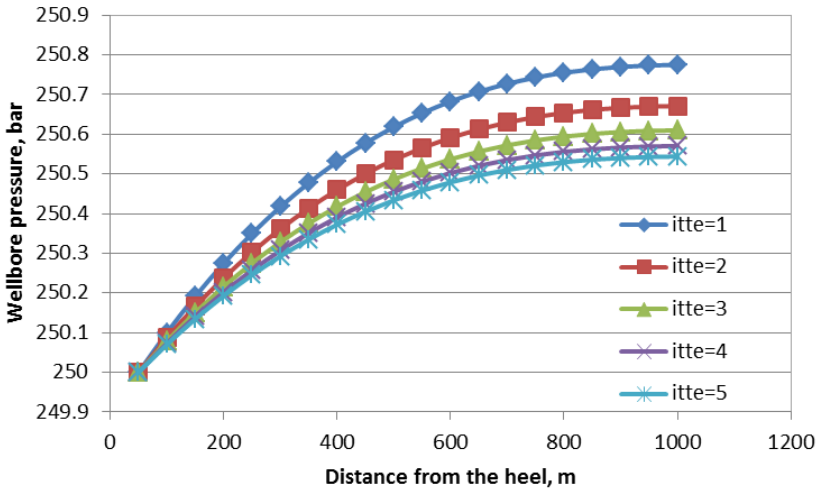

Figure 4.35: The well inflow in different iterations for the first time step

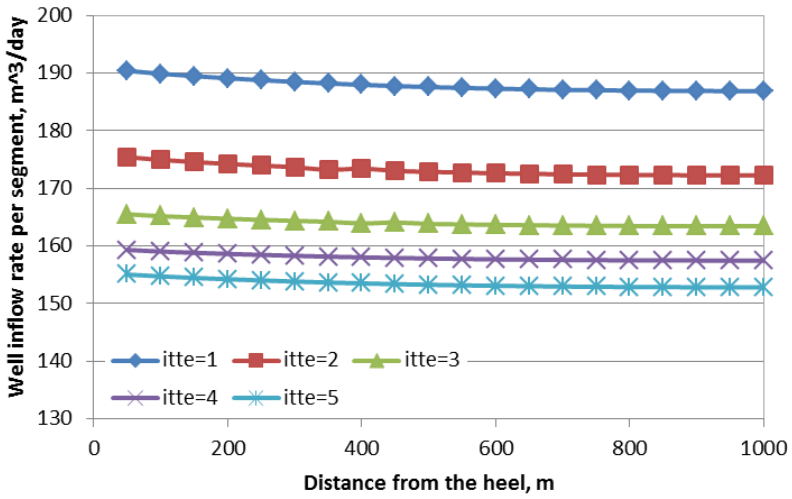

Figure 4.36: The well inflow in different iterations for the first time step

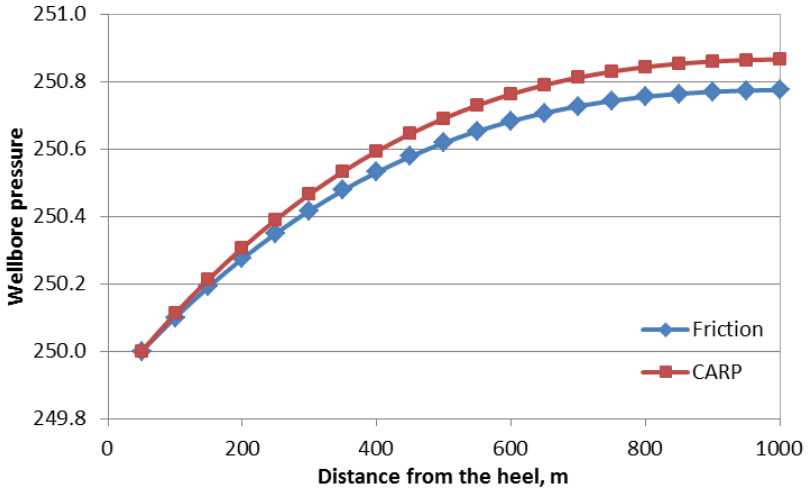

Figure 4.37: Comparison of wellbore pressure between well models for the first time step

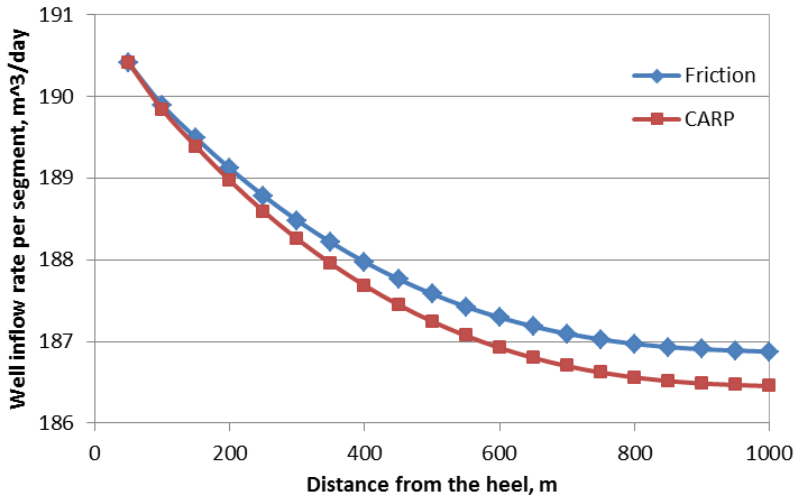

Figure 4.38: Comparison of well inflow rates between well models for the first time step

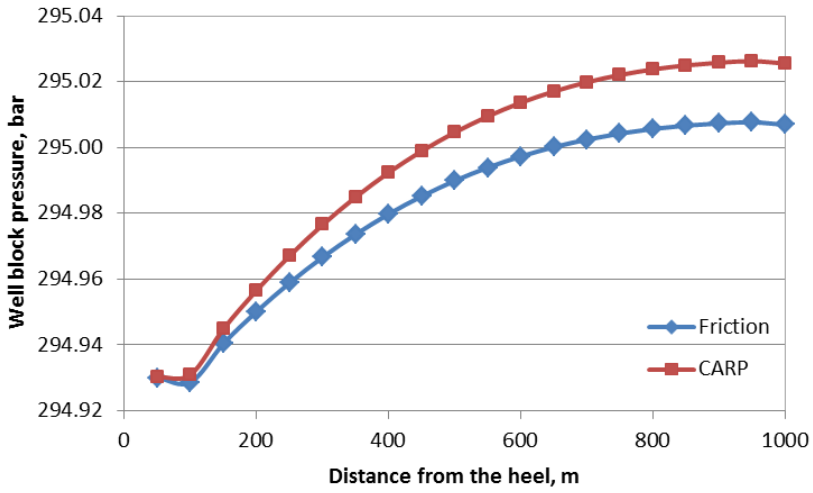

Figure 4.39: Comparison of well block pressure between well models for the first time step

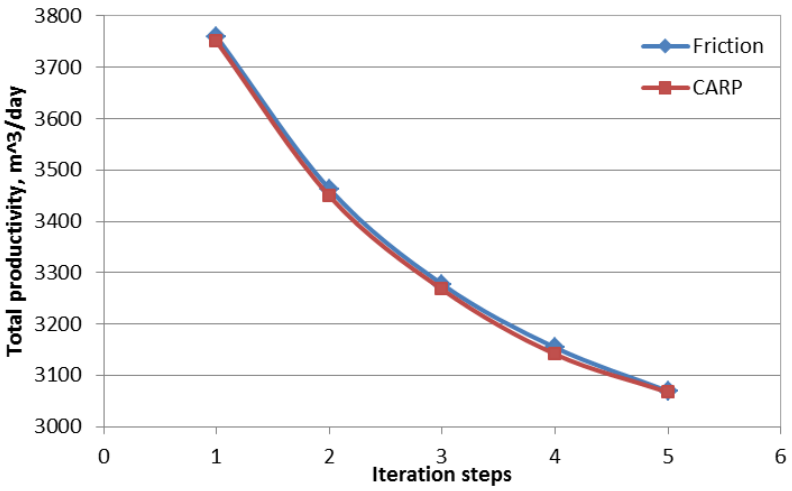

Figure 4.40: Comparison of total productivity between well models for various time steps

Ex. S-2: Unevenly distributed skin factor

In the second example, unevenly distributed skin factors are introduced in the near-well region. The non-uniform skin distribution is usually caused by varying mud invasion along the wellbore, and is usually assumed to be cone shaped (Frick and Economides (1993) and Furui et al. (2003)). Here, the local skin factor by Furui et al. (2003) is applied; i.e.

$$s(x) = \left(\frac{k}{k_d(x)} - 1\right) \ln\left\{\frac{1}{1+I_{ani}}\left[\frac{r_{dh}(x)}{r_w} + \sqrt{\left(\frac{r_{dh}(x)}{r_w}\right)^2 + I_{ani}^2 - 1}\right]\right\} \tag{4.15}$$

where $\frac{k}{k_d} = 3$; maximum damaged zone radius $r_{dh} = 5inch$; anisotropy ratio $I_{ani} = 1$; permeability $K = 200\ mD$ and the skin factor distribution is shown in Figure 4.41. The skin factors are used in the reservoir model when coupling with the Friction well model and in the well model when coupling with the well/near well model. In the well/near-well model, the axial relative permeability is affected accordingly, which can be determined by applying Hawking skin definition in directional permeability, i.e.

$$s(x) = \left(\frac{k_x}{k_{x,d}} - 1\right) ln\left(r_e/r_w\right), \tag{4.16}$$

where k_x is the directional permeability along wellbore, $k_{x,d}$ is this axial damaged permeability considering formation damage and $\frac{k_x}{k_{xd}} = \frac{k}{k_d}$. With the same procedures as used in Ex. S-1, the results from two models are compared for the first time step in terms of wellbore pressure (Figure 4.42), well inflow rate (Figure 4.43) and well block pressure (Figure 4.44). Continuing the coupling for 5 time steps, the total well productivity from both models are compared in Figure 4.45. The total productivity from the two well models (the Friction Model and the new Well Model) shows clear difference with around $7-8\%$ relative errors in each time steps. The new well model results in a lower total productivity due to extra near-well reservoir pressure drop in the axial direction for formation damaged reservoirs.

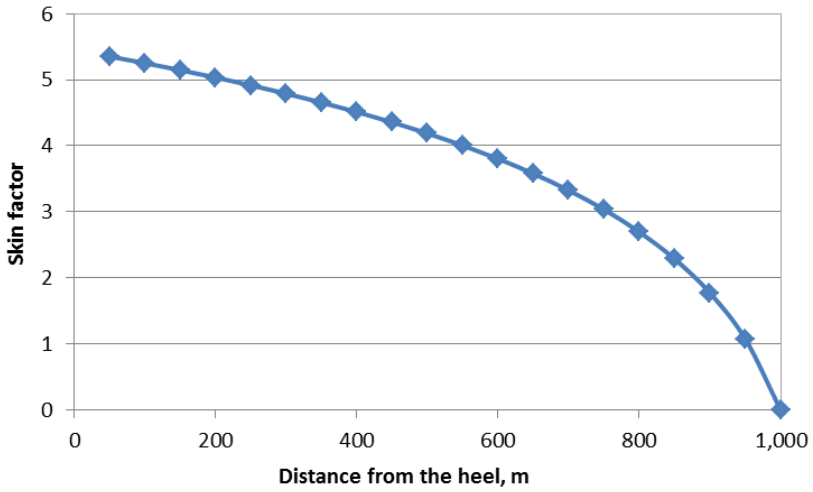

Figure 4.41: Skin factors distribution along wellbore

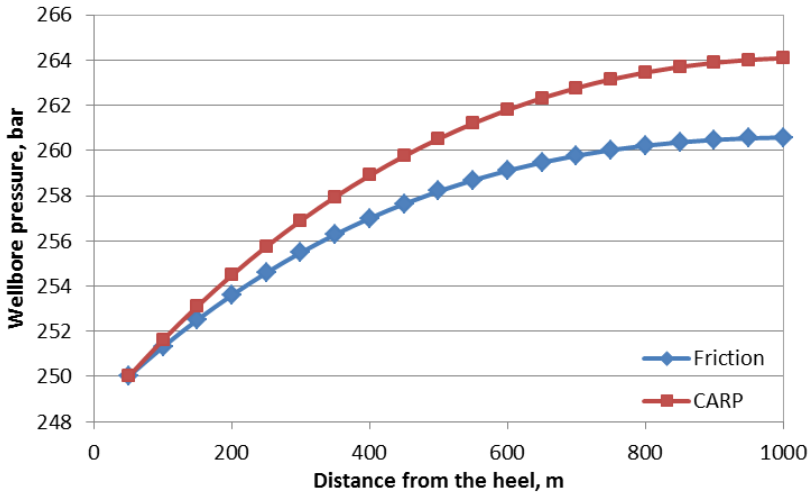

Figure 4.42: Comparison of wellbore pressure between well models with unevenly distributed skin factors

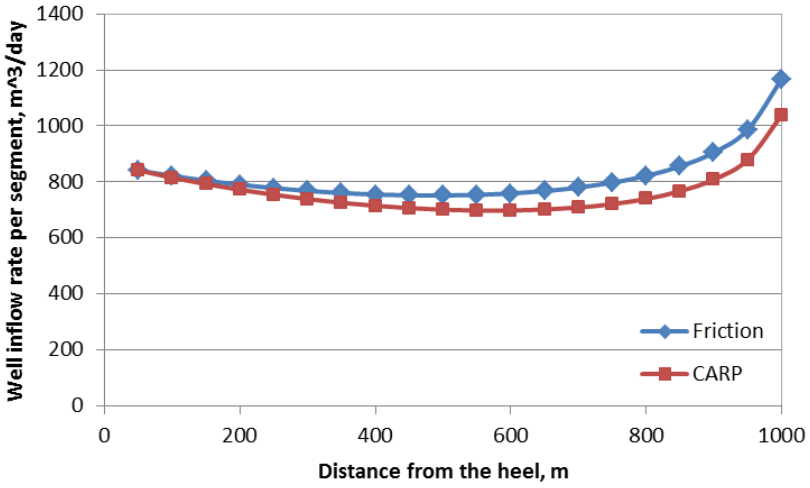

Figure 4.43: Comparison of well inflow rates between well models with unevenly distributed skin factors

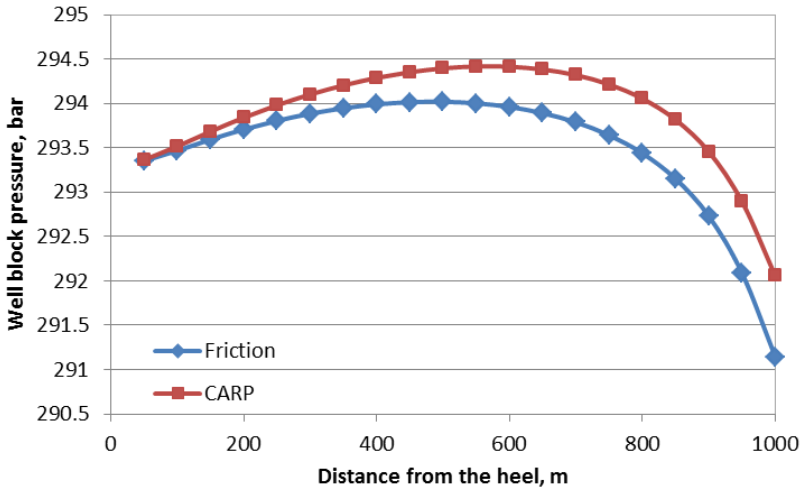

Figure 4.44: Comparison of well block pressure between well models with unevenly distributed skin factors

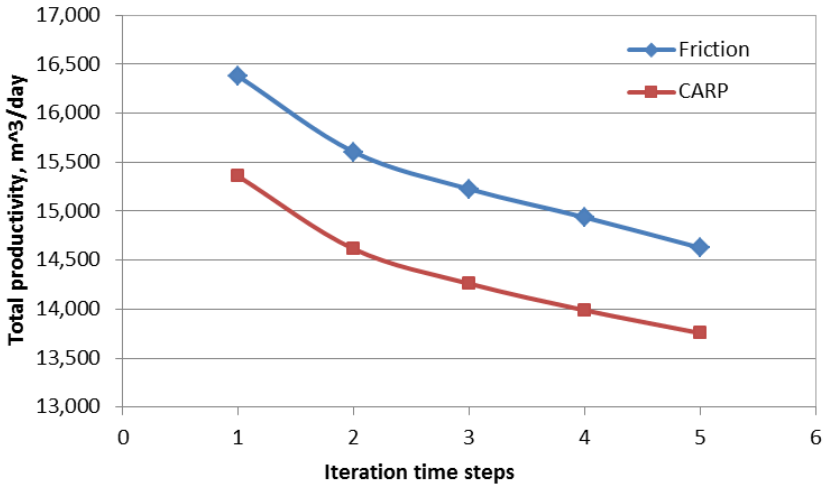

Figure 4.45: Comparison of total well productivity with unevenly distributed skin factors in various time steps

4.6 Conclusion

An analytical model has been implemented in a numerical modeling for the entire well trajectory and near-well region. The pressure distribution is piecewise linear/logarithmic as opposed to a piecewise constant distribution as in a standard finite difference method. It is demonstrated that the new semi-analytical approach is superior to the standard approach in the sense that the standard approach requires more well segments to achieve the same accuracy as the high-order method. The numerical solution is in good agreement with analytical results; the conclusion is that the axial flow along the well trajectory in the reservoir cannot be ignored, particular in high permeability, high productivity reservoirs.

The new well/near-well model is applied in cases of heterogeneous reservoirs, with various external reservoir pressure distributions and coupling with a reservoir model. The results show that the model can handle a large range of permeability heterogeneity, represent cross flow between well and near-well reservoirs, model horizontal well formation damage accurately with unevenly distribution skin factors. It also demonstrates that the new Well Model coupled with the reservoir model results in a lower productivity due to consideration

of axial reservoir pressure drop along well trajectory.

Appendix 4-A: Proof of high order method

In this section, we assume that the flow inside the well bore is laminar flow. Hence the flow equation include friction is

$$Q_f = T'_f \Delta P^{(\frac{4}{7})}, \tag{4.17}$$

different from Eq. (4.8) which is for turbulent flow. Here,

$$T'_f = -\frac{\pi r_w^4}{8\mu\Delta x}. \tag{4.18}$$

For standard finite difference method, the momentum balance equations in reservoir block (i,j) and well segment $(i,j-1)$ are expressed as

$$\begin{aligned} P_{i,j} - P_{i,j-1} - r_1(2P_{i,j-1} - P_{i+1,j-1} - P_{i-1,j-1}) &= 0, \\ 2P_{i,j} - P_{i,j+1} - P_{i,j-1} + r_2(2P_{i,j} - P_{i+1,j} - P_{i-1,j}) &= 0. \end{aligned} \tag{4.19}$$

Here, $r_1 = \frac{T'_{fl}}{2*T_r} = -\frac{r_w^4 ln(r_{j+1}/r_j)}{16K\Delta x^2}$ and $r_2 = \frac{T_x}{2T_r} = \frac{(r_{j+1}^2 - r_j^2) ln(r_{j+1}/r_j)}{2\Delta x^2}$. Note that $p_{x_i,y_j} = p_(i,j)$ is the real solution of the pressure; it would not satisfy the discrete equations in general and the discrepancy is the local truncation error, noted by $\epsilon_{i,j}$. Substituting the real solution in Eq. (4.18) we get

$$\begin{aligned} \epsilon_{i,j-1} &= p_{i,j} - p_{i,j-1} - r_1(2p_{i,j-1} - p_{i+1,j-1} - p_{i-1,j-1}), \\ \epsilon_{i,j} &= 2p_{i,j} - p_{i,j+1} - p_{i,j-1} + r_2(2p_{i,j} - p_{i+1,j} - p_{i-1,j}). \end{aligned} \tag{4.20}$$

We apply Taylor serious expansion for the pressure in the neighborhood of $p_{i,j}$ and get

$$\begin{aligned} p_{i+1,j} &= p_{i,j} + \frac{\partial p_{i,j}}{\partial x}\Delta x + O(\Delta x^2), \\ p_{i-1,j} &= p_{i,j} - \frac{\partial p_{i,j}}{\partial x}\Delta x + O(\Delta x^2), \\ p_{i,j+1} &= p_{i,j} + \frac{\partial p_{i,j}}{\partial r}\Delta r + O(\Delta r^2), \\ p_{i,j-1} &= p_{i,j} - \frac{\partial p_{i,j}}{\partial r}\Delta r + O(\Delta r^2). \end{aligned} \tag{4.21}$$

Then the truncation errors become

$$\begin{aligned} \epsilon_{i,j-1} &= O(\Delta x^2) + O(\Delta r), \\ \epsilon_{i,j} &= O(\Delta x^2) + O(\Delta r^2). \end{aligned} \tag{4.22}$$

Therefore, the standard finite difference method is second order accurate in axial direction and first order accurate in radial direction for well grid blocks. While it is second order accurate in both axial and radial direction for reservoir grid blocks.

For for the new semi-analytical method, the momentum balance equations in reservoir block (i,j) and well segment $(i,j-1)$ are expressed as

$$P_{i,j} - P_{i,j-1} + P_{i+1,j} - P_{i+1,j-1} - m_1(2P_{i,j-1} - P_{i+1,j-1} - P_{i-1,j-1}) = 0, \tag{4.23}$$

and

$$\begin{aligned} &2P_{i,j} - P_{i,j+1} - P_{i,j-1} - (2P_{i+1,j} - P_{i+1,j+1} - P_{i+1,j-1}) \\ &+m_2\left[2P_{i,j-1} - P_{i+1,j-1} - P_{i-1,j-1} - (2P_{i,j} - P_{i+1,j} - P_{i-1,j})\right] \\ &+m_3(2P_{i,j} - P_{i+1,j} - P_{i-1,j}) = 0. \end{aligned} \tag{4.24}$$

Here, $m_1 = \frac{T'_{fl}}{T_r} = 2r_1, m_2 = \frac{T_{x1}}{T_r}, m_3 = \frac{T_{x2}}{T_r}$. Again, note that $p_{x_i,y_j} = p_(i,j)$ is the real solution of the pressure. Substituting the real solution in Eq. (4.22) and (4.23) will provide

$$\varepsilon_{i,j-1} = p_{i,j} - p_{i,j-1} + p_{i+1,j} - p_{i+1,j-1} - m_1(2p_{i,j-1} - p_{i+1,j-1} - p_{i-1,j-1}), \tag{4.25}$$

and

$$\begin{aligned} \varepsilon_{i,j-1} &= 2p_{i,j} - p_{i,j+1} - p_{i,j-1} - (2p_{i+1,j} - p_{i+1,j+1} - p_{i+1,j-1}) \\ &+ m_2\left[2p_{i,j-1} - p_{i+1,j-1} - p_{i-1,j-1} - (2p_{i,j} - p_{i+1,j} - p_{i-1,j})\right] \\ &+ m_3(2p_{i,j} - p_{i+1,j} - p_{i-1,j}). \end{aligned} \tag{4.26}$$

Applying Taylor series for the pressure in the neighborhood of $P_{i.j}$ provides

$$\begin{aligned} p_{i+1,j} &= p_{i,j} + \frac{\partial p_{i,j}}{\partial x}\Delta x + \frac{1}{2}\frac{\partial^2 p_{i,j}}{\partial x^2}\Delta x^2 + O(\Delta x^3), \\ p_{i-1,j} &= p_{i,j} - \frac{\partial p_{i,j}}{\partial x}\Delta x + \frac{1}{2}\frac{\partial^2 p_{i,j}}{\partial x^2}\Delta x^2 + O(\Delta x^3), \\ p_{i,j+1} &= p_{i,j} + \frac{\partial p_{i,j}}{\partial r}\Delta r + \frac{1}{2}\frac{\partial^2 p_{i,j}}{\partial x^2}\Delta r^2 + O(\Delta r^3), \\ p_{i,j-1} &= p_{i,j} - \frac{\partial p_{i,j}}{\partial r}\Delta r + \frac{1}{2}\frac{\partial^2 p_{i,j}}{\partial r^2}\Delta r^2 + O(\Delta r^3), \\ p_{i+1,j+1} &= p_{i,j} + \frac{\partial p_{i,j}}{\partial x}\Delta x + \frac{1}{2}\frac{\partial^2 p_{i,j}}{\partial x^2}\Delta x^2 + O(\Delta x^3) + \frac{\partial p_{i,j}}{\partial r}\Delta r + \frac{1}{2}\frac{\partial^2 p_{i,j}}{\partial x^2}\Delta r^2 + O(\Delta r^3), \\ p_{i+1,j-1} &= p_{i,j} + \frac{\partial p_{i,j}}{\partial x}\Delta x + \frac{1}{2}\frac{\partial^2 p_{i,j}}{\partial x^2}\Delta x^2 + O(\Delta x^3) - \frac{\partial p_{i,j}}{\partial r}\Delta r + \frac{1}{2}\frac{\partial^2 p_{i,j}}{\partial r^2}\Delta r^2 + O(\Delta r^3), \\ p_{i-1,j-1} &= p_{i,j} - \frac{\partial p_{i,j}}{\partial r}\Delta r + \frac{1}{2}\frac{\partial^2 p_{i,j}}{\partial x^2}\Delta r^2 + O(\Delta r^3) - \frac{\partial p_{i,j}}{\partial r}\Delta r + \frac{1}{2}\frac{\partial^2 p_{i,j}}{\partial r^2}\Delta r^2 + O(\Delta r^3), \\ p_{i-1,j+1} &= p_{i,j} - \frac{\partial p_{i,j}}{\partial x}\Delta x + \frac{1}{2}\frac{\partial^2 p_{i,j}}{\partial x^2}\Delta x^2 + O(\Delta x^3) + \frac{\partial p_{i,j}}{\partial r}\Delta r + \frac{1}{2}\frac{\partial^2 p_{i,j}}{\partial x^2}\Delta r^2 + O(\Delta r^3). \end{aligned} \tag{4.27}$$

Substituting above equations in Eq. A-9 and A-10 will result in

$$\begin{aligned} \varepsilon_{i,j-1} &= O(\Delta x^2) + O(\Delta r), \\ \varepsilon_{i,j} &= O(\Delta x^3) + O(\Delta r^2). \end{aligned} \tag{4.28}$$

Therefore, the new semi-analytical method is second order accurate in axial direction and first order accurate in radial direction for well grid blocks. But it is second order accurate in radial direction and third order accurate in axial direction for reservoir blocks. It is therefore proved that the new semi-analytical method presented in this paper is a higher order method than the standard finite difference method.

References

- Archer, R. A., and Agbongiator, E. O., 2005. Correcting for Frictional Pressure Drop in Horizontal-Well Inflow-Performance Relationships, *SPE Production & Facilities*, doi:10.2118/80528-PA.

- Babu, D.K. and Odeh, A., 1989. Productivity of a Horizontal Well. *SPE Reservoir Engineering*, 4(4), 417-421.

- Brekke, K., Johansen, T. E. and Olufsen, R., 1993. A New Modular Approach to Comprehensive Simulation of Horizontal Wells. Paper SPE 26518 presented at SPE Annual Technical Conference and Exhibition, 3-6 October, Houston, Texas.

- Cao, J., James, L.A., and Johansen, T.E., 2015. A New Coupled Axial-Radial Productivity Model with Application to High Order Numerical Well Modeling. Presented at SPE Reservoir Characterisation and Simulation Conference and Exhibition, Abu Dhabi, UAE, September 2015.

- Dikken, B., 1990. Pressure Drop in Horizontal Wells and Its Effect on Production Performance. *Journal of Petroleum Technology*, 42(11): 1426-1433.

- Economides, M. J., Brand, C. W. and Frick, T. P., 1996. Well Configurations in Anisotropic Reservoirs. *SPE Formation Evaluation* 11: 257-262.

- Haaland, S. E., 1983. Simple and Explicit Formulas for the Friction Factor in Turbulent Pipe Flow. *Journal of Fluids Engineering* 105(1), 89-90.

- Holmes, J. A., Barkve, T., and Lund, O., 1998. Application of a Multisegment Well Model to Simulate Flow in Advanced Wells. Paper SPE 50646 presented at the European Petroleum Conference, 20-22 October, The Hague, Netherlands.

- Johansen, T. E. and Khoriakov, V., 2007. Iterative Techniques in Modeling of Multi-phase Flow in Advanced Wells and the Near Well Region. *Journal of Petroleum Science and Engineering*, 58(1): 49-67.

- Joshi, S. D., 1988. Augmentation of Well Productivity with Slant and Horizontal Wells (includes associated papers 24547 and 25308). *Journal of Petroleum Technology* 40.06: 729-739.

- Khoriakov, V., Johansen, A. C., Johansen, T. E. 2012. Transient Flow Modeling of Advanced Wells. *Journal of Petroleum Science and Engineering*, 86, 99-110.

- Novy, R.A., 1996. Pressure Drop in Horizontal Wells: When Can They be Ignored?. *SPERE 29; Trans., AIME*, 299

- Peaceman, D. W., 1983. Interpretation of Well-Block Pressures in Numerical Reservoir Simulation with Nonsquare Grid Blocks and Anisotropic Permeability. *SPE Journal* 23.03: 531-543.

- Tabatabaei, M., and Ghalambor, A., 2011. A New Method to Predict Performance of Horizontal and Multilateral Wells. *SPE Production & Facilities*. doi:10.2118/141164-PA.

Chapter 5

Semi-Steady State Flow Solution to Coupled Axial-Radial Productivity Model and Its Numerical Application

5.1 Overview

This Chapter presents analytical solution to coupled axial-radial flow model in semi-steady state flow and numerical modeling of near-well and horizontal well flow performance. The analytical part, Section 5.2 to Section 5.5, is reprinted from the paper "Coupled Axial-Radial Semi-Steady State Productivity Model for Horizontal Wells" accepted by *International Journal of Petroleum Engineering*.[1] This paper extends the coupled axial-radial productivity model for semi-steady state flow. Based on this analytical productivity model, a numerical

[1]Johansen, T.E., **Cao, J.**, and James, L.A., Analytical Coupled Axial-Radial Semi-Steady State Productivity Model for Horizontal Wells in Anisotropic Medium. Accepted by *Internation Journal of Petroleum Engineering*. September 2016.

modeling scheme is also developed and applied in simulation of near-well and horizontal well flow performance. The numerical part for semi-steady state flow is presented in Section 5.6.

The thesis author contributes to the aspects of applying the coupled axial-radial productivity for semi-steady state flow in numerical modeling, programming the horizontal well and near-well simulator, and preparing the manuscripts.

5.2 Introduction

Advances in drilling and completion technology have dramatically promoted the application of advanced wells in reservoir development since the 1990s, including horizontal, deviated, multilateral and smart wells. The great demand for highly accurate and efficient well models arrives from the fact that simulation techniques have been developed at a slower pace compared to the drilling and completion technologies. The well model, usually coupled with the reservoir model and solved simultaneously, is crucial to well productivity estimates.

The classical productivity models are solutions to one-dimensional radial flow for vertical wells at different flow conditions. In reservoir simulation, well grid block representation methods have been developed and used for vertical wells (Peaceman, 1983). Most of the analytical productivity models for horizontal wells, for example Joshi (1988) and Babu and Odeh (1989), assume steady state or semi-steady state flow in a certain shape of reservoir, such as a cuboid, elliptical cylinder or ellipsoid. Both models result in productivity equations that have the same form as the classical inflow equations, incorporating other effects in the skin term.

Most analytical models are easy to use and it is straightforward to calculate a productivity index ($PI = q/\Delta p$). However, they are restricted by certain outer boundary conditions and inner boundary conditions. The outer boundary conditions are no flow boundaries with certain shaped reservoirs such as an elliptic reservoir (Giger et al., 1984), laterally infinite

slab reservoir (Cinco-Lay et al., 1975) and a box reservoir (Joshi, 1988; Babu and Odeh, 1989). The inner boundary conditions are either uniform flux or uniform pressure in the wellbore. The uniform flux condition assumes that the inflow along the well trajectory is constant, which results in a symmetrical pressure distribution decreasing from both ends of the wellbore to the middle. The bottom hole pressure can be determined by taking the average pressure along the well trajectory (Kuchuk et al., 1990) or taking the midpoint pressure (Babu and Odeh, 1989). The uniform pressure condition assumes the pressure is constant inside the wellbore and the well has an infinite conductivity. The uniform pressure condition is more realistic considering that the flow rates increase from the toe to the heel in real cases.

These productivity equations are of great importance for initial estimation of well productivity index. However, the pressure losses due to friction and acceleration are ignored in these analytical models. Dikken (1990) presented an analytical method coupling single-phase turbulent well flow with stabilized reservoir flow. Pressure losses, especially caused by friction in turbulent flow, along the horizontal well is considered a significant factor in productivity calculations. The productivity index is used to calculate the flow rate in the near-well reservoir. Numerical methods are usually used to incorporate the pressure losses in the wellbore.

Since the axial reservoir flow along the well trajectory is ignored in most of the current analytical well models, it is instead solved numerically e.g. by a finite difference method. In Johansen et al., (2015), coupled axial-radial productivity model was presented, providing analytical solution to both well inflow and axial reservoir flow for steady state flow. In this paper, we extend the coupled axial-radial flow model to semi-steady state flow conditions.

In general, the conservation equation for the flow in porous medium can be described by

$$-\nabla \cdot (\rho u) + q = \frac{\partial (\phi \rho)}{\partial t}, \tag{5.1}$$

where the fluid velocity is given by Darcy's law as

$$u = -\frac{1}{\mu}\underline{K} \cdot \nabla \left(p - \rho g z\right) \tag{5.2}$$

Here, $\underline{K}$ is the permeability tensor expressed as

$$\underline{K} = \begin{bmatrix} K_{xx} & K_{xy} & K_{xz} \\ K_{yx} & K_{yy} & K_{yz} \\ K_{zx} & K_{zy} & K_{zz} \end{bmatrix}. \tag{5.3}$$

If the coordinate directions (x, y and z) are parallel to the principal directions, the permeability tensor is diagonal with three principal permeabilities K_1, K_2 and K_3, which becomes

$$\underline{K} = \begin{bmatrix} K_1 & 0 & 0 \\ 0 & K_2 & 0 \\ 0 & 0 & K_3 \end{bmatrix}. \tag{5.4}$$

In the near-well region, cynlindrical coordinates (x, r and θ) are normally used. This honors the radial inflow nature in the near-well region and can be coupled with the outer reservoir in a hybrid grids system (Pedrosa and Aziz, 1986). The permeability tensor then becomes

$$\underline{K} = \begin{bmatrix} K_x & 0 & 0 \\ 0 & K_r & K_\theta \\ 0 & K_\theta & K_t \end{bmatrix}, \tag{5.5}$$

where (see e.g. Skinner and Johansen, 2012),

$$\begin{aligned} K_r &= K_2 \cos^2\theta + K_3 \sin^2\theta, \\ K_t &= K_2 \sin^2\theta + K_3 \cos^2\theta, \\ K_\theta &= (K_2 - K_3)\sin\theta\cos\theta. \end{aligned} \tag{5.6}$$

The general conservation equation in the cynlindrical coordinates, ignoring gravity for simplicity, is

$$\frac{\partial}{\partial x}\left(K_x \frac{\rho}{\mu}\frac{\partial p}{\partial x}\right) + \frac{1}{r}\frac{\partial}{\partial r}\left(r K_r \frac{\rho}{\mu}\frac{\partial p}{\partial r}\right) + \frac{1}{r}\frac{\partial}{\partial r}\left(K_\theta \frac{\rho}{\mu}\frac{\partial p}{\partial \theta}\right) + \frac{1}{r}\frac{\partial}{\partial \theta}\left(K_\theta \frac{\rho}{\mu}\frac{\partial p}{\partial r}\right) + \frac{1}{r^2}\frac{\partial}{\partial \theta}\left(K_t \frac{\rho}{\mu}\frac{\partial p}{\partial \theta}\right) = \frac{\partial\left(\rho\phi\right)}{\partial t}. \tag{5.7}$$

In the coupled axial-radial flow model, radial inflow into the wellbore and axial reservoir flow along the well trajectory are considered while the angular flow is ignored, which means that only the first two terms in Eq. (5.7) are non-zero. Therefore, the coupled axial-radial

flow model is a two dimensional problem as shown in Figure 5.1; the conservation equation for single phase flow in this case is given by

$$\frac{\partial}{\partial x}\left(K_x\frac{\rho}{\mu}\frac{\partial p}{\partial x}\right)+\frac{1}{r}\frac{\partial}{\partial r}\left(K_r\frac{\rho}{\mu}r\frac{\partial p}{\partial r}\right)=\frac{\partial\left(\phi\rho\right)}{\partial t}, \tag{5.8}$$

with appropriate boundary conditions in a segment of the wellbore and the near-well reservoir.

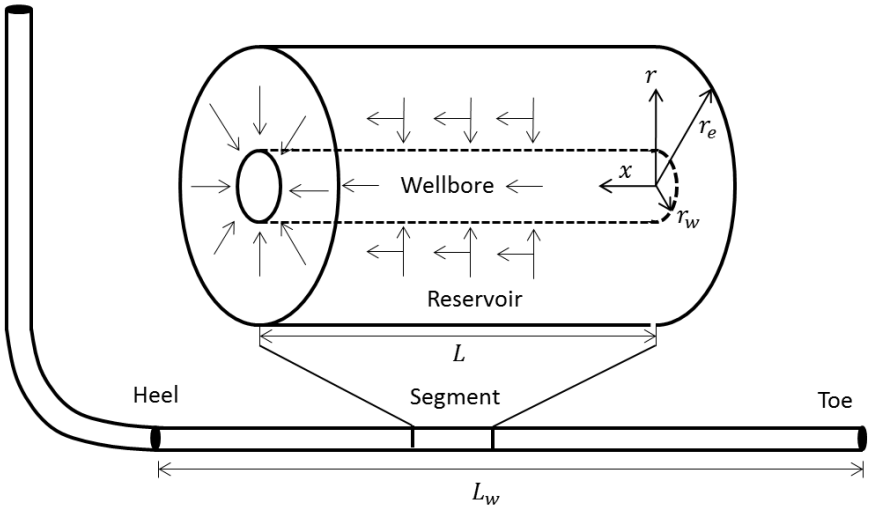

Figure 5.1: Segment model with coupled axial-radial flow (Johansen et al., 2015)

In this paper, the coupled axial and radial flow rates are solved analytically for semi-steady state flow. The above equation Eq. (5.8) can be simplified to the two-dimensional radial diffusivity equation for a slightly compressible fluid (oil), i.e. the viscosity and the total compressibility $c_T = c_R + S_{wc}c_w + (1-S_{wc})c_o$ are constant and $c_T r\partial p/\partial r << 1.0$. Here, c_R is the pore compressibility, c_w and c_o are the water and oil compressibilities, respectively and S_{wc} is connate water saturation. Subject to these assumptions, the radial diffusivity equation for a homogeneous, isotropic cylindrical medium with a well located along the cylinder axis (x) is

$$\frac{\partial^2 p}{\partial x^2}+\frac{1}{r}\frac{\partial}{\partial r}\left(r\frac{\partial p}{\partial r}\right)=\frac{\phi\mu c_T}{K}\frac{\partial p}{\partial t}. \tag{5.9}$$

For semi-steady state flow we have

$$\frac{\partial^2 p}{\partial x^2}+\frac{1}{r}\frac{\partial}{\partial r}\left(r\frac{\partial p}{\partial r}\right)=C_0, \tag{5.10}$$

where $C_0=\frac{\phi\mu c_T}{K}\frac{\partial p}{\partial t}$ is constant. For steady state flow, $C_0=0$.

Based on Eq. (5.10), the analytical solution for coupled axial and radial flow rates for single phase, steady state flow was presented in Johansen et al. (2015). The analytical pressure solution exhibits a linear pressure distribution in the axial direction and a logarithmic pressure distribution in the radial direction. Johansen et al. (2015) also proved that the solution reduces to the classical radial inflow model when assuming a zero axial pressure gradient, and to the linear Darcy equation when assuming zero radial inflow. This analytical solution was also implemented in a multi-segment numerical algorithm for a horizontal well incorporating frictional losses in Cao et al. (2015), where the numerical method was also proved to be higher order. This is a consequence of the pressure distribution being continuous over segment boundaries, as opposed to a piecewise constant distribution as in a first order method.

In this Chapter, the solution to the coupled axial-radial productivity model in semi-steady state, single phase flow mode is presented. The method of solution follows the same steps as for steady state flow as in Johansen et al. (2015). This model includes the wellbore inflow and axial reservoir flow along the well trajectory. The model is built in cylindrical coordinates, which honours the radial inflow in the near-well region. In Section 5.3, the analytical solution to the coupled axial-radial flow model is presented, describing the pressure distribution and radial and axial flow rates in a homogeneous and isotropic well/reservoir segment for semi-steady state flow. The flow equations in the near-well region are expressed using external reservoir pressure and also average reservoir pressure. These analytical solutions reduce to the classical inflow equations under conditions where only radial flow exists. In Section 5.4, the solutions are modified to be used in an anisotropic medium by implementing a space transformation in the near-well region. Hence, the solution to the coupled axial-radial flow model under semi-steady state flow is completed for both isotropic and anisotropic media. Examples of using the coupled axial-radial productivity model in a single segment and in multi segments are presented in Section 5.5.

5.3 Analytical solution to the coupled axial-radial productivity model

5.3.1 General solution using external reservoir pressure

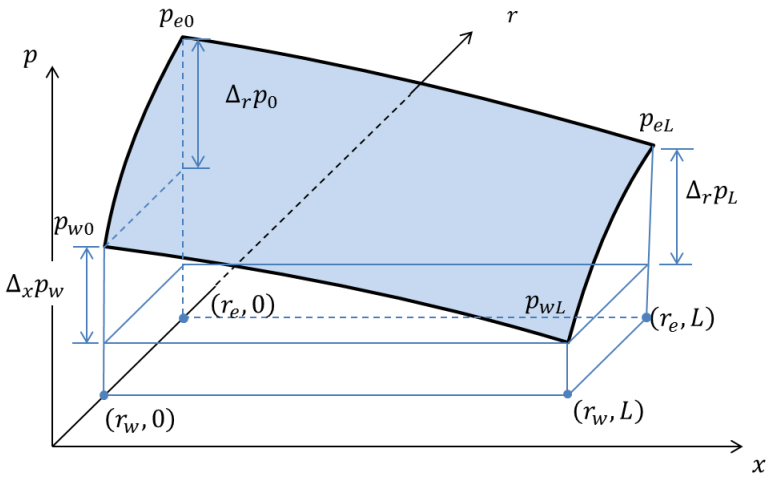

Figure 5.2: Pressure distribution in one segment

We consider a boundary value problem for Eq. (5.9) with the following condition:

$$\frac{\partial p}{\partial t} = const < 0;\ \forall x, t, \tag{5.11}$$

i.e. we assume the flow is semi-steady state. The equation is solved for a general well segment as shown in Figure 5.2. It is shown in Appendix 5-A that

$$C_o = -\frac{Q_{net}\mu}{\pi K L\left(r_e^2 - r_w^2\right)}. \tag{5.12}$$

Here, L is the length of the segment; Q_{net} is the constant net volumetric flow rate being produced from the porous part of the segment. Furthermore, we assume the boundary pressure differences are given; they are $\Delta_x p_w = p_{wL} - p_{w0}$; $\Delta_r p_0 = p_{e0} - p_{w0}$; $\Delta_x p_e = p_{eL} - p_{e0}$; $\Delta_r p_L = p_{eL} - p_{wL}$, as shown in Figure 5.2. These pressure differences are constant according to the SSS assumption. It is first observed that the function

$$p\left(x, r\right) = axln\left(r/r_w\right) + bx + cln\left(r/r_w\right) + dx^2 + er^2 + f \tag{5.13}$$

satisfies Eq. (5.10) if

$$2d + 4e = C_0. \tag{5.14}$$

Therefore, the analytical solution to the pressure profile in each segment is a quadratic-logarithmic surface as shown in Figure 5.2, which differs from the linear-logarithmic surface for steady state flow (Johansen et al., 2015).

To satisfy the boundary condition for the pressure differences, it is straightforward to show using Eq. (5.13) that we must have

$$aLln\left(r_e/r_w\right) + bL + dL^2 = \Delta_x p_e, \tag{5.15}$$

$$bL + dL^2 = \Delta_x p_w, \tag{5.16}$$

$$cln\left(r_e/r_w\right) + e\left(r_e^2 - r_w^2\right) = \Delta_r p_0. \tag{5.17}$$

We assume that the total net well inflow rate, Q_{net}, is constant and given. Hence, we have five unknowns a, b, c, d, e (f is not needed, as we consider pressure differences only) and four equations, Eq. (5.14), (5.15), (5.16) and (5.17). An additional equation, such as specifying any one of the remaining flow rates, is needed to close the problem.

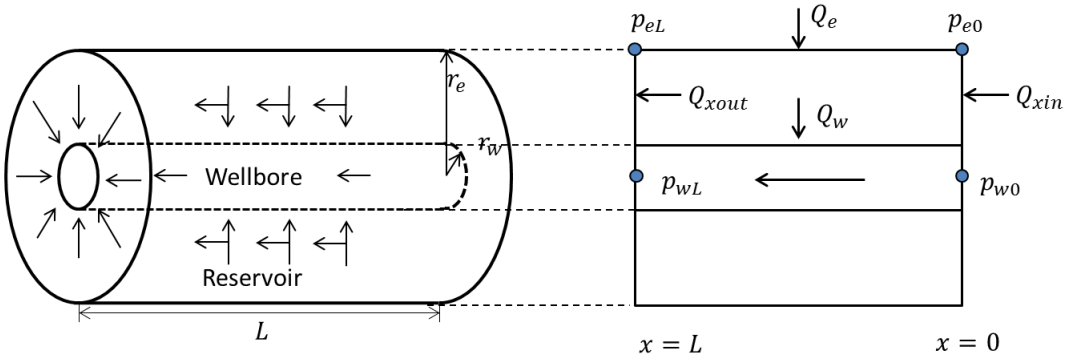

Figure 5.3: The well and near-well reservoir segment and the cross section view

Using the explicit pressure, Eq. (5.13), the flow rates shown in Figure 5.3 are given by

Darcy's Law as

$$Q_w = \frac{2\pi K}{\mu}\int_0^L \left[r\frac{\partial p}{\partial r}\right]_{r=r_w} dx = \frac{2\pi KL}{\mu}\left(\frac{1}{2}aL + c + 2er_w^2\right), \tag{5.18}$$

$$Q_e = \frac{2\pi K}{\mu}\int_0^L \left[r\frac{\partial p}{\partial r}\right]_{r=r_e} dx = \frac{2\pi KL}{\mu}\left(\frac{1}{2}aL + c + 2er_e^2\right), \tag{5.19}$$

$$Q_{xin} = -\frac{2\pi K}{\mu}\int_{r_w}^{r_e} \left[r\frac{\partial p}{\partial x}\right]_{x=0} dr = \frac{\pi K}{\mu}\left[\left(r_e^2 - r_w^2\right)\left(\frac{a}{2} - b\right) - ar_e^2 ln\left(r_e/r_w\right)\right], \tag{5.20}$$

and

$$Q_{xout} = -\frac{2\pi K}{\mu}\int_{r_w}^{r_e} \left[r\frac{\partial p}{\partial x}\right]_{x=L} dr = \frac{\pi K}{\mu}\left[\left(r_e^2 - r_w^2\right)\left(\frac{a}{2} - b - 2dL\right) - ar_e^2 ln\left(r_e/r_w\right)\right]. \tag{5.21}$$

For example, suppose the radial inflow rate to the near-well reservoir Q_e is given. Then, Eq. (5.19) gives

$$\frac{1}{2}aL + c + 2er_e^2 = \frac{Q_e\mu}{2\pi KL}. \tag{5.22}$$

The five unknown coefficients can now be determined from Eq. (5.14), (5.15), (5.16), (5.17) and (5.22). In the case of a no-flow external reservoir boundary, i.e. the external flow rate Q_e equals to zero, Eq. (5.22) becomes

$$\frac{1}{2}aL + c + 2er_e^2 = 0. \tag{5.23}$$

Details of solving the equations, Eq. (5.14), (5.15), (5.16), (5.17) and (5.23) for the coefficients are shown in Appendix B, which yields a main result of this paper:

For single phase flow of a slightly compressible fluid in the segment geometry described above and with no-flow external boundary ($Q_e = 0$), the radial well inflow rate Q_w is given by Eq. (5.18); the axial inflow rate Q_{xin} is given by Eq. 5.20 and the axial reservoir outflow rate Q_{xout} is given by Eq. (5.21), where the coefficients $a, ..., e$ are given by

$$\begin{cases} a = \frac{\Delta_x p_e - \Delta_x p_w}{L \ln(r_e/r_w)}; \\ b = \frac{\Delta_x p_w}{L} + \frac{\Delta_r p_0 + \Delta_r p_L}{{r_e}^2(1-2\ln(r_e/r_w))} L - \frac{C_0}{2} L; \\ c = -\frac{\Delta_r p_0 + \Delta_r p_L}{1-2\ln(r_e/r_w)} - \frac{\Delta_x p_e - \Delta_x p_w}{2\ln(r_e/r_w)}; \\ d = \frac{C_0}{2} - \frac{\Delta_r p_0 + \Delta_r p_L}{{r_e}^2(1-2\ln(r_e/r_w))}; \\ e = \frac{\Delta_r p_0 + \Delta_r p_L}{2{r_e}^2(1-2\ln(r_e/r_w))}. \end{cases} \tag{5.24}$$

Hence, the analytical solution to semi-steady state flow with coupled axial-radial flow has been determined. When the well and near-well model is coupled with the outer reservoir model, these unknown pressures and flow rates can be solved simultaneously. Substituting these coefficients in the flow equations will give

$$\begin{cases} Q_w = T_w \left(p_{el} + p_{e0} - p_{wl} - p_{w0} \right); \\ Q_{xin} = \alpha_1 p_{el} + \alpha_2 p_{e0} + \alpha_3 p_{wl} + \alpha_4 p_{w0} - \frac{Q_{net}}{2}; \\ Q_{xout} = -\alpha_2 p_{el} - \alpha_1 p_{e0} - \alpha_4 p_{wl} - \alpha_3 p_{w0} + \frac{Q_{net}}{2}, \end{cases} \tag{5.25}$$

where $\alpha_1 = \frac{\pi K}{\mu}\left[\frac{{r_e}^2}{2Lln(r_e/r_w)} + \frac{L}{2ln(r_e/r_w)-1} - \frac{{r_e}^2}{L}\right]$; $\alpha_2 = \frac{\pi K}{\mu}\left[-\frac{{r_e}^2}{2Lln(r_e/r_w)} + \frac{L}{2ln(r_e/r_w)-1} + \frac{{r_e}^2}{L}\right]$; $\alpha_3 = \frac{\pi K}{\mu}\left[-\frac{{r_e}^2}{2Lln(r_e/r_w)} - \frac{L}{2ln(r_e/r_w)-1}\right]$; $\alpha_4 = \frac{\pi K}{\mu}\left[\frac{{r_e}^2}{2Lln(r_e/r_w)} - \frac{L}{2ln(r_e/r_w)-1}\right]$; $T_w = \frac{2\pi KL}{\mu[2ln(r_e/r_w)-1]}$ and Q_{net} is the net outflow in the segment. This flow rate could be determined easily given the total well productivity Q_T since $\sum Q_{net} = Q_T$.

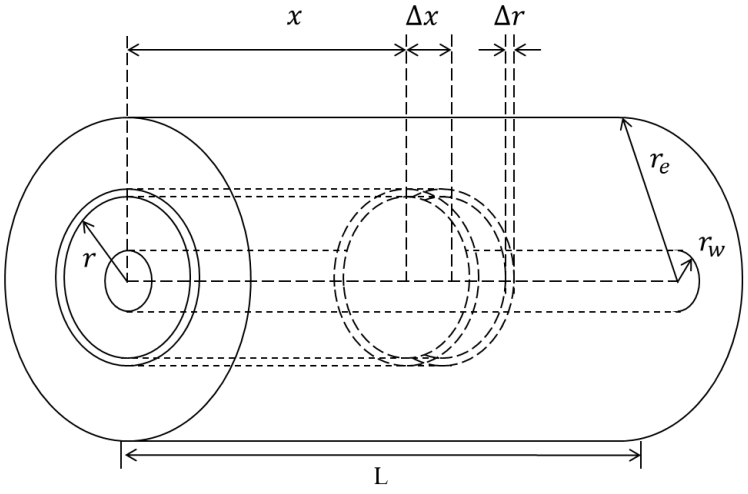

Figure 5.4: Cylindrical control volume geometry

5.3.2 General solution using average reservoir pressure

In the above solutions, external near-well reservoir pressures are used. We next solve the model with average reservoir pressures instead of external reservoir pressures. The average reservoir pressure in the radial plane (shown in Figure 5.4) can be determined by

$$\overline{p}_r = \frac{1}{A}\int_{r_w}^{r_e} 2\pi r p\,(x,r)\,dr, \tag{5.26}$$

where $A = \pi(r_e^2 - r_w^2)$. Integrating over the segment excluding the wellbore will give the average reservoir pressure;

$$\overline{p}_r = (ax+c)\left(ln\,(r_e/r_w) - \frac{1}{2}\right) + bx + dx^2 + \frac{e}{2}{r_e}^2 + f. \tag{5.27}$$

The average reservoir pressure is integrated radially to obtain the average pressure in the cross plane. It is still a parabolic function of x in the axial direction along the well trajectory. Specifically we then have

$$\begin{cases} p_{w0} = er_w^2 + f, \\ p_{wL} = bL + dL^2 + er_w^2 + f, \\ \bar{p}_{r0} = c\left(ln\,(r_e/r_w) - \frac{1}{2}\right) + \frac{e}{2}{r_e}^2 + f, \\ \bar{p}_{rL} = (aL+c)\left(ln\,(r_e/r_w) - \frac{1}{2}\right) + bL + dL^2 + \frac{e}{2}{r_e}^2 + f. \end{cases} \tag{5.28}$$

This is similar to those pressures shown in Figure 5.2. Solving the coefficients from Eq. (5.14) and (5.28) will give

$$\begin{cases} a = \frac{\overline{p}_{rL} - \overline{p}_{r0} - p_{wL} + p_{w0}}{L[ln(r_e/r_w) - 1/2]}; \\ b = \frac{p_{wL} - p_{w0}}{L} - \frac{\overline{p}_{rL} + \overline{p}_{r0} - p_{w0} - p_{wL}}{4{r_e}^2[ln(r_e/r_w) - 3/4]}L - \frac{C_0}{2}L; \\ c = \frac{\overline{p}_{r0} - p_{w0}}{ln(r_e/r_w) - 1/2} + \frac{\overline{p}_{rL} + \overline{p}_{r0} - p_{w0} - p_{wL}}{8[ln(r_e/r_w) - 1/2][ln(r_e/r_w) - 3/4]}; \\ d = \frac{C_0}{2} + \frac{\overline{p}_{rL} + \overline{p}_{r0} - p_{w0} - p_{wL}}{2{r_e}^2[ln(r_e/r_w) - 3/4]}; \\ e = -\frac{\overline{p}_{rL} + \overline{p}_{r0} - p_{w0} - p_{wL}}{4{r_e}^2[ln(r_e/r_w) - 3/4]}. \end{cases} \tag{5.29}$$

Substituting the coefficients in the flow equations and integrating, we will find

$$\begin{cases} Q_w = T_w\,\overline{\Delta_r p}; \\ Q_{xin} = -T_a\left(\overline{p}_{rL} - \overline{p}_{r0}\right) + \frac{1}{2}T_w\overline{\Delta_r p} - \frac{1}{2}Q_{net}; \\ Q_{xout} = -T_a\left(\overline{p}_{rL} - \overline{p}_{r0}\right) - \frac{1}{2}T_w\overline{\Delta_r p} + \frac{1}{2}Q_{net}. \end{cases} \tag{5.30}$$

Here, $\overline{\Delta_r p} = (\overline{\Delta_r P_0} + \overline{\Delta_r P_L})/2$; $T_w = \frac{2\pi KL}{\mu ln(re/rw)-3/4}$ and $T_a = \frac{\pi K r_e^2}{\mu L}$.

5.3.3 Special cases: classical productivity models

Similar to Johansen et al. (2015) for steady state flow, we next discuss how the general solution in Section 5.3 reduces to the special cases of pure radial and pure axial flow in sub-sections 5.3.3.1 and 5.3.3.2, respectively.

5.3.3.1 Pure radial flow

Consider the special case where there is only radial flow, i.e. $\Delta_x p_e = \Delta_x p_w = 0$ with closed boundaries at $x = 0$ and $x = L$. We then have $a = 0$. Also, the closed boundary assumption means that

$$\left.\frac{\partial P}{\partial x}\right|_{r=r_e} = aln\left(r_e/r_w\right) + b + 2dx = 0. \tag{5.31}$$

At $x = 0$, this gives $b = 0$ and therefore $d = 0$. From the boundary conditions we then get $e = C_0/4$ and $c = (\Delta_r p - er_e^2)/ln(r_e/r_w)$, where $\Delta_r p = p_e - p_w$. The pressure is then given by

$$p\left(r\right) = cln\left(r_e/r_w\right) + er^2 + f. \tag{5.32}$$

From Eq. (5.18) we obtain the flow rate into the well

$$Q_w = \frac{2\pi KL}{\mu}\left[c + 2er_w^2\right]. \tag{5.33}$$

Substituting for C_0, c, and e we find

$$Q_w = \frac{2\pi KL\Delta_r p}{\mu ln\left(r_e/r_w\right)} + \frac{Q_{net}}{2ln\left(r_e/r_w\right)}, \tag{5.34}$$

where Q_{net} is total fluid removal rate from the porous part of the segment. In the case when all boundaries are closed, we have $Q_w = Q_{net}$. Inserting this into Eq. (5.34) and solving for Q_w we find

$$Q_w = \frac{2\pi KL\Delta_r p}{\mu\left[ln\left(r_e/r_w\right) - 0.5\right]}, \tag{5.35}$$

which is the classical skin free inflow equation for SSS flow using external segment pressure. Also, if $Q_{net} = 0$, the well inflow rate is equal to the radial inflow rate across the outer boundary, which means the flow is steady state. Letting $Q_{net} = 0$, Eq. (5.34) gives

$$Q_w = \frac{2\pi KL\Delta_r p}{\mu ln\left(r_e/r_w\right)}, \tag{5.36}$$

which is the classical inflow equation for steady state flow.

5.3.3.2 Pure axial flow

Consider the special case where the wellbore pressure equals to the reservoir pressure, i.e. $\Delta_r p_L = \Delta_r p_0 = 0$. In this case, flow only occurs in the axial direction. Applying this condition to the pressure solution Eq. 5.13 results in $a = c = e = 0$; $b = (\Delta_x p_e)/L - L/2C_0$; $d = \frac{1}{2}C_0$. Since there is no radial inflow into the wellbore, the net outflow in the segment is zero. Then, substituting the coefficients into the flow equations, the radial flow is indeed zero and the axial flow rate is

$$Q_{xin} = Q_{xout} = Q_x = \frac{\pi K}{\mu L}\left(r_e^2 - r_w^2\right)\Delta_x p_e. \tag{5.37}$$

This is the Darcy's law in the cross section area between the wellbore and the outer reservoir radius ($\pi(r_e^2 - r_w^2)$). Here, $\Delta_x p_e = \Delta_x p_w = \Delta_x p$ and this is the axial pressure difference.

5.3.3.3 Radial flow with average reservoir pressure

The above description uses wellbore pressures and external boundary pressures. Since external reservoir pressure is usually not known, it is more convenient to use average reservoir pressure which can be determined from a well test or history matching. Consider an arbi-

trary cylinder ring at (x, r) with width Δr and length Δx, as shown in Figure 5.4.

Since we know the pressure at any point (r, x) in Eq. (5.13), we can calculate average pressure $p_{av} = \frac{1}{V}\int\int [2\pi r p(x,r)]\, dr dx$ in the near-well reservoir segment, where $V = \pi(r_e^2 - r_w^2)L$ and integration is over the segment excluding the wellbore, i.e.

$$p_{av} = \frac{2\pi}{\pi({r_e}^2 - {r_w}^2)L}\int_0^L \left[\int_{r_w}^{r_e} rp\,(x,r)\, dr\right] dx. \tag{5.38}$$

Carrying out this integration using Eq. (5.13) will give

$$p_{av} = \left(\frac{1}{2}aL + c\right)\left[\frac{{r_e}^2 ln\,(r_e/r_w) - \frac{1}{2}r_e^2 + \frac{1}{2}r_w^2}{{r_e}^2 - {r_w}^2}\right] + \frac{1}{2}bL + \frac{1}{3}dL^2 + \frac{e}{2}\left({r_e}^2 + {r_w}^2\right) + f. \tag{5.39}$$

If $r_e \gg r_w$, this simplifies to

$$p_{av} = \left(\frac{1}{2}aL + c\right)\left(ln\,(r_e/r_w) - \frac{1}{2}\right) + \frac{1}{2}bL + \frac{1}{3}dL^2 + \frac{e}{2}{r_e}^2 + f. \tag{5.40}$$

Consider the special case where we have only radial flow with average pressure. It is demonstrated (in Appendix B) that the well inflow becomes

$$Q_w = \frac{2\pi KL\Delta_r \bar{p}}{\mu\,[ln\,(r_e/r_w) - 0.75]}, \tag{5.41}$$

which is the classical skin free inflow equation for SSS flow using average reservoir pressure. Also, if net outflow is zero, the well inflow rate is equal to the radial inflow rate across the outer boundary, which means the flow is steady state. This assumption gives

$$Q_w = \frac{2\pi KL\Delta_r \bar{p}}{\mu\,[ln\,(r_e/r_w) - 0.5]}, \tag{5.42}$$

which is the classical expression for steady state flow using average reservoir pressure.

5.4 Solution to coupled axial-radial flow model in anisotropic media

The solution above is based on the assumption that the porous medium is isotropic. In an anisotropic medium, the permeability tensor in Eq. (5.5) should be used. In coupled axial-radial flow model where angular flow is ignored, the directional permeability K_x along

well trajectory and the plane permeability K_r perpendicular to well trajectory need to be determined. If the well trajectory is along one of the principal direction, the directional permeability K_x is equal to this principal directional permeability. If the well trajectory direction $\overrightarrow{n}$ is not along any principal direction, the directional permeability K_n can be determined given the principal permeability since any directional permeabilities can be determined by

$$K_n = K_1 \cos^2\theta_x + K_2 \cos^2\theta_y + K_3 \cos^2\theta_z, \tag{5.43}$$

where θ_x, θ_y and θ_z are the angle between the given direction and the principal directions (Scheidegger, 1960).

The plane permeability K_r normal to the well trajectory is determined through a space transformation implemented in the near-well region only. Details are found in Appendix C. The solutions to the coupled axial-radial flow model expressed using external pressure and average reservoir pressure are generally the same as Eq. (5.25) and (5.30), except that the permeability in T_w uses K_r and in α_1, α_2, α_3, α_4 and T_a uses K_x.

Although similar to other transformation methods in the literature, for example Muskat (1937), the transformation here is only implemented in the near-well region. The advantage of this is that it does not affect the reservoir grids and outer boundary conditions. In this transformation, the volume is preserved and therefore the average pressure. Hence, the transformation provides flexibility in choosing a near-well grid block configuration. The unknown becomes the Dietz shape factor of the grid block configuration chosen in numerical methods. This can be determined by previous results, as for example Matthews et al. (1954), Dietz (1965) and Peaceman (1990).

5.5 Application of coupled axial-radial productivity model

5.5.1 Calculation example in single segment case

The coupled axial-radial productivity model can be applied in each segment of the well and near-well reservoir. The calculation is carried out for a single segment in this subsection. The pressure differences, reservoir properties and dimensions are given in Table 5.1.

Table 5.1: Basic parameters for single segment case

Parameter	Unit	Value
K	$[mD]$	200
μ	$[cP]$	1
L	$[m]$	100
r_w	$[m]$	0.1
r_e	$[m]$	10
ρ	$[kg/m^3]$	800
Q_{net}	$[m^3/day]$	500
$\Delta_x p_w$	$[bar]$	-3.8726
$\Delta_r p_0)$	$[bar]$	1.8750
$\Delta_x p_e$	$[bar]$	-3.8772

The pressure surface in this segment can be determined by Eq. (5.13) and associated coefficients. This pressure, shown in Figure 5.5, is quadratic in axial direction and quadratic-logarithmic in radial direction. The axial inflow and outflow and well inflow rates can also be determined. In Figure 5.6, the axial inflow, outflow and well inflow rates are shown. They are determined based on Eq. (5.18) to (5.21) for various permeability values. The flow rate constraint in semi-steady state flow is that the total net outflow is constant, determined by the segment size and total compressibility. As the permeability increases, the axial flow rate increases and the well inflow rate decreases linearly. The negative values mean that the flow is opposite to the defined positive direction (as shown in Figure 5.3).

5.5.2 Implementation in multi-segment case

In this section, we apply the analytical model to determine pressure distribution and flow rates in the case when the well and near-well reservoir is divided into multiple segments. A

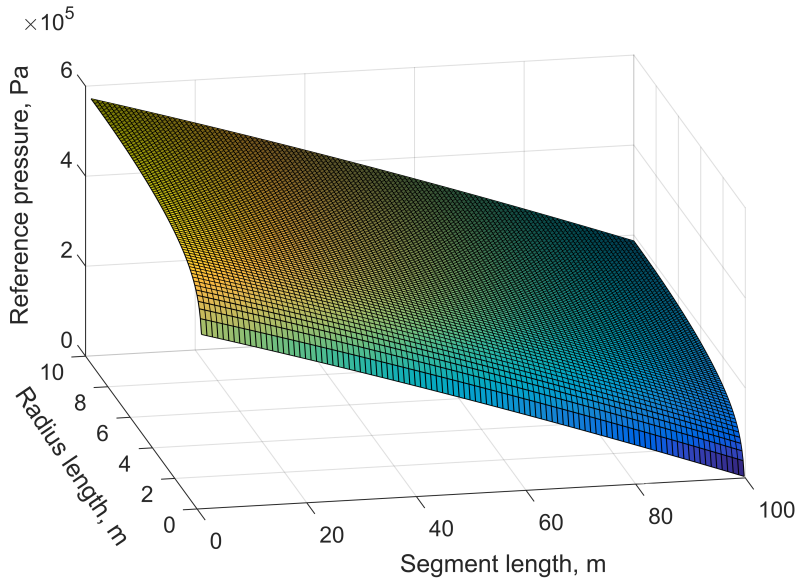

Figure 5.5: Pressure surface in single segment

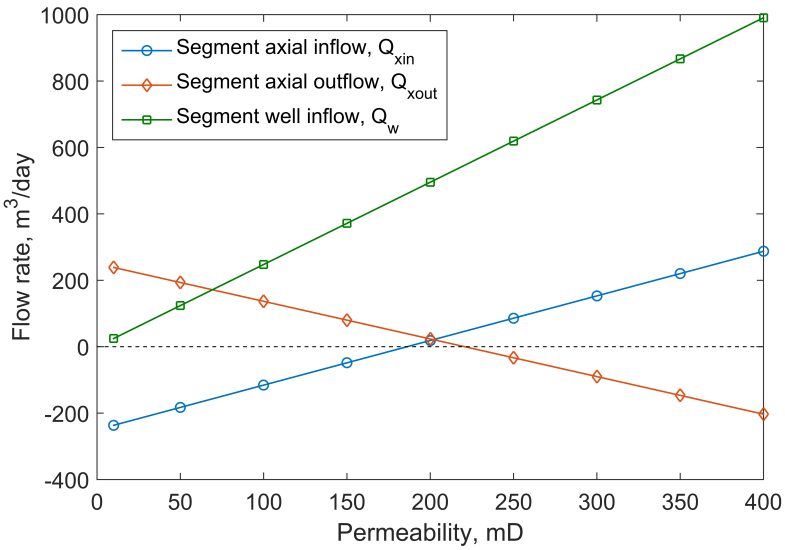

Figure 5.6: Flow rates in single segment with various reservoir permeability

simple calculation example of a multi-segment case is demonstrated, similar to the steady state flow in Johansen et al. (2015). Consider a multi-segment model with five segments ($N_x = 5$). The reservoir pressure and the heel pressure at a certain time t_1 are assumed to be known; at this time the well productivity converges to a constant under semi-steady state flow and the wellbore pressure distribution is determined iteratively:

1) Assume the wellbore pressure for each segment is given, $p_i = p_{res}; i = 1, 2, ..., 5$

2) Calculate the well inflow $Q_w(i)$, axial flow rate $Q_x(i)$ according to Eq. (5.25).

3) Determine the pressure gradient along the wellbore caused by friction,

$$\frac{\Delta p}{L} = \frac{f \rho v^2}{2D}, \tag{5.44}$$

where f is the Darcy friction factor; ρ is the fluid density; v is the velocity and D is the diameter of the wellbore. The flow rate inside the wellbore is determined by mass balance, i.e. net fluid accumulation in a wellbore segment equals to zero.

4) Determine the wellbore pressure using the frictional pressure loss from step 3).

5) Repeat steps 2) to 4) with wellbore pressure from 4) until the pressure has converged.

Table 5.2: Basic parameters for multi-segment case

Parameter	Unit	Value
K	$[D]$	1
μ	$[cP]$	1
L_w	$[m]$	1000
r_w	$[m]$	0.1
r_e	$[m]$	10
ρ	$[kg/m^3]$	800
p_{res}	$[kPa]$	2
$p_{heel}(t_1)$	$[kPa]$	1
$p_{heel}(t_2)$	$[kPa]$	0.8

The friction calculation in Eq. (5.44) only considers friction in a smooth pipe for simplicity. It could be extended to pressure losses considering acceleration, well inflow effects and roughness of the pipe. Following the calculation algorithm given above, a simple calculation is performed with data from Table 5.2 for time t_1 . The pressure is assumed to be the same with initial reservoir pressure at the initial iteration step (the first row in Table 5.3). The convergence criteria used in this example is that the total relative error satisfies

$$\eta = \sum_{i}^{N_x+1} |\frac{p_i^{n+1} - p_i^n}{p_i^n}| < 10^{-5}, \tag{5.45}$$

where N_x is the number of segments; n is the iteration step; i is the segment number with $i = 1$ at the heel. Following the procedures 1) to 5) above, the pressure in each iteration

step is shown in Table 5.3. The iteration stops at $n = 7$ when the convergence criteria is satisfied.

Table 5.3: Results from each iteration step at time t_1

n Step	p_1 Pa	p_2 Pa	p_3 Pa	p_4 Pa	p_5 Pa	p_6 Pa	η %
0	1000	1000	1000	1000	1000	1000	N/A
1	1000	1083.19	1156.43	1218.56	1267.84	1301.00	102.70
2	1000	1074.52	1138.58	1191.76	1233.13	1260.52	10.39
3	1000	1075.63	1140.89	1195.26	1237.72	1265.92	1.40
7	1000	1075.50	1140.62	1194.86	1237.19	1265.30	4.09×10^{-6}

The same iteration for another time t_2 is repeated when the reservoir preesure at the heel $p_{res} = 800Pa$. The resulting pressure profiles at both times (t_1 and t_2) are plotted in Figure 5.7. The pressure distribution for multi-segments is piecewise quadratic, different from the piecewise constant obtained by finite difference methods and piecewise linear for steady state flow as in Johansen et al. (2015). The pressure profiles under semi-steady state flow shift linearly with time. It demonstrates that this model can be implemented in numerical simulation of a horizontal well and near-well reservoir given various boundary conditions.

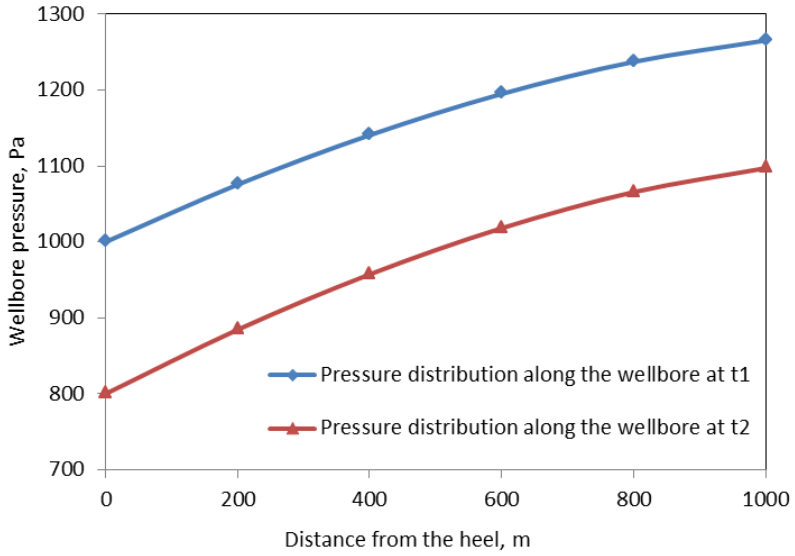

Figure 5.7: Pressure distribution along the horizontal wellbore

5.6 Numerical model for horizontal well and near-well region

5.6.1 Flow performance in the near-well region

Suppose a horizontal well is producing in the center of a cylindrical reservoir at a constant flow rate Q_{tot}. The outer reservoir is completely closed and the flow, after lower pressure is felt anywhere in the reservoir, is semi-steady state. At this flow period, the pressure decreases at the same rate anywhere in the reservoir, and the net outflow Q_{net} for each reservoir segment is the same given by Eq. (5.6), i.e. $\frac{\phi\mu c_T}{K}\frac{\partial p}{\partial t} = \frac{Q_{net}\mu}{\pi KL}(r_e^2 - r_w^2)$. This net outflow in each segment (see Figure 5.3) is the sum of the axial inflow, the axial outflow and the radial inflow to the well, except for the left most and right most segments, which have no axial outflow and no axial inflow, respectively. Considering the boundary condition for the whole system, the total flow rate at the heel is actually the summation of each radial inflow to the well since the outer boundary is closed. Therefore, the net outflow for each segment is $Q_{net} = Q_{tot}/N_x$ and N_x is the segment number. With a closed outer reservoir boundary, the external flow rate into the reservoir block $Q_e = 0$. If $r_e \gg r_w$ holds, the flow rates are determined by Eq. (5.24) and associated coefficients. The analytical solution determines the inflow and outflow rates given the four corner pressures for each grid block. Hence, the unknowns in this problem are all pressures.

It is easy to verify that the accumulation of flow rate is the net outflow, i.e.

$$\sum (Q_{out} - Q_{in}) = Q_{net}. \tag{5.46}$$

This also demonstrates that the net outflow of each segment is a constant. Since the flow rates are continuous between adjacent segments, the outflow of the upstream grid block must equal the inflow of the adjacent downstream grid block, i.e.

$$Q_{xout,i} = Q_{xin,i+1}, \;\; i = 1, 2, \; N_x - 1. \tag{5.47}$$

This gives$N_x - 1$ continuity equations for reservoir grid blocks if N_x is the number of grid blocks in the axial direction. Besides boundary conditions, hydraulic equations in the

wellbore are needed, which are given in next section.

5.6.2 Flow in the horizontal well

The horizontal well is assumed to be completed open hole from toe to heel with a cylindrical reservoir around it. Since the flow is semi-steady state, the pressure changes linearly in both the reservoir and the wellbore. The transient behavior is not expected to appear in wellbore pressure gradient. Pressure loss inside the wellbore can be expressed by

$$\frac{\partial p_f}{\partial x} = -\frac{f\rho v^2}{2D} - \Delta\left(\rho v^2\right) - \rho g \Delta h. \tag{5.48}$$

Here, pressure loss due to acceleration is ignored since it is usually insignificant compared to the pressure loss caused by friction (Novy, 1996). In Eq.(5.40), f is the Darcy friction factor; $f = 0.3164/\sqrt[4]{Re}$ for turbulent flow in smooth pipes, where Re is the Reynolds number. Here, it is assumed that the flow inside the horizontal well is turbulent and the well pipe is smooth, however is equally applicable to rough pipes. The friction factors for rough pipes are given by Haaland (1983) for example. In the case of a smooth pipe, the momentum balance equation in the well segment is given by

$$Q_f = T_f \Delta p^{4/7},\ T_f = \frac{2^{9/7}\pi r_w^{19/7}}{0.1364^{4/7}\rho^{3/7}\mu^{1/7}\Delta x^{4/7}} = \frac{23.91\, r_w^{19/7}}{\rho^{3/7}\mu^{1/7}\Delta x^{4/7}}. \tag{5.49}$$

In the numerical model, the unknowns are the pressures at the grid corner, in total $2(N_x+1)$ unknowns. The schematic of the numerical model is shown in Figure 5.8. For well segments, we have N_x mass balance equations and one constant flow rate condition at the heel. For reservoir segments, there are two no flow boundary conditions for the leftmost and rightmost reservoir grid blocks, and $N_x - 1$ continuity equations. Therefore, the total number of governing equations are $2(N_x+1)$, equal to the number of unknowns and hence the problem is closed. Since some of the equations are nonlinear, this system of equations is solved by iterative methods. Newtown methods are used in this paper.

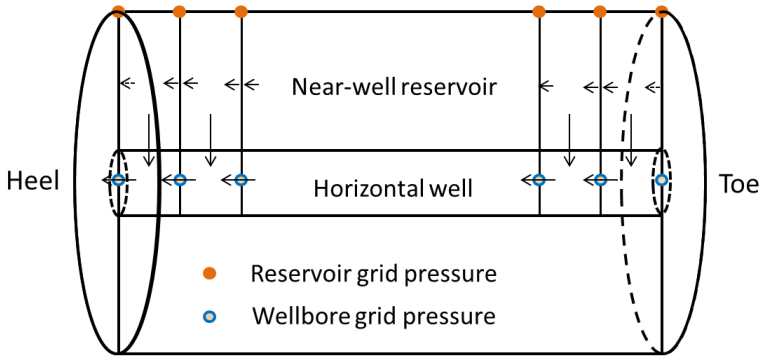

Figure 5.8: The numerical schematic of well segment model for semi-steady state flow

5.7 Results and analysis

5.7.1 Pressure distributions

The pressure decreases linearly with time everywhere in the reservoir in semi-steady state flow. The semi-steady state flow starts when lower pressure than the initial pressure is felt everywhere in the reservoir. Given anyone of the grid pressure, the pressure surface can be determined. In the following calculations, we assume that the external reservoir pressure is given; the total flow rate, or the well productivity, is known and the wellbore and near-well reservoir pressure are unknowns. Both the standard finite difference method and the new method proposed in this paper are used in example calculations. The diffferences is that the standard finite differences calculate the axial flow rate numerically according to Darcy's Law and the new method applies the analytical solution from the coupled axial-radial productivity mode. They have the same boundary and initial conditions. Pressure distributions for the horizontal wellbore are shown in Figure 5.9 and Figure5.10. Basic parameters used are given in Table 5.4.

The most refined finite difference case with 1000 grid blocks in the axial direction ($N_x = 1000$) and 100 grid blocks in the radial directions ($N_y = 100$) is assumed to be the true

Table 5.4: Basic parameters used in calculation

Parameter symbol	Unit	Value
K	$[D]$	1
ρ	$[kg/m^3]$	800
μ	$[cP]$	1
L_w	$[m]$	1000
r_w	$[m]$	0.1
r_e	$[m]$	20
p_{res}	bar	300
Q_T	STB/Day	3000

solution. The pressure profiles generated using both the standard method and the new method are shown in Figure 5.9. Both methods use $N_x = 10$ and $N_y = 2$. Figure 5.9 shows that the pressure profile resulting from the new method is much closer to the true solution than the one generated by the standard method using the same discretization. The result of the new method is most accurate for wellbore pressure near the toe, and deviates away from the true solution as it approaches the heel. The deviation could be caused by insufficient axial grid blocks. Figure 5.10 verifies that it is indeed the case; as the grids are refined in the axial direction, the pressure profile approaches the solution. This also indicates that the new method and the standard finite difference method converge to the true solution as grid blocks are refined; however the new method is more efficient.

Figure 5.11 plots the relative error of pressure profiles generated using different methods with different refinements. The new method achieves less relative error than the standard finite difference method. Futhermore, the convergence rate of the new method is higher than the standard method when axial grid blocks are equally refined. This is mainly due to the quadratic pressure surface in the new method instead of constant pressure surface in finite difference method. Hence, the new method is expected to be higher order of accuracy as is proved using bilinear pressure surface (Cao et al., 2015).

Several cases of grid blocks refined in both the axial and radial directions were studied to determine the accuracy and efficiency of bottom hole pressure; the results of which are shown in Figure 5.12. The two methods result in different curve tendencies for the bottom hole pressure. However, the new method is more efficient in approaching the solution than

the standard method when using same number of grid blocks. Figure 5.12 demonstrates that the new method is able to achieve a higher accuracy than the standard finite difference method when using the same number of grid blocks. For example, when $N_x = 100$, the new method using $N_y = 2$ results in bottom hole pressure with the same accuracy as that from the standard method using $N_y = 100$. The new method requires as less refined grid blocks than the standard method to achieve the same accuracy. Compared with standard method, the new method saves efforts in refining radial grid blocks to achieve same accuracy.

5.7.2 Flow rates

In this section, flow rates in both the axial and radial directions were compared between the new method and the standard finite difference method in several cases. Figure 5.13 shows how the axial flow rate changes when the axial grid blocks are refined. It shows that the axial flow rates start from zero because of the no flow boundary on the toe side and increase to a peak and then decrease to zero caused by the no flow boundary on the heel side. The new method achieves a more accurate representation of axial flow along the well trajectory than that achieved by using the standard finite difference methods.

Figure 5.14 shows the axial and radial flow rates, and the axial to radial flow ratio. The radial flow from the reservoir segments to the well segments are almost constant since there is no obvious difference between the axial inflow and outflow rates in each segment. However, the radial flow increases when it is near the heel. The reason is that the no flow boundary on the heel side causes a dramatic decrease in axial flow, as the axial flow curve has a steep slope around $x = 0$. In this region, the axial outflow is smaller than the inflow, resulting in an increased radial flow since the net flow is still constant. The axial to radial flow ratio has a peak value of 30%, which means that the axial flow rate in general cannot be ignored.

5.7.3 Calculation efficiency

The efficiency of the new method and standard finite difference method is analyzed in this section. The convergence criteria for both numerical methods is the same; i.e.

$$\frac{1}{N}\sum_{i=1}^{N}\left|\frac{p_i^{n+1}-p_i^n}{p_i^n}\right| < 10^{-10}. \tag{5.50}$$

Using various number of grid blocks under the same convergence criteria, the CPU time needed is gathered and plotted in Figure 5.15. It is shown clearly that the new method requires much less CPU time to achieve the same accuracy than the standard finite difference method. The CPU time costs by both methods differ by up to more than two orders of magnitude.

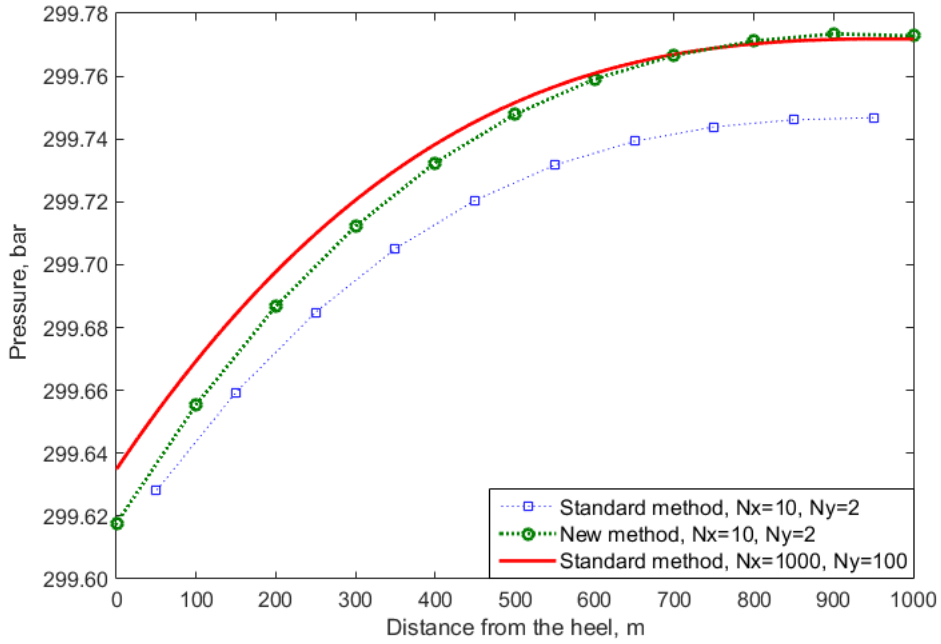

Figure 5.9: Numerical schematic of flow rate and pressure

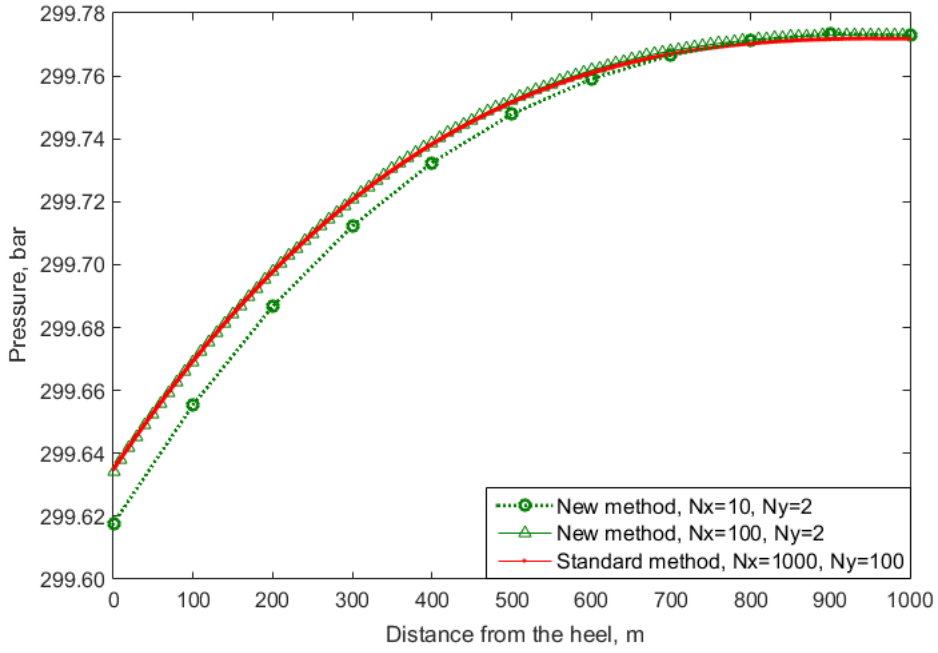

Figure 5.10: The wellbore pressure distribution as determined by different methods

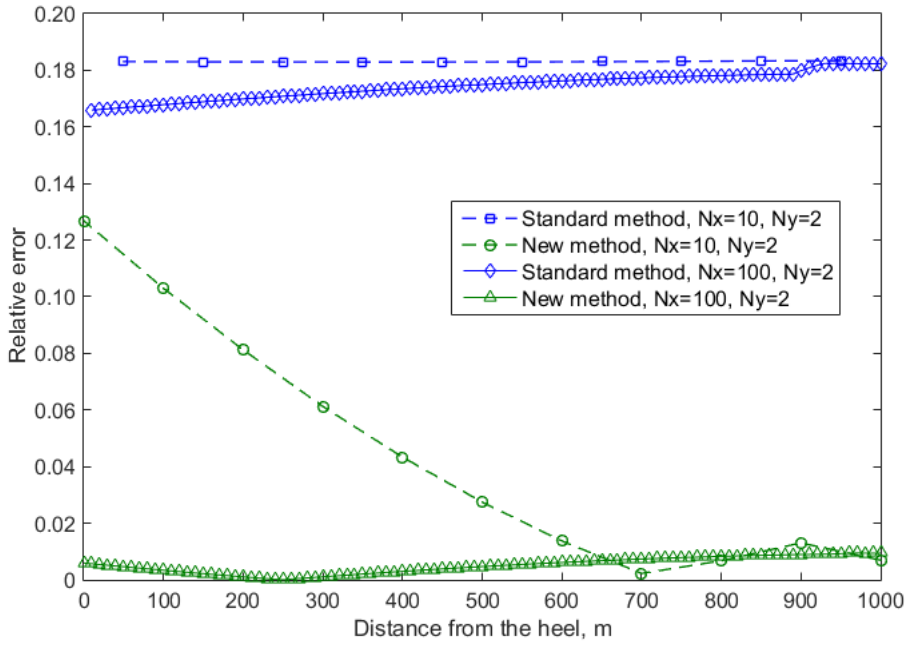

Figure 5.11: The wellbore pressure distribution with refined new methods

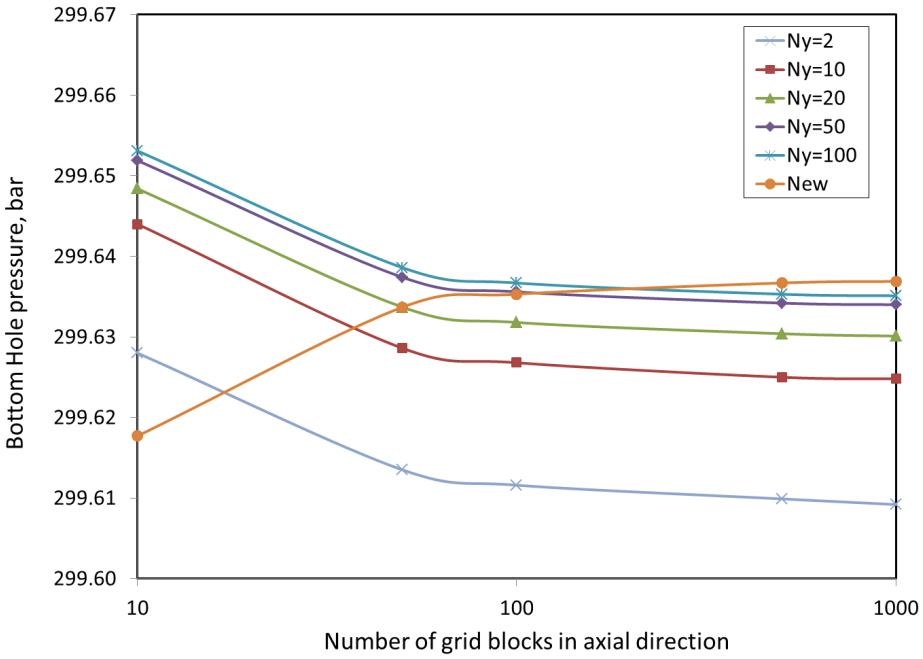

Figure 5.12: Bottom hole pressure in grid blockrefinement case study

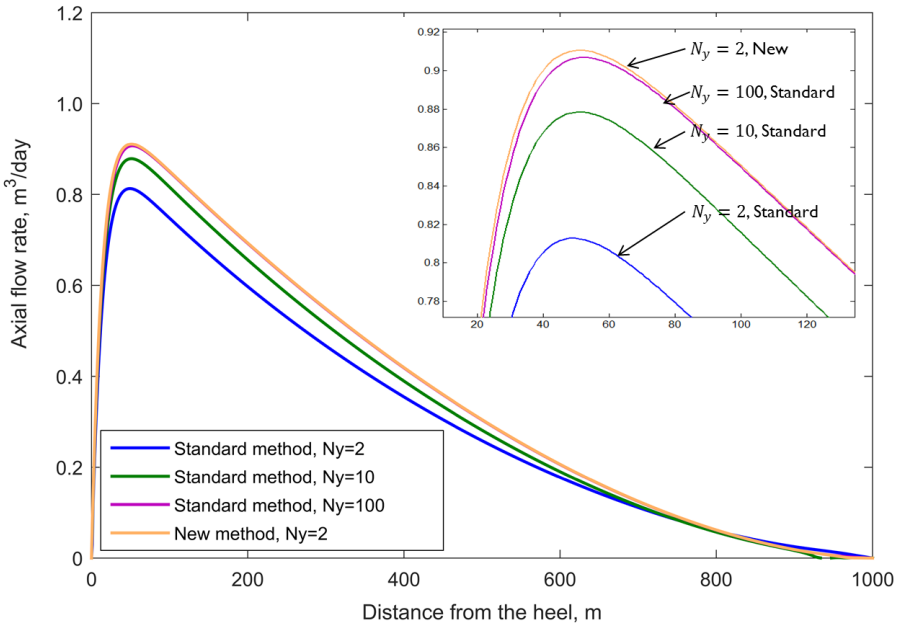

Figure 5.13: Axial flow rate distribution in the near-well reservoir

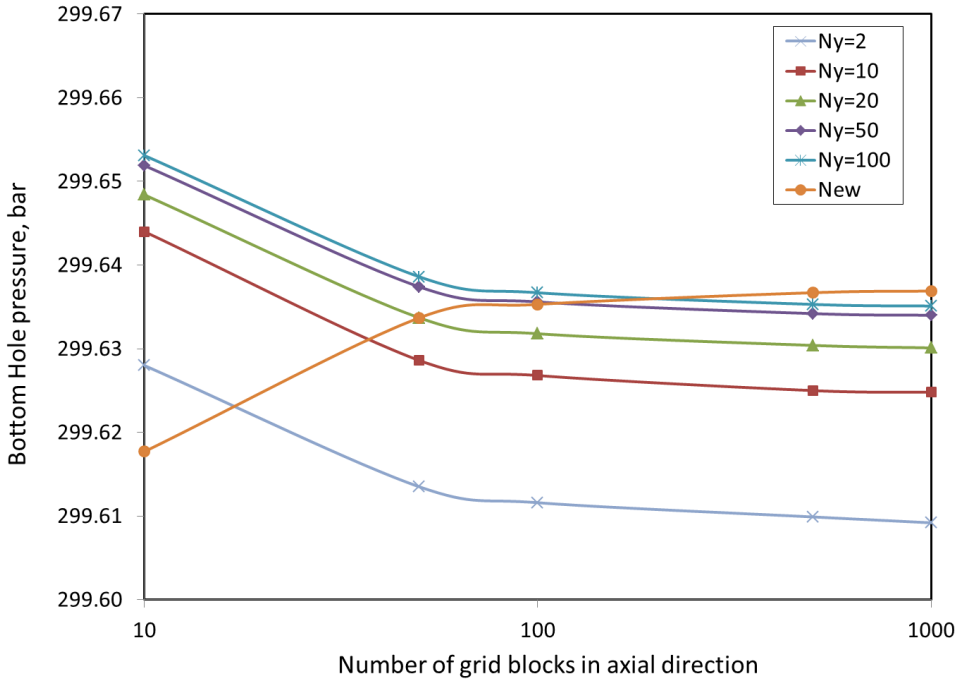

Figure 5.14: Axial and radial flow rates and flow ratio

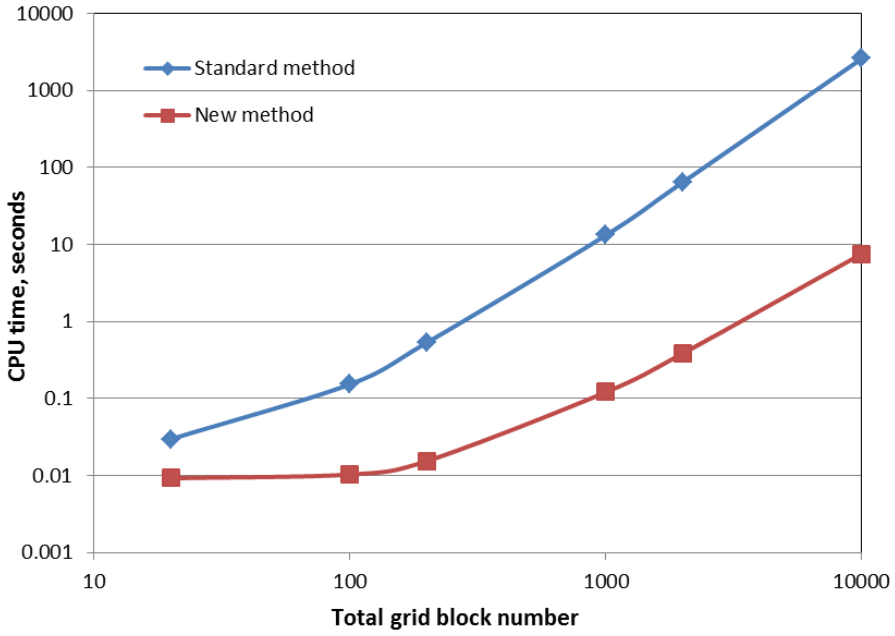

Figure 5.15: CPU time consuded by standard finite difference and new methods

5.8 Conclusions

The analytical solution to the coupled axial-radial flow model for semi-steady state flow is presented in this paper. The analytical solution provides the flow rates in the radial and the axial directions in the near-well reservoir. It simplifies to the classical radial well inflow equation for semi-steady state flow under the condition that only radial flow exists. The coupled flow model is also expressed in terms of average reservoir pressure. This also reduces to the classical formulas in the absence of axial flow. This productivity model has expressions using both external and average reservoir pressure, for isotropic and anisotropic media. It can be used in the numerical simulation of horizontal wells with pressure loss due to friction, and potentially improve the calculation efficiency of the numerical model.

The analytical solution is used in the numerical model for horizontal well simulation. Pressure loss due to friction is included in the numerical model. The results (pressure profiles and flow rates) from both the new method proposed in this paper and the standard finite difference method are compared. This shows that the new method achieves less relative error for wellbore pressure profiles and higher convergence rate using grid refinement. Hence, the new method is proven more accurate and efficient than the standard method. The new method also demonstrates a significant improvement in mimicking the axial reservoir flow. The efficiency of the new method is proved to be much higher than standard finite difference method; the CPU time cost of the new method is around one to two order of magnitude less than the standard finite difference method to achieve same accuracy.

Appendix 5-A

Assume that the flowing boundary condition is given by Eq. (5-11). The definition of total compressibility gives that

$$c_T = -\frac{1}{V}\frac{\partial V}{\partial p} = -\frac{1}{V}\frac{\partial V}{\partial t}\frac{\partial t}{\partial p}, \tag{5.51}$$

where $\frac{\partial V}{\partial t} = q$ is the flow rate. Solving for $\frac{\partial p}{\partial t}$ gives

$$\frac{\partial p}{\partial t} = -\frac{q}{c_T V} = -\frac{q}{c_T \phi \pi \left(r_e^2 - r_w^2\right) L}. \tag{5.52}$$

Substituting $\frac{\partial p}{\partial t}$ back into C_0 will result in

$$C_0 = -\frac{\phi \mu c_T}{K} \frac{q}{c_T \phi \pi \left(r_e^2 - r_w^2\right) L} = \frac{q\mu}{\pi \left(r_e^2 - r_w^2\right) KL}. \tag{5.53}$$

Appendix 5-B

The average pressure is determined by Eq. (5-27). In the special case where we have only radial flow, the zero axial flow rates result in $a = b = d = 0$. From the boundary conditions we get $e = C_0/4$ and $c = \frac{\Delta_r p - e r_e^2}{ln(r_e/r_w)}$ where $\Delta_r p = p_e - p_w$. By integrating the pressure given in Eq.(32), we find that

$$p_{av} = c\left(\frac{{r_e}^2 ln\left(r_e/r_w\right)}{{r_e}^2 - {r_w}^2} - \frac{1}{2}\right) + \frac{e}{2}\left({r_e}^2 + {r_w}^2\right) + f. \tag{5.54}$$

Here, f is a coefficient that cancels when using pressure differences. It could also be determined by any wellbore pressure; for example $p(0, w) = f$ according to Eq. (5-13). Suppose that $r_w \ll r_e$, the drawdown between average reservoir pressure and wellbore pressure is

$$\Delta_r \bar{p} = p_{av} - p_w = c\left(\frac{{r_e}^2 ln\left(r_e/r_w\right)}{{r_e}^2 - {r_w}^2} - \frac{1}{2}\right) + \frac{e}{2}\left({r_e}^2 - {r_w}^2\right) = c\left(ln\left(r_e/r_w\right) - \frac{1}{2}\right) + \frac{e}{2}{r_e}^2. \tag{5.55}$$

Then, we have $c = \frac{\Delta_r p - \frac{e}{2} r_e^2}{ln(r_e/r_w) - \frac{1}{2}}$, and substituting in (12) will give

$$Q_w = \frac{2\pi KL\Delta_r \bar{p}}{\mu\left[ln\left(r_e/r_w\right) - 0.5\right]} + \frac{Q_{net}}{4\left[ln\left(r_e/r_w\right) - 0.5\right]}. \tag{5.56}$$

Here, Q_{net} is the total fluid removal rate from the porous part of the segment. In the case when all boundaries are closed, i.e. $Q_w = Q_{net}$, we finally have

$$Q_w = \frac{2\pi KL\Delta_r \bar{p}}{\mu\left[ln\left(r_e/r_w\right) - 0.75\right]}. \tag{5.57}$$

Appendix 5-C

The permeability tensor in the principal directions (shown in Figure 5.16) is

$$\underline{K} = \begin{bmatrix} K_1 & 0 & 0 \\ 0 & K_2 & 0 \\ 0 & 0 & K_3 \end{bmatrix}. \tag{5.58}$$

The Laplacian for any medium without source or sink is derived from material balance considerations, which leads to

$$\nabla \cdot \overrightarrow{u} = 0. \tag{5.59}$$

Substituting the $\overrightarrow{u}$ given by Darcy's Law with $\underline{K}$ given by Eq. (5.59), we get

$$\frac{\partial}{\partial x}\left(K_1 \frac{\partial \Phi}{\partial x}\right) + \frac{\partial}{\partial y}\left(K_2 \frac{\partial \Phi}{\partial y}\right) + \frac{\partial}{\partial z}\left(K_3 \frac{\partial \Phi}{\partial z}\right) = 0. \tag{5.60}$$

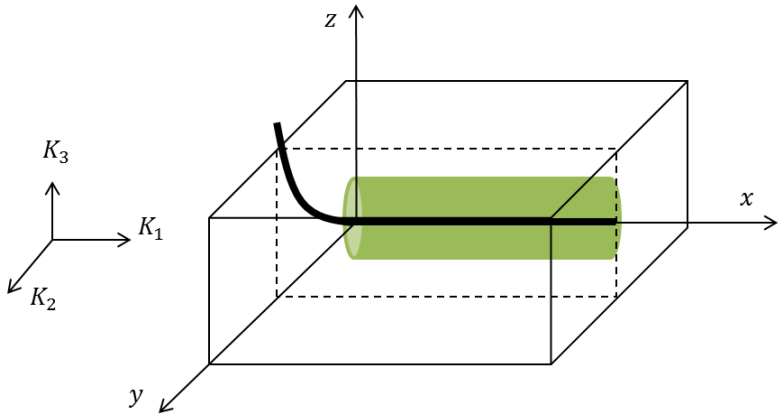

Figure 5.16: Horizontal well and near-well region in anisotropic reservoir

One commonly used transform is defined by stretching the x and z axes by constant multiplication. Letting

$$\xi = \sqrt[4]{\frac{K_2}{K_3}}, \tag{5.61}$$

the transform becomes

$$\Gamma : \begin{cases} x' = x \\ y' = \xi^{-1} y \\ z' = \xi z \end{cases} . \tag{5.62}$$

We assume ξ is a constant. This is valid for most reservoir engineering problems. It physically means that the force causing anisotropy over geological time has acted the same everywhere, even though the medium is heterogeneous.

Since $dx'dy'dz' = dxdydz$, the transform Ξ preserves volumes and hence flow rates. It is straightforward to show that Eq. (5.60) becomes

$$\frac{\partial}{\partial x'}\left(K_1 \frac{\partial \Phi}{\partial x'}\right) + \frac{\partial}{\partial y'}\left(\sqrt{K_2 K_3}\frac{\partial \Phi}{\partial y'}\right) + \frac{\partial}{\partial z'}\left(\sqrt{K_2 K_3}\frac{\partial \Phi}{\partial z'}\right) = 0. \tag{5.63}$$

The permeability tensor becomes

$$\underline{K'} = \begin{bmatrix} K_1 & 0 & 0 \\ 0 & \sqrt{K_2 K_3} & 0 \\ 0 & 0 & \sqrt{K_2 K_3} \end{bmatrix} . \tag{5.64}$$

This means that the plane yz, perpendicular to the well trajectory, becomes isotropic and the permeability in this plane is $K_r = \sqrt{K_2 K_3}$. During the transformation, volume is preserved as is the pressure. Therefore, the inflow equation using average pressure is adequate and convenient. At the same time, the radial cylinder of the near-well segment is converted to an elliptical cylinder, of which the major radius $b = r_e \sqrt[4]{K_2/K_3}$ and the minor radius $a = r_e \sqrt[4]{K_3/K_2}$, as shown in Figure 5.17.

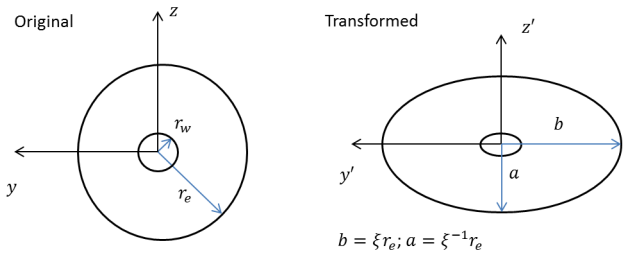

Figure 5.17: The cross section of the reservoir cylinder, before and after transformation

References

- Babu, D.K. and Odeh, A., 1989. Productivity of a Horizontal Well. *SPE Reservoir Engineering*, 4(4), 417-421.

- Cao, J., James, L. A. and Johansen, T. E., 2015. A New Coupled Axial-Radial Productivity Model for Horizontal Wells with Application to High Order Numerical Modeling, Paper SPE 175591 presented at SPE Reservoir Characterization and Simulation Conference and Exhibition, 14-16 September, Abu Dhabi, UAE.

- Cinco-Ley, H., Ramey, H.J. and Miller, F.G., 1975. Pseudo-Skin Factors for Partially-Penetrating Directionally Drilled Wells. paper SPE 5589, presented at 50th Annual Fall Meeting, Dallas, September 28-October 1.

- Dietz, D.N., 1965. Determination of Average Reservoir Pressure from Build-up Surveys. *Journal of Petroleum Technology*, 17(8), 955-959.

- Giger, F.M., Reiss, L.H., and Jourdan, A.P., 1984. The Reservoir Engineering Aspects of Horizontal Drilling, SPE 13024 presented at 59th Annual Technical Conference and Exhibition of the Society of Petroleum Engineering, Houston, TX, 16-19 September.

- Johansen, T.E., James, L.A. and Cao, J., 2015. Analytical Coupled Axial and Radial Productivity Model for Steady-State Flow in Horizontal Wells. *Internation Journal of Petroleum Engineering*,1(4), 290-307.

- Joshi, S.D., 1988. Augmentation of Well Productivity with Slant and Horizontal Wells (includes associated papers 24547 and 25308). *Journal of Petroleum Technology*, 40.06: 729-739.

- Kuchuk, F.J., Goode, P.A., Brice, B.W., Sherrard, D.W. and Thambynayagam, R.K.M., 1990. Pressure-Transient Analysis for Horizontal Wells. *Journal of Petroleum Technology* 42.8: 1028-1031.

- Matthews, C.S., Brons, F., and Hazebroek, P., 1954. A Method for Determination of Average Pressure in a Bounded Reservoir. *Trans., AIME*, 201, 182-191.

- Muskat, M., 1937. The Flow of Homogeneous Fluids Through Porous Media. McGraw-Hill, New York.

- Peaceman, D.W., 1983. Interpretation of Well-Block Pressures in Numerical Reservoir Simulation with Nonsquare Grid Blocks and Anisotropic Permeability, *SPE Journal*, 531-43.

- Peaceman, D.W., 1990. Recalculation of Dietz Shape Factor for Rectangles. Unsolicited Paper SPE, 21256.

- Pedrosa Jr, O.A. and Aziz, K., 1986. Use of a Hybrid Grid in Reservoir Simulation. *SPE Reservoir Engineering*, 1.06: 611-621.

- Scheidegger, E., 1960. The Physics of Flow Through Porous Media. University of Toronto Press, first edition.

- Skinner, J.H., and Johansen, T.E., 2012. Near Wellbore Streamline Modeling: Its Novelty, Application, and Potential Use. In SPE International Symposium and Exhibition on Formation Damage Control, 15-17 February, Lafayette, Louisiana, USA.

Chapter 6

Modeling Horizontal Well and Near-Well Flow Performance in Anisotropic Media

6.1 Overview

6.1.1 Preface

This Chapter is a reprint of the paper "Coupled Axial-Radial Flow Model for Horizontal Well Simulation in Anisotropic Reservoir" presented at 15th European Conference on the Mathematics of Oil Recovery. [1] This paper focuses on the development of the coupled axail-radail productivity model for anisotropic reservoirs.

The thesis author contributes to this paper mainly on the aspects of developing the numerical model, applying the spatial transformation method in near-well region, determining Dietz

[1] **Cao, J.**, James, L.A., and Johansen, T.E., 2016. Modelling Near-well Flow Performance for Horizontal Wells in Anisotropic Media, 15th European Conference on the Mathematics of Oil Recovery (ECMOR XV), 29 August - 1 September, Amsterdam, Netherlands.

shape factor for ellipse numerically, presenting calculation examples, and preparing the manuscript.

6.1.2 Introduction

Modeling the flow performance in the near-well region is gaining research interest for horizontal or unconventional wells due to the complexity of well trajectory, various well completion methods and application of inflow control devices. The near-well region and the wellbore constitute the reservoir model consider in this paper (as shown in Figure 6.1). The accurate calculation of inflow performance is of crucial importance in determining the well productivity. For example, various advanced completion methods for horizontal wells such as the application of inflow control devices complicate the pressure distribution and flow behavior in the near-well region.

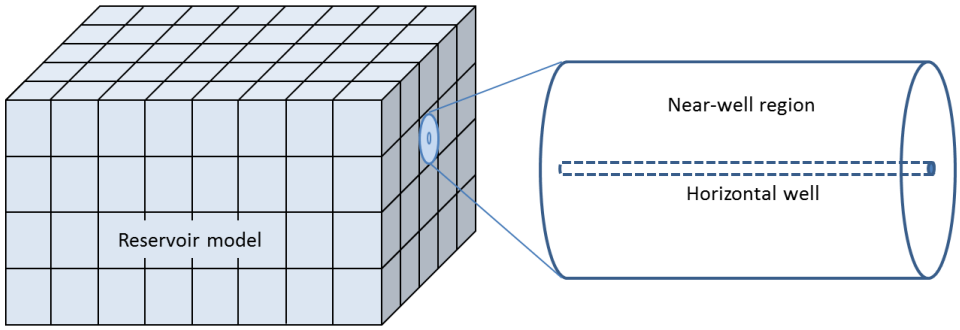

Figure 6.1: The near-well region with a horizontal well in reservoir model

Estimating the productivity of horizontal wells has been a topic of research as these wells have been widely and commonly used since 1990s. Both analytical and numerical methods have been proposed to predict and simulate the flow performance of the horizontal wells. Mathematical models for horizontal wells have been solved under different inner and outer boundary conditions, for example Borisov (1984), Giger et al. (1984), Joshi (1988), Babu and Odeh (1989), and Economides et al. (1991). These solutions can be used to estimate

the well productivity and calculate a productivity index, but are limited to certain inner and outer boundary conditions. The inner boundary conditions used in most analytical solutions are either constant pressure (no pressure gradient in the wellbore) or constant flux (same inflow in every well section). However, neither assumption is valid for long wellbores or highly productive wells since wellbore pressure gradients cannot be ignored. This is because in such wells the pressure decreases from the toe to the heel primarily due to friction in the well, and the inflow into the well therefore will vary (Dikken, 1990). A semi-analytical well/reservoir coupling model was presented by Penmatcha and Aziz (1999) for infinite and finite conductivity wells. A coupled axial-radial flow model has been recently presented (Johansen et al. (2015) and Johansen et al. (2016a)), which incorporates axial pressure gradient and flow along the well trajectory analytically. These models were also applied in numerical modeling of horizontal wells in isotropic near-well regions (Cao et al., 2015).

In an anisotropic reservoir, the permeability is a rank 2 tensor, which must be used in determining the productivity of horizontal wells. The flow model in anisotropic media was solved analytically (Cinco-Ley et al., 1975) assuming the well is a line source in an infinite slab reservoir. A spatial transformation has also been used to convert the real anisotropic media to a virtual isotropic media, for example in Besson and Aquitaine (1990), thereby enabling analytical solutions. It is well-known that the well inflow is typically radial in isotropic media and elliptical in anisotropic media. The hybrid grid approach (Pedrosa and Aziz, 1986) obtained accurate well treatment by using cylindrical (or elliptical in anisotropic media) fine grids in the near-well region and rectangular coarse grids for remote parts of the reservoir.

Numerical simulation techniques are necessary in representing reservoir heterogeneity and wellbore hydraulics. An interpretation of well-block pressure for anisotropic media in numerical simulation using an effective well-block radius was presented in Peaceman (1983). A multisegment model was proposed in Holmes et al. (1998) to represent the well, in which pressure and flow rate were solved implicitly. An iterative approach was presented to model

multi-phase flow in horizontal wells with advanced completion in Johansen and Khoriakov (2007). For heterogeneous and anisotropic formations, a near-well radial upscaling method was proposed in Wolfsteiner and Durlofsky (2002) using multiblock grids. Using near-well subdomain simulation, Guyaguler et al. (2010) determined the Inflow Performance Relationship curves for horizontal wells, which were applied in the coupling of a surface facility model and a reservoir model.

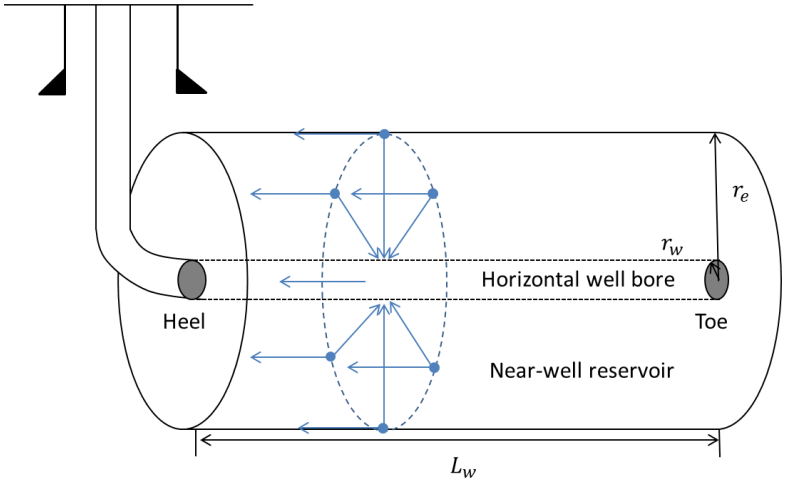

Figure 6.2: Coupled axial-radial flow segment in the near-well region

This research provides an accurate treatment of the anisotropic near-well region using cylindrical grids to construct a numerical model of the well and near-well region. This is based on the analytical coupled axial-radial productivity model for semi-steady state flow presented in Johansen et al. (2016a) for isotropic reservoirs. The coupled axial-radial productivity model, as shown in Figure 6.2, represents a two-dimensional problem in each near-well segment, which combines the axial flow in the near-well reservoir and the radial flow from reservoir into the wellbore. The analytical solution to the coupled axial-radial flow model is briefly summarized in the next Section. Since the permeability is a tensor in anisotropic reservoirs, the principal permeabilities alone cannot in general be directly used in the well inflow equations. A transformation method is therefore applied to convert the real anisotropic media to a virtual isotropic media in the plane perpendicular to the well trajectory. This transformation is only applied in the near-well region, without changing the outer boundary

conditions. This methodology is implemented in the numerical well/near-well simulation and calculated examples are presented.

6.2 Methodology of the near-well/well numerical model

6.2.1 Coupled axial-radial Flow model in the near-well region

The need for high resolution grids near wellbores is much larger compared to the remote reservoir parts because of the relatively large pressure gradients in the near-well region. The near-well region is usually simulated by standalone simulators or by using local grid refinements. Local productivity indices, resulting from analytical solutions, are commonly used to determine the flow from a well grid block to the wellbore. In this, the axial reservoir flow in the near-well region is usually either ignored or simply determined numerically. However, the pressure gradient along the well trajectory in general cannot be ignored in horizontal or deviated wells. In this Section, and further detailed in Section 6.2.3, a semi-analytical approach for single phase semi-steady state flow using a coupled axial-radial productivity model is described for anisotropic reservoirs.

Assume that the well trajectory is alligned with one of the principal permeability directions x, y, z. The general form of Darcy's Law for single phase flow in porous media reads

$$\vec{u} = -\frac{1}{\mu}\underline{K} \cdot \nabla\Phi; \Phi = p - \rho g z, \tag{6.1}$$

where u is the volumetric flux; μ is the fluid viscosity; ρ is the fluid density; $\underline{K}$ is the permeability tensor and Φ is the potential. The permeability tensor using the principal directions is

$$\underline{K} = \begin{bmatrix} K_x & 0 & 0 \\ 0 & K_y & 0 \\ 0 & 0 & K_z \end{bmatrix}. \tag{6.2}$$

In the near-well region, cylindrical coordinates (x, r and θ) are normally used, as shown in

Figure 6.3. This honors the radial inflow nature in the near-well region and can be coupled with the outer reservoir using a hybrid grid system (Pedrosa and Aziz, 1986) or an iterative approach like Brekke et al. (1983) and Johansen and Khoriakov (2007). The permeability tensor then becomes

$$\underline{K} = \begin{bmatrix} K_x & 0 & 0 \\ 0 & K_r & K_\theta \\ 0 & K_\theta & K_t \end{bmatrix}, \tag{6.3}$$

where, (see for example Skinner and Johansen (2012)),

$$\begin{aligned} K_r &= K_y \cos^2\theta + K_z \sin^2\theta, \\ K_t &= K_y \sin^2\theta + K_z \cos^2\theta, \\ K_\theta &= (K_y - K_z)\sin\theta\cos\theta. \end{aligned} \tag{6.4}$$

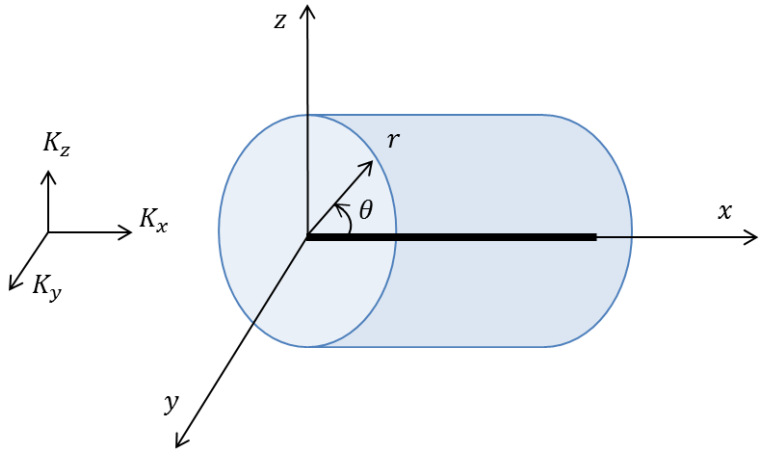

Figure 6.3: Horizontal well and anisotropic near-well region in Cartesian coordinates and cylindrical coordinates

Therefore, the general conservation equation in cylindrical coordinates, ignoring gravity for simplicity, is

$$\frac{\partial}{\partial x}\left(K_x \frac{\rho}{\mu}\frac{\partial p}{\partial x}\right) + \frac{1}{r}\frac{\partial}{\partial r}\left(rK_r \frac{\rho}{\mu}\frac{\partial p}{\partial r}\right) + \frac{1}{r}\frac{\partial}{\partial r}\left(K_\theta \frac{\rho}{\mu}\frac{\partial p}{\partial \theta}\right) + \frac{1}{r}\frac{\partial}{\partial \theta}\left(K_\theta \frac{\rho}{\mu}\frac{\partial p}{\partial r}\right) + \frac{1}{r^2}\frac{\partial}{\partial r}\left(K_t \frac{\rho}{\mu}\frac{\partial p}{\partial \theta}\right) = \frac{\partial(\rho\phi)}{\partial t}, \tag{6.5}$$

where ϕ is the medium porosity. In the coupled axial-radial flow model, radial inflow into the wellbore and axial reservoir flow along the well trajectory are considered while the angular

flow is ignored, which means that only the first two terms in Eq. 6.5 are non-zero. Therefore, the coupled axial-radial flow model represents a two dimensional problem; the conservation equation for slightly compressible single phase flow in this case is given by

$$\frac{\partial}{\partial x}\left(K_x \frac{\rho}{\mu}\frac{\partial p}{\partial x}\right) + \frac{1}{r}\frac{\partial}{\partial r}\left(K_r \frac{\rho}{\mu} r \frac{\partial p}{\partial r}\right) = \phi \mu c_t \frac{\partial p}{\partial t}, \tag{6.6}$$

with appropriate boundary conditions in a *segment* of the wellbore and the near-well reservoir, see Figure 6.4. Here, c_t is the total compressibility. This coupled flow model was solved analytically for steady state flow in Johansen et al. (2015) and semi-steady state flow with both external (p_e) and average reservoir pressures (p_r) in Johansen et al. (2016a).

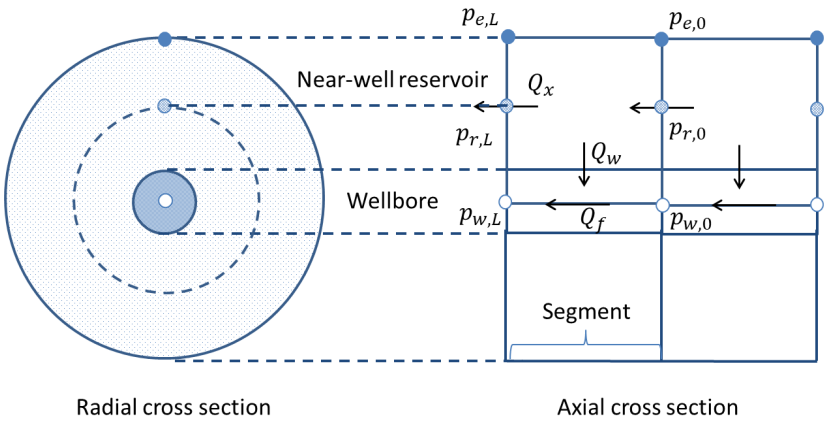

Figure 6.4: The schematic of the well/near-well segment

The productivity model can be implemented in the numerical well/near-well model considering axial reservoir flow (Q_x), radial well inflow (Q_r), and pipe flow in the wellbore/annulus (Q_f), as shown in Figure 6.4. The productivity equations in terms of average reservoir pressure (p_r) for a *segment* are derived in Johansen et al. (2016a) as

$$\begin{cases} Q_w = T_w \, \overline{\Delta_r p}; \\ Q_x = -T_a \left(p_{r,L} - p_{r,0}\right) - \frac{1}{2} T_w \overline{\Delta_r p} + \frac{1}{2} Q_{net}; \end{cases} \tag{6.7}$$

where

$$T_w = \frac{2\pi K L}{\mu \left[ln(r_e/r_w) - 3/4\right]}; T_a = \frac{\pi K r_e^2}{\mu L}; \tag{6.8}$$

$\overline{\Delta_r p} = \left(\Delta_r p_0 + \Delta_r p_L\right)/2$; $\Delta_r p_0 = p_{r,0} - p_{w,0}$; $\Delta_r p_L = p_{r,L} - p_{w,L}$; Q_{net} is the net outflow

for each near-well reservoir grid in semi-steady state, i.e.

$$Q_{net} = c_t \phi \pi (r_e^2 - r_w^2) L \frac{\partial p}{\partial t}, \tag{6.9}$$

where for semi-steady state flow $\frac{\partial p}{\partial t}$ is constant in both space and time. Here, L is the axial length of the segment and Q_{net} equals to the well total productivity (Q_T) when L is the length of the reservoir (L_w). This analytical solution determines the well inflow (Q_w) and the axial reservoir flow (Q_x) simultaneously for each segment given the four pressures ($p_{r,L}, p_{r,0}, p_{w,L}$ and $p_{w,0}$) in each segment. These results are also presented in Johansen et al. (2016a) based on external reservoir pressure ($p_{e,L}$ and $p_{e,0}$) instead of average reservoir pressures; however, this is not used here. Recalling the assumption that no flow is assumed in the $\theta-$direction, pressure is constant on each circle perimeter in Figure 6.4. This well inflow model is similar to the classical semi-steady state well inflow equation. It reduces to the classical semi-steady state inflow equation if the radial pressure gradient is uniform ($p_{r,0} - p_{w,0} = p_{r,L} - p_{w,L}$), i.e.

$$Q_w = \frac{2\pi K L \left(p_r - p_w\right)}{\mu \left[ln \left(r_e / r_w\right)\right]} \tag{6.10}$$

6.2.2 Application of Dietz shape factor in near-well reservoir blocks

The productivity model in the previous Section is valid for isotropic media only. In order to apply the productivity equations in anisotropic media, two directional permeabilities are needed; one along the well trajectory (K_x) and one in the plane perpendicular to the well trajectory (K_r). If the well is along one of the principal axis, for example the x axis shown in Figure 6.3, the axial principal permeability (K_x) can be used for the axial flow along the wellbore. To find the permeability for the well inflow, a simple method is introduced to convert the plane perpendicular to the well trajectory to be an equivalent isotropic medium. This is achieved through a commonly used space transformation in the near-well region, scaling the y and z axes by constant factors. Letting

$$\xi = \sqrt[4]{\frac{K_y}{K_z}}, \tag{6.11}$$

the transformation is then defined as

$$\Gamma : \begin{cases} x' = x, \\ y' = \xi^{-1} y, \\ z' = \xi z. \end{cases} \tag{6.12}$$

We assume ξ is a constant, which is valid for most reservoir engineering problems. It is well known that subject to the transform (Eq. 6.12) the permeability tensor becomes

$$\underline{K}' = \begin{bmatrix} K_x & 0 & 0 \\ 0 & \sqrt{K_y K_z} & 0 \\ 0 & 0 & \sqrt{K_y K_z} \end{bmatrix}. \tag{6.13}$$

Here, $K_r = K_t = \sqrt{K_y K_z}$ and $K_\theta = 0$ in Eq. 6.4.

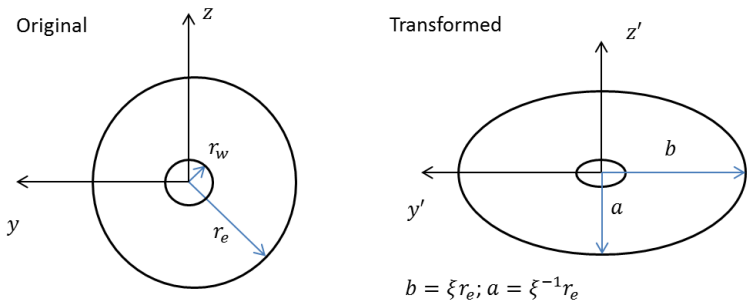

Figure 6.5: The cross section of the reservoir cylinder, before and after transformation Γ

The transform Γ used in the above derivation represents a distortion of the geometry of the porous medium. This simple transformation is implemented only in the near-well region. It maps a circular cylinder along the $x-$axis of radius r onto an elliptical cylinder with the same axis and with major, minor radius being $r_e \sqrt[4]{K_y/K_z}$ and $r_e \sqrt[4]{K_z/K_y}$ respectively, as shown in Figure 6.5. To use the productivity model (Eq. (6.7) and (6.8)), we must know the pressure on the outer boundary in the real medium for an elliptic iso-pressure contour because an ellipse transforms to a circle by Eq. (6.12), and the use of Eq. (6.7) and (6.8) is based on a circular geometry. Alternatively, for semi-steady flow, we can use another

formulation (Dietz, 1965) for flow in an arbitrary shaped geometry, i.e.

$$Q_w = \frac{2\pi K_r L}{\mu \ln\left(\frac{4A}{\gamma C_A r_w^2}\right)} \overline{\Delta_r p}, \tag{6.14}$$

where C_A is the Dietz shape factor for the elliptic reservoir configuration in Figure 6.5 and A is the cross sectional area, $\gamma \approx 1.781$ and $K_r = \sqrt{K_y K_z}$. For an anisotropic reservoir, Eq. (6.7) still holds true with the permeability in the cross plane perpendicular to the well trajectory (K_r) and in the direction along the well trajectory (K_x). The wellbore is also transformed to an ellipse, which has an effective wellbore radius (r'_w) given by Kuchuk and Brigham (1979) as

$$r'_w = r_w \frac{c+1}{2\sqrt{c^2-1}}, \tag{6.15}$$

where $c = a_w/b_w$; a_w and b_w is the major and minor axis of transformed wellbore ellipse, respectively. Therefore, Eq. 6.7 is used for the elliptic reservoir configurations with

$$T_w = \frac{2\pi K_r L}{\mu ln(\frac{4A}{\gamma C_A r_w^2})}; T_a = \frac{K_x A}{\mu L}. \tag{6.16}$$

The only parameter needed to be determine is the Dietz shape factor for the reservoir configuration, which is the ellipse in our case.

This transformation converts the near-well region perpendicular to the well trajectory to a virtually equivalent isotropic media and is implemented only in the near-well region. This provides the flexibility in choosing near-well region grid block configurations. The mostly recognized near-well region is circular-cylindrical or elliptical-cylindrical. The Dietz shape factor for ellipses with different major to minor axes ratio is determined numerically, see Appendix 6-A.

If the well is not aligned with a principal direction, the cross section plane permeability perpendicular to the well trajectory (K_r) and the axial permeability along the well trajectory can still be determined provided $K_x = K_y$ (Johansen et al, 2016b).

The focus of this paper is on the flow in the wellbore and near-well region, which can be solved simultaneously with the reservoir model. If coupled with the reservoir model, a full

permeability tensor is necessary for anisotropic reservoir (Fanchi,2008) and (Gupta et al., 2001). The transformation method applied to the whole reservoir (Besson and Aquitaine, 1990) is another approach, which involves complicated treatment of inner and outer boundary conditions.

6.2.3 The well/near-well numerical model

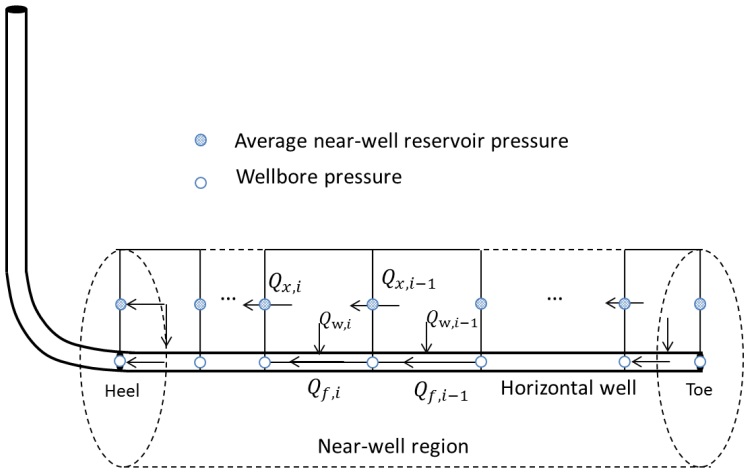

Figure 6.6: Schematics of the well/near-well numerical model

In this Section, the numerical model for horizontal well and near-well simulation is described considering coupled axial-radial flow, formation anisotropy and wellbore hydraulics. The well model providing the relationship between the pressure drop and well inflow and reservoir axial flow rate is given by Eq. (6.7) and Eq. (6.16) in the previous Section for anisotropic media. For anisotropic media, the Dietz shape factor needed is determined numerically in Appendix A. In this Section, the numerical model for the wellbore and the near-well reservoir is described.

The wellbore hydraulics may be significant in long horizontal wells. For semi-steady state flow, the wellbore pressure is decreasing at a constant rate as is the pressure in the reservoir.

The pressure gradient in the wellbore is simplified as

$$\frac{\partial p}{\partial x} = -\frac{f\rho v^2}{2D} - \Delta\left(\rho v^2\right) - \rho g \Delta h, \tag{6.17}$$

where, f is the Darcy friction factor; $f = 0.3164/\sqrt[4]{Re}$ for turbulent flow in smooth pipes, and Re the Reynolds number. It is assumed that the flow inside the horizontal well is turbulent and for the sake of simplicity, gravity ($\rho g \Delta h$) is ignored. Furthermore, pressure loss due to acceleration caused by radial inflow ($\Delta\left(\rho v^2\right)$) is ignored since it is insignificant compared to the pressure loss caused by friction (Novy, 1996). The pipe is assumed to be smooth, however Eq. (6.17) is equally applicable to rough pipes using for example Haaland (1983) for the friction factor f. The momentum balance equation (Eq. (6.17)) in the well grid block is then given by

$$Q_f = T_f \Delta p^{1/2}, T_f = \sqrt{\frac{2DA^2}{f\rho\Delta x}}. \tag{6.18}$$

In this numerical model, the governing equations are the conservation equation in the wellbore part of the segments (wellbore grid blocks) and in the near-well reservoir part of the segments (reservoir grid blocks). Since the angular flow is ignored, the numerical model is two dimensional with flow in the axial and radial directions; a schematic of the numerical model and flow rates are shown in Figure 6.6. In wellbore grid blocks, mass balance equations read

$$Q_{f,i} - Q_{f,i-1} - Q_{w,i} = 0, \quad i = 1, 2, ...N_x, \tag{6.19}$$

where N_x is the number of segments in the axial direction. For the leftmost grid block (at the heel), the outflow is the total productivity of the horizontal well, i.e.

$$Q_{f,Nx} = Q_T; \tag{6.20}$$

for the rightmost grid block (at the toe), the inflow ($Q_{f,0}$) is zero. The governing equation in near-well reservoir grid blocks is formulated based on an upstream discretization;

$$Q_{x,i} + Q_{w,i} - Q_{x,i-1} = Q_{net,i}, \quad i = 1, 2, ...N_x, \tag{6.21}$$

where Q_{net} is determined by Eq. (6.18) given Q_T. The rightmost reservoir grid block (at the toe) have zero axial inflow ($Q_{x,0} = 0$). The leftmost reservoir grid block (at the heel)

have zero outflow; i.e.

$$Q_{x,Nx} = 0. \tag{6.22}$$

Since flow rates in Eq. (6.19) to (6.21) are expressed in terms of pressures by Eq. (6.7) and Eq. (6.17), we eventually have a system of equations entirely in terms of pressures. The number of equations here are $2 * N_x + 2$. The unknowns are the wellbore pressures $(N_x + 1)$, the near-well reservoir pressures $(N_x + 1)$ and the total productivity, which in total is $2 * Nx + 3$. One more boundary condition must be defined, either constant bottom hole pressure at the heel (P_{heel}) or the total well productivity (Q_T), to close the problem. Since the momentum equations in the wellbore grid blocks are nonlinear, the system of equations is solved by iterative methods. The Newton method is used in this paper.

6.3 Calculated Examples

Using the model described in the previous Section, typical solutions of the average reservoir pressure (p_r) and wellbore pressure (p_w) profiles are determined with axial grid block number $N_x = 100$, as shown in Figures 6.7 and 6.8, respectively. Here, the horizontal well is assumed to be fully penetrating the reservoir from toe to heel with a cylindrical reservoir around it. Furthermore, it is assumed that the well is producing at a constant flow rate $(Q_T = 3000\ m^3/day)$ with closed outer boundaries. The basic parameters used are shown in Table 6.1. The permeability in the x and y directions are assumed to be equal (horizontal permeability K_H), but different from that in the z direction (vertical permeability K_V). The anisotropy is described by the vertical to horizontal permeability ratio, i.e. K_V/K_H . In this case, $K_V/K_H = 0.5$. The well is producing a slightly compressible fluid from the closed cylindrical reservoir at a constant flow rate. As mentioned earlier, the assumption of closed outer boundary is made for demonstration purpose and can be replaced by coupling with a reservoir simulator (Johansen and Khoriakov, 2007). In the semi-steady state flow period, the pressure decreases linearly everywhere in the reservoir and at the same rate, which means

Table 6.1: Basic parameters for calculation examples

Parameter	Unit	Value
Horizontal permeability, K_H	mD	100
Vertical permeability, K_V	mD	50
Viscosity, μ	cP	1.0
Well length, L_w	m	1000
Wellbore radius, r_w	m	0.1
Reservoir radius, r_e	m	10
Density, ρ	kg/m^3	800
Initial reservoir pressure, p_{init}	bar	300
Total well productivity, Q_T	m^3/day	3000

the pressure curve shifts downward linearly. The time t_1 corresponds to the time when the largest reservoir pressure (p_{Toe}) equals to initial reservoir pressure (p_i), i.e. the beginning of semi-steady state flow; while at time t_2, $p_{Toe}(t_2) = 290bar$. The piecewise parabolic pressure solution in the axial direction, instead of piecewise constant pressure obtained from a standard finite difference method, results in a higher order numerical method, as shown in Cao et al., 2015. To verify the accuracy, a standard finite difference method with classical productivity equations, is also used to compare the results for isotropic cases ($K_V/K_H = 1$). The refined case with standard finite difference method using $Nx = 1000$ and $Ny = 100$ is treated as the solution. Then a coarse grid ($Nx = 10$ and $Ny = 2$) using both finite difference method and the new method are compared with the solution in Figure 6.9. The relative errors of both methods are plotted in Figure 6.10. Both figures confirmed that the new method achieved more accurate results than the finite difference method with the same number of grid blocks.

Using the same parameters given in Table 6.1, the axial grid is refined to examine the convergence of the numerical model. The wellbore and reservoir pressure profiles are plotted at time t_1 in Figure 6.11 and 6.12, respectively, with $N_x = 10$, $N_x = 100$ and $N_x = 1000$. Both figures demonstrate that the pressure profiles converge when the axial grid is refined in the numerical model. When the number of axial grid blocks is larger than 100, the pressure profiles for average reservoir and wellbore pressure are almost indistinguishable. Under the same conditions with $N_x = 1000$, the pressure profiles at time t_1 are also calculated given different anisotropy ratios with constant horizontal permeability . These results are plotted

in Figure 6.13 and 6.14. They show that the average reservoir pressure profiles are very close for different anisotropy ratios, while the wellbore pressure profiles vary significantly. The main reason is that horizontal permeability supreeses the axial pressure gradient and vertical permeability enlarges the difference between the reservoir pressure and wellbore pressure, if the productivity remains the same. As anisotropy ratio (K_V/K_H) decreases, vertical permeability decreases, hence higher pressure differences between the reservoir and the wellbore grid blocks are needed for the same flow rate. This results in a lower wellbore pressure profile, whereas horizontal permeability remains constant and the axial pressure profiles are generally similar in curvature.

To investigate the conditions that affect the axial pressure gradient, various well productivities are considered to calculate the pressure profiles. The results are shown in Figure 6.15 and 6.16 for average reservoir pressure and wellbore pressure, respectively. Both figures confirm that higher productivity results in larger wellbore pressure loss and larger axial pressure gradient. Axial pressure drop, both in the near-well reservoir and the wellbore, is mainly affected by the productivity of the well; with higher axial pressure drop in high productivity wells. The axial pressure gradient cannot be ignored, especially in high productivity wells.

To quantitatively compare the pressure drop in the axial and radial directions of the wellbore and the near-well reservoir, the following pressure differences are defined: the total pressure drop Δp_T (the difference between the reservoir pressure at the toe and wellbore pressure at the heel (p_{heel})), axial reservoir pressure drop ($\Delta_x p_e = p_{r,L} - p_{r,0}$), reservoir pressure drop at the toe ($\Delta_r p_L = p_{r,L} - p_{w,L}$) and wellbore pressure drop ($\Delta_x p_w = p_{w,L} - p_{w,0}$). These pressure drops are plotted for different anisotropy ratios, by fixing $K_H = 100$ in Figure 6.17 and fixing $K_V = 100$ in Figure 6.18, respectively. It clearly shows that more severe anisotropy results in a larger radial reservoir pressure drop. The axial reservoir pressure drop changes slightly with different anisotropy ratios. It also indicates that axial pressure drop in both wellbore and near-well reservoir contributes to the total pressure drop and in general cannot be ignored.

6.4 Conclusions

A new method is developed for coupled axial-radial flow model in anisotropic reservoirs. This method uses both well inflow equations and reservoir axial flow equations with average reservoir pressure in addition to the transformed permeability tensor for well inflow and reservoir axial flow. For anisotropic reservoirs, a classic transformation method is applied in the near-well region to convert the real anisotropic media to a virtual isotropic media in the plane perpendicular to the well trajectory. A new permeability tensor is therefore obtained and used in the coupled axial-radial flow model in determining the well inflow and the axial reservoir flow. This transformation is only used in the near-well region, without changing the outer boundary conditions. Since the near-well reservoir cylinder is transformed to an elliptical cylinder, Dietz shape factors for ellipses with different major to minor axis ratio are needed for the well inflow equation. The Dietz shape factor is determined numerically. Calculation examples of the numerical well/near-well model using coupled axial-radial productivity model in anisotropic reservoir are presented. In high productivity wells, the axial pressure gradient in wellbore and near-well reservoir cannot be ignored.

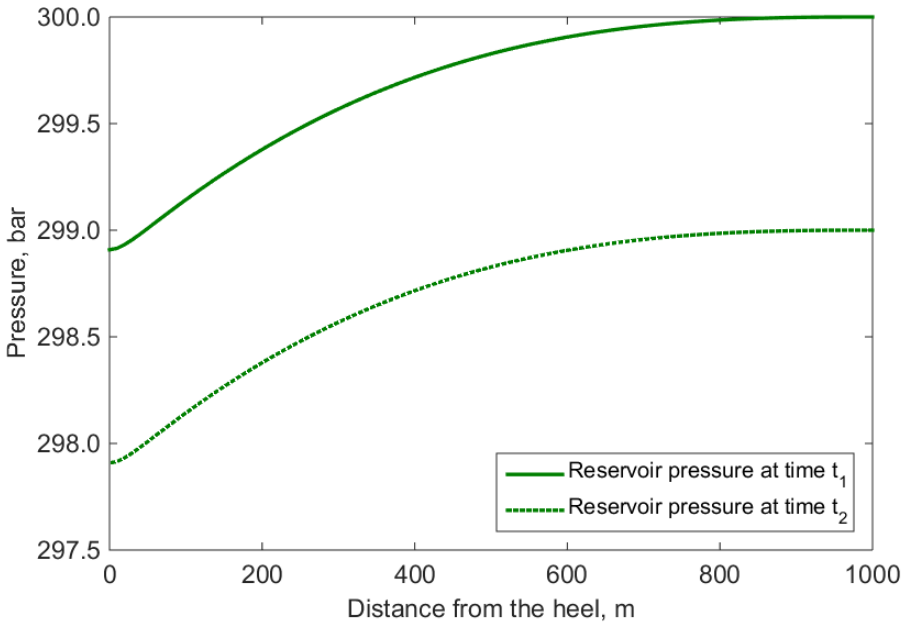

Figure 6.7: Typical solution of the reservoir pressure profiles

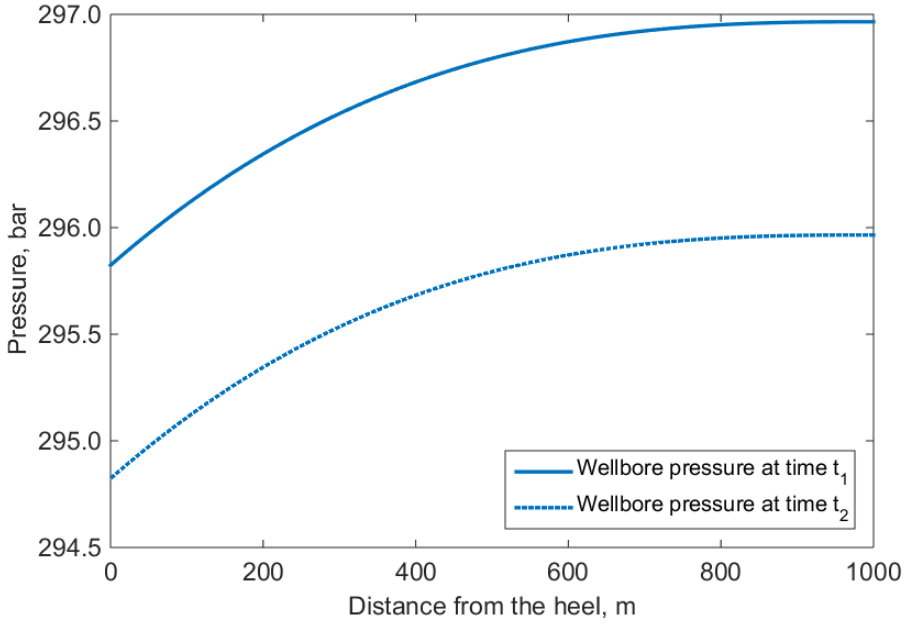

Figure 6.8: Typical solution of the wellbore pressure profiles

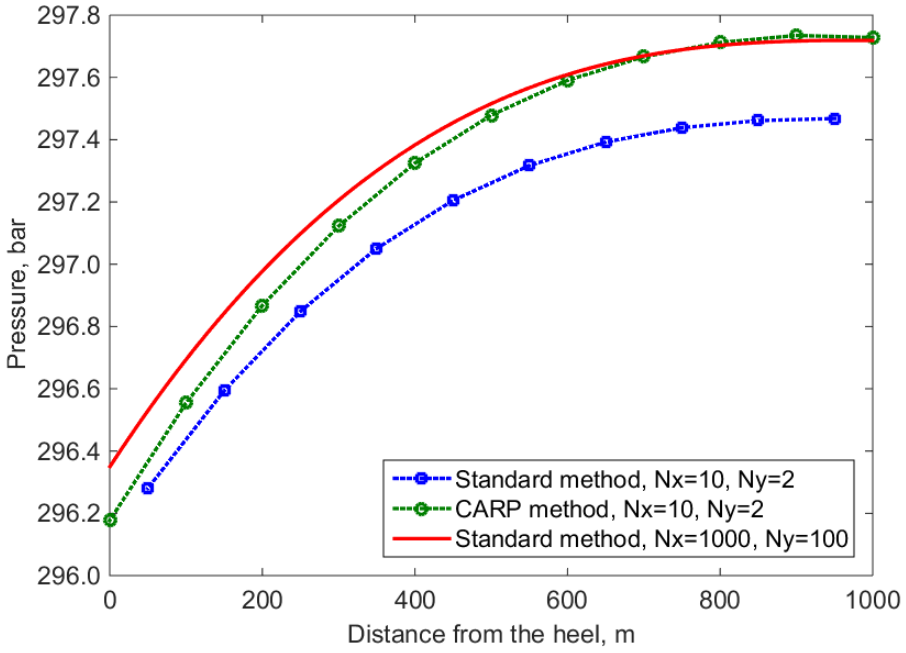

Figure 6.9: Wellbore pressure distributions from different methods

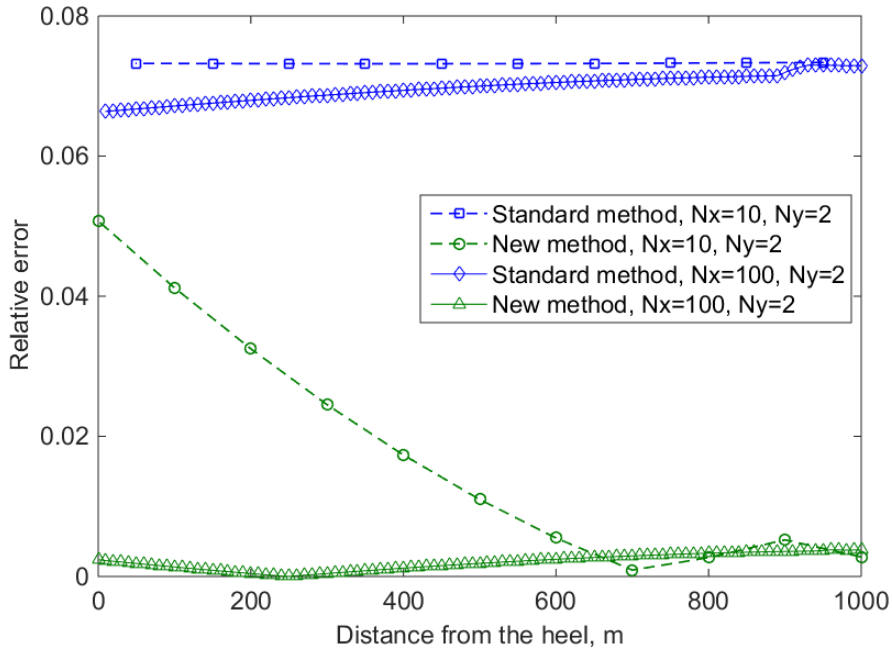

Figure 6.10: Relative error of the wellbore pressure from different methods

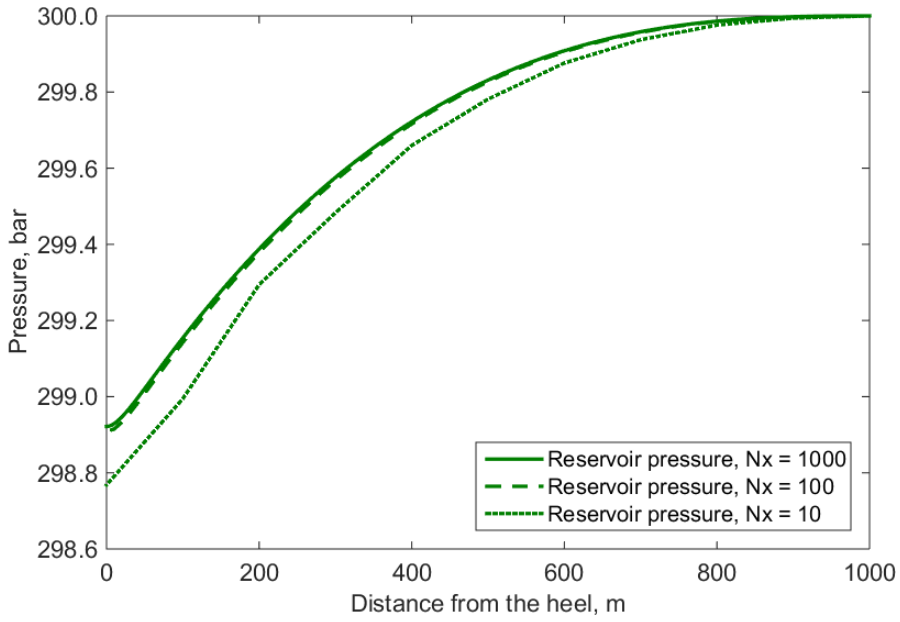

Figure 6.11: Reservoir pressure profiles in axial grid block refinement

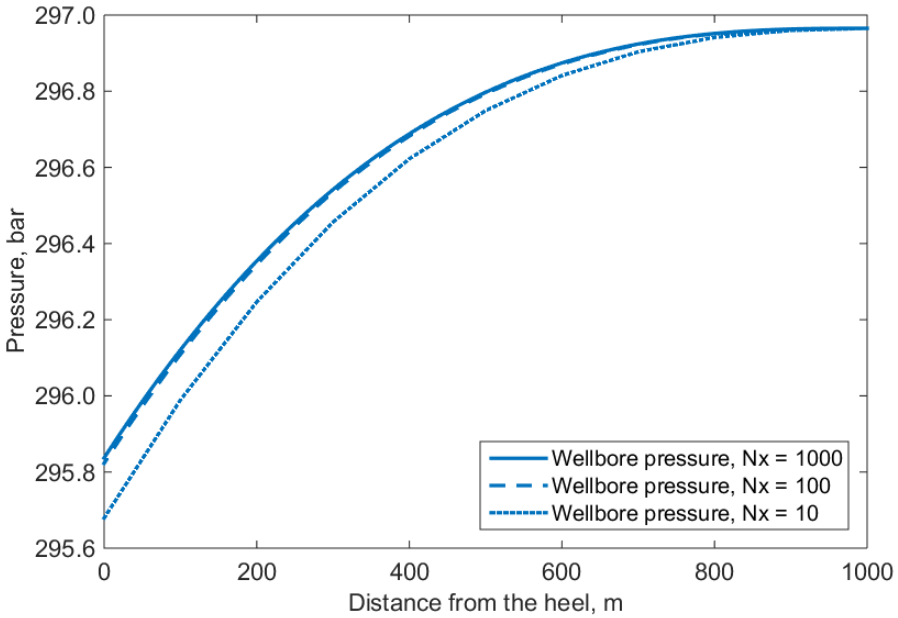

Figure 6.12: Wellbore pressure profiles in axial grid block refinement

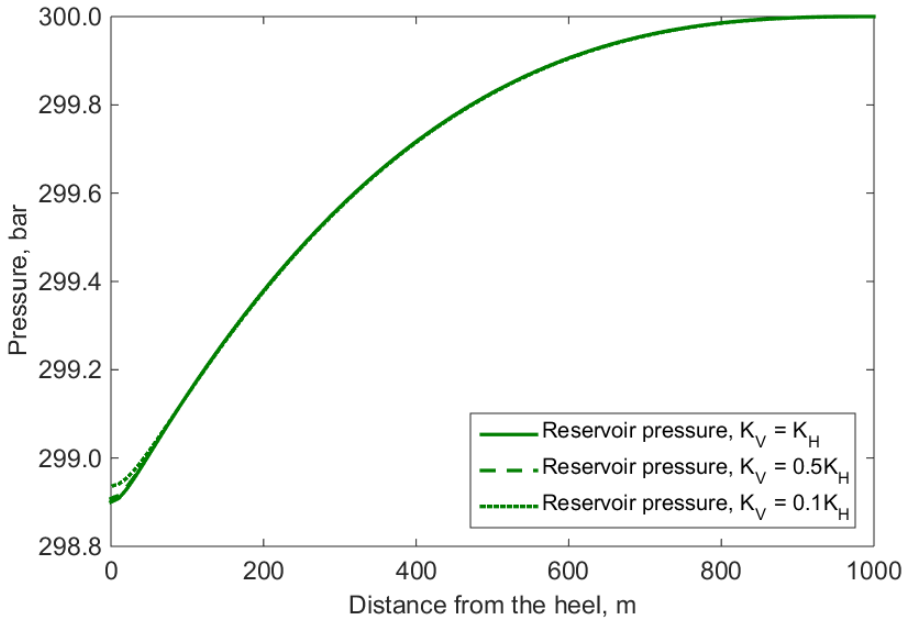

Figure 6.13: Reservoir pressure profiles with different anisotropy ratios

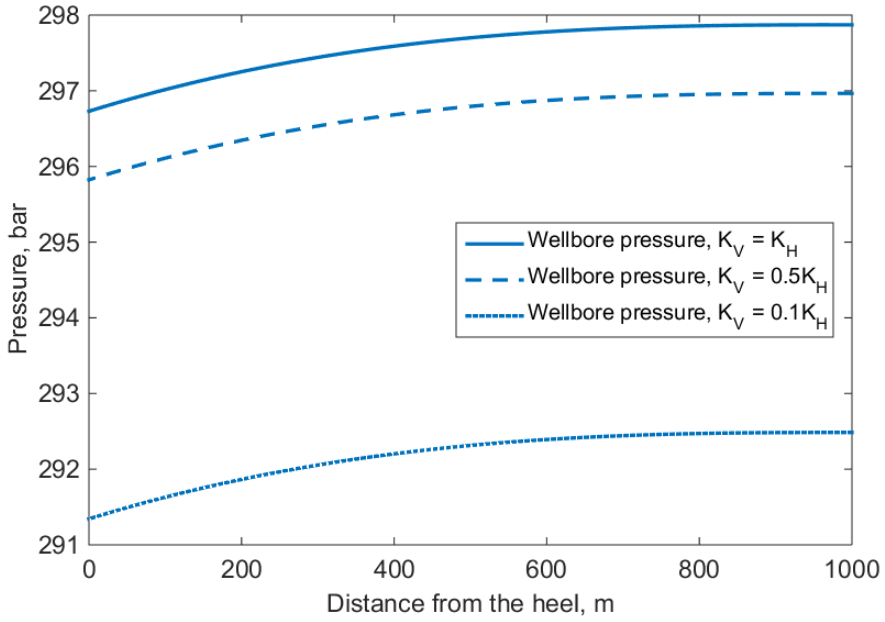

Figure 6.14: Wellbore pressure profiles with different anisotropy ratios

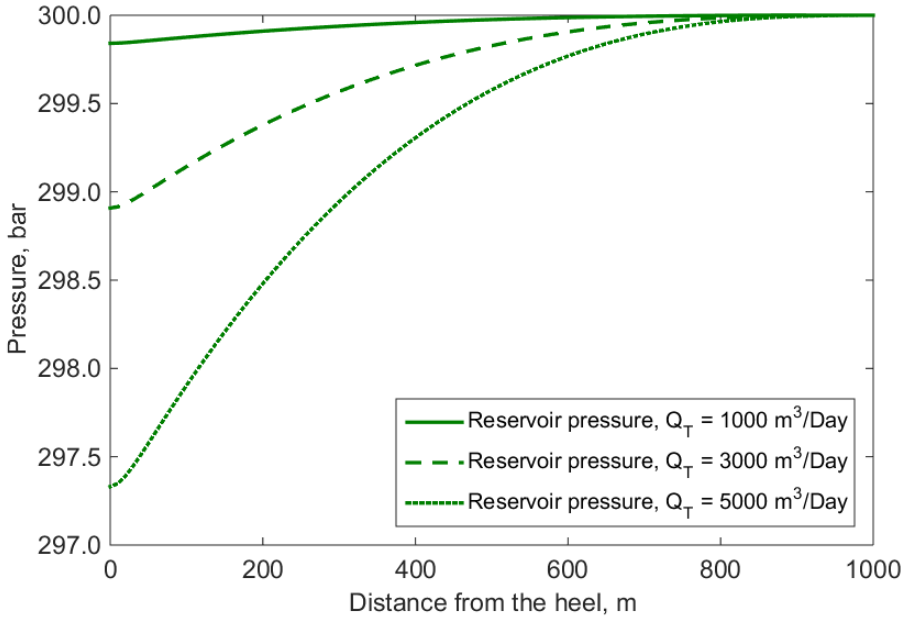

Figure 6.15: Axial reservoir pressure profiles with different total well productivity

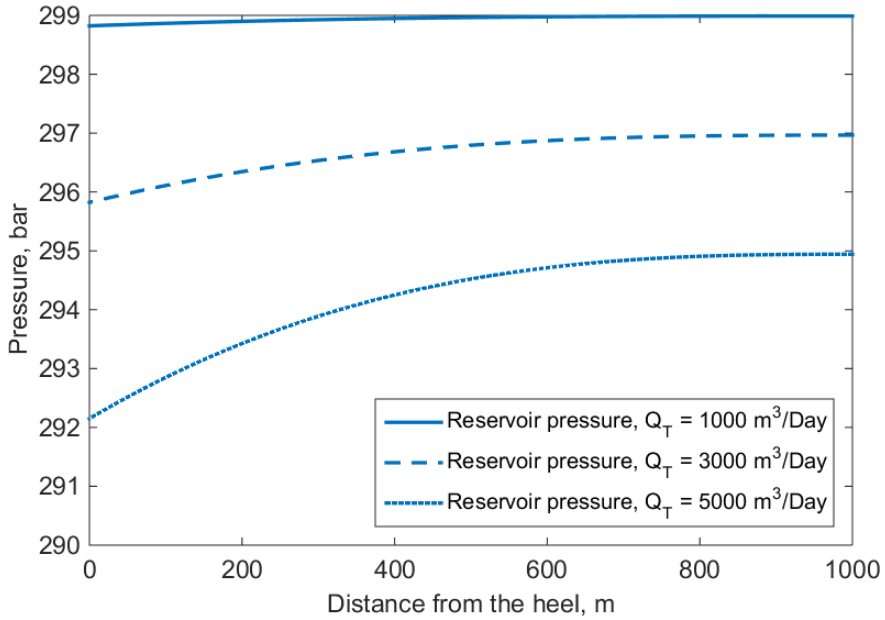

Figure 6.16: Wellbore pressure profiles with different total well productivity

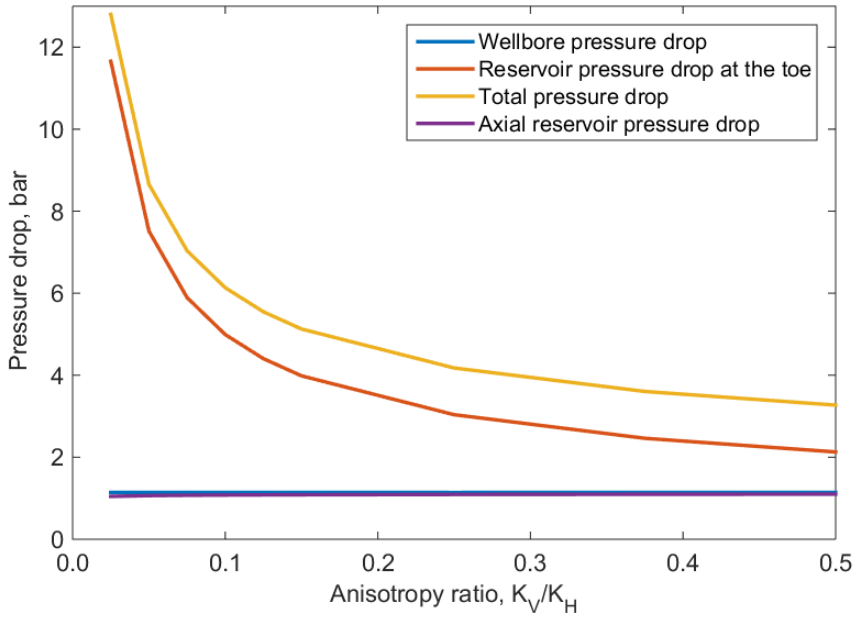

Figure 6.17: Pressure drops in the well/near-well model, $K_H = 100$

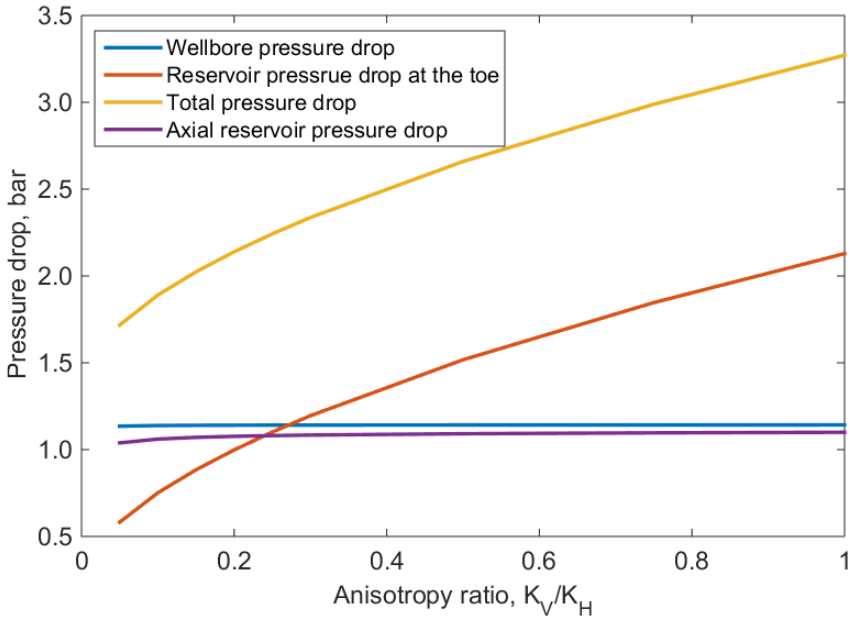

Figure 6.18: Pressure drops in the well/near-well model, $K_V = 100$

Appendix 6-A

The Dietz shape factor for ellipses with different major to minor axes ratios and with the well in the center is determined numerically in this Appendix. Previous research by Mattews et al. (1954), Dietz (1965) and Peaceman (1990) calculated the Dietz shape factor for triangular and rectangular configurations.

Consider a well producing a single phase, slightly compressible fluid from the center of an elliptical reservoir, which is homogeneous and isotropic. The well is producing at a constant flow rate and the outer boundary of the reservoir is a no flow boundary. Using the above assumptions and boundary conditions, the conservation equation is

$$\phi c_t \frac{\partial p}{\partial t} = \frac{K}{\mu}\frac{\partial^2 p}{\partial x^2} + \frac{K}{\mu}\frac{\partial^2 p}{\partial y^2}. \tag{6.23}$$

An implicit discretization (Aziz and Settari, 1979) of Eq. 6.23 is

$$\left(1 + 2T_x + 2T_y\right) p_{i,j}^{n+1} - T_x p_{i+1,j}^{n+1} - T_x p_{i-1,j}^{n+1} - T_y p_{i,j+1}^{n+1} - T_y p_{i,j-1}^{n+1} = p_{i,j}^{n} \tag{6.24}$$

using a fixed point source well rate, where $T_x = \frac{K}{\phi\mu c_t}\frac{\Delta t}{\Delta x^2}$ and $T_y = \frac{K}{\phi\mu c_t}\frac{\Delta t}{\Delta y^2}$. The reservoir is defined by an ellipse with a major to minor axes ratio b/a. The equivalent wellbore radius (Peaceman, 1983) in the square grid blocks is given by

$$\widetilde{r_w} = G\Big[(\Delta x)^2 + (\Delta y)^2\Big]^{1/2}, \tag{6.25}$$

where, $G \approx 0.1404$. Matching the productivity equation, the Dietz shape factor can be determined by

$$lnC_A = ln\frac{4A}{\gamma \widetilde{r_w}^2} - \frac{4\pi Kh}{q\mu}\left(\bar{p} - p_w\right). \tag{6.26}$$

A calculation example with $b/a = 2$ is given below using parameters from Table 6.2. The odd number of grid blocks is convenient in order to locate the well in the center. The pressure distribution after 30 hours is shown in Figure 6.19. The red grid blocks are inactive, with no communication with the elliptic reservoir. The average reservoir pressure and the wellbore pressure vs. time are plotted in Figure 6.20. The semi-steady state flow period can be determined by observing linearly decreasing pressure everywhere. It is observed that

the flow is stabilized after approximately three hours, which means the flow after that is semi-steady state. After that point, the average reservoir pressure curve is parallel to the wellbore pressure, i.e. the difference between them is a constant. Substituting this constant pressure difference into Eq. (6.24), the Dietz shape factor of this major to minor axes ratio ($b/a = 1/2$) can be determined. Repeating the same simulation process for different major to minor axes ratios will finally results in the Dietz shape factor function for an elliptical reservoir. This function is plotted in Figure 6.22.

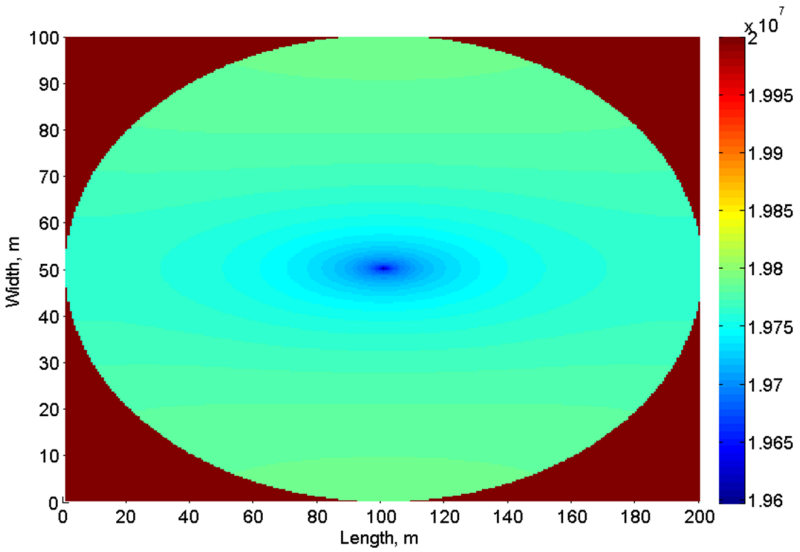

Figure 6.19: Pressure distribution in an elliptical reservoir

The grid orientation effect is also tested in this research to confirm that it does not affect the results we achieved using a finite difference method. Reservoir simulators using finite difference methods are affected by grid orientation effects (Brand et al., 1991), i.e. fluids tend to flow in the direction of the grid axes rather than diagonal to them. To verify the previous results, the elliptic reservoir is rotated by $\pi/4$ from the original one. The shape factor calculation process is repeated again for the rotated elliptical reservoir. An example of pressure distribution for the rotated elliptical reservoir is shown in Figure 6.21. The Dietz shape factor results, using both the original elliptic reservoir and the rotated one are plotted in Figure 6.22, which indicates the grid orientation effect is insignificant. The details of programming and the code are given in Appendix B.

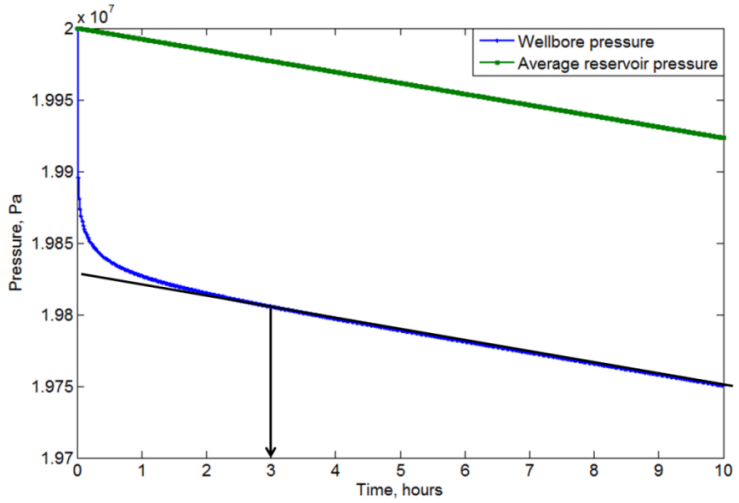

Figure 6.20: Wellbore and average reservoir pressure profiles

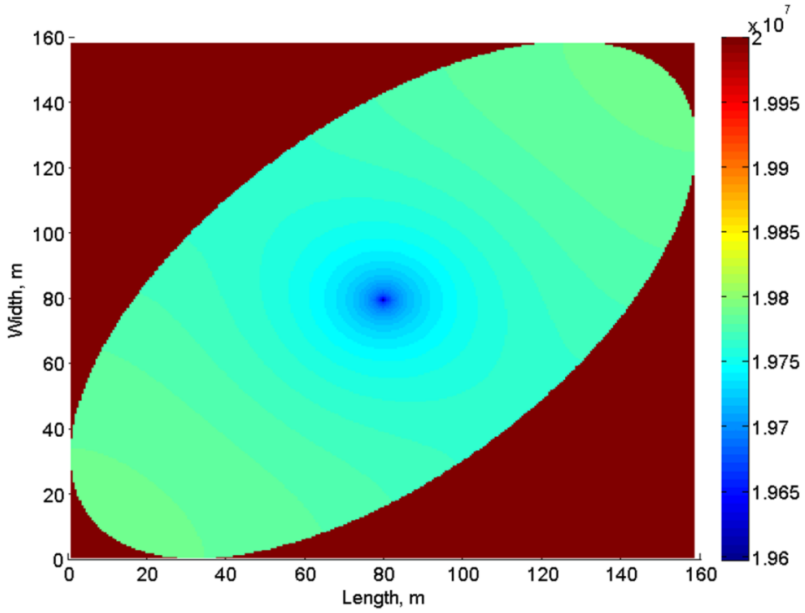

Figure 6.21: Pressure distribution in a rotated elliptic reservoir

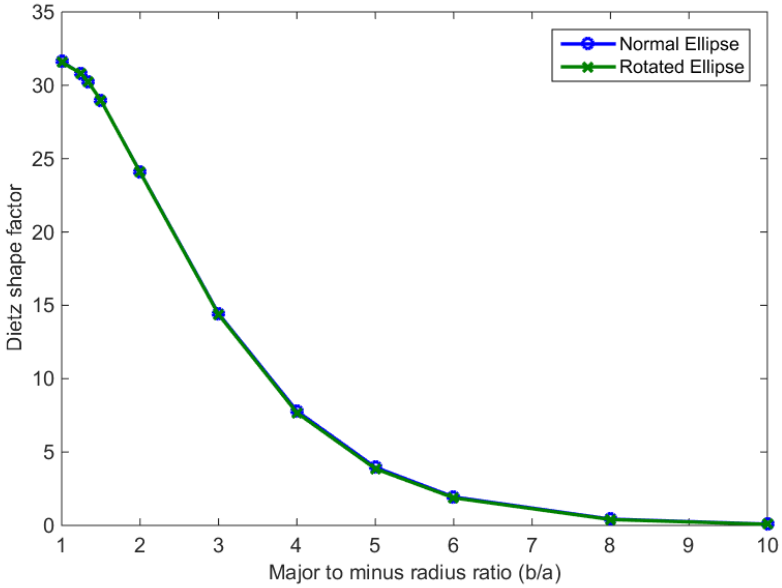

Figure 6.22: Dietz shape factor for ellipses with different major to minor radius ratio

Table 6.2: Basic parameters in ellipse reservoir simulator

Parameter	Unit	Value
Reservoir permeability, K	D	1.0
Major radius of the ellipse, a	m	300
Reservoir thickness, h	m	1.0
Grid number in x direction, N_x		301
Grid number in y direction, N_y		301
Porosity, ϕ		0.2
Viscosity, μ	cP	1.0
Total compressibility, c_t	Pa^{-1}	$2.75 \cdot 10^{-8}$
Initial pressure, p_{init}	Bar	20
Well productivity, Q_T	m^3/day	16

References

- Aziz, K., and Settari, A., Petroleum Reservoir Simulation. Vol. 476., Applied Science Publishers, London (1979)
- Babu, D.K., Odeh, A., Productivity of a Horizontal Well. *SPE Reservoir Engineering*, 4(4), 417-421 (1989)
- Besson, J., Aquitaine, E., Performance of Slanted and Horizontal Wells on an Anisotropic Medium. SPE 20965 presented at European Petroleum Conference, The Hague, Netherlands, October 21-24 (1990)
- Borisov, J.P., Oil production Using Horizontal and Multiple Deviation Wells, Nedra, Moscow, 1964. Translated into English by Strauss J, Edited by Joshi S D. Philips (1984)
- Brand, C.W., Heinemann, J. E., Aziz, K., The Grid Orientation Effect in Reservoir Simulation. SPE Symposium on Reservoir Simulation, Anaheim, California, February 17-20 (1991)
- Brekke, K., Johansen, T.E. and Olufsen, R., A New Modular Approach to Comprehensive Simulation of Horizontal Wells. In SPE Annual Technical Conference and Exhibition, Society of Petroleum Engineers, January (1993)
- Cao, J., James, L.A., and Johansen, T.E., A New Coupled Axial-Radial Productivity Model with Application to High Order Numerical Well Modeling. Presented at SPE Reservoir Characterisation and Simulation Conference and Exhibition, Abu Dhabi, UAE, September (2015)
- Cinco-Ley, H., Ramey, H.J. and Miller, F.G., Pseudo-Skin Factors for Partially-Penetrating Directionally Drilled Wells, paper SPE 5589, Presented at 50th Annual Fall Meeting, Dallas, September 28 - October 1 (1975)
- Dietz, D.N., Determination of Average Reservoir Pressure from Build-up Surveys. *Journal of Petroleum Technology*, 17(8), 955-959 (1965)
- Dikken, B., Pressure Drop in Horizontal Wells and Its Effect on Production Performance. *Journal of Petroleum Technology*, 42(11): 1426-1433 (1990)
- Economides, M., Deimbachor, F.X., Brand, C.W. and Heinemann, Z.E., Comprehensive-Simulation of Horizontal-Well Performance. *SPE Formation Evaluation*, 6(04), pp.418-426 (1991)

- Fanchi, J.R., Directional Permeability. *SPE Reservoir Evaluation and Engineering*, 11(3), 565 (2008)

- Giger, F.M., Reiss, L.H. and Jourdan, A.P., The Reservoir Engineering Aspect of Horizontal Drilling, SP 13024 presented at the SPE 59th Annual Technical Conference and Exhibition, Houston, Texas, Sept. 16-19 (1984)

- Gupta, A., Penuela, G., and Avila, R., An Integrated Approach to the Determination of Permeability Tensors for Naturally Fractured Reservoirs. *Journal of Canadian Petroleum Technology*, 40(12) (2001)

- Guyaguler, B., Zapata, V.J., Cao, H., Stamati, H.F. and Holmes, J.A., Near-Well-Subdomain Simulations for Accurate Inflow-Performance-Relationship Calculation to Improve Stability of Reservoir/Network Coupling, SPE Canadian Unconventional Resources and International Petroleum Conference, Calgary, Alberta, Canada. 19-21 October (2010)

- Haaland, S. E., Simple and Explicit Formulas for the Friction Factor in Turbulent Pipe Flow. *J. Fluids Eng.*, 105(1), 89-90 (1983)

- Holmes, J.A., Barkve, T., and Lund, O., Application of a Multisegment Well Model to Simulate Flow in Advanced Wells. Paper SPE 50646 presented at the European Petroleum Conference, 20-22 October, The Hague, Netherlands (1998)

- Johansen, T.E. and Khoriakov, V., Iterative Techniques in Modeling of Multi-phase Flow in Advanced Wells and the Near Well Region. *Journal of Petroleum Science and Engineering*, 58(1): 49-67 (2007)

- Johansen, T.E., James, L.A. and Cao, J., Analytical Coupled Axial-radial Productivity Model for Steady-State Flow in Horizontal Wells. *International Journal of Petroleum Engineering*, 1(4), 290-307. (2015)

- Johansen, T.E., Cao, J. and James, L.A., Coupled Axial and Radial Semi-Steady State Productivity Model for Horizontal Wells. Accepted by *International Journal of Petroleum Engineering* (2016a)

- Johansen, T.E., Hender, D.G. and James, L.A., Inflow Modeling for Arbitrary Well Trajectory in Laterally Isotropic, Spatially Anisotropic Porous Media, Accepted for publication in *SPE Journal* (2016b)

- Joshi, S.D., Augmentation of Well Productivity with Slant and Horizontal Wells (includes associated papers 24547 and 25308). *Journal of Petroleum Technology*, 40.06: 729-739 (1988)

- Kuchuk, F. and Brigham, W.E., Transient Flow in Elliptical Systems. *SPE Journal*, 19(06), 401-410 (1979)

- Matthews, C.S., Brons, F., and Hazebroek, P., A Method for Determination of Average Pressure in a Bounded Reservoir. *Trans., AIME*, 201, 182-191 (1954)

- Novy, R.A., Pressure Drop in Horizontal Wells: When Can They be Ignored?. *SPE Reservoir Engineering*, 10(01), 29-35 (1996)

- Penmatcha, V., Aziz, K., Comprehensive Reservoir/wellbore Model for Horizontal Wells. *SPE Journal*, 4(3): 224-234 (1999)

- Peaceman, D.W., Interpretation of Well-block Pressures in Numerical Reservoir Simulation with Nonsquare Grid Blocks and Anisotropic Permeability. *SPE Journal*, 23.03: 531-543 (1983)

- Peaceman, D.W., Recalculation of Dietz Shape Factor for Rectangles. Unsolicited Paper SPE, 21256 (1990)

- Pedrosa Jr, O.A., and Aziz, K., Use of a Hybrid Grid in Reservoir Simulation. *SPE Reservoir Engineering*, 1(06): 611-621 (1986)

- Skinner, J.H., and Johansen, T.E., Near Wellbore Streamline Modeling: Its Novelty, Application, and Potential Use. In SPE International Symposium and Exhibition on Formation Damage Control, 15-17 February, Lafayette, Louisiana, USA (2012)

- Wolfsteiner, C. and Durlofsky, L.J., Near-Well Radial Upscaling for the Accurate Modeling of Nonconventional Wells. SPE Western Regional/AAPG Pacific Section Joint Meeting, Anchorage, Alaska, 20-22 May (2002)

Chapter 7

Conclusions

7.1 Summary

The major contribution of this dissertation is the application of the coupled axial-radial productivity models to horizontal wells and near-well simulation. The coupled axial-radial models are analytical solutions to pressure and flow rate distribution considering pressure gradients along and normal to the well trajectory, both for steady state flow and semi-steady state flow. It is applied on individual segments of the well and near-well reservoir that are numerically coupled.

For long, high productivity wells, frictional pressure loss in the wellbore cannot, in general, be ignored. The axial flow along the well trajectory in the near well region must also be considered. The fully analytical productivity model for coupled radial well inflow and axial reservoir flow has been applied. For steady state flow, the coupled model results in a linear pressure distribution in the axial direction and a logarithmic distribution in the radial direction. For the semi-steady state flow, the coupled axial-radial flow model results in a quadratic pressure profile in the axial direction and a quadratic-logarithmic pressure profile in the radial direction.

The coupled axial-radial productivity models are implemented in the formulation of a numerical scheme for simulation of coupled well inflow and near well reservoir flow. The well/near-well model applies the analytical pressure distribution in the axial direction and in the radial direction in each near-well reservoir segment. Therefore, the pressure distribution is piecewise linear/logarithmic in steady state flow, and piecewise quadratic for semi-steady state flow, contrary to existing piecewise constant distribution resulting from a standard finite difference method. The calculation examples are presented applying the new model and standard finite difference method to determine the pressure profiles in both the wellbore and the near-well reservoir. Numerical results show that the new method represents an improvement compared to the standard finite difference method, requiring fewer grid blocks to achieve the same accuracy. This numerical scheme is also proven to be higher order accurate in space discretization than a standard finite difference scheme. Since the radial pressure is built into the new model analytically, this reduces the need for local grid refinements around horizontal well.

The new well/near-well model is applied in heterogeneous reservoirs with various permeability distributions. The results demonstrate that the new model is capable of dealing with large permeability contrasts in near-well reservoir. By solving flow directions as unknowns, the model can determine cross flow between wellbore and near-well reservoir, in the cases where reservoir compartments are poorly communicating. It also can be coupled with standard finite difference reservoir simulators such that the remote reservoir parts in addition to the well completion effects are taken into consideration. An iterative coupling scheme is presented. An application on this coupling considering unevenly distributed skin factors also demonstrates the capability of the new well/near-well model.

The methodology to apply the coupled axail-radial productivity model in anisotropic reservoir is also developed. The analytical solution to the coupled axial and radial flow in semi-steady state flow is generated using average reservoir pressure. This solution brings flexibility in choosing the configuration of reservoir grids, and only requires the Dietz shape

factor of the grid configuration. It is also consistent with the classical semi-steady state well inflow equations using average reservoir pressure. The model results in flow equations in both the radial and axial directions. In order to apply this in an anisotropic reservoir, the directional permeability in the wellbore cross section perpendicular to the well trajectory and along the well trajectory, for well inflow and axial reservoir flow respectively, must be determined. In previous work, a transformation method was applied to convert the anisotropic reservoir to an equivalent virtual isotropic media in the cross sectional plane. This transformation preserves the volume and the average pressure, however transforms the circular near-well cylinder into an elliptical cylinder. This requires the Dietz shape factor of the ellipse, which is determined numerically. A numerical model considering axial-radial flow in the near-well region, the formation anisotropy and wellbore hydraulics has therefore been achieved. This produced a high accuracy simulation of the horizontal well and near-well region. Numerical results demonstrate that a larger permeability anisotropy ratio results in a larger radial reservoir pressure drop whereas the axial pressure drop in the near-well reservoir and in the wellbore is dominated by well productivity.

In summary, this research represents a new numerical well/near-well model and associated simulation technique. This well/near-well model applies the analytical coupled axial-radial productivity models for both steady state and semi-steady state flow, incorporates wellbore hydraulics and near-well heterogeneity and anisotropy. It was demonstrated to achieve high accuracy, potentially reduce local grid refinements in near-well region, determine both wellbore and near-well reservoir flow performance, and can be easily coupled with current reservoir simulators.

7.2 Further Work

The coupled axial-radial productivity model has been developed and applied in simulation of horizontal wells and the near-well region. Further research work is recommended in the

following aspects:

1. Multi phase flow

   The well/near-well model in this thesis mainly focuses on single phase flow. Multi phase flow can be incorporated in future works. In the reservoir, multi phase flow is basically represented using relative permeability of each phase. In the wellbore and the annulus, correlations of frictional pressure loss are needed. Furthermore, Drift Flux models should be included for phase slippage.

2. Well completion methods

   The well/near-well model can be modified for various well completions, for example wells with slotted liners, cemented and partial perforated wells, inflow control devices and multi-lateral wells. The near-well/well model has three basic rings for near-well reservoir, annulus or damaged reservoir and liner or production tubing. The middle ring can represent the annulus when the well is completed with a liner and when the well is partially completed; and can represent the damage zone region when considering formation damage effects. Inflow control devices can be added in the middle ring given the pressure loss correlation through the devices.

3. Thermal model

   The well/near-well model can be augmented with thermal dynamic models, solving for both pressure and temperature in the near-well region. This is applicable to cases with precipitation of scale, asphaltenes and wax, when the fluid properties are sensitive to the temperature.

Bibliography

[1] Archer, R.A., and Agbongiator, E.O., 2005. Correcting for Frictional Pressure Drop in Horizontal-Well Inflow-Performance Relationships, *SPE Production & Facilities*, doi:10.2118/80528-PA.

[2] Aziz, K., and Settari, A., 1979. Petroleum Reservoir Simulation. Vol. 476. London: Applied Science Publishers.

[3] Aziz, K., 1993. Reservoir Simulation Grids: Opportunities and Problems. *Journal of Petroleum Technology*, 45(07).

[4] Aziz, K., 2001. A General Single-Phase Wellbore/Reservoir Coupling Model for Multilateral Wells, *SPE Reservoir Evaluation & Engineering*, 4(4): 327-335.

[5] Babu, D.K. and Odeh, A., 1989. Productivity of a Horizontal Well. *SPE Reservoir Engineering*, 4(4), 417-421.

[6] Beggs, D.H., and Brill, J.P., 1973. A Study of Two-Phase Flow in Inclined Pipes. *Journal of Petroleum technology*, 25(05), 607-617.

[7] Besson, J. and Aquitaine, E., 1990. Performance of Slanted and Horizontal Wells on an Anisotropic Medium. SPE 20965 presented at European Petroleum Conference, 21-24 October, The Hague, Netherlands.

[8] Brand, C.W., Heinemann, J.E. and Aziz, K., 1991. The Grid Orientation Effect in Reservoir Simulation. SPE Symposium on Reservoir Simulation.

[9] Brekke, K., Johansen, T. E. and Olufsen, R., 1993. A New Modular Approach to Comprehensive Simulation of Horizontal Wells. Paper SPE 26518 presented at SPE Annual Technical Conference and Exhibition, 3-6 October, Houston, Texas.

[10] Brekke, K. and Thompson, L.G., 1996. Horizontal Well Productivity and Risk Assessment. SPE 36578 presented at Annual Technical Conference and Exhibition, 6-9 October, Denver, Colorado.

[11] Brill, J.P. and Mukherjee, H.K., 1999. Multiphase flow in wells (Vol. 17). Society of Petroleum Engineers.

[12] Cao, J., James, L.A., and Johansen, T.E., 2015. A New Coupled Axial-Radial Productivity Model with Application to High Order Numerical Well Modeling. Presented at SPE Reservoir Characterisation and Simulation Conference and Exhibition, Abu Dhabi, UAE, September.

[13] Cao, J., James, L.A., and Johansen, T.E., 2016. Modelling Near-well Flow Performance for Horizontal Wells in Anisotropic Media, 15th European Conference on the Mathematics of Oil Recovery (ECMOR XV), 29 August - 1 September, Amsterdam, Netherlands.

[14] Chen, Z., and Hou, T., 2003. A Mixed Multiscale Finite Element Method for Elliptic Problems with Oscillating Coefficients. *Mathematics of Computation*,72(242), 541-576.

[15] Cinco-Ley, H., Ramey, H.J. and Miller, F.G., 1975. Pseudo-Skin Factors for Partially-Penetrating Directionally Drilled Wells. paper SPE 5589, presented at 50th Annual Fall Meeting, Dallas, September 28 – October 1.

[16] Civan, F., 1996. Interactions of the Horizontal Wellbore Hydraulics and Formation Damage. In Permian Basin Oil and Gas Recovery Conference, January.

[17] Civan, F., 2011. Reservoir Formation Damage. Second edition. Gulf Professional Publishing.

[18] Crane Co., 1988. Flow of Fluids through Valves, Fittings, and Pipes, Technical Paper No. 410, Chicago.

[19] Dietz, D.N., 1965. Determination of Average Reservoir Pressure from Build-up Surveys. *Journal of Petroleum Technology*, 17(8), 955-959.

[20] Dikken, B., 1990. Pressure Drop in Horizontal Wells and Its Effect on Production Performance. *Journal of Petroleum Technology*, 42(11): 1426-1433.

[21] Ding, Y., Longeron, D., Renard, G., and Audibert, A., 2004. Modeling of both Near-Wellbore Damage and Natural Cleanup of Horizontal Wells Drilled with Water-Based Drilling Fluids. *SPE Journal*, 9(03), 252-264.

[22] Economides, M.J., Brand, C. W. and Frick, T.P., 1996. Well Configurations in Anisotropic Reservoirs. *SPE Formation Evaluation* 11: 257-262.

[23] Economides, M.J., Hill, A.D., Ehlig-Economides, C. 1994. Petroleum Production Systems. New Jersey: Prentice Hall.

[24] Energy Information Administration U.S., 2016. Trends in U.S. Oil and Natural Gas Upstream Costs, `https://www.eia.gov/analysis/studies/drilling/`.

[25] Fanchi, J.R., 2008. Directional Permeability. *SPE Reservoir Evaluation and Engineering*, 11(3), 565.

[26] Francis, P., 1997. Dominating Effects Controlling the Extent of Drilling-Induced Formation Damage. In SPE European Formation Damage Conference, January.

[27] Frick, T.P., and Economides, M.J., 1993. Horizontal Well Damage Characterization and Removal. *SPE Production & Facilities*, 8(01), 15-22.

[28] Furui, K., Zhu, D. and Hill, A.D., 2002a. A New Skin Factor Model for Perforated Horizontal Wells. In SPE Annual Technical Conference and Exhibition, 29 September-2 October, San Antonio, Texas.

[29] Furui, K., Zhu, D. and Hill, A.D., 2002b. A Rigorous Formation Damage Skin Factor and Reservoir Inflow Model for a Horizontal Well, the SPE International Symposium and Exhibition on Formation Damage Control held in Lafayette, Louisiana, 20-21 February.

[30] Furui, K., Zhu, D., and Hill, A.D., 2004a, A New Skin Factor Model for Gravel-Packed Completions, the SPE Annual Technical Conference and Exhibition held in Houston, Texas, 26-29 September.

[31] Furui, K., Zhu, D., and Hill, A.D., 2004b. A Comprehensive Model of Horizontal Well Completion Performance. SPE Annual Technical Conference and Exhibition held in Denver, Colorado, 5-8 October.

[32] Giger, F.M., Reiss, L. H., and Jourdan, A.P., 1984. The Reservoir Engineering Aspects of Horizontal Drilling, SPE 13024 presented at 59th Annual Technical Conference and Exhibition of the Society of Petroleum Engineering, Houston, TX, 16-19 September.

[33] Gupta, A., Penuela, G. and Avila, R., 2001. An Integrated Approach to the Determination of Permeability Tensor for Naturally Fractured Reservoirs. *Journal of Canadian Petroleum Technology*, 40(12).

[34] Haaland, S.E., 1983. Simple and Explicit Formulas for the Friction Factor in Turbulent Pipe Flow. *Journal of Fluids Engineering* 105(1), 89-90.

[35] Hagedorn, A.R., and Brown, K.E., 1965. Experimental Study of Pressure Gradients Occurring During Continuous Two-phase Flow in Small-diameter Vertical Conduits. *Journal of Petroleum Technology*, 17(04), 475-484.

[36] Hawkins Jr, M.F., 1956. A Note on the Skin Effect. *Journal of Petroleum Technology*, 8(12), 65-66.

[37] Holmes, J.A., Barkve, T., and Lund, O., 1998. Application of a Multisegment Well Model to Simulate Flow in Advanced Wells. Paper SPE 50646 presented at the European Petroleum Conference, 20-22 October, The Hague, Netherlands.

[38] Holmes, J.A. 2001. Modeling Advanced Wells in Reservoir Simulation. *Journal of Petroleum Technology* 53.11: 54-66.

[39] Hwang, M.K., and Odeh, A.S., 1995. Estimation of Condensate Dropout Effects on Well Productivity as Skin Change with Multiplicative Interactions among Skin Components. In Middle East Oil Show. Society of Petroleum Engineers.

[40] Hwang, M.K., 2000. Modeling Nonlinear Interactions Among Near-well Flow Restrictions in Well-Deliverability Prediction and Simulation. *SPE Reservoir Evaluation & Engineering*, 3(04), 360-368.

[41] Jenny, P., Lee, S.H., and H. A. Tchelepi, 2003. Multi-Scale Finite-Volume Method for Elliptic Problems in Subsurface Flow Simulation. *Journal of Computational Physics* 187.1: 47-67.

[42] Johansen, T.E. and Khoriakov, V., 2007. Iterative Techniques in Modeling of Multi-phase Flow in Advanced Wells and the Near Well Region. *Journal of Petroleum Science and Engineering*, 58(1): 49-67.

[43] Johansen, T.E., 2012a, A Generalization of the Steady State Inflow Model Incorporating Axial Flow, `www.petreng-thormod.ca` .

[44] Johansen, T.E., 2012b, A Generalization of the Semi-Steady State Well Inflow Model Incorporating Axial Flow, `www.petreng-thormod.ca` .

[45] Johansen, T.E., 2013, Inflow Modeling for Wells with Arbitrary Trajectories in Anisotropic Media, `www.petreng-thormod.ca`.

[46] Johansen, T.E., James, L.A., and Cao, J., 2015. Analytical Coupled Axial and Radial Productivity Model for Steady-State Flow in Horizontal Wells, *Internation Journal of Petroleum Engineering*, Vol.1, No.4, pp.290 - 307.

[47] Johansen, T.E., Cao, J., and James, L.A., 2016a. Analytical Coupled Axial-Radial Semi-Steady State Productivity Model for Horizontal Wells in Anisotropic Medium. Accepted by *Internation Journal of Petroleum Engineering.*

[48] Johansen, T.E., Hender, D.G. and James, L.A., 2016b. Inflow Modeling for Arbitrary Well Trajectory in Laterally Isotropic, Spatially Anisotropic Porous Media, Accepted by *SPE Journal.*

[49] Joshi, S.D., 1988. Augmentation of Well Productivity with Slant and Horizontal Wells (includes associated papers 24547 and 25308). *Journal of Petroleum Technology* 40.06: 729-739.

[50] Joshi, S.D., 2003. Cost/benefits of horizontal wells. SPE Western Regional/AAPG Pacific Section Joint Meeting. Society of Petroleum Engineers.

[51] Kabir, A. and Sanchez, G., 2009. Accurate Inflow Profile Prediction of Horizontal Wells Through Coupling a Reservoir and a Wellbore Simulator. SPE Reservoir Simulation Symposium. The Woodlands, Texas, USA, 2-4 February.

[52] Karakas, M., and Tariq, S.M., 1991. Semianalytical Productivity Models for Perforated Completions. *SPE Production Engineering*, 6(01), 73-82.

[53] Karimi-Fard, M., and Durlofsky, L., 2012. Accurate resolution of near-well effects in upscaled models using flow-based unstructured local grid refinement. *SPE Journal* 17.04 :1-084.

[54] Khoriakov, V., Johansen, A.C., Johansen, T.E. 2012. Transient Flow Modeling of Advanced Wells. *Journal of Petroleum Science and Engineering*, 86, 99-110.

[55] Krogstad S. and Durlofsky L.J., 2007. Multiscale Mixed-Finite-Element Modeling of Coupled Wellbore/Near-Well Flow. Paper SPE 106179, presented at the SPE Reservoir Simulation Symposium held in Houston, Texas, U.S.A., 26-28 February.

[56] Krogstad, S., and Durlofsky, L.J., 2009. Multiscale Mixed-finite-element Modeling of Coupled Wellbore/near-well Flow. *SPE Journal*, 14(01), 78-87.

[57] Kuchuk, F.J., Goode, P.A., Brice, B.W., Sherrard, D.W. and Thambynayagam, R.K.M. 1990. Pressure-transient Analysis for Horizontal Wells. *Journal of Petroleum Technology* 42.8: 1028-1031.

[58] Kurtoglu, B., Medeiros, F., Ozkan, E., and Kazemi, H., 2008. Semianalytical Representation of Wells and Near Well Flow Convergence in Numerical Reservoir Simulation. In SPE Annual Technical Conference and Exhibition.

[59] Lake, L.W., 1988. The Origins of Anisotropy (includes associated papers 18394 and 18458). *Journal of Petroleum Technology*, 40(04), 395-396.

[60] Longeron, D.G., Alfenore, J., Salehi, N., and Saintpere, S., 2000. Experimental approach to characterize drilling mud invasion, formation damage and cleanup efficiency in horizontal wells with openhole completions. SPE International Symposium on Formation Damage Control, January.

[61] Lohne, A., Han, L., Van Der Zwaag, C., van Velzen, H., Mathisen, A.M., Twyman, A., and Hatzignatiou, D.G., 2010. Formation damage and well productivity simulation. *SPE Journal*, 15(03), 751-769.

[62] Matthews, C.S., Brons, F., and Hazebroek, P., 1954. A Method for Determination of Average Pressure in a Bounded Reservoir. *Trans., AIME*, 201, 182-191

[63] Muskat, M., 1938. The Flow of Homogeneous Fluids Through Porous Media. Soil Science, 46(2), p.169.

[64] Novy, R.A., 1996. Pressure Drop in Horizontal Wells: When Can They be Ignored?. *SPERE 29; Trans., AIME*, 299

[65] Ouyang, L.B., Arbabi, S., and Aziz, K., 1998. A Single-Phase Wellbore Flow Model for Horizontal, Vertical, and Slanted Wells, *SPE Journal* , 124.

[66] Ozkan, E., and Raghavan, R., 1997. Estimation of Formation Damage in Horizontal Wells. In SPE Production Operations Symposium, January.

[67] Palagi, C.L. and Aziz, K., 1994. Use of Voronoi Grid in Reservoir Simulation. *SPE Advanced Technology Series*, 2(02), 69-77.

[68] Peaceman, D.W. 1978. Interpretation of Well-Block Pressure in Numerical Reservoir Simulation, *SPE Journal* 18.03: 183-194.

[69] Peaceman, D.W., 1983. Interpretation of Well-Block Pressures in Numerical Reservoir Simulation with Nonsquare Grid Blocks and Anisotropic Permeability. *SPE Journal* 23.03: 531-543.

[70] Peaceman, D.W., 1990. Recalculation of Dietz Shape Factor for Rectangles. Unsolicited Paper SPE, 21256.

[71] Pedrosa Jr, O.A., and Aziz, K., 1986. Use of a Hybrid Grid in Reservoir Simulation. *SPE Reservoir Engineering* . 1.06: 611-621.

[72] Penmatcha, V., Aziz, K., 1999. Comprehensive Reservoir/Wellbore Model for Horizontal Wells. *SPE Journal* 4(3): 224-234.

[73] Pucknell, J.K., and P.J. Clifford., 1991. Calculation of Total Skin Factors. SPE Offshore Europe Conference and Exhibition held in Aberdeen, 3-6 September.

[74] Rosenberg, D.U., 1982. Local Mesh Refinement for Finite Difference Methods. paper SPE 10974 presented at the SPE Annual Technical Conference and Exhibition, New Orleans, Sept. 26-29

[75] Schlumberger, Eclipse Reference Manual (2010), `www.slb.com/eclipse.`

[76] Semmelbeck, M.E., Dewan, J. T., and Holditch, S.A., 1995. Invasion-Based Method for Estimating Permeability from Logs. In SPE Annual Technical Conference and Exhibition, January.

[77] Schulkes, R.M. and King, A.C., 2002. Boundary-Layer Behaviour in a Hydraulic Theory of Horizontal Oil Wells. *Journal of engineering mathematics*, 42(1), pp.23-44.

[78] Schulkes, R.M., Rinde, T. and Utvik, O.H., 1999. Pipe Flow with Radial Inflow: Experimental and Modeling Work. *Journal of fluids engineering*, 121(1), pp.106-111.

[79] Schulkes, R.M. and Utvik, O.H., 1998. Pressure Drop in a Perforated Pipe with Radial Inflow: Single-Phase Flow. *SPE Journal*, 3(01), 77-85.

[80] Skinner, J.H., and Johansen, T.E., 2012. Near Wellbore Streamline Modeling: Its Novelty, Application, and Potential Use. In SPE International Symposium and Exhibition on Formation Damage Control, 15-17 February, Lafayette, Louisiana, USA.

[81] Su, Z., and Gudmundsson, J.S., 1994. Pressure Drop in Perforated Pipes: Experiments and Analysis. In SPE Asia Pacific Oil and Gas Conference. Society of Petroleum Engineers.

[82] Suryanarayana, P.V., Wu, Z., Ramalho, J. and Himes, R.E., 2007. Dynamic Modeling of Invasion Damage and Impact on Production in Horizontal Wells. *SPE Reservoir Evaluation & Engineering*, 10(04), pp.348-358.

[83] Tabatabaei, M., and Ghalambor, A., 2011. A New Method to Predict Performance of Horizontal and Multilateral Wells. *SPE Production & Facilities*. doi:10.2118/141164-PA.

[84] Vicente, R., Sarica, C., and Ertekin, T., 2002. A Numerical Model Coupling Reservoir and Horizontal Well-flow Dynamics: Transient Behavior of Single-phase Liquid and Gas Flow. *SPE Journal*, 7(01), 70-77.

[85] Voronoï, G., 1908. Nouvelles applications des paramètres continus à la théorie des formes quadratiques. Deuxième mémoire. Recherches sur les paralléllοèdres primitifs. *Journal für die reine und angewandte Mathematik*,134, 198-287.

[86] Wolfsteiner, C., Lee, S. H. and Tchelepi, H. A., 2006. Well Modeling in the Multiscale Finite Volume Method for Subsurface Flow Simulation. *Multiscale Modeling & Simulation*, 5(3), 900-917.

[87] Wolfsteiner, C. and Durlofsky, L.J., 2002. Near-well Radial Upscaling for the Accurate Modeling of Nonconventional Wells. In SPE Western Regional/AAPG Pacific Section Joint Meeting. Society of Petroleum Engineers.

[88] Zain, Z.M., Suri, A., and Sharma, M.M., 2000. Mechanisms of Mud Cake Removal During Flowback. In SPE International Symposium on Formation Damage Control, February.

Appendixes

Appendix A

The horizontal well and near-well simulator is coded using MATLAB. It implements coupled axial-radial productivity model for steady state flow and semi-steady state flow in the near-well region and considers friction pressure loss in the wellbore. The numerical schematic of the horizontal well and near-well region simulator is discussed in Chapter 3 and Chapter 5, for steady state and semi-steady state flow respectively.

The code using the numerical schematic developed in this research for steady state flow and semi-steady state flow together with the Newton's method solver is given below. The code A-1 is the steady state CARP Well Model. In this code, basic parameters and pre-calculated coefficients are given in the beginning, as well as the initial guess of the pressure distribution. The initial guess of solution may change from case to case and bad choice of initial guess would result in errors or non-converged results. In the main body, the first part defines the system of nonlinear equations for the momentum balance euqations in the wellbore and continuity equations in the near-well region. The second part generates the Jacobian function of the nonlinear system analytically. The Jacobian matrix is defined as a sparse matrix, which reduced computation time in solve the nonlinear equations. Finally, the pressure is updated given the Newton Raphson method until the convergence criteria is satisfied.

In the second code A-2, the CARP Well Model is given in a similar structure with A-1. The main difference is that the well productivity Q_t is given as a constant. The axial and radial flow rate equations are different, as illustrated in Chapter 5. The nonlinear system of equations and the jacobian matrix are described in part 1 and 2, respectively.

In the third code A-3, the Reservoir Model is presented using Eclipse 100. This code only represent one time step. The wellbore pressure is given from the Well model in each iteration step until the coupling scheme converges. The pressure and saturation values will be saved and used for the next time step.

In the forth code A-4, the simple Friction Model is given in Matlab. This code is used for coupling the reservoir model with the a simple well model considering frictional pressure loss only, for comparison reasons.

- *Code A-1: CARP Well Model for steady state flow*

```
%%%%%%%%%%%%%%%%%%%%Horizontal well model_Linear Pressure Drop%%%%%%%%%%%%%%%%%%
clear all
% Schematic
% flow type: frictional qf; radial qr; axial qx
% segments:              two * Nseg
% unknowns:     Pressure    2*Nseg+1
%               total       2*Nseg+1
% equations:    mat.bal.    2*Nseg
%                B.C        1
%               total       2*Nseg+1
% (flowrate is represented by rpessure)
%
%  B.C     o——o————...o——o——o——o Pres=const
%          |    |        |    |    |    |
%          o——o————...o——o——o——o  P(Nseg+1)                    row3
%  Res.    |    |        |    |    |    |
%          o——o————...o——o——o——o P(1)(equal to first row)  row2
% H.well   |    |        |    |    |    |
%          o——o————...o——o——o——o                            row1
%        Pbh   P(Nseg)             P(2)  P(1)


%=========================================================================%
% Basic parameters
% Ny: number of segments, Nx: number of rows
Nx=200;Ny=2;N=Ny*Nx;
% Reservoir and wellbore dimension
% Wellbore radius, m
rw=0.1;
% External reservoir radius, m
re=20;
```

```
% Segment length, m
dx=5;
% Formation and fluid properties
ke    = 50;             % unit: mD, permeability
rou = 800;              % unit: kg/m3, density
miu = 0.001;            % unit: pa*s, viscosity
bo   = 1.3;             % Oil formation volume factor
itte= 0;                % Iteration number
er   = 10;              % Initial relative error value > tolerance

%Formation damage model (Furui et al., 2002)
Lw=Nx*dx*3.281; %well length in inch
Iani=1; kkd=5; rdhm=4; % unit inch
rdh=(3.281*rw-rdhm)/Nx/dx*(1000:-dx:dx)+rdhm;   % unit inch
%sx=(kkd-1)*log(1/(1+Iani)*(rdh/0.3281+sqrt((rdh/0.3281).^2+Iani^2-1)));
sx=zeros(1,Nx);
k=ke*ones(1,Nx);
k(1:Nx/2)=1000;k(Nx/2+1:Nx)=5;
% Below listed a few other permeability distributions
% k=50:-45/200:5+45/200;
% k=10:90/200:100-90/200;
% k=(180)*rand(1,200)+20;

%Pre-calculated parameters: Transimisibility
%Pressure is always multiplied with transimisibility, Tf Tr Tx
%pressure: bar; flow rate: m^3/day
Tf=1.4006*10^8*(2*rw)^(19/7)/(miu^(1/7)*rou^(3/7)*dx^(4/7));
Tr=0.008527*2*pi*k*dx./(bo*miu*(log((re/rw)^0.5)+sx));
Tx1=0.000864*pi*k*(re^2*log(re/rw)+0.5*rw^2-0.5*re^2)/(bo*miu*dx*log(re/rw));
Tx2=0.000864*pi*k*(re^2-rw^2)/(bo*miu*dx);

%Boundaries conditions
```

```
Pres=320;                %unit: bar
Pbh =300;                %unit: bar
%Pres=[320:-10/Nx:310];
Pres=Pres*ones(1,Nx+1);

% Initial values- pressure and flowrate

%P=(300.5:-.05/Nx:300.4);
P=(300.3:-.05/Nx:300.2);
%=========================================================================%
  while er>1e-9

 itte=itte+1;

%%%%%%%%%%%%%%%%%%%%%%%%% PART_1 %%%%%%%%%%%%%%%%%%%%%%%%%%%%%%%%%%%%%%%%%%%%
% Momentum balance euqation: f=flow_out-flow_in=0
f=zeros(1,2*Nx+1);
%in the first row(nodes inside horizontal well)
f(1)             =Tf*abs(P(1)-P(2))^(4/7)-Tr(1)*(P(Nx+1)+P(Nx+2)-P(1)-P(2));
for i=2:Nx-1
f(i)             =Tf*abs(P(i)-P(i+1))^(4/7)...
                 -Tf*abs(P(i-1)-P(i))^(4/7)...
                 -Tr(i)*(P(i+Nx)+P(i+Nx+1)-P(i)-P(i+1));
end
f(Nx)            =Tf*abs(P(Nx)-Pbh)^(4/7)...
                 -Tf*abs(P(Nx-1)-P(Nx))^(4/7)...
                 -Tr(Nx)*(P(2*Nx)+P(2*Nx+1)-P(Nx)-Pbh);
%in the second row(nodes in the near reservoir)
f(Nx+1)          =Tr(1)*(P(Nx+1)+P(Nx+2)-P(1)-P(2))...
                 +Tx1(1)*(P(Nx+1)-P(Nx+2))+(Tx2(1)-Tx1(1))*(P(2)-P(1))...
                 -Tr(1)*(Pres(1)+Pres(2)-P(Nx+2)-P(Nx+1));
for i=2:Nx-1
```

```
f(Nx+i)          =Tr(i)*(P(Nx+i)+P(Nx+i+1)-P(i)-P(i+1))...
                 +Tx1(i)*(P(Nx+i)-P(Nx+i+1))+(Tx2(i)-Tx1(i))*(P(i+1)-P(i))...
                 -Tr(i)*(Pres(i)+Pres(i+1)-P(Nx+i+1)-P(Nx+i))...
                 -Tx1(i)*(P(Nx+i-1)-P(Nx+i))-(Tx2(i)-Tx1(i))*(P(i)-P(i-1));
end
f(2*Nx)          =Tr(Nx)*(P(2*Nx+1)+P(2*Nx)-P(Nx)-Pbh)...
                 -Tr(Nx)*(Pres(Nx)+Pres(Nx+1)-P(2*Nx+1)-P(2*Nx))...
                 -Tx1(Nx)*(P(2*Nx-1)-P(2*Nx))-(Tx2(Nx)-Tx1(Nx))*(P(Nx)-P(Nx-1));
%boundary conditions for the left end reservoir block: qx=0
f(2*Nx+1)        =Tx1(Nx)*(P(2*Nx)-P(2*Nx+1))+(Tx2(Nx)-Tx1(Nx))*(Pbh-P(Nx));

%%%%%%%%%%%%%%%%%%%%%%%%%%%% PART_2 %%%%%%%%%%%%%%%%%%%%%%%%%%%%%%%%%%%%%%%%%%%%
%Jacobian matrix of material balance function, Jac(f)
Jac=zeros(2*Nx+1,2*Nx+1);

% %Deritive of f in the first row
Jac(1,1)         =Tr(1)+4/7*Tf*sign(P(1)-P(2))*abs(P(1)-P(2))^(-3/7);
Jac(1,2)         =Tr(1)-4/7*Tf*sign(P(1)-P(2))*abs(P(1)-P(2))^(-3/7);
Jac(1,Nx+1)      =-Tr(1);
Jac(1,Nx+2)      =-Tr(1);
for i=2:Nx-1
Jac(i,i-1)       =-4/7*Tf*sign(P(i-1)-P(i))*abs(P(i-1)-P(i))^(-3/7);
Jac(i,i)         =Tr(i)+4/7*Tf*sign(P(i-1)-P(i))*abs(P(i-1)-P(i))^(-3/7)...
                 +4/7*Tf*sign(P(i)-P(i+1))*abs(P(i)-P(i+1))^(-3/7);
Jac(i,i+1)       =Tr(i)-4/7*Tf*sign(P(i)-P(i+1))*abs(P(i)-P(i+1))^(-3/7);
end
Jac(Nx,Nx-1)     =-4/7*Tf*sign(P(Nx-1)-P(Nx))*abs(P(Nx-1)-P(Nx))^(-3/7);
Jac(Nx,Nx)       =Tr(Nx)+4/7*Tf*sign(P(Nx-1)-P(Nx))*abs(P(Nx-1)-P(Nx))^(-3/7)...
                 +4/7*Tf*sign(P(Nx)-Pbh)*abs(P(Nx)-Pbh)^(-3/7);
Jac(1:Nx,Nx+1:2*Nx)=-Tr(Nx)*(diag(ones(1,Nx))+diag(ones(1,Nx-1),1));
Jac(Nx,2*Nx+1)   =-Tr(Nx);
```

```
%%Deritive of f in the second row
Jac(Nx+1,1)          =-Tr(1)+Tx1(1)-Tx2(1);
Jac(Nx+1,2)          =-Tr(1)-Tx1(1)+Tx2(1);
Jac(Nx+1,Nx+1)       =2*Tr(1)+Tx1(1);
Jac(Nx+1,Nx+2)       =2*Tr(1)-Tx1(1);
for i=2:Nx-1
Jac(Nx+i,i-1)        =Tx2(i)-Tx1(i);
Jac(Nx+i,i)          =-2*(Tx2(i)-Tx1(i))-Tr(i);
Jac(Nx+i,i+1)        =Tx2(i)-Tx1(i)-Tr(i);
Jac(Nx+i,Nx+i-1)     =-Tx1(i);
Jac(Nx+i,Nx+i)       =2*Tr(i)+2*Tx1(i);
Jac(Nx+i,Nx+i+1)     =2*Tr(i)-Tx1(i);
end
Jac(2*Nx,Nx-1)       =Tx2(Nx)-Tx1(Nx);
Jac(2*Nx,Nx)         =Tx1(Nx)-Tx2(Nx)-Tr(Nx);
Jac(2*Nx,2*Nx-1)     =-Tx1(Nx);
Jac(2*Nx,2*Nx)       =2*Tr(Nx)+Tx1(Nx);
Jac(2*Nx,2*Nx+1)     =2*Tr(Nx);
%%Deritive of B.C.
Jac(2*Nx+1,Nx)       =Tx1(Nx)-Tx2(Nx);
Jac(2*Nx+1,2*Nx)     =Tx1(Nx);
Jac(2*Nx+1,2*Nx+1)=-Tx1(Nx);

%Jac=Jac+500*max(Tr)*eye(2*Nx+1);
%=========================================================================%


%visulization of pressure in each iteration steps
   plot((Nx:-1:0)*dx,[P(1:Nx) Pbh],...
        (Nx:-1:0)*dx, P(Nx+1:2*Nx+1),...
        (Nx:-1:1)*dx,Pres(1:Nx),'linewidth',1.5)
   title(sprintf('solution after %d steps',itte-1))
```

```
   xlabel('Distance from bottom hole /m')
   ylabel('Pressure /bar')
   axis([0 dx*Nx Pbh max(Pres)])
   pause(.1)
%
% update values
Pnew=P-f/Jac;
Relative_error=abs((f/Jac)./P);
%er=max(f(:));
er=max(Relative_error(:));
P=Pnew;

   end
toc
%=========================================================================%
% Plot the result of pressure distribution
figure
plot((Nx:-1:0)*dx,[P(1:Nx) Pbh],...
     (Nx:-1:0)*dx, P(Nx+1:2*Nx+1),'linewidth',1.5)
 title(sprintf('solution after %d steps',itte-1))
 xlabel('Distance from bottom hole /m')
 ylabel('Pressure /bar')
 axis([0 dx*Nx Pbh Pres])
% Determination of flow rates
qr=Tr*(P(Nx+1:2*Nx)+P(Nx+2:2*Nx+1)-P(1:Nx)-[P(2:Nx) Pbh]);
qf=Tf*abs(P(1:Nx)-[P(2:Nx) Pbh]).^(4/7);
qx=Tx1*(P(Nx+1:2*Nx)-P(Nx+2:2*Nx+1))+(Tx2-Tx1)*([P(2:Nx) Pbh]-P(1:Nx));
```

- *Code A-2: CARP Well Model for semi-steady state flow*

```
clear all
% Grid definition and reservoir/wellbore size
Nx=200;dx=10;Ny=2;N=Nx*Ny;
% Wellbore radius rw and external reservoir radius re, unit: m
rw=0.1;re=10;

% Basic parameters
k   = 1*10^(-12);          %unit: m2, permeability
rho = 800;                 %unit: kg/m3, density
miu = 0.001;               %unit: pa*s, viscosity
er=10; itte=0;             %Relative error and iteration count
Qt=1000/(24*3600);         %unit: m^3/s
qt=Qt/Nx;                  %Net out flow in each segment

%Pre-calculated parameters: Transimisibility
%Pressure is always multiplied with Transimisibility
%Pre-multiply 10^5 to transmisibility factors
%to convert pressures in units of bar
Tf=10^(20/7)*2.8681*(2*rw)^(5/7)*pi*rw^2/((rho)^(3/7)*miu^(1/7)*dx^(4/7));
Tw=10^5*2*pi*k*dx/(miu*(2*log(re/rw)-1));
a1=10^5*pi*k/miu*(re^2/(2*dx*log(re/rw))+dx/(2*log(re/rw)-1)-re^2/dx);
a2=10^5*pi*k/miu*(-re^2/(2*dx*log(re/rw))+dx/(2*log(re/rw)-1)+re^2/dx);
a3=10^5*pi*k/miu*(-re^2/(2*dx*log(re/rw))-dx/(2*log(re/rw)-1));
a4=10^5*pi*k/miu*(re^2/(2*dx*log(re/rw))-dx/(2*log(re/rw)-1));

% Initial guess of pressure
Pinit=(302:-0.01/(2*Nx+2):301.99+0.01/(2*Nx+2));
P=[Pinit(Nx+2:2*Nx+2) Pinit(1:Nx+1)];

%Pressure unit: 10^5 pa (bar)
```

```
%Reservoir pressure
Pres=300;

while er>10^-16*N
    % er: convergence criteria
    % itte: iteration step
  itte=itte+1;

 %%%%%%%%%%%%%%%%%%%%%%%%%%% PART_1 %%%%%%%%%%%%%%%%%%%%
```

```
end

% left boundary, outflow equals zero
f(2*Nx+2)=a2*P(2*Nx+2)+a1*P(2*Nx+1)+a4*P(Nx+1)+a3*P(Nx)-qt/2;

%%%%%%%%%%%%%%%%%%%%%%%%%%%% PART_2 %%%%%%%%%%%%%%%%%%%%
```

```
Jac(Nx+1,Nx+1)=4/7*Tf*sign(P(Nx)-P(Nx+1))*abs(P(Nx)-P(Nx+1))^(-3/7);

%%%%%%%%%%%%%%%%%%
% Near-well reservoir continuity functions
Jac(Nx+2,1)    =a4;
Jac(Nx+2,2)    =a3;
Jac(Nx+2,Nx+2)=a2;
Jac(Nx+2,Nx+3)=a1;
for i=2:Nx
    Jac(Nx+i+1,i-1)    =a3;
    Jac(Nx+i+1,i)      =2*a4;
    Jac(Nx+i+1,i+1)    =a3;
    Jac(Nx+i+1,Nx+i)   =a1;
    Jac(Nx+i+1,Nx+i+1)=2*a2;
    Jac(Nx+i+1,Nx+i+2)=a1;
end
Jac(2*Nx+2,Nx)     =a3;
Jac(2*Nx+2,Nx+1)   =a4;
Jac(2*Nx+2,2*Nx+1)=a1;
Jac(2*Nx+2,2*Nx+2)=a2;
Jac=Jac+.5*Tw*eye(2*Nx+2);
%=========================================================================%
Jacs=sparse(Jac);
%visulization of pressure in each iteration steps
%    plot((Nx:-1:0)*dx,P(1:Nx+1),...
%         (Nx:-1:0)*dx, P(Nx+2:2*Nx+2),'linewidth',1.5)
%    title(sprintf('solution after %d steps',itte-1))
%    xlabel('Distance from bottom hole /m')
%    ylabel('Pressure /bar')
%    pause(.1)

%========== update values ================================================%
```

```
Pnew=P-f/Jacs;
Relative_error=abs((f/Jacs)./P);
er=sum(Relative_error(:))/N;
P=Pnew;
end

% Convert pressure to the beginning of SSS flow
 dp=P(Nx+2)-Pres;
 P=P-dp;
 plot((Nx:-1:0)*dx,P(1:Nx+1),(Nx:-1:0)*dx,P(Nx+2:2*Nx+2))

% Determine flow rates
% Axial flow
qxin=(a1*pe2+a2*pe1+a3*pw2+a4*pw1)/10^5-qt/2;
qxout=(-a2*pe2-a1*pe1-a4*pw2-a3*pw1)/10^5+qt/2;
% Radial inflow
qw=Tw*(pe2+pe1-pw2-pw1)/10^5;
% plot((Nx:-1:1)*dx,qxin,(Nx:-1:1)*dx,qw)
```

- *Code A-3: Reservoir Model in Eclipse 100*

```
RUNSPEC
TITLE
TILTED RESERVOIR WELL MODEL
SAVE
FORMATTED/
DIMENS
    20      10      5   /
OIL
WATER
METRIC
EQLDIMS
     1 20000/
TABDIMS
     1     1    20    20     1    20 /
WELLDIMS
     20    5     1     20 10 2 4   /
START
    1 'APR' 2016   /
GRID
ECHO
GRIDFILE
     1     /
DXV
    20*50
/
DYV
    10*50
/
-- Depth to top layer must be specified
TOPS
200*3000
```

```
/
DZ
 1000*50
/
EQUALS
    'PORO'      0.20      /
    'PERMX'     200       /
    'PERMY'     200       /
    'PERMZ'     200       /
/
INIT
RPTGRID
  -- Report Levels for Grid Section Data
  --
   'DX'  'DY'  'DZ'
 /
PROPS
PVDO
  250  1.4  1.177
  300  1.35  1.181
 /
PVTW
 150    1.0     4.0E-05    1.0     0.00E+00 /
DENSITY
 850   1000   /
ROCK
 150         0.40E-05 /
SWOF
    0.1000  0.0000  0.7    0
    0.1600  0.0005  0.610  0
    0.2200  0.0040  0.526  0
    0.2800  0.0135  0.448  0
```

```
    0.3400  0.0320  0.376  0
    0.4000  0.0625  0.311  0
    0.4600  0.1080  0.252  0
    0.5200  0.1720  0.199  0
    0.5800  0.2560  0.152  0
    0.6400  0.3650  0.112  0
    0.7000  0.5000  0.078  0
    0.8000  0.6670  0.035  0
    0.9000  0.8330  0.009  0
    1.0000  1.0000  0      0
/
RPTPROPS
    -- PROPS Reporting Options
    --
     'PVDO'  'PVTW'
/
SOLUTION
PRESSURE
1000*300
/
SWAT
1000*0.1
/
DATUM
   3000.0 /
RPTSOL
   -- Initialisation Print Output
   --
 'SWAT'  'RESTART=2'  'FIP=1' /
SUMMARY
FOPR
FWCT
```

```
FOE
FOPT
FPR
WOPR
/
BPR
1  5  3/
2  5  3/
3  5  3/
4  5  3/
5  5  3/
6  5  3/
7  5  3/
8  5  3/
9  5  3/
10  5  3/
11  5  3/
12  5  3/
13  5  3/
14  5  3/
15  5  3/
16  5  3/
17  5  3/
18  5  3/
19  5  3/
20  5  3/
/
SCHEDULE
--
--  WELSPECS and COMPDAT define well information in both
--  standard and LGC models.
--
```

```
WELSPECS
'OP1','GROUP1',  3, 3, 3000,'OIL' /
'OP2','GROUP1',  3, 3, 3000,'OIL' /
'OP3','GROUP1',  3, 3, 3000,'OIL' /
'OP4','GROUP1',  3, 3, 3000,'OIL'  /
'OP5','GROUP1',  3, 3, 3000,'OIL'  /
'OP6','GROUP1',  3, 3, 3000,'OIL'  /
'OP7','GROUP1',  3, 3, 3000,'OIL'  /
'OP8','GROUP1',  3, 3, 3000,'OIL'  /
'OP9','GROUP1',  3, 3, 3000,'OIL'  /
'OP10','GROUP1',  3, 3, 3000,'OIL'  /
'OP11','GROUP1',  3, 3, 3000,'OIL'  /
'OP12','GROUP1',  3, 3, 3000,'OIL'  /
'OP13','GROUP1',  3, 3, 3000,'OIL'  /
'OP14','GROUP1',  3, 3, 3000,'OIL'  /
'OP15','GROUP1',  3, 3, 3000,'OIL'  /
'OP16','GROUP1',  3, 3, 3000,'OIL'  /
'OP17','GROUP1',  3, 3, 3000,'OIL'  /
'OP18','GROUP1',  3, 3, 3000,'OIL'  /
'OP19','GROUP1',  3, 3, 3000,'OIL'  /
'OP20','GROUP1',  3, 3, 3000,'OIL'  /
/
COMPDAT
'OP1'  1  5  3  3 'OPEN'  1*  1*  0.2  1*  5.3521  1*  'x' /
'OP2'  2  5  3  3 'OPEN'  1*  1*  0.2  1*  5.2516  1*  'x' /
'OP3'  3  5  3  3 'OPEN'  1*  1*  0.2  1*  5.1457  1*  'x' /
'OP4'  4  5  3  3 'OPEN'  1*  1*  0.2  1*  5.0340  1*  'x' /
'OP5'  5  5  3  3 'OPEN'  1*  1*  0.2  1*  4.9157  1*  'x' /
'OP6'  6  5  3  3 'OPEN'  1*  1*  0.2  1*  4.7899  1*  'x' /
'OP7'  7  5  3  3 'OPEN'  1*  1*  0.2  1*  4.6556  1*  'x' /
'OP8'  8  5  3  3 'OPEN'  1*  1*  0.2  1*  4.5117  1*  'x' /
'OP9'  9  5  3  3 'OPEN'  1*  1*  0.2  1*  4.3567  1*  'x' /
```

```
'OP10' 10  5  3  3 'OPEN'  1*    1*    0.2   1*   4.1886   1*  'x' /
'OP11' 11  5  3  3 'OPEN'  1*    1*    0.2   1*   4.0050   1*  'x' /
'OP12' 12  5  3  3 'OPEN'  1*    1*    0.2   1*   3.8029   1*  'x' /
'OP13' 13  5  3  3 'OPEN'  1*    1*    0.2   1*   3.5781   1*  'x' /
'OP14' 14  5  3  3 'OPEN'  1*    1*    0.2   1*   3.3247   1*  'x' /
'OP15' 15  5  3  3 'OPEN'  1*    1*    0.2   1*   3.0346   1*  'x' /
'OP16' 16  5  3  3 'OPEN'  1*    1*    0.2   1*   2.6950   1*  'x' /
'OP17' 17  5  3  3 'OPEN'  1*    1*    0.2   1*   2.2858   1*  'x' /
'OP18' 18  5  3  3 'OPEN'  1*    1*    0.2   1*   1.7708   1*  'x' /
'OP19' 19  5  3  3 'OPEN'  1*    1*    0.2   1*   1.0753   1*  'x' /
'OP20' 20  5  3  3 'OPEN'  1*    1*    0.2   1*   0        1*  'x' /
/
WCONPROD
'OP1',   'OPEN'  ,'BHP'  1*    1*    1*    1*    1*    250.0000/
'OP2',   'OPEN'  ,'BHP'  1*    1*    1*    1*    1*    251.6136/
'OP3',   'OPEN'  ,'BHP'  1*    1*    1*    1*    1*    253.0998/
'OP4',   'OPEN'  ,'BHP'  1*    1*    1*    1*    1*    254.4657/
'OP5',   'OPEN'  ,'BHP'  1*    1*    1*    1*    1*    255.7177/
'OP6',   'OPEN'  ,'BHP'  1*    1*    1*    1*    1*    256.8614/
'OP7',   'OPEN'  ,'BHP'  1*    1*    1*    1*    1*    257.9022/
'OP8',   'OPEN'  ,'BHP'  1*    1*    1*    1*    1*    258.8450/
'OP9',   'OPEN'  ,'BHP'  1*    1*    1*    1*    1*    259.6945/
'OP10',  'OPEN'  ,'BHP'  1*    1*    1*    1*    1*    260.4550/
'OP11',  'OPEN'  ,'BHP'  1*    1*    1*    1*    1*    261.1305/
'OP12',  'OPEN'  ,'BHP'  1*    1*    1*    1*    1*    261.7249/
'OP13',  'OPEN'  ,'BHP'  1*    1*    1*    1*    1*    262.2419/
'OP14',  'OPEN'  ,'BHP'  1*    1*    1*    1*    1*    262.6851/
'OP15',  'OPEN'  ,'BHP'  1*    1*    1*    1*    1*    263.0578/
'OP16',  'OPEN'  ,'BHP'  1*    1*    1*    1*    1*    263.3634/
'OP17',  'OPEN'  ,'BHP'  1*    1*    1*    1*    1*    263.6055/
'OP18',  'OPEN'  ,'BHP'  1*    1*    1*    1*    1*    263.7876/
'OP19',  'OPEN'  ,'BHP'  1*    1*    1*    1*    1*    263.9137/
```

```
'OP20', 'OPEN' ,'BHP' 1* 1* 1* 1* 1* 263.9882/
/
RPTSCHED
    'RESTART=2' 'FIP=1' 'WELLS=1' 'SUMMARY=1' 'CPU=2'
    'WELSPECS' 'NEWTON=1' 'BASIC=2'
/
TSTEP
     1*0.5
/
SAVE
TSTEP
   1*0.5
/
END
```

- *Code A-4: Friction Well Model*

```
%%%%%%%%%%%%%%%%%%%%%%%%Friction Well Model%%%%%%%%%%%%%%%%%%%%%%%%%%%%%%%%%%%%
clear all
% Friction Well Model
% Frictional pressure loss is determined between adjacent well segments
% Flow rate in unit of m^3/s
itte=0;% Iteration numbers
er=10; % Initial relatie error
Nx=20; % Number of well segments
Ny=2;  % Row number
N=Nx*Ny;
% Well and reservoir dimension
rw=0.1;dx=1;re=20;  %unit: m
% Formation and fluid property
k=.2*10^(-12);              %unit: m2
rou=800;                    %unit: kg/m3
miu=0.001;                  %unit: pa*s
%Pressure in unit of bar, 10^5pa
Tf=2.8681*(2*rw)^(5/7)*pi*rw^2/((rou)^(3/7)*miu^(1/7)*dx^(4/7))*10^(20/7);

% Pressure determination
Pbh=200; %bar
P=zeros(1,Nx);
P(1)=Pbh;
for i=2:Nx
    P(i)=P(i-1)+(abs(q(i)/Tf))^(7/4);
end
```

Appendix B

The Dietz shape factor for an elliptic drainage region with the well in the center is determined numerically in Chapter 6 using a Laplacian solver. The implicit Laplacian solver for an elliptical reservoir is given below. Boundary conditions are specified and explained in details.

The general mass balance equation for slightly compressible single phase fluid is

$$\phi\rho c_t\frac{\partial p}{\partial t}=\nabla\left(\frac{\rho}{\mu}K\cdot\nabla p\right)+q. \tag{B-1}$$

For homogeneous and isotropic media, the conservation equation in two dimensions becomes

$$\phi c_t\frac{\partial p}{\partial t}=\frac{K}{\mu}\frac{\partial^2 p}{\partial x^2}+\frac{K}{\mu}\frac{\partial^2 p}{\partial y^2}+q. \tag{B-2}$$

An implicit discretization for the above PDE is

$$(1+2T_x+2T-y)p_{i,j}^{n+1}-T_x p_{i+1,j}^{(}n+1)-T_x p_{i-1,j}^{n+1}-T_y p_{i,j+1}^{(}n+1)-T_y p_{i,j-1}^{n+1}=p_{i,j}^{n}+\frac{\Delta tq}{\phi c_t}, \tag{B-3}$$

which is unconditional stable. Here, $T_x=\frac{K}{\phi\mu c_t}\frac{\Delta t}{\Delta x^2}$ and $T_y=\frac{K}{\phi\mu c_t}\frac{\Delta t}{\Delta y^2}$ are the transmissibility in $x-$ and $y-$ directions, respectively.

The challenge in this part is to define of the closed elliptical reservoir and boundary conditions in each boundary grid block. In the code, the active grids are first defined by satisfying the following equation

$$\frac{(x_i-a)^2}{a^2}+\frac{(y_j-b)^2}{b^2}\leq 1, \tag{B-4}$$

which means that they are inside the ellipse with major axis a and minor axis b. The active grid blocks is shown as light blue grids in Figure B-1 as an example. The inactive grid blocks, dark blue grid blocks in Figure B-1, have no connectivity to the ellipse reservoir, which indicates a closed boundary for the reservoir.The boundary is define by finite squared grid blocks, and the grid block on the boundary has closed boundary conditions but of three

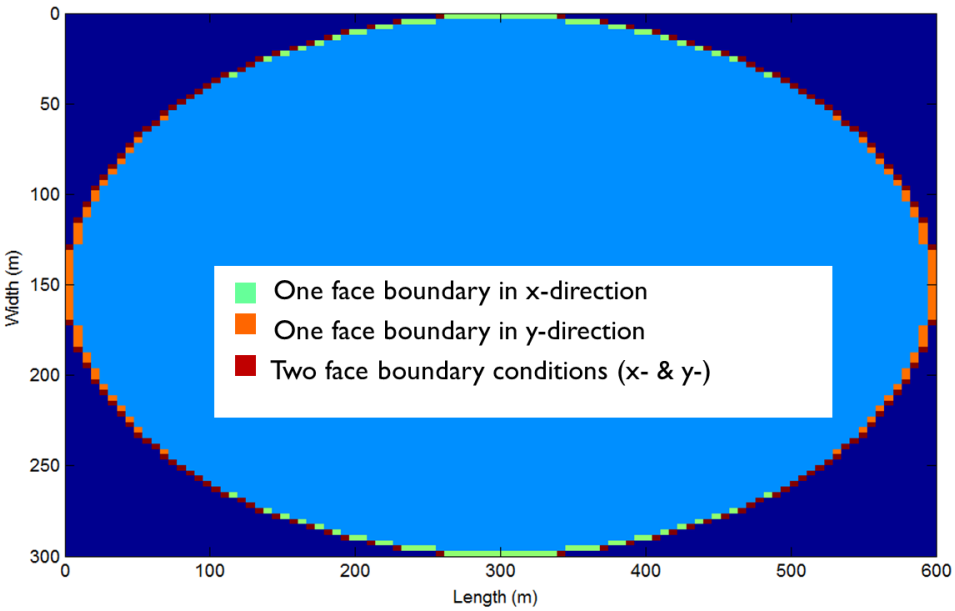

Figure B-1: Define boundary conditions for elliptical reservoir

different kinds: one face boundary in $x-$ direction, one face boundary in $y-$ direction and two face boundary in $x-$ and $y-$ directions, as shown in Figure B-1 below.

The coefficients of pressure vary on the boundary and are calculated accordingly. The problem finally results in a system of linear equations, the coefficient of which is a diagonal sparse matrix. The wellbore pressure and average reservoir pressure are solved as a function of time.

Reservoir simulators using finite difference methods are affected by grid orientation effects (Brand et al., 1991), i.e. fluid tends to flow in the direction of the grid axes rather than diagonal to them. To examine the grid orientation effects for the finite difference schematics, a rotated ellipse reservoir is defined. The reservoir is rotated by $\pi/4$ in Cartesian coordinates system, which is equivalent to using rotated Cartesian grids by $\pi/4$. The rotation of the ellipse is achieved by applying a linear transformation

$$M = \begin{bmatrix} cos(\pi/4) & -sin(\pi/4) \\ sin(\pi/4) & cos(\pi/4) \end{bmatrix}. \tag{B-5}$$

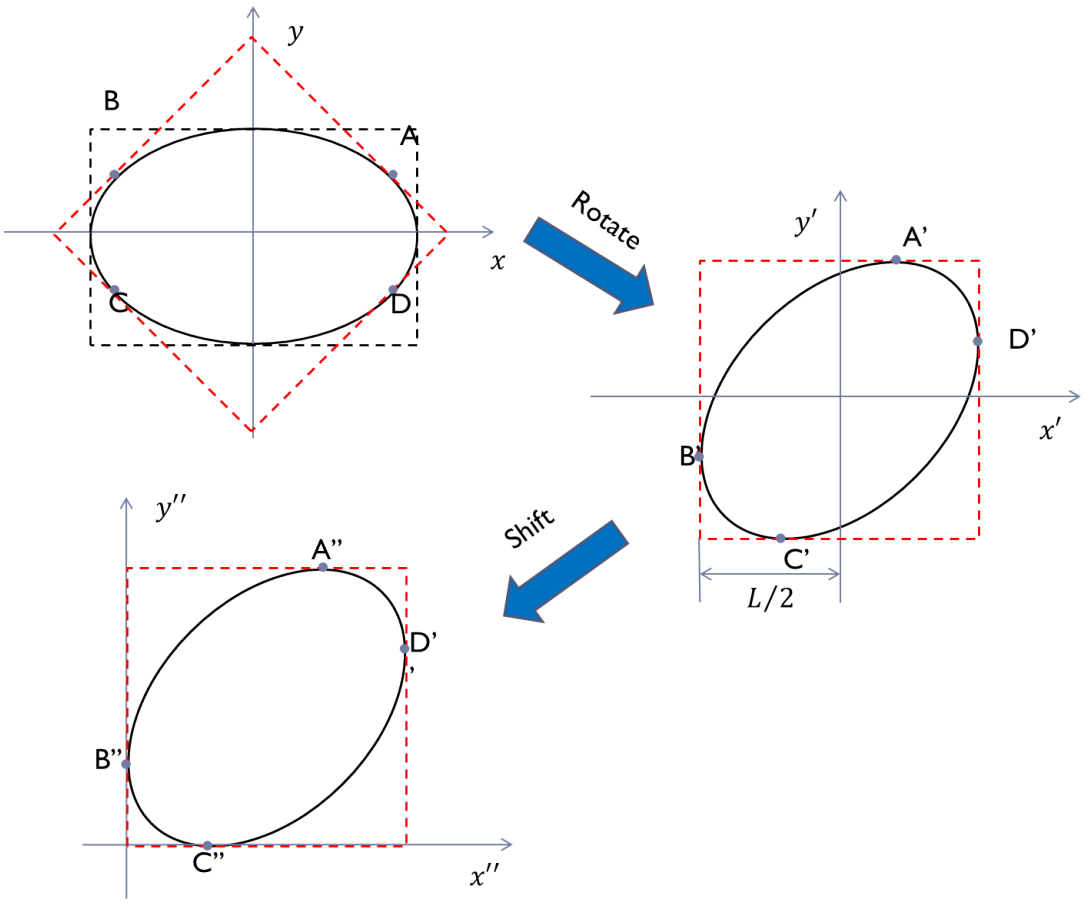

Figure B-2: Rotate and shift the ellipse reservoir

Shifting the eclipse by $(L/2L/2)$, the ellipse has the equation

$$\frac{[cos(\pi/4)(x_i - \frac{L}{2}) + sin(\pi/4)(y_j - \frac{L}{2})]^2}{a^2} + \frac{[cos(\pi/4)(y_j - \frac{L}{2}) - sin(\pi/4)(x_i - \frac{L}{2})]^2}{b^2} = 1, \tag{B-6}$$

where $L = \sqrt{2(a^2 + b^2)}$. Hence, the rotate ellipse reservoir is defined and the rest of calculation keeps the same as discussed before. For both original and rotated elliptical drainage region, the results of Dietz shape factor are shown in Figure B-3.

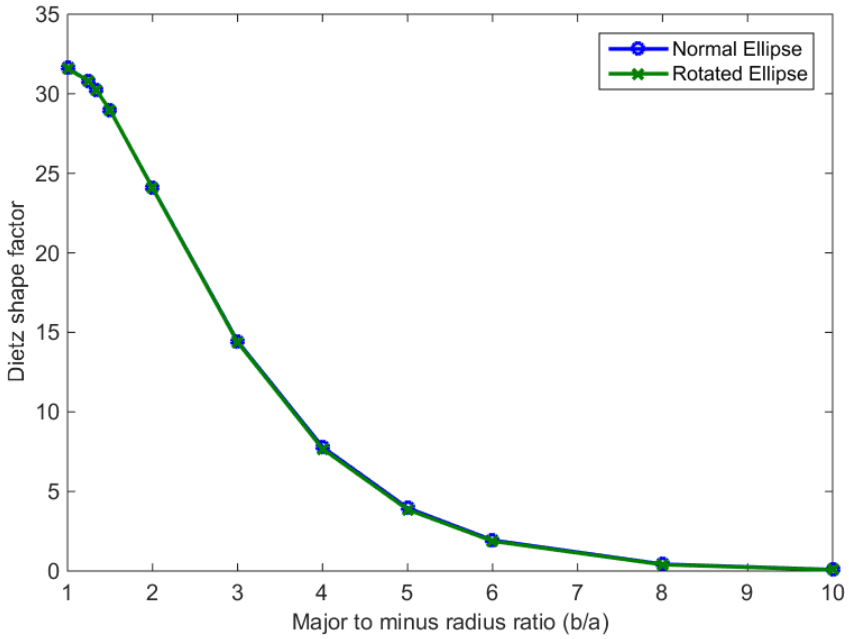

Figure B-3: Dietz shape factor for ellipses with different major to minor radius ratio

- *Code B-1: Elliptical reservoir simulator in two dimensions*

```
clear all
% Reservoir dimension
Nx=301;Ny=301;N=Nx*Ny;
a=100;b=100/(2/1);          % Ellipse major and minor radius, unit m
L=sqrt(2*(a^2+b^2));        % Length of the out boundary
dx=L/Nx;dy=L/Ny;            % Block length in X & Y direction
dz=1;                       % Depth, unit: m
% Wellbore radius, m
rw=0.140365*(dx^2+dy^2)^(0.5);
% Grid mesh
xi=0.5*dx+(0:Nx-1)*dx;
yi=0.5*dy+(0:Ny-1)*dy;
phi=0.2;            % Formation porosity
mu=10^(-3);         % Viscosity, pa s
ct=2.75*10^(-8); % Total compressibility, pa^-1
dt=3600;            % Time step, unit: second
%Sink term, flow rate per volume, unit: s^-1,
q=1.84*10^(-4)/(dx*dy*dz);
cc=sqrt(2)/2;       %constant ratio
K=zeros(Nx,Ny);
% Rotated and shift ellipse function
for i=1:Nx
    for j=1:Ny
        if (cc*(xi(i)-L/2)+cc*(yi(j)-L/2))^2/(a^2)+(cc*(yi(j)-L/2)-cc*(xi(i)-L/2))^2/
            K(i,j)=1;
        else
            K(i,j)=0;
        end
    end
end
% Transmissibility between grid blocks
```

```
tx=0.1818*dt/dx^2;   % K/(phi*mu*ct)=0.1818
ty=0.1818*dt/dy^2;
Tx=0.1818*dt/dx^2.*K;
Ty=0.1818*dt/dy^2.*K;
%surface(K)
[indi,indj]=find(K~=0);
% Active grid number, K not equal to 0
Kn=size(indi,1);
% Visulazation of active grid blocks
%surface(xi,yi,K)

% Initial pressure
pinit=20*10^(6); %pa
p0=pinit*ones(1,Nx*Ny);

% Coefficients used to define three types of boundary conditions
bdleft=zeros(Nx,Ny);
bdright=zeros(Nx,Ny);
bdup=zeros(Nx,Ny);
bddown=zeros(Nx,Ny);
for i=2:Nx-1
    for j=2:Ny-1
        if (K(i,j)==1) && (K(i-1,j)==0) && (K(i+1,j)==1)
            bdup(i,j)=1;
        elseif (K(i,j)==1) && (K(i-1,j)==1) && (K(i+1,j)==0)
            bddown(i,j)=1;
        end
    end
end
for i=2:Nx-1
    for j=2:Ny-1
        if (K(i,j)==1) && (K(i,j+1)==1) && (K(i,j-1)==0)
```

```
            bdleft(i,j)=1;
        elseif (K(i,j)==1) && (K(i,j-1)==1) && (K(i,j+1)==0)
            bdright(i,j)=1;
        end
    end
end
bdup(1,:)=K(1,:);
bddown(Nx,:)=K(Nx,:);
bdleft(:,1)=K(:,1);
bdright(:,Ny)=K(:,Ny);
yno=find(K(1,:),1,'first');bdleft(1,yno)=1;
yno=find(K(Nx,:),1,'first');bdleft(Nx,yno)=1;
xno=find(K(:,1),1,'first');bdup(xno,1)=1;
xno=find(K(:,Ny),1,'first');bdup(xno,Ny)=1;
yno=find(K(1,:),1,'last');bdright(1,yno)=1;
yno=find(K(Nx,:),1,'last');bdright(Nx,yno)=1;
xno=find(K(:,1),1,'last');bddown(xno,1)=1;
xno=find(K(:,Ny),1,'last');bddown(xno,Ny)=1;

K1=zeros(Nx,Ny);
for i=2:Nx-1
    for j=2:Ny-1
        if (K(i,j)~=0) && (K(i-1,j)+K(i+1,j)==1) && (K(i,j+1)+K(i,j-1)==2)
            K1(i,j)=1;  %one face boundary; left or right only
        elseif (K(i,j)~=0) && (K(i-1,j)+K(i+1,j)==1) && (K(i,j+1)+K(i,j-1)==1)
            K1(i,j)=2; %two face boundary;left or right PLUS up or down
        elseif (K(i,j)~=0) && (K(i-1,j)+K(i+1,j)==2) && (K(i,j+1)+K(i,j-1)==1)
                K1(i,j)=1.5; % one face boundary; up or down only
        elseif K(i,j)~=0
                    K1(i,j)=0.5;
        end
    end
```

```
end
K1(1,:)=K(1,:);
K1(Nx,:)=K(Nx,:);
K1(:,1)=1.5*K(:,1);
K1(:,Ny)=1.5*K(:,Ny);
yno=find(K1(1,:),1,'first');K1(1,yno)=2;
yno=find(K1(Nx,:),1,'first');K1(Nx,yno)=2;
xno=find(K1(:,1),1,'first');K1(xno,1)=2;
xno=find(K1(:,Ny),1,'first');K1(xno,Ny)=2;
yno=find(K1(1,:),1,'last');K1(1,yno)=2;
yno=find(K1(Nx,:),1,'last');K1(Nx,yno)=2;
xno=find(K1(:,1),1,'last');K1(xno,1)=2;
xno=find(K1(:,Ny),1,'last');K1(xno,Ny)=2;

K2=zeros(Nx,Ny);
for i=1:Nx
    for j=1:Ny
        if K1(i,j)==1
            K2(i,j)=tx;
        elseif K1(i,j)==1.5
            K2(i,j)=ty;
        elseif K1(i,j)==2
            K2(i,j)=tx+ty;
        end
    end
end



m1a=-Tx;m1a(:,1)=0;%left
m1b=-Tx;m1b(:,Nx)=0;%right
m2a=-Ty;m2a(1,:)=0;%up
m2b=-Ty;m2b(Ny,:)=0;%down
```

```
for i=1:Nx
    for j=1:Ny
        if bdleft(i,j)==1
            m1a(i,j)=0;
        elseif bdright(i,j)==1
            m1b(i,j)=0;
        end

    end
end
for i=1:Nx
    for j=1:Ny
        if  bdup(i,j)==1
            m2a(i,j)=0;
        elseif bddown(i,j)==1
            m2b(i,j)=0;
        end

    end
end

m1a=m1a'; m1b=m1b'; m2a=m2a'; m2b=m2b';
m11=reshape(m1a,Nx*Ny,1);
m12=reshape(m1b,Nx*Ny,1);
m22=reshape(m2b,Nx*Ny,1);
m21=reshape(m2a,Nx*Ny,1);

m33=1+2*Tx+2*Ty;%principal(center)
m33=m33-K2;
m3=reshape(m33,Nx*Ny,1);
```

```
% Linear solver using MATLAB, sparse coefficient matrix
DiagVecs=[m22, m12, m3, m11, m21];
DiagIndx=[-Nx, -1, 0, 1, Nx];
M=spdiags(DiagVecs, DiagIndx, Nx*Ny, Nx*Ny);

% Transient of pressure in each time step
% i is the number of time step,
for i=1:30
B=p0;B(ceil(Nx*Ny/2))=B(ceil(Nx*Ny/2))-q*dt/phi/ct;
p=B/M;
p0=p;
t(i)=i;
pw(i)=p0(ceil(Nx*Ny/2));
pta(i)=sum(p0(:))/(Nx*Ny);
activep=reshape(p0,Nx,Ny).*K;
pa(i)=(sum(activep(:))-pw(i))/(Kn-1);
end

pt=reshape(p,Nx,Ny);
[NX,NY] = meshgrid((1:Nx)*dx,(1:Ny)*dy);
% Visualization of pressure distribution
surface(NX,NY,pt)
%plot([0 t],[pinit pw],[0 t],[pinit pa])
Ca=exp(log(4*pi*a*b/(1.781*rw^2))-4*pi*10^(-12)*dz*(pa(end)-pw(end))/(q*dx*dy*dz*mu)
```